Modélisation de la dynamique virale du SARS-CoV-2 : implication pour l'évaluation thérapeutique

Guillaume Lingas

Université Paris Cité

Ecole Doctorale 393 Pierre Louis de Santé Publique : Epidémiologie et Sciences de l'Information Biomédicale

Unité de recherche : UMR 1137 - Infections, Antimicrobiens, Modélisation, Evolution

Equipe : Modélisation biostatistique, pharmacométrie et investigation clinique dans les maladies infectieuses

MODÉLISATION DE LA DYNAMIQUE VIRALE DU SARS-COV-2 : IMPLICATION POUR L'ÉVALUATION THÉRAPEUTIQUE

Guillaume Lingas

Thèse de doctorat de biostatistiques

Dirigée par le Docteur Jérémie Guedj

Présentée et soutenue publiquement le 11 octobre 2022

Composition du jury de thèse

Rapporteur	Mr Samuel Alizon, DR	CNRS
Rapporteur	Mr Guillaume Martin-Blondel, PU-PH	Université de Toulouse
Examinatrice	Mme Sylvie Van Der Werf, PU	Université Paris Cité
Examinateur	Mr Fabrice Carrat, PU-PH	Sorbonne Université
Examinatrice	Mme Mélanie Prague, CR	INRIA
Directeur de thèse	Mr Jérémie Guedj, DR	INSERM

Table des matières

Remerciements

Merci à Jérémie, mon directeur de thèse, pour avoir souvent (pas toujours) cru en moi et avoir été patient malgré toutes les réunions manquées pour problèmes d'oreiller, les deadlines non respectées et les présentations préparées à la dernière minute. Merci pour tout ce que tu m'as appris, notamment pour le professionnalisme que j'ai acquis durant ces 3 dernières années. Merci de m'avoir transmis ta passion et tes connaissances. J'espère collaborer avec toi encore longtemps, au-delà des 3 prochaines années en tout cas. Ne soit pas trop strict cependant, sinon je m'envole à Bordeaux ou à Pasteur.

Merci également à France de m'avoir accueilli dans ce laboratoire exceptionnel, rempli de personnes exceptionnelles, ce qui m'a permis de vivre une expérience exceptionnelle. Merci à Julie de transmettre cette maladie appelée « bonne humeur » et de me donner de l'espoir concernant certains domaines.

Je remercie également les membres de mon jury pour avoir accepté d'évaluer ce travail, et tout particulièrement les deux rapporteurs, Samuel Alizon et Guillaume Martin-Blondel, pour leurs retours et commentaires très enrichissants. Merci également à Sylvie Van Der Werf, Fabrice Carrat et Mélanie Prague d'avoir accepté de faire partie de mon jury.

Merci à toutes les personnes brillantes qu'il m'a été donné l'occasion de rencontrer, notamment Emmanuelle Comets, Solen Kernéis et Delphine Planas. Mention spéciale à Benoit Visseaux et Benjamin Tellier, qui au milieu d'échanges de mails très professionnels sont toujours capables de sortir des punchlines.

Merci à Nadège/Nadia, pour m'avoir supporté malgré toutes les boulettes que j'ai pu faire qui nous ont fait perdre un temps monstre et finir au téléphone à 5h du mat ou dans le bateau pour la Corse.

Merci de m'avoir transmis une partie (seulement) de ta rigueur, pour tout le travail que nous avons accompli ensemble, et surtout pour ton amitié sans faille qui nous a permis de survivre à la pression imposée par la fameuse communauté. Je viendrai faire des roues arrières en T-max dans ton quartier pour réveiller Augustus, mais seulement une fois que j'aurai fini de faire tourner mon modèle bancal. Après tout, ti es quasiment la famille, vu que selon certains on serait mariés.

Merci à Victor, pour m'avoir nourri ces 2 dernières années (je pense vraiment que j'aurais fini en service de nutrition sans toi), dans cette coloc qui n'aurais vraiment pas pu mieux se passer. Merci pour ces moments, entre les éclatages de manettes sur le sol, les parties en coop sur Divinity et pour toutes les fois où j'ai buté dans les bouteilles du cimetière. J'espère que tu kifferas ta vie quelle que soit l'endroit où tu t'en vas, et que ton futur coloc si tu en as un n'étaleras pas ses fringues mouillées sur tous les meubles de l'appart. Fais gaffe à pas péter ton canapé avec ton gros fiak et quand tu t'étoufferas dans le curry de la veille étalé sur le tapis. Long live la coloc du $wag, et surtout n'oublie pas de prendre ta tisane.

Merci à Chloé de patienter 3 semaines avant que je réponde à ses messages sans péter un câble. Promis on se voit bientôt hein. Bises à Bruno et Andrée.

Merci à Royksopp, Cwaneuw, Swarper et thibza, pour toutes ces soirées endiablées, entre inting, insultes, clash, poker et tarot africain. Merci de m'avoir porté dans votre petit sac. Comme quoi on peut être bac +8 et Bronze 8.

Merci à tout IAME, passé présent et futur.

Merci à Aurélien, mon collègue de bureau, de rot, d'Alt Tab au moindre bruit de pas et de beauferie en général. Je ne pensais jamais m'assoir dans le métro sur les genoux d'un collègue rencontré 3 mois avant. J'attends toujours tes méthodes et ton Lydia de 15 balles. Merci à Drifa, notre petit soleil à tous, pour toujours répondre présente, souriante et incroyablement incroyable. Bravo pour avoir

réussi à survivre à ces 3 dernières années, pour avoir fait en 6 semaines ce que tu aurais dû faire en 6 ans. Merci de ne pas nous avoir étranglés Nadège et moi lorsqu'on te posait 30000 fois les mêmes questions et qu'on incitait des personnes à te rajouter du boulot (« Tiens Drifa pourrait le faire »). Je suis fier de connaitre une Française comme toi, qui n'a même pas besoin de permis de séjour. Merci à Emilie (et Naïade), pour ces karaokés Disney, pour cette motivation à organiser des trucs parce que tu es entourée de glandus et cette auto dérision (là j'espère juste que ça en est vraiment) qui t'es unique. Ne change rien, à part peut-être de taf au pire. Jinju tu es bonne sa mère. A Alsexandra, et nos discussions profondes sur des sujets de société que je ne mentionnerai pas ici. A Selmamacita, que je n'ai pas vu depuis longtemps mais dont le rire hante mes cauchemars. A Mélanight, aka le poney qui cavale au milieu de Saint-Malo avec une bière à la main à 4h du matin. Je te déteste. A Antoine, mon futur cuisinier et colocataire. J'ai hâte de regarder des matchs de foots de Bastia avec toi. A Morgane l'enfant-bulle hystérique, on fait du Double-Up quand tu veux. A Julien, mon stagiaire de M2 devenu poto, qui a été une belle expérience professionnelle. A bientôt quand tu feras ta thèse chez nous. A Ibtissem, la surexcitée, compagne de clopes et d'histoires croquantes. Appelle Yacine on a un projet à réaliser. A Antonio, pour m'avoir beaucoup aidé à mon arrivée au laboratoire, et qui m'a permis de ne pas passer totalement pour une quiche. A Ruben, Rudy et Nico la team du -2, pour tous ces moments passés ensembles à rigoler comme des cons, parfois bourrés, et parler de tout sauf de sciences. Enfin, à Houda, Jimmy, Cédric, Coralie, Romain, Lionel, Marilou, Niccolo, Hind, Lucie, Gaëlle, Maxime, Jérémy, Arthur, Aloïs (ma ptite crème), Marie, Nour et tous ceux que j'oublie.

A Marion K, pour m'avoir fait vivre des montagnes russes plus rudes que Space Moutain sous crack. Je n'aime pas dire du mal des gens, mais tu es gentille. C'est vraiment compliqué ces remerciements tu m'as volé les compliments que je voulais dire à ton sujet dans ta thèse. Ouais je veux me battre ouais, tu vas faire quoi ? Répond pas dfaçon ça sert à rien.

A Océ, source de plein de découvertes culturelles du dimanche, et puis un jour peut-être ce sera un dimanche de décuvage comme au bon vieux temps.

A Béné, pour être la référence de mon échelle de « je me kiffe de ouf ». Oui, tu es folle. Mais on peut faire le GR20 l'été prochain si tu trouves le temps entre 2 mails.

A tous ces couples qui m'ont mis un coup de vieux en décidant de se marier bientôt : Sibybylle et Carl, Mam' Gat et Philippe, Loyo et Momo et enfin Hermine et Guillaume. Vous mettez pas du tout la pression autour de vous hein.

Merci à Gomar Paris-Marseille pour toutes ces séances d'escalade, les pates aux légumes et autres délicatesses. Un jour il faudra que tu récupères ton cadeau de Secret Santa quand même (au pire je t'offre du Loxapac). Merci à Kantos d'être une machine. J'espère qu'à l'heure où j'écris ces lignes tu auras réussi à intuber. Merci à Sousou pour être toujours hilarante à ses dépens (Zboubloubloublou). Merci à mon co-DJ Denos, à bientôt dans les tonus. Eh Clem, est-ce que t'as … ? A Adrien, Baptiste, Albane et tous ceux que j'oublie.

A mes vieux amis, qu'il faut que je revoie un jour : Aymar, Elliott et Victor. Maintenant que je peux ressortir de mon trou, on part se faire un kébab à Berlin ?

A Thibault, qui en est je ne sais ou dans sa vie, peut-être un jour tu reviendras en France.

A Marion H. Si je disais toutes les choses pour lesquelles je te suis reconnaissant ce manuscrit coûterait 1200€ à faire imprimer. Mais merci quand même d'avoir résisté au Lydia.

Merci à Pappa, pour toujours t'être intéressé à ce que je faisais (tu l'as mon titre de thèse maintenant). Merci de m'avoir toujours supporté dans mes idées et de faire ton maximum pour que j'arrive à mes fins, même quand j'ai décidé de partir de la maison. J'espère te rendre fier de moi, et ce n'est que le début. Merci à mes frères et sœurs, d'être toujours autant chaotiques. Mention spéciale à Amira, la petite nouvelle de la famille.

Enfin, merci à Nils et au Dr Tonnellier, sans qui cette thèse n'aurait jamais vu le jour.

Maintenant, préparez-vous à lire une belle histoire écrite de 23h à 7h du matin sous une combinaison de Red Bull, café, coca, amphétamines, cocaïne, anxiolytiques et antidépresseurs, le tout en IV Bolus.

Comme dirait un grand homme : « Tous les modèle sont faux, surtout les tiens ».

Contexte de la thèse

Ce travail de thèse a commencé en octobre 2019 et portait sur la modélisation de la dynamique virale de virus émergents chez des primates non-humains traités par une molécule redirigée, le favipiravir. Le premier volet de cette thèse portait sur le virus de Lassa administré chez des primates non-humains, qui a donné lieu à une publication dans PLoS Computational Biology (en annexe). A partir de mars 2020, grâce à l'implication de mon laboratoire dans l'étude de la pandémie de SARS-CoV-2, j'ai redirigé mes efforts vers la description de la dynamique virale de cette nouvelle maladie. J'ai tout d'abord abordé la problématique de l'histoire naturelle de la maladie chez des patients hospitalisés qui n'étaient pas traités. Au cours de l'année 2021, j'ai pu utiliser ce que nous avions appris du virus afin d'évaluer l'efficacité virologique d'un traitement antiviral, le remdesivir, dans le cadre de l'essai DisCoVeRy. Enfin, j'ai pu continuer à travailler sur le favipiravir et son impact sur la dynamique virale du SARS-CoV-2, étudié chez le hamster syrien doré puis le primate non-humain.

Production scientifique liée à la thèse

Publication principales

— Néant N*, Lingas G*, Le Hingrat Q*, Ghosn J, Engelmann I, Lepiller Q, Gaymard A, Ferré V, Hartard C, Plantier JC, Thibault V, Marlet J, Montes B, Bouiller K, Lescure FX, Timsit JF, Faure E, Poissy J, Chidiac C, Raffi F, Kimmoun A, Etienne M, Richard JC, Tattevin P, Garot D, Le Moing V, Bachelet D, Tardivon C, Duval X, Yazdanpanah Y, Mentré F, Laouénan C*, Visseaux B*, Guedj J* ; French COVID Cohort ; Modeling SARS-CoV-2 viral kinetics and association with mortality in hospitalized patients from the French COVID cohort, *Proceedings of the National Academy of Sciences*, 2021

— Lingas G*, Néant N*, Gaymard A, Belhadi D, Peytavin G, Hites M, Staub T, Greil R, Paiva JA, Poissy J, Peiffer-Smadja N, Costagliola D, Yazdanpanah Y, Wallet F, Gagneux-Brunon A, Mentré F, Ader F, Burdet C, Guedj J*, Bouscambert-Duchamp M* ; DisCoVeRy study group ; Effect of remdesivir on viral dynamics in COVID-19 hospitalized patients : a modelling analysis of the randomized, controlled, open-label DisCoVeRy trial, *Journal of Antimicrobial Chemotherapy*, 2022

— Marlin R*, Desjardins D*, Contreras V*, Lingas G*, Solas C*, Roques P*, Naninck T, Pascal Q, Behillil S, Maissonnsse P, Lemaitre J, Kahlaoui N, Delache B, Pizzorno A, Nougairede A, Ludot C, Terrier O, Deruddre-Bosque N, Relouzat F, Chapon C, Ho Tsong Fang R, Van Der Werf S, Rosa Calatravas M, Malvy D, de Lamballerie X, Guedj J*, Le Grand R* ; Antiviral efficacy of favipiravir against Zika and SARS-CoV-2 viruses in non-human primates, Publié dans *Nature Communications*

Autres publications

— Lingas G, Rosenke K, Safronetz D, Guedj J ; Lassa viral dynamics in non-human primates treated with favipiravir or ribavirin, *PLoS Computational Biology*, 2021 (Annexe 1)

— Driouich JS, Cochin M, Lingas G, Moureau G, Touret F, Petit PR, Piorkowski G, Barthélémy K, Laprie C, Coutard B, Guedj J, de Lamballerie X, Solas C, Nougairède A ; Favipiravir antiviral efficacy against SARS-CoV-2 in a hamster model, *Nature Communications*, 2021 (Annexe 2)

— Driouich JS, Lingas G, Luciani L, Cochin M, Saba Villarroel PM, Moureau G, Petit P-R, Touret F, Guedj J, de Lamballerie X, Nougairède A ; Activity of Tixagevimab/Cilgavimab against the Omicron variant of SARS-CoV-2 in a hamster model, en révision dans *eBioMedicine* (Annexe 3)

*contribution équivalente

Chapitre 1

Introduction au SARS-CoV-2

1.1 Epidemiologie

Apparu en décembre 2019 dans la province de Wuhan en Chine [1, 2], le SARS-CoV-2 (Severe Acute Respiratory Syndrom - Coronavirus - 2), agent étiologique du Covid-19 (COronaVIrus Disease 2019) a touché plus de 500 millions de personnes [3]. Ce virus a été en 2 ans la cause directe de plus de 6 millions de décès et provoquant une surmortalité de 18 millions d'individus [4]. La létalité de cette pathologie est moindre que celle d'autres épidémies de maladies infectieuses [5, 6]. Cependant, sa diffusion a été extrêmement rapide à travers le monde et facilitée par son mode de transmission respiratoire par gouttelettes/aérosols et par des phénomènes de transmission asymptomatiques. De ce fait, moins de 3 mois après l'apparition des premiers cas et avec 114 pays touchés, l'Organisation Mondiale de la Santé a qualifié le phénomène de "pandémie" [7]. Le nombre de reproduction initial R_0, soit le nombre de personnes que contamine une personne infectée dans la population totalement susceptible au début de l'épidémie, a été estimé à 3 [8]. L'impact des différentes vagues sur les populations a varié selon les mesures sanitaires mises en place dans chaque pays et sur les caractéristiques des souches apparues au cours du temps. Les premières mesures mises en place ont été des interventions non-pharmaceutiques telles que l'instauration de la distanciation sociale associée au

port du masque obligatoire, ainsi que la fermeture des écoles permettant une grande réduction de la transmission [9, 10]. Les mesures les plus drastiques ont été l'instauration d'un couvre-feu ainsi que le confinement à domicile, qui ont permis de réduire les contacts inter-personnes [11, 12]. Enfin, la mesure la plus récente pour endiguer la surcharge hospitalière a été l'arrivée de la vaccination, qui a permis de réduire considérablement le risque d'évolution vers une forme grave [13-15]. La combinaison de toutes ces mesures a permis d'endiguer l'épidémie, cependant, chacune de ces mesures a ses limites, comme décrit par le modèle du "Swiss Cheese" (Figure 1.1). Il est nécessaire également d'avoir des thérapeutiques permettant de traiter la population qui développe une forme sévère malgré ces mesures, comme les personnes immunodéprimées ne répondant pas à la vaccination. Celle-ci connaît également d'autres limites, d'une part à cause de la diminution de son efficacité au cours du temps et d'autre part suite à l'émergence de nouveaux variants d'intérêt (*Variants of concerns*, VoC). Afin de perpétuer son efficacité au cours du temps, il est donc nécessaire d'administrer des doses de rappels régulièrement. La longévité de la protection contre l'acquisition de forme grave dure environ 6 mois, mais cette durée connaît une certaine hétérogénéité [16]. De plus les différents VoC qui ont émergé présentent des mutations sur la protéine Spike, la cible principale des anticorps produits suite à une infection naturelle ou à la vaccination. Les VoC principaux qui sont apparus ont été successivement les variants Alpha, Beta, Gamma, Delta puis Omicron, et ont été responsables des différentes vagues de contamination en France.

1.2 Virologie

Le SARS-CoV-2 fait partie de la famille des *coronaviridae*, plus précisément du genre *betacoronavirus*, similairement aux deux autres coronavirus responsables d'épidémies de ce siècle : le SARS-CoV(-1) (2003) et le MERS-CoV (2012), avec lesquels il partage certaines caractéristiques [17]. Il s'agit

FIGURE 1.1 – Modèle de l'emmental

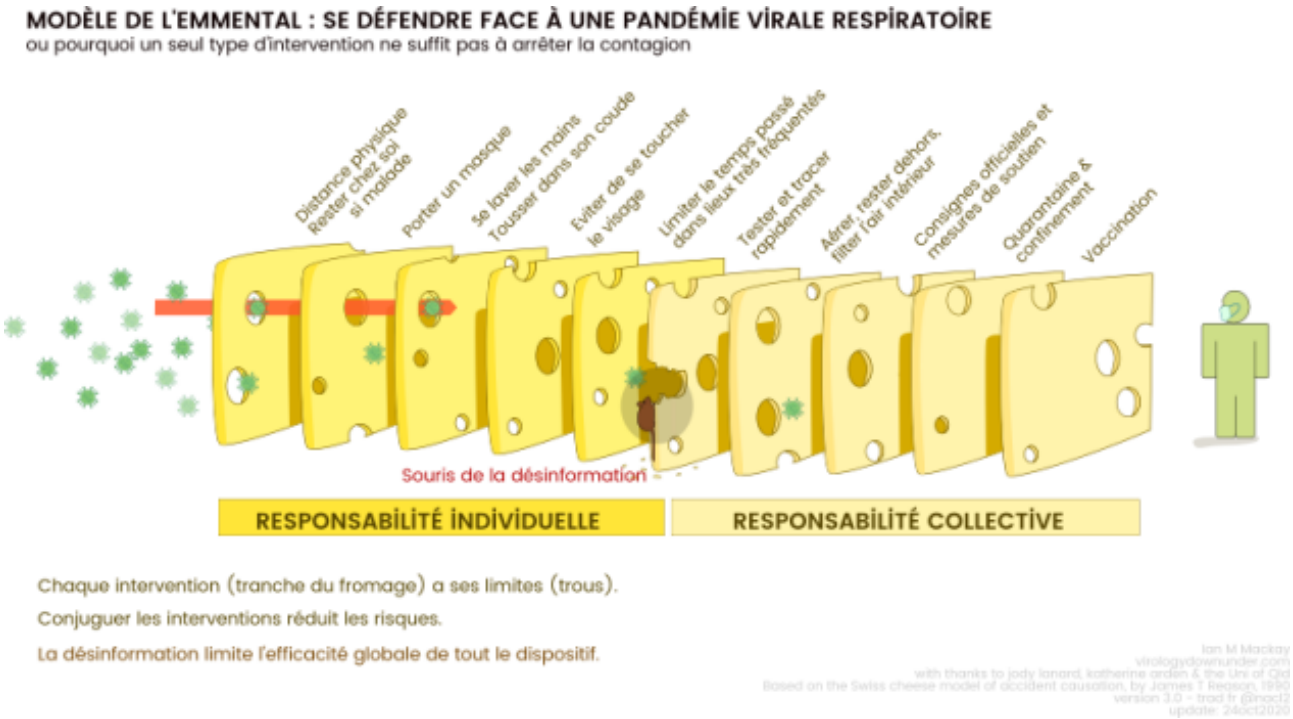

d'un virus à ARN simple brin, dont le diamètre est compris entre 60 et 140 nm ([18], Figure 1.2). Son génome est identique à 80% au SARS-CoV-1 et 50% au MERS-CoV [19]. Composé d'environ 30 kilobases [20], il encode pour différentes protéines, dont les 4 protéines structurales : l'enveloppe (E), la membrane (M), le nucléocapside (N) et enfin la protéine spiculaire, dite Spike (S). Ce sont les mutations de cette dernière qui confèrent des avantages de résistance face aux anticorps monoclonaux.

Cycle de réplication

Le virus cible particulièrement les cellules exprimant le récepteur à l'enzyme de conversion de l'angiotensine 2 (ACE2), la pénétration du virus pouvant être facilitée par la présence de co-récepteurs, comme la protéase transmembranaire à sérine 2 (TMPRSS2). Il existe deux modes d'entrée principaux dans une cellule exprimant ACE2, la voie endosomale et la voie directe par fusion de membrane [21]. Ces mécanismes reposent tous les deux sur la reconnaissance du recepteur ACE2, exprimé à la surface des cellules cibles, par la protéine Spike (S) [22, 23]. Cette protéine Spike est

FIGURE 1.2 – Schéma du SARS-CoV-2 et génome

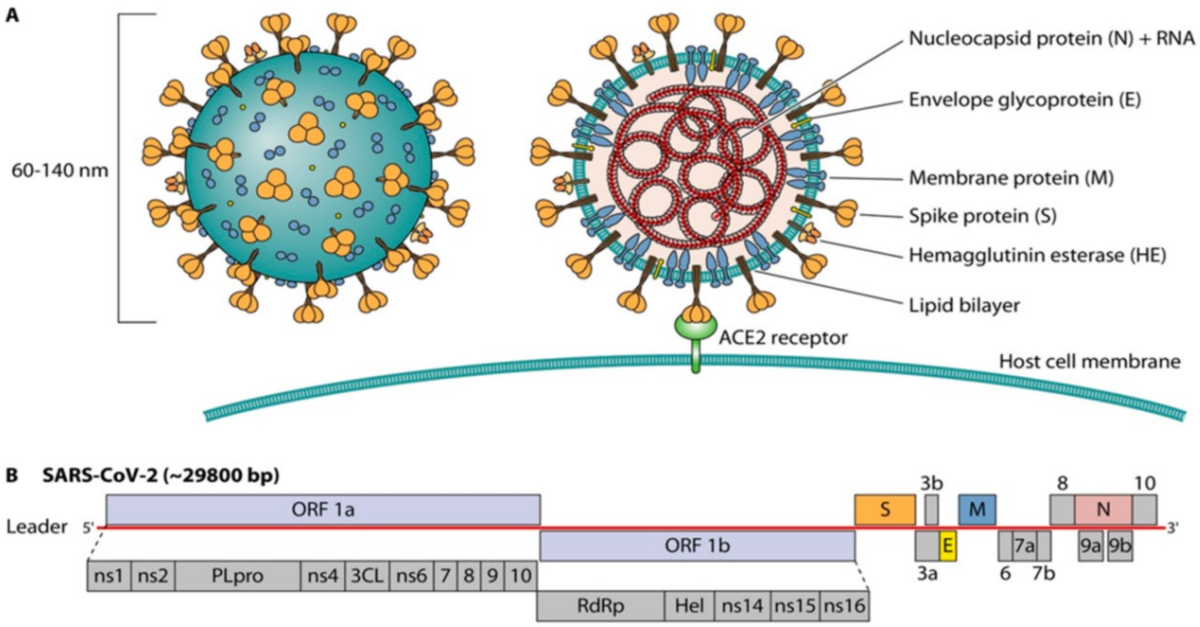

clivée lors de sa formation par la furine, une proprotéine convertase, en deux sous-parties associées de manière non covalente, S1 et S2 [24]. La sous-partie S2, exposée suite à un changement de conformation subséquent à la reconnaissance du recepteur ACE2, doit être clivée par le biais d'enzyme afin de permettre l'exposition du peptide de fusion de membrane, mécanisme qui précède la libération de l'ARN viral dans le cytoplasme de la cellule [25]. Dans le cas de la voie endosomale, le virus va être internalisé selon un processus d'endocytose à l'intérieur d'un "manteau de clathrine" [26], pour former un endolysosome. A la suite de l'acidification de l'endolysosome, la sous-partie S1 de la protéine S va être excrétée, exposant ainsi la sous-partie S2. L'enzyme cathepsine-L va ensuite cliver cette sous-partie S2, permettant l'exposition du peptide de fusion. Ceci permet ainsi la fusion avec la membrane plasmatique de l'endolysosome, et la libération de l'ARN viral dans le cytoplasme. Dans le cas de la voie directe, la réaction enzymatique permettant l'exposition du peptide de fusion se produit au niveau de la membrane plasmatique de la cellule, grâce au co-récepteur TMPRSS2. Dans ce cas, la membrane du virus fusionne avec la membrane de la cellule elle-même et la molécule d'ARN

est libérée à l'intérieur du cytoplasme [27].

Une fois libre, cette molécule d'ARN va être ensuite répliquée puis traduite en polypeptides qui vont être protéolysés, pour donner notamment l'ARN polymérase (RdRP). Celle-ci va pouvoir transcrire la molécule d'ARN initiale dans son entièreté vers de l'ARN sous-génomique qui encode pour les protéines structurales. Cet ARN va ensuite être traduit dans le réticulum endoplasmique et aller dans l'appareil de Golgi, où le virion va être assemblé puis relâché (Figure 1.3).

FIGURE 1.3 – Cycle de réplication du SARS-CoV-2 et traitements, réalisé à partir de Jackson et al. et Bailey et al. [27, 28]

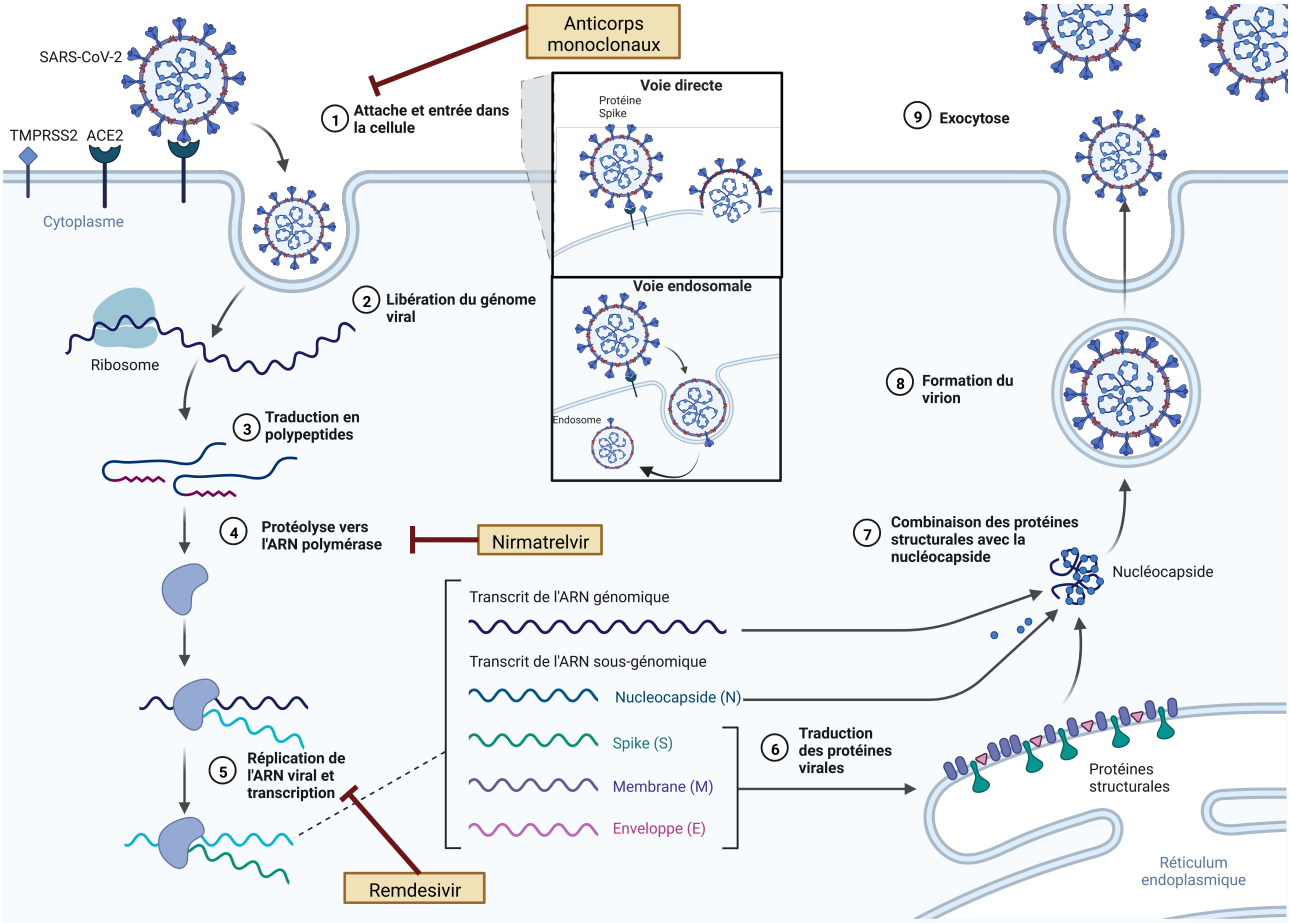

1.3 Physiopathologie

Du fait de son mode de transmission aéroporté, le tropisme primaire se situe principalement dans les voies respiratoires, supérieures (oropharynx et nasopharynx) tout d'abord, puis se diffuse dans les voies respiratoires inférieures (système broncho-pulmonaire).

Au sein de ces voies respiratoires, il existe un gradient d'infectivité, qui évolue de manière parallèle à celui de l'expression du récepteur ACE2. En effet, les cellules ciliées présentes à la surface de la muqueuse nasale ont un haut taux d'expression d'ACE2, et ce taux d'expression diminue au fur et à mesure que l'on descend dans l'appareil pulmonaire [29]. Les cellules ciliées de la cavité nasale sont ainsi le lieu de réplication principal dans l'infection initiale, de par leur taux d'expression d'ACE2 et par le fait qu'elles soient les cellules les plus exposées au pôle apical de la muqueuse nasale [30]. La dissémination se poursuit ensuite dans la trachée de par leur proximité spatiale. Les sécrétions de l'oropharynx permettent ensuite l'infection des poumons de manière mécanique, par aspiration [31, 32], faite pendant le sommeil. Un autre site de prédilection de réplication du virus est le système digestif. En effet, c'est là qu'on retrouve une grande expression d'ACE2 [33]. De plus, on retrouve également une expression de TMPRSS2 dans les pneumocytes de type 2, les entérocytes iliaux et les cellules nasales goblets [34]. L'ARN viral a été retrouvé également dans les selles et les urines [32, 35, 36]. Des autopsies post-mortem [33] ont également noté la présence d'ARN viral dans de nombreux organes, notamment le système lymphatique, le système endocrine avec les glandes thyroïdes et surrénales, le système nerveux, le système cardiovasculaire, le système uro-génital et enfin dans le sang (Figure 1.4).

FIGURE 1.4 – Tropisme du SARS-CoV-2, issu de Wong et al. [37]

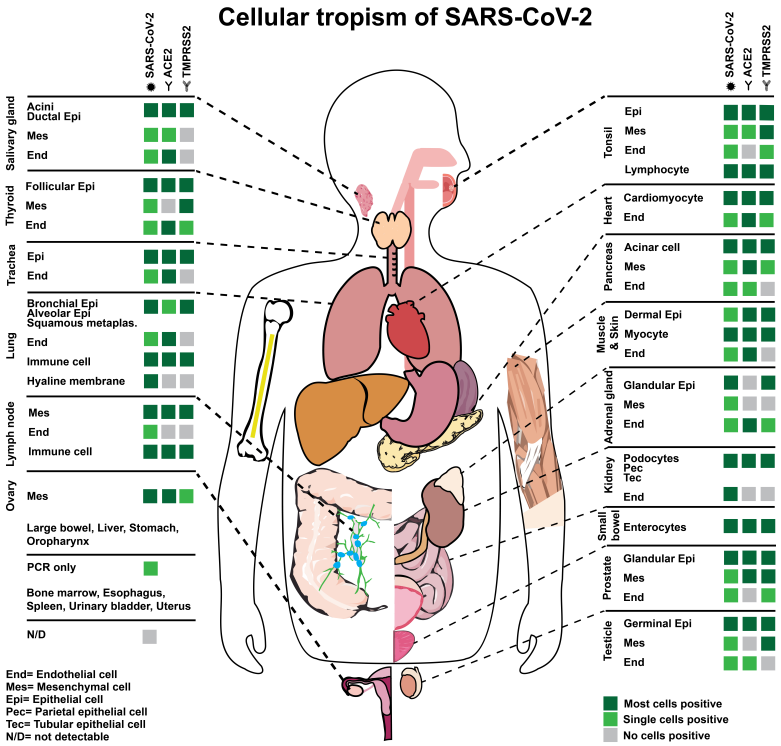

1.4 Symptomatologie

L'OMS classe les patients en trois catégories, selon la gravité de leurs symptômes : la forme bénigne (exempte de signes de forme grave ou critique), grave (saturation en oxygène < 90%, signes de pneumonie ou signes de détresse respiratoire grave) et critique, qui regroupe les syndrômes de détresse respiratoire aiguë, un état ou un choc septique, ou encore la nécessité de soins vitaux tels que la ventilation mécanique ou l'administration de vasopresseurs [38].

Symptômes principaux chez le patient ambulatoire

Le tropisme extrêmement divers de ce virus va de pair avec les différents symptômes retrouvés. Le siège initial de la réplication virale étant le nasopharynx, la plupart des personnes présentent de la fièvre (83-99 %), une toux (59-82 %), une fatigue (44-70 %), une anorexie (40-84 %), un essouf-

flement (31-40 %) et des myalgies (11-35 %) [39]. De plus, le SARS-CoV-2 étant capable d'infecter les neurones olfactifs sensoriels [40], l'inflammation provoquée et la perte des cils de ces neurones présents dans la muqueuse nasale a été proposée comme responsable de l'anosmie [41]. Un autre symptômes neurologique couramment retrouvé également est l'agueusie, dont la physiopathologie est encore non expliquée. Cependant, la capacité du SARS-CoV-2 à infecter le système nerveux central et les cellules épithéliales de la langue est une piste envisagée pour expliquer ce phénomène [37].

1.5 Réponse immunitaire

La réponse primaire innée à l'infection par un virus consiste en la production d'interférons de type I (IFN-α & β) et III (IFN-λ). Dans les infections virales aigües, la production d'interféron entraîne la transcription de gènes dits "IFN-stimulated", qui confèrent des propriétés antivirales et rendent notamment les cellules réfractaires à l'infection [42]. Cependant, le SARS-CoV-2 a montré une certaine capacité à échapper à cette réponse immunitaire, notamment en la neutralisant, et à induire une réponse inflammatoire importante [43]. De nombreux travaux ont de plus montré qu'une réponse immunitaire dérégulée ou déficiente était corrélée à une maladie plus sévère (Figure 1.5) [33, 43-46], ceci même à charges virales équivalentes [34]. Les patients décédés/sévères ont également des niveaux plasmatiques de cytokines pro-inflammatoires élevées et une quantité importante de macrophages proinflammatoires dans les poumons [46]. Outre la production d'interférons I et III, une marque communément retrouvée dans les cas les plus sévères est une réponse cellulaire déficiente [43], marquée par une lymphopénie ainsi qu'une baisse du taux de monocytes, eosinophiles et basophiles [45]. La réponse anticorps, médiée par les lymphocytes B, se développe entre 5 et 15 jours après apparition des symptômes [43]. Les immunoglobulines produites sont dirigées contre

la nucléocapside (IgG anti-N) et la protéine Spike (IgG anti-S), cette dernière étant potentiellement la plus importante, étant corrélée à la neutralisation *in vitro* [47, 48]. La présence de ces anticorps procure de plus une protection contre les réinfections présente pendant plusieurs mois [49, 50].

FIGURE 1.5 – Différences de réponse immunitaires entre les cas non-sévères et les cas sévères, reproduit à partir de Sette et al. [43]

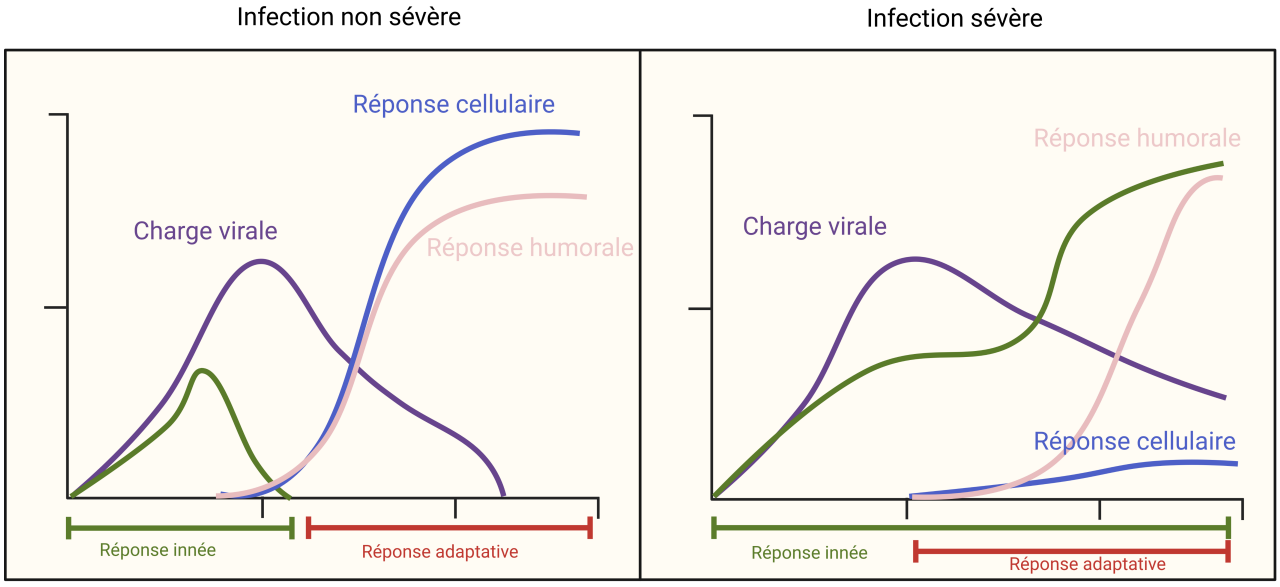

1.6 Vaccins

La vaccination contre le SARS-CoV-2 a été introduite fin 2020 en France. Les premiers vaccins qui ont été approuvés ont été les vaccins des laboratoires Pfizer-BioNTech, Moderna (à ARN messagers) et Oxford-AstraZeneca (à vecteur viral non réplicatif). Ceux-ci ont montré une efficacité respective entre 90-95% dans la protection contre l'acquisition d'une infection symptomatique, et une réduction du taux d'évolution vers une forme sévère chez les populations vaccinées >95%, ceci contre les

souches en vigueur au moment de leurs approbations [51-53]. Cependant, ces vaccins ont des limites aujourd'hui. En effet, la réponse immunitaire induite par la vaccination consiste en la production d'anticorps qui sont dirigés contre la protéine Spike du virus, qui consiste la principale problématique de l'émergence des variants d'intérêt. La protéine Spike est un domaine hyper-variable qui consiste la principale source de variabilité des variants émergents. Ainsi, l'efficacité de la réponse anticorps induite par la vaccination diminue d'une part avec le temps mais également avec les VoC, pouvant atteindre jusqu'à seulement 45% d'efficacité contre le variant Omicron malgré une dose de rappel [54].

1.7 Thérapeutique

Grâce à des résultats préliminaires obtenus sur le MERS-CoV et le SARS-CoV-1 *in vitro* et sur des modèles animaux, beaucoup de molécules antivirales déjà indiquées dans d'autres pathologies ont été redirigées. Des traitements spécifiques ont ensuite été développés, tels que les anticorps monoclonaux ou la combinaison nirmatrelvir+ritonavir.

Le patient ambulatoire

Chez le patient ambulatoire traité précocement (<7 jours), plusieurs molécules ont prouvé leur efficacité dans la prévention de l'évolution vers un stage sévère de la maladie et de l'hospitalisation. Les thérapeutiques les plus efficaces aujourd'hui sont la combinaison nirmatrelvir+ritonavir, le remdesivir et certains anticorps monoclonaux (Figure 1.3) tels que le sotrovimab ou les combinaisons casirivimab+imdevimab et bamlanivimab+etesevimab. Ces molécules ont montré une efficacité supérieure à 70% pour réduire le taux d'hospitalisation ou de décès [55-58]. La combinaison tixagevimab+cilgavimab a quant à elle montré une réduction de 77% d'apparition d'une forme symptoma-

tique chez des patients à risque d'être non-répondeur à la vaccination ou à risque de forme sévère [59].

Le patient hospitalisé

Certaines de ces molécules ont été étudiées également chez le patient hospitalisé, cependant avec une réussite moindre, voire controversée. Le remdesivir seul a montré de faibles effets voire aucun selon le critère de jugement considéré. L'essai Solidarity a par exemple retrouvé une mortalité légèrement réduite chez les patients non-ventilés [60]. L'essai DisCoVeRy en revanche n'a retrouvé aucune amélioration clinique, mesurée sur l'échelle ordinale de l'OMS [61]. En combinaison avec le bamlanivimab [62], aucune efficacité clinique n'a été retrouvée. L'essai ACTIV-3/TICO quant à lui n'a retrouvé aucune efficacité clinique du bamlavinimab, sotrovimab ou de la combinaison BRII-196+BRII-198 [63, 64], mesurée sur l'échelle ordinale de l'OMS . Cependant, un facteur qui semble important dans l'évaluation des thérapeutiques est la séropositivité à l'initiation du traitment. En effet, l'essai RECOVERY a retrouvé une efficacité de la combinaison d'anticorps monoclonaux casirivimab+imdevimab dans la sous-population de patients n'ayant pas encore développé de réponse anticorps (30% -> 24% de mortalité) [65].

Molécules d'intérêt dans le cadre de cette thèse

Les thérapeutiques sur lesquelles nous nous sommes particulièrement concentrés dans le cadre de cette thèse ont été le remdesivir et le favipiravir.

Remdesivir

Le remdesivir est un analogue nucléosidique panviral qui inhibe l'ARN polymérase (RdRP) d'un

certain nombre de virus [66]. Le remdesivir en tant que tel n'est pas actif, mais nécessite de passer par une cascade de métabolisation afin d'atteindre sa forme de nucléoside tri-phosphate (RTP) qui peut ainsi s'intégrer à l'ARN polymérase (Figure 1.6). Chez le primate non-humain, ce traitement a montré une diminution de la charge virale pulmonaire accompagnée d'une amélioration clinique [67, 68]. Chez le patient ambulatoire, il a montré une réduction du taux d'hospitalisation de 87% [56], mais chez le patient hospitalisé son efficacité est contestée. En effet, certains essais trouvent une amélioration clinique [60, 69], tandis que d'autres ne retrouvaient pas ces résultats [61, 70, 71].Cependant, il est difficile de comparer l'efficacité du remdesivir dans cette dernière population selon les essais, car les critères de jugement principaux pouvaient différer. Certains prenaient comme critère de jugement principale la réduction de mortalité [71] ou le passage sous ventilation [60], alors que d'autres essais appréciaient l'effet antiviral mesuré sur l'échelle clinique ordinale de l'OMS en 7 points [61, 69, 70].

FIGURE 1.6 – Bioactivation du remdesivir

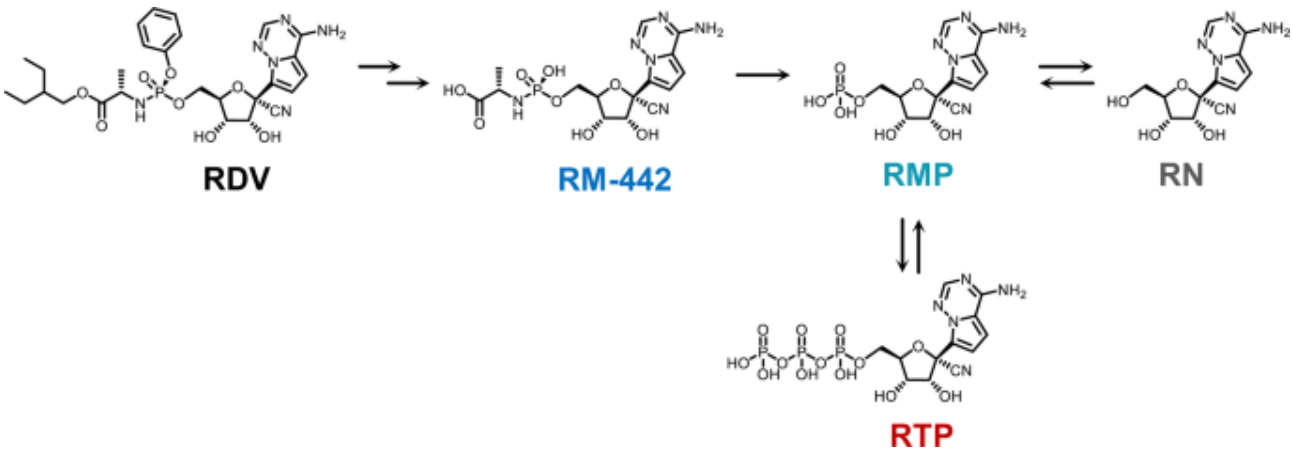

Favipiravir

Le favipiravir est une molécule pan-virale prescrite dans le traitement de la grippe A au Japon. Elle a été testée contre plusieurs virus tels qu'Ebola ou Lassa ([72-74]. Contre le SARS-CoV-2, cette molécule a montré des résultats prometteurs *in vitro* [75] et dans un modèle rongeur, mais pas dans

le modèle primate non-humain (cf chapitre 7). Chez l'humain, il a été étudié dans plus d'une centaine d'essais cliniques [76], avec des résultats discordants chez le patient hospitalisé, que ce soit au niveau clinique ou viral [77-79]. Chez le patient ambulatoire, aucun essai contrôlé randomisé n'a trouvé d'efficacité clinique [80, 81]. Malgré cela, il reste approuvé dans plusieurs pays tels que le Japon, la Russie, la Serbie, Turquie, Inde et Thaïlande.

Chapitre 2

Dynamique virale du SARS-CoV-2

2.1 Méthodes de quantification

La charge virale, au sens communément utilisé, correspond à une concentration de copies d'ARN viral présent dans un échantillon. Dans le SARS-CoV-2, sauf mention contraire, la charge virale mentionnée est la charge virale nasopharyngée, collectée sous forme d'écouvillons nasopharyngés. Cet échantillon subit une procédure de *Polymerase Chain Reaction* (PCR), qui va amplifier le gène grâce à des cycles qui répliquent la molécule d'ARN initiale, et le nombre de cycles d'amplification nécessaires à la détection du virus va être inversement proportionnel à la quantité de virus présent dans l'échantillon. Pour obtenir le nombre de copies d'ARN par millitre d'échantillon, il faut avoir accès à des courbes de calibrations qui dépendent du gène ciblé. Les courbes de calibrations différant entre ces gènes, la conversion vers des copies/mL peut donner des concentrations différentes pour le même prélèvement. De plus, on peut avoir à faire à différentes qualités de prélèvements, qui peuvent contenir plus ou moins de cellules. Pour pallier à ce biais, dans l'essai DisCoVeRy, la charge virale était normalisée par le nombre de cellules présentes dans le prélèvement. De plus, on assimile couramment le nombre de copies d'ARN viral au nombre de virus produits par les cellules infectées, cependant ce raccourci est contesté [82].

Au sein des particules virales produites, un grand nombre d'entre elles ne sont pas infectieuses dû aux erreurs faites par l'ARN polymérase, rendant la molécule non viable. Il convient donc de ne pas associer quantité d'ARN produite et infectivité du virus. D'autres méthodes de quantifications existent pour déterminer la quantité de virus infectieux produite par millilitre d'échantillon. Parmi celles-ci, les plus courantes sont les essais de plaques (donnant des résultats en *Plaque Forming Unit*/mL) ou une méthode de titrage donnant comme résultat le TCID50 (*Tissue Culture Infective Dose*), soit la quantité de virus nécessaire pour détruire 50% des cellules.

2.2 Evolution naturelle de la charge virale

La modélisation intra-hôte de la dynamique virale effectuée sur des données répétées au cours de la maladie permet de reconstituer la totalité de l'histoire naturelle de l'infection depuis la contamination jusqu'à la clairance virale. Connaître l'intégralité de cette évolution a permis d'attribuer la présence de deux pentes de décroissance à l'action du système immunitaire [83, 84], ceci également dans le compartiment salivaire [83]. La période d'incubation du virus a été estimée à 5 jours [84-86], pouvant se prolonger jusqu'à 14 jours [86]. Le charge virale atteint son pic également 5 jours après l'infection ([84], Figure 2.1), ce qui a été confirmé par une étude contrôlée qui a étudié la dynamique virale chez des volontaires infectés [87]. Ce pic est atteint beaucoup plus vite que pour le SARS-CoV-1 ou le MERS-CoV, qui en comparaison atteignent ce pic entre 10-14 et 7-10 jours respectivement [88]. De nombreux travaux ont montré des trajectoires virales qui diffèrent selon l'âge. En effet, la littérature s'accorde aujourd'hui sur le fait que les patients âgés ont une excrétion virale prolongée [88-90]. L'impact de cette différence a été retrouvée notamment par notre travail de modélisation de la dynamique virale chez une cohorte de patients hospitalisés ([84], cf chapitre 5).

FIGURE 2.1 – Histoire naturelle de la maladie, issu de Killingley et al. [87]

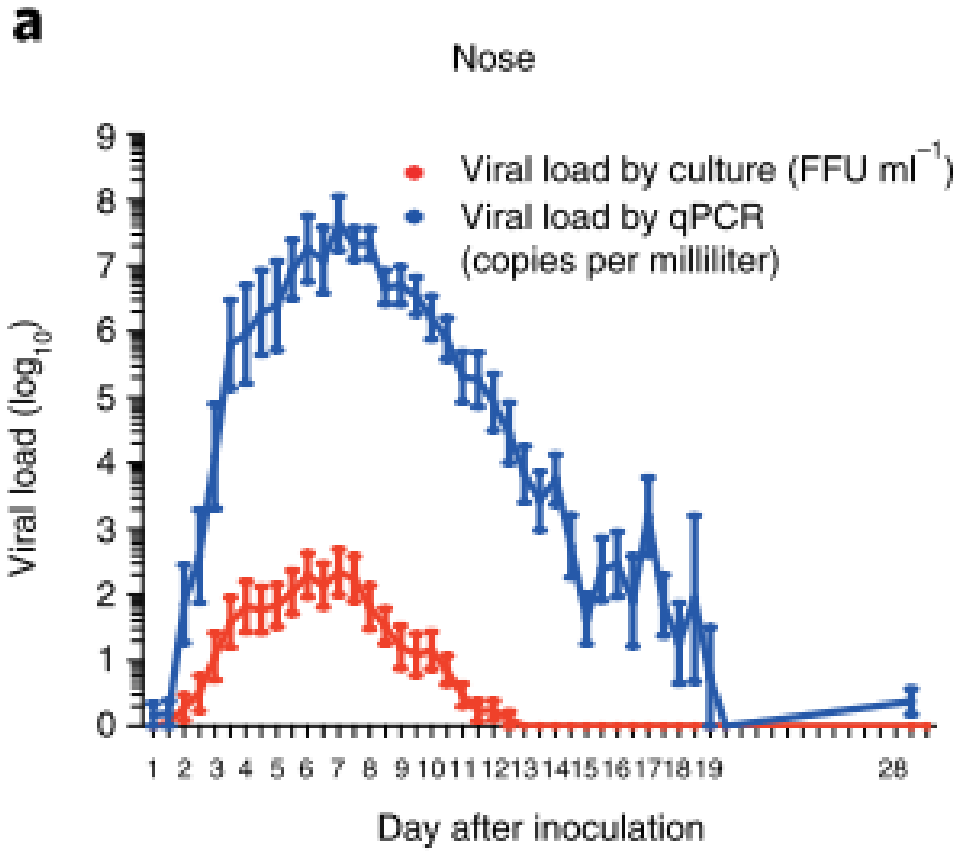

2.3 Charge virale et transmission

La charge virale a été montré dans de nombreux travaux comme étant corrélée à la transmission. Notamment, la charge virale nasopharyngée est positivement corrélée à la charge virale présente dans les gouttelettes excrétées dans l'environnement [91]. Cela représente donc un inoculum viral plus important et donc une probabilité de transmission accrue. Marks et al ont également corrélé cette probabilité de transmission au niveau de charge virale nasopharyngée obtenue chez l'index au moment du diagnostic [92]. Plusieurs auteurs ont quant à eux, grâce à la modélisation intra-hôte, quantifié la probabilité de transmission [93-95], confirmant que la probabilité de transmission est la plus élevée lors du pic de charge virale. De plus, le pic de charge virale

étant atteint au moment des symptômes, cela a un impact important sur la part de transmission pré-symptomatique/asymptomatique [87, 96]. Cependant, afin d'infecter de nouveaux individus, la charge virale excrétée par le biais de gouttelettes ou d'aérosol doit être capable d'infecter de nouvelles cellules, donc qualifiée de charge virale "cultivable" ou "infectieuse". Cette charge virale infectieuse a été montré comme disparaissant plus rapidement que la charge virale génomique après le début des symptômes/pic de charge virale (médianes : 10.2 jours vs 14.6 jours, [87]). En ce sens, la charge virale génomique et la probabilité de transmission n'évoluent plus de manière conjointe après le début des symptômes/pic de charge virale. De plus, il existe une grande hétérogénéité inter-individuelle entre la quantité de virus infectieux produit et la charge virale totale (ARN génomique), ce qui implique que d'autres mécanismes que la charge virale sont impliqués dans la capacité d'un individu à infecter ses pairs [83]. La transmission peut également être impactée selon la souche du virus concernée. Par exemple, le variant Alpha a montré une charge virale plus élevée que le variant historique, avec un potentiel de transmission plus élevé [97, 98]. Également, le variant Delta semble avoir une charge virale plus élevée que les autres variants [99, 100]. De plus, sa charge virale infectieuse est également supérieure aux autres VoC [101], ce qui explique son infectivité accrue. Cependant, il convient de faire attention aux biais existants dans ces comparaisons entre VoC, notamment lorsque ceux-ci présentent des différences de période d'incubation ainsi que l'impact de la vaccination.

2.4 Charge virale et évolution clinique

Chez le patient ambulatoire, la durée de portage est associée à la présence/absence de symptômes [102] et la charge virale au risque d'évolution vers une forme sévère donc une hospitalisation [103]. Une fois hospitalisé, la charge virale nasopharyngée du patient à l'admission à l'hôpital a été montrée

dans de nombreux travaux comme étant corrélée à la gravité de la maladie [104-110]. que ce soit le risque d'intubation ou le risque de décès. De plus, la modélisation a permis de quantifier ce lien entre mortalité et charge virale (CF chapitre 5). Dans le cadre des VoC, le variant Alpha a notamment été associé à une mortalité accrue de 61% par rapport au variant historique et aux autres variants non of concern (VOI) [111]. Cette mortalité accrue va de pair avec une charge virale plus élevée. Cependant, il convient toujours de faire attention aux mêmes biais qui sont présents pour la transmission.

2.5 L'effet des vaccins et des thérapeutiques antivirales sur la dynamique virale

La vaccination a montré un impact significatif sur la charge virale. En effet, de nombreux travaux ont montré une clairance plus rapide de la charge virale génomique chez des individus vaccinés. De plus, la charge virale infectieuse est également diminuée [99, 112-114]. L'efficacité de cette vaccination diminue cependant avec l'émergence des VoC. Par exemple, le variant Omicron nécessite un rappel supplémentaire pour observer la même diminution que chez les patients infectés par le variant Delta par rapport aux personnes non vaccinées [115]. Plusieurs thérapeutiques ont également montré une diminution de la charge virale génomique, ainsi que de la charge virale infectieuse. Chez les patients ambulatoires, la combinaison casirivimab et imdevimab ont permis une réduction allant de 0.71 à 0.87 $\log_{10}$ copies d'ARN/mL 7 jours après le début du traitement [58]. Similairement, la combinaison nirmatrelvir+ritonavir a permis une réduction de 0.87 $\log_{10}$ copies d'ARN/mL 5 jours après l'initiation du traitement chez les patients traités précocement ($\leq$ 3 jours après le début des symptômes). Enfin, le bamlanivimab en combinaison avec l'etesevimab a montré une réduction de 0.57 $\log_{10}$ copies d'ARN/mL 11 jours (+/- 4) après randomisation. Ces réductions de charge virales ont été également montrées comme étant corrélées à la diminution du risque d'aggravation [103].

En ce sens, la réduction minime de charge virale induite par le remdesivir que nous avons retrouvée dans le chapitre 6 va de pair avec l'absence totale d'efficacité clinique.

2.6 La charge virale dans les autres compartiments

Comme dit précédemment, le SARS-CoV-2 a un tropisme extrêmement divers. La charge virale que l'on peut mesurer en dehors des autopsies peut être présente dans les compartiments salivaire, pulmonaire, ou encore dans le sang sous forme d'antigénémie. La charge virale salivaire a un intérêt particulier [116], puisque les tests se réalisent de manière indolore, voire sont plus sensibles que dans le nasopharynx [117]. Ainsi, certains auteurs présentent le test salivaire comme une alternative à l'écouvillon nasopharyngé [118]. L'antigénémie quant à elle représente un marqueur plus global de l'infection. En effet, elle rend compte de l'extension de l'infection à la fois au niveau nasopharyngé, mais également au niveau pulmonaire et dans les autres organes. En terme de stratégie de test, elle procure une très bonne sensibilité et spécificité lorsque collectée dans les 14 jours suivant les symptômes, et pourrait donc représenter une alternative à l'écouvillon nasopharyngé pour le diagnostic [119]. Chez le patient hospitalisé, la charge virale pulmonaire, bien qu'étant présente au siège de l'infection dans les cas nécessitant une hospitalisation, n'est pas aisément récupérée. En effet, afin de collecter celle-ci, il est nécessaire de réaliser un lavage broncho-alvéolaire. Cet examen étant douloureux, il n'est réalisable de manière répétée que chez des patients sédatés ou intubés en service de réanimation, donc potentiellement plus graves que la population hospitalisée dans des services de salle (voir discussion du chapitre 5).

Chapitre 3

La modélisation au service de l'évaluation thérapeutique

3.1 Les modèles hôtes pathogènes

Les modèles historiques

La modélisation de la dynamique virale intra-hôte a servi à décrire en premier lieu des pathologies chroniques comme le VIH ou l'hépatite C [120, 121].

Ces modèles ont ensuite été adaptés pour décrire l'évolution de la charge virale de pathologies virales aiguës. L'une des premières de ces pathologies à avoir été décrite par le biais de la modélisation a été celle de la grippe A (Influenza A, [122, 123]). Le modèle le plus simple dans ce cas se compose d'une population de cellules saines T et d'une population de cellules infectées I. Ces dernières produisant p particules virales par jour et par cellules, qui réinfectent les cellules saines à une vitesse β, poursuivant le cycle jusqu'à ce que plus aucune cellule saine ne soit disponible. En ce sens, ce modèle est dénommé "Target-Cell-Limited model", le facteur limitant du cycle étant le nombre de cellules cibles. Il est possible d'incorporer une population de cellules supplémentaires infectées mais non-productrice de virus, I_1, dite "en phase d'éclipse" d'une durée de k jours, qui pourrait s'assi-

miler dans un cadre épidémiologique à une période d'incubation où l'individu contaminé ne peut pas provoquer d'infection subséquente. Les cellules infectées productrices de virus constituent donc une deuxième population dénotée I_2, éliminées à une vitesse δ. Ce modèle a été utilisé pour décrire plusieurs maladies virales aiguës telles qu'Ebola ou Zika [73, 124]. Enfin, l'ARN polymérase des virus a un taux d'erreur de réplication assez élevé, et peut donc produire des particules virales qui sont mesurées par RT-qPCR, mais qui ne sont pas viables pour réinfecter de nouvelles cellules. Ainsi, il est possible de diviser la production virale en 2 populations, les virus dits "non-infectieux" et ceux dits "infectieux", ces derniers représentant une proportion μ de la production virale totale. Des paramètres de dynamique virale peut se dériver le nombre de reproduction R_0, qui représente le nombre de cellules infectées secondairement par une cellule infectée au début de l'infection, tel que $R_0 = \frac{\beta p \mu T_0}{c\delta}$, avec T_0 le nombre total de cellules cibles.

Ce modèle peut s'écrire sous la forme d'équations différentielles ordinaires comme suit :

$$\frac{dT}{dt} = -\beta V_i T$$

$$\frac{dI_1}{dt} = \beta V_i T - kI_1$$

$$\frac{dI_2}{dt} = kI_1 - \delta I_2$$

$$\frac{dV_{ni}}{dt} = pI_2\mu - cV_{ni}$$

$$\frac{dV_i}{dt} = pI_2(1-\mu) - cV_i$$

Les modèles incorporant la réponse immunitaire

La réponse immunitaire lors d'une infection virale peut agir sur la dynamique virale, par le biais de plusieurs actions potentielles sur les différents compartiments. Cette réponse immunitaire peut avoir différents modes d'action :

- Rendre cellules cibles réfractaires à l'infection, qui serait médiée par l'action d'interférons de type

1 [42, 125]. Ce type de réponse immunitaire a notamment été utilisé pour modéliser la charge virale nasopharyngée dans le SARS-CoV-2 [83].

- Une action cytotoxique qui augmente l'élimination des cellules infectées, diminuant de ce fait leur demi vie, qui serait médiée par une réponse CD8+ ou NK [126]. Ce type de réponse immunitaire a également été utilisé pour décrire la charge virale nasopharyngée [84, 127, 128] et la charge virale salivaire du SARS-CoV-2 [83].
- Une augmentation de la clairance du virus, par l'apparition d'anticorps qui se fixeraient au virus et permettraient leur élimination par les macrophages.
- Un blocage de la production de virus, de manière similaire à un antiviral qui inhiberait l'ARN polymérase du virus, potentiellement médiée par les interferons [83, 129].
- Un blocage de l'infection des cellules cibles qui s'apparenterait à l'action d'anticorps qui bloquerait stériquement les virus [130].

L'utilisation de ces modèles peut se faire de manière agnostique, en l'absence de connaissances précises sur l'action du système immunitaire sur la charge virale. Dans le cadre du SARS-CoV-2, plusieurs travaux de modélisation ont utilisé des modèles d'action cytotoxique afin de décrire au mieux la dynamique virale nasopharyngée [84, 127, 128].

La paramétrisation de ce genre de modèle peut être faite de manières diverses. Une manière générique est de considérer la production de l'effecteur immunitaire considéré comme stimulée par la quantité d'antigène présent et proportionnel au nombre de cellules infectées. Dans notre modèle, cela se traduira par un compartiment F décrit de la manière suivante :

$$\frac{dF}{dt} = qI_2 - dF$$

Cet effecteur F peut agir de manière linéaire ou non-linéaire. Ainsi, pour un modèle qui incorporerait une réponse immunitaire cytotoxique, cela se traduirait par :

$$\frac{dI_2}{dt} = kI_1 - \delta I_2 - \Phi \frac{F}{F+\pi} I_2$$

Ou de manière simplifiée :

$$\frac{dI_2}{dt} = kI_1 - \delta I_2 - \Phi I_2$$

Avec Φ l'effet maximal de cette réponse immunitaire, dont l'estimation doit être dans les ordres de grandeurs du paramètre qu'elle complète, ici δ, et dans le cas non linéaire, π un paramètre de saturation qui peut s'apparenter à une concentration efficace 50%, soit la valeur de F nécessaire pour atteindre 50% de Φ.

D'autres auteurs ont également modélisé la réponse immunitaire de manière différente. Ke et al. [83] ont simplement considéré que l'élimination des cellules cibles δ est un paramètre dépendant du temps comme suit :

$$\delta(t) = \begin{cases} \delta_1 & (\text{si t} < t_1) \\ \delta_1 + \delta_2 & (\text{si t} \geq t_1) \end{cases}$$

D'autres paramétrisations plus complexes comprenant la dynamique de recrutement des cellules cytotoxiques effectrices ont été également envisagées [127, 128]. Cependant, l'augmentation de la complexité de la paramétrisation de la réponse immunitaire va de pair avec la complexité des données nécessaire à estimer correctement les paramètres concernant cette réponse immunitaire. Cela peut donc compromettre les capacités d'inférence et de prédiction du modèle.

FIGURE 3.1 – Différentes actions du système immunitaire sur la dynamique virale. Bleu :blocage de l'infection ; rouge : augmentation de l'élimination du virus ; vert : augmentation de l'élimination des cellules infectées ; jaune : diminution de la production virale ; gris : cellules cibles rendues réfractaires à l'infection

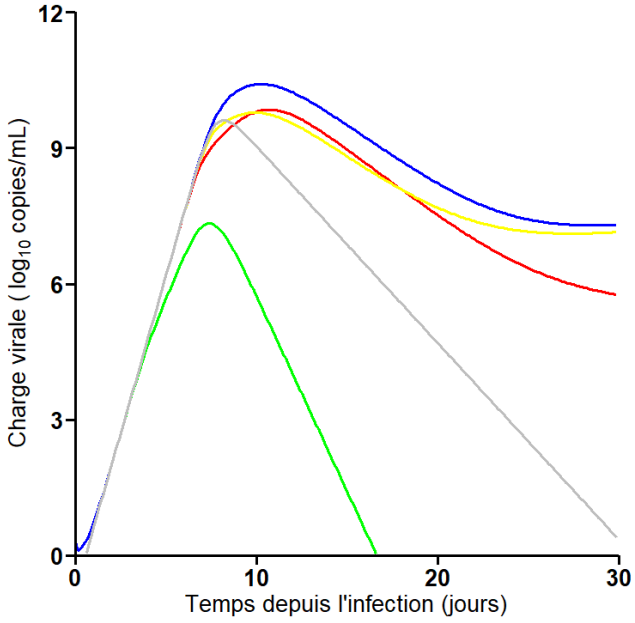

Les modèles incorporant un traitement

La modélisation d'une dynamique virale d'un individu traité peut se faire différemment selon le mode d'action du traitement. Par exemple, les analogues nucléosidiques sont incorporés par l'ARN polymérase du virus, bloquent ainsi la production de virus, soit complètement, soit en le rendant non infectieux dû à une chaine d'ARN incomplète.

Cet effet s'incorpore dans le modèle de dynamique virale sous la forme d'un paramètre ϵ qui diminue la production de virus p d'un facteur (1-ϵ_p) comme suit :

$$\frac{dV_{ni}}{dt} = pI_2\mu(1-\epsilon_p) - cV_{ni}$$

$$\frac{dV_i}{dt} = pI_2(1-\mu)(1-\epsilon_p) - cV_i$$

Les anticorps monoclonaux quant à eux peuvent avoir plusieurs modes d'action, que ce soit protéger les cellules cibles en bloquant l'infection ou diminuer la demi-vie des cellules infectées.

FIGURE 3.2 – Modèle Target-Cell-Limited avec traitement diminuant la production virale

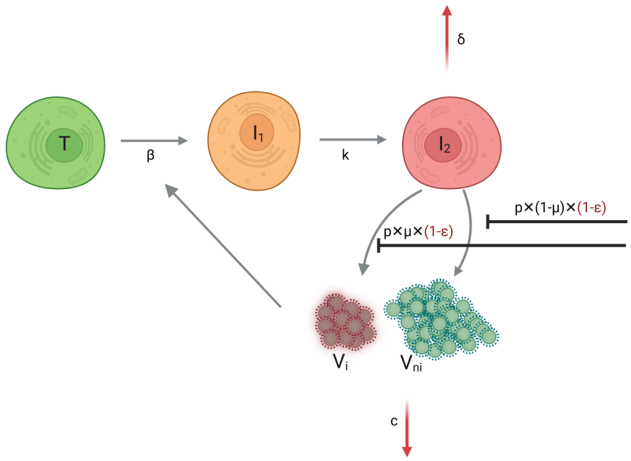

Cela se traduira ainsi par une diminution de la vitesse d'infection β par un facteur (1-ϵ_β) :

$$\frac{dT}{dt} = -\beta(1-\epsilon_\beta)V_i T$$

$$\frac{dI_1}{dt} = \beta(1-\epsilon_\beta)V_i T - kI_1$$

ou par une augmentation de l'élimination des cellules infectées δ par un facteur $(1+\epsilon_\delta)$:

$$\frac{dI_2}{dt} = kI_1 - \delta(1+\epsilon_\delta)I_2$$

3.2 L'apport de la modélisation intra-hôte en période épidémique

En période épidémique, modéliser la dynamique virale permet d'apprendre beaucoup sur l'histoire naturelle de la maladie et de faire des prédictions, notamment sur l'introduction de traitements, en prenant en compte le stade de la maladie auquel ils sont introduits et leur mode d'action. De nombreux modèles intra-hôtes du SARS-CoV-2 ont été publiés (tableau ci-dessous). Ces modèles ont permis notamment de définir une cible pharmacodynamique (90%) permettant de réduire le R0 (cellulaire) en dessous de 1 et donc stopper l'infection de nouvelles cellules et et l'importance de l'administration précoce des traitements antiviraux [131]. Czuppon et al. ont quant à eux permis

de discriminer les types de traitements les plus à même de prévenir l'établissement de l'infection, selon l'inoculum initial et l'efficacité du traitement [132]. Les modèles de dynamique virale ont également permis permet d'inférer avec précision notamment le risque de transmission, qui ici est lié à la quantité de charge virale présente dans le nasopharynx, et donc maximal autour du pic et du début des symptômes [93, 95]. Cela permet également de proposer des stratégies de tests optimales pour détecter le plus sensiblement les patients infectés [95]. De plus, il est possible d'identifier les populations les plus à risques à cause de leur dynamique virale/réponse immunitaire déficiente, indépendamment des facteurs de risques de mortalités connus (age, sexe etc) [84].

La modélisation permet également d'évaluer l'efficacité virologique d'un traitement déjà administré dans un essai clinique, en prenant en compte à la fois le mode d'action et les nombreuses hétérogénéités dans la population, apportant ainsi une plus grande puissance statistique [74]. Enfin, il est possible d'identifier les populations les plus susceptibles de répondre à certains traitements, afin d'optimiser la stratégie thérapeutique [74]. Au-delà de décrire l'histoire naturelle de la maladie, la modélisation intra-hôte permet de réaliser des prédictions de scénarios d'interventions (non)-pharmacologiques. Goyal et al. ont modélisé grâce à un modèle liant dynamique virale et infectiosité l'impact de différents scénarios selon la compliance au port du masque sur la transmission [133].

Auteur	Nombre de sujets	Résultats principaux
Wang et al. [127]	25	Déclin virologique en trois phase
Gastine et al. [134]	645	Temps de clairance virale prolongé chez les patients âgés,les hommes et ceux atteints d'une maladie sévère
Gonçalves et al. [131]	13	Importance d'un traitement antiviral précoce et puissant pour réduire la charge virale
Néant et al. [84]	665	La charge virale facteur de risque de mortalité. Nécessité de traitements puissants pour obtenir un effet clinique
Ke et al. [95]	17	Durée d'infectiosité médiane de 5.5 jours. Transmission pré-symptomatique liée à la période d'incubation. Infectiosité réduite par la vaccination
Ke et al. [83]	60	Hétérogénéité de la dynamique virale liée au "superspreading". Charge virale salivaire meilleur marqueur pour la détection précoce

Table 3.1 – Modèles publiés de dynamique virale du SARS-CoV-2

Chapitre 4

Méthodes d'inférence

4.1 Modèles non linéaires à effets mixtes

Prendre en compte les variabilités biologiques existant dans la réponse à une infection requiert des outils statistiques complexes et une approche globale dite populationnelle. L'approche des modèles à effets mixtes permet de prendre en compte l'intégralité des données longitudinales répétées au cours du temps dans une population.

Les modèles à effets mixtes permettent de décrire l'observation $y_{i,j}$ de l'individu i au temps j suivant la structure suivante :

$$y_{i,j} = f(t_{i,j}, \Theta_i) + g(t_{i,j}, \Theta_i) \times \epsilon_{i,j}$$

où $f(t_{i,j}, \Theta_i)$ correspond au modèle structural qui dépend du temps d'observation j de l'individu i et du vecteur de paramètres individuels $\Theta_i = \{\theta_{1,i}; \theta_{2,i} ...; \theta_{n,i}\}$. Chaque paramètre individuel θ_i peut se décomposer en deux composantes : la valeur de population μ, appelée "effet fixe" et la déviation de l'individu i par rapport à cette valeur de population, η_i, appelée "effet aléatoire" (d'où l'appellation de ce type de modèle "effet mixtes"), qui est distribué selon une loi normale de moyenne

0 et de variance ω^2. L'ensemble des effets aléatoires $\{\eta_{1,i}; \eta_{2,i}...; \eta_{n,i}\}$ permettent de former la matrice de variance-covariance des effets aléatoires notée Ω. Pour obtenir la valeur d'un paramètre individuel, on peut combiner l'effet fixe et l'effet aléatoire de plusieurs manières différentes, selon la distribution du paramètre θ considéré :

$\theta_i = \mu + \eta_i$, si le paramètre θ suit une loi normale.

$\theta_i = \mu \times exp(\eta_i)$, si le paramètre θ suit une loi log-normale, le cas le plus courant en biologie, puisque cette loi contraint le paramètre à être positif.

$\theta_i = \mu \times expit(\eta_i)$, si le paramètre θ suit une loi logit-normale, c'est à dire qu'il est contraint à être compris dans l'intervalle]0 ;1[.

On peut rajouter également des effets de covariables/caractéristiques individuelles pour expliquer une partie de la variabilité inter-individuelle (i.e. réduisent la variance de l'effet aléatoire). Dans le cas d'une distribution log-normale du paramètre θ, cela s'écrira de la manière suivante :

$\theta_i = \mu \times exp(\eta_i) \times exp(z_{C_i} \times \zeta_C)$

avec z_{C_i} le vecteur de covariables C de l'individu i (qui peuvent être continues ou discrètes), et ζ_C le vecteur des paramètres d'association entre les covariable C et l'effet aléatoire.

Pour décrire notre observation $y_{i,j}$, il convient d'ajouter au modèle structural un terme d'erreur résiduelle $g(t_{i,j}, \Theta_i) \times \epsilon_{i,j}$, inhérent aux techniques de mesures utilisées et à l'imprécision d'un modèle, où $\epsilon_{i,j}$ suit une loi normale de moyenne 0 et de variance 1. La fonction g qui caractérise la forme du modèle d'erreur résiduelle s'écrit : $g(t_{i,j}, \Theta_i) = a + b \times f(t_{i,j}, \Theta_i)$. a est ici le terme d'erreur dit "additif" ou "constant", puisqu'il ne dépend pas de la valeur de $f(t_{i,j})$, et b est le terme d'erreur dit "proportionnel".

4.2 Modèles conjoints

Les modèles de cinétique virale nous permettent de reconstruire l'évolution naturelle de la charge virale voire d'autres biomarqueurs qui peuvent être immunologiques. Comprendre l'impact de ces biomarqueurs sur la survenue d'événements comme le passage en réanimation, la mise sous ventilation mécanique et la létalité pourrait permettre d'optimiser les stratégies thérapeutiques. Les modèles dits conjoints sont un moyen de quantifier l'impact d'un biomarqueur longitudinal comme covariable dépendant du temps sur la probabilité de survenue d'un événement d'intérêt au cours du temps [135]. En ce sens, un modèle conjoint se composera de deux sous-modèles, le premier décrivant l'évolution longitudinale temporelle du biomarqueur d'intérêt, tel qu'un modèle de cinétique virale, et tandis que le second décrivant le délai de survenue de l'événement d'intérêt, dit sous-modèle de survie. Ce dernier permet de prendre en compte le fait que l'événement ne survienne jamais durant la période d'observation, appelé phénomène de censure. Cet événement peut également se répéter, puisqu'il ne se limite pas uniquement à la létalité mais peut concerner tout événement clinique.

Dans le cas d'une survenue unique de l'événement d'intérêt à un temps T, celle-ci est caractérisée tout d'abord par une fonction de risque instantané *h(t)*, qui représente le risque de faire l'événement aux alentours du temps t, conditionnellement au fait que l'événement ne soit pas survenu avant t : $h(t) = \lim_{\Delta_t \to 0} \frac{P(t<T<=t+\Delta_t|T>t)}{\Delta_t}$.

Dans le cadre d'un modèle conjoint, cette fonction de risque peut être redéfinie comme suit : $h(t) = h_0(t)exp(VL(t) \times \alpha)$, où $h_0(t)$ est appelée fonction de risque de base, $VL(t)$ est la valeur de la charge virale au temps t, obtenue grâce au sous-modèle longitudinal, et α représente la force d'association entre la valeur de $VL(t)$ et le risque instantané $h(t)$. La fonction $h_0(t)$ peut prendre soit une forme soit non-paramétrique (non-spécifiée) soit paramétrique. Parmi ces formes spécifiées, les plus

courantes incluent les fonctions exponentielle (ou constante) : $h_0(t) = \frac{1}{\lambda}$, indépendante du temps, Weibull : $h_0(t) = \frac{k}{\lambda}(\frac{t}{\lambda})^{k-1}$ ou encore Gompertz : $h_0(t) = a \times exp(-b \times t)$.

On peut dériver de cette fonction de risque instantané la fonction de survie, dénotée $S(t)$, la probabilité que le patient soit toujours à risque de faire l'événement au temps t : $S(t) = P(T > t) = exp(-\int_0^t h(u)du)$

Pour estimer le lien entre biomarqueur longitudinal et probabilité d'événement, on peut les approximer en utilisant une approche dite *two-stages*. Cependant, cette approche ne permet pas de prendre en compte dans l'estimation des paramètres du modèle longitudinal la censure informative liée aux sorties d'études (ou *dropout*), et est donc sujette à un biais. Ainsi, il est préférable d'estimer au sein de la même procédure les paramètres longitudinaux et les paramètres de survie. La vraisemblance conjointe s'écrit comme suit :

$$\mathcal{L}(\Psi, y) = \prod_{i=1}^{N} \int p(y_i|\eta_i, \Psi)p(T_i, \delta_i|\eta_i, \Psi)p(\eta_i, \Psi)d\eta_i$$

4.3 Estimation des paramètres

Le vecteur de l'ensemble des paramètres estimés est dénoté Ψ, et comprend les effets fixes des paramètres μ, la matrice de variance-covariance des effets aléatoires Ω, les termes d'erreur résiduelles a et b, et enfin les potentiels effets des covariables ζ_C.

Les algorithmes les plus couramment utilisés en approche fréquentiste pour estimer ce vecteur Ψ reposent sur le principe de maximisation de la vraisemblance de l'ensemble des données observées. Celle-ci est dénotée $\mathcal{L}(\Psi, y)$ et peut se décomposer en le produit des vraisemblances individuelles, en faisant l'hypothèse d'indépendance conditionnelle des individus. La vraisemblance est donc calculée comme l'intégrale de la vraisemblance des données complètes par rapport à la distribution des

effets aléatoires, ce qui donne :

$$\mathcal{L}(\Psi, y) = \prod_{i=1}^{N} \mathcal{L}(\Psi; y_i) = \prod_{i=1}^{N} p(y_i|\Psi) = \prod_{i=1}^{N} \int p(y_i|\eta_i, \Psi) p(\eta_i, \Psi) d\eta_i$$

Cette expression de la vraisemblance n'a pas d'expression analytique dans les modèles non-linéaires. Elle peut cependant être approximée. Les premières méthodes développées dans les années 80-90 (First-Order puis First Order Conditional Estimate) étaient basées sur une linéarisation du système, et ont été utilisé pour des modèles uniquement longitudinaux. Pour approximer la vraisemblance conjointe, des algorithmes plus récents ont été utilisés tel que l'approximation de Laplace [136]. Enfin, des algorithmes se basant sur la méthode EM (*Expectation-Maximization*) développée dans les années 90 par Dempster et al. [137] permettent une estimation de la vraisemblance sans linéariser le modèle. En particulier, l'algorithme SAEM (SA : *Stochastic approximation*) développé par Delyon et al en 1999 [138], puis implémenté dans le logiciel Monolix par Lavielle et Kuhn [139] en 2004, s'est montré assez robuste, bien que sensible aux paramètres initiaux fournis par l'utilisateur [140]. Dans le cadre de cette thèse, nous avons utilisé cet algorithme pour estimer tous les paramètres qui seront présenté dans les travaux des chapitres suivants.

4.4 Model Averaging

Pour simplifier les modèles afin d'obtenir une identifiabilité pratique, il est possible de fixer certains paramètres à des valeurs connues de la littérature ou en faisant des hypothèses biologiques. Dans un second temps, une analyse de sensibilité ou par profil de vraisemblance permet d'évaluer le poids de la variation du paramètre dans le modèle. Enfin, il est possible de sélectionner le meilleur modèle selon des critères dérivés de la vraisemblance. Cependant, cette approche de sélection de modèle comprend des limites puisque l'incertitude autour du paramètre considéré n'est pas évaluée. Pour prendre en compte cette incertitude, il est possible d'utiliser une approche de Model Averaging

(MA), développée en 1997 par Buckland et al. [141] puis étendue aux modèles de dynamique virale [142]. Cette méthode permet d'obtenir non pas une seule estimation de paramètres, mais des distributions qui prendraient en compte l'intégralité des n modèles testés et la précision d'estimation de ces paramètres dans chacun des M modèles.

A chacun des modèles M est assigné un poids, proportionnel à la vraisemblance du modèle. Ainsi, il est possible de prendre en compte l'incertitude liée au modèle. Le poids w_M du modèle M est défini comme suit :

$$w_M = \frac{e^{\frac{-AIC_M}{2}}}{\sum_{i=1}^{n} e^{\frac{-AIC_M}{2}}}$$

L'AIC étant l'*Akaike Information Criterion*, un dérivé de la vraisemblance [143]. Enfin, pour chaque paramètre θ estimé, son incertitude d'estimation va être prise en compte en tirant un grand nombre de paramètres proportionnel au poids de chaque modèle dans une loi normale $\mathcal{N} \sim (0, SE(\theta_M)^2)$. Le paramètre θ va donc suivre une mixture de loi gaussienne, d'où il est possible d'extraire un intervalle de confiance au seuil α en calculant les quantiles $\alpha/2$ et $1-(\alpha/2)$ de cette loi.

Objectifs de la thèse

Ces travaux de thèse ont eu différents objectifs qui ont évolué en fonction de l'épidémie, des données disponibles et de la connaissance acquise pendant ces 3 dernières années. En premier lieu, nous avons eu pour but de reconstruire l'histoire naturelle de charge virale chez le patient hospitalisé en l'absence de traitement antiviral, et caractériser la variabilité inter patients. Pour ce faire, nous avons utilisé les données de charge virales nasopharyngées des premiers patients de la cohorte French Covid et avons appliqué des modèles non-linéaires à effets mixtes qui ont permis d'obtenir une description populationnelle de la dynamique virale. Nous avons ensuite pu prédire l'impact de thérapies antivirales puissantes sur la mortalité. Dans un second temps, nous avons évalué l'impact du remdesivir sur la charge virale nasopharyngée en utilisant les données des patients des bras SoC et SoC + remdesivir de l'essai DisCoVeRy. En utilisant le modèle développé précédemment, nous avons pu quantifier l'efficacité du remdesivir en l'incorporant en tant qu'inhibiteur de la production virale.

Chapitre 5

Dynamique virale du patient hospitalisé en l'absence de traitement

5.1 Résumé

La cohorte French Covid a été lancée le 5 février 2020, peu de temps après l'arrivée des premiers patients à l'hôpital Bichat. Grâce à l'étroite collaboration entre notre laboratoire et l'hôpital, nous avons été tout de suite impliqués dans la collecte des données concernant ces premiers patients. Nous avons ensuite étendu notre étude à d'autres centres de cette cohorte nationale, nous donnant ainsi accès à la charge virale de 655 patients, dont 284 d'entre eux avaient cette information répétée au cours de leur hospitalisation.

Certaines études ont montré un lien entre âge et charge virale à l'admission à l'hôpital, ainsi qu'une corrélation avec la mortalité [104-110]. Cependant, au delà de ne pas faire consensus au moment où nous avons mené ce projet, ces études n'étudiaient ces liens que de manière transversale, sans prendre en compte l'évolution naturelle de la charge virale. Les objectifs de ce projet ont évolué au fur et à mesure de la compréhension des données : nous avons donc tout d'abord cherché à reconstruire la cinétique virale à un niveau populationnel chez une cohorte importante de patients hospitalisés et à caractériser sa variabilité. Nous avons ensuite cherché à identifier le meilleur mo-

dèle nous permettant de décrire nos données. Enfin, nous avons cherché à quantifier l'impact de la charge virale sur le risque de décès, et en conséquence prédire l'effet d'un traitement antiviral puissant sur la mortalité, administré lors de l'admission à l'hôpital.

Grâce à notre approche populationnelle effectuée sur un grand nombre de patients aux prélèvements répétés, nous avons pu estimer la période d'incubation entre l'infection et l'arrivée des premiers symptômes à 5 jours. Nous avons également constaté que le pic de charge virale coïncide avec ce déclenchement des symptômes, confirmant ainsi l'importance des phénomènes de transmission asymptomatique. Nous avons ensuite exploré les covariables individuelles associées au paramètres de dynamique virale, et avons identifié le fait d'être âgé de 65 ans et plus comme étant associé à une réponse immunitaire moins efficace, et donc à une excrétion virale prolongée par rapport aux patients âgés de moins de 65 ans (16 jours contre 13 jours).

A l'aide d'un modèle conjoint liant l'évolution longitudinale de la charge virale et la probabilité de décès, nous avons ensuite montré que la charge virale est un facteur prédictif de la mortalité (Hazard Ratio = 1.31, $P<10^{-3}$), indépendamment des autres facteurs de risques identifiés dans notre cohorte (être âgé de 65 ans et plus, être un homme et avoir une maladie pulmonaire chronique). Enfin, nous nous sommes interrogés sur l'impact d'un traitement introduit à l'admission à l'hôpital, qui réduirait la production de charge virale, à l'instar d'analogues nucléosidiques. Nous avons prédit qu'un tel traitement efficace à 99% réduirait la mortalité relative chez les patients les plus à risque de 41% (passant de 17 à 10%).

5.2 Article 1

Modeling SARS-CoV-2 viral kinetics and association with mortality in hospitalized patients from the French COVID cohort

Nadège Néant, Guillaume Lingas, Quentin Le Hingrat, Jade Ghosn, Ilka Engelmann, Quentin Lepiller, Alexandre Gaymard, Virginie Ferré, Cédric Hartard, Jean-Christophe Plantier, Vincent Thibault, Julien Marlet, Brigitte Montes, Kevin Bouiller, François-Xavier Lescure, Jean-François Timsit, Emmanuel Faure, Julien Poissy, Christian Chidiac, François Raffi, Antoine Kimmoun, Manuel Etienne, Jean-Christophe Richard, Pierre Tattevin, Denis Garot, Vincent Le Moing, Delphine Bachelet, Coralie Tardivon, Xavier Duval, Yazdan Yazdanpanah, France Mentré, Cédric Laouénan, Benoit Visseaux, Jérémie Guedj

Proceedings of the National Academy of Sciences, 2021.

Modeling SARS-CoV-2 viral kinetics and association with mortality in hospitalized patients from the French COVID cohort

Nadège Néant[a,1,2], Guillaume Lingas[a,1], Quentin Le Hingrat[a,b,1], Jade Ghosn[a,c], Ilka Engelmann[d], Quentin Lepiller[e], Alexandre Gaymard[f,g], Virginie Ferré[h], Cédric Hartard[i,j], Jean-Christophe Plantier[k], Vincent Thibault[l], Julien Marlet[m,n], Brigitte Montes[o], Kevin Bouiller[p,q], François-Xavier Lescure[c], Jean-François Timsit[a,r], Emmanuel Faure[s], Julien Poissy[t], Christian Chidiac[u], François Raffi[v,w], Antoine Kimmoun[x], Manuel Etienne[y], Jean-Christophe Richard[z,aa], Pierre Tattevin[bb], Denis Garot[cc], Vincent Le Moing[dd], Delphine Bachelet[ee], Coralie Tardivon[ee], Xavier Duval[a,ff], Yazdan Yazdanpanah[a,c], France Mentré[a,ee], Cédric Laouénan[a,ee,1], Benoit Visseaux[a,b,1], Jérémie Guedj[a,1],
and for the French COVID Cohort Investigators and French Cohort Study groups

[a]Université de Paris, INSERM, IAME, F-75018 Paris, France; [b]AP-HP, Hôpital Bichat, Laboratoire de Virologie, F-75018 Paris, France; [c]AP-HP, Hopital Bichat, Service de Maladies Infectieuses et Tropicales, F-75018 Paris, France; [d]Univ. Lille, Virology Laboratory, EA3610, Institute of Microbiology, Centre Hospitalier-Universitaire de Lille, F-59037 Lille Cedex, France; [e]Laboratoire de Virologie, Centre Hospitalier-Universitaire de Besançon, F-25000 Besançon, France; [f]Laboratoire de Virologie, Institut des Agents Infectieux, Hospices Civils de Lyon, Groupement Hospitalier Nord, F-69004 Lyon, France; [g]Centre National de Référence des Virus Respiratoires, Hospices Civils de Lyon, Groupement Hospitalier Nord, F-69004 Lyon, France; [h]Service de Virologie, Centre Hospitalier-Universitaire de Nantes, F-44093 Nantes, France; [i]Laboratoire de Microbiologie, Centre Hospitalier-Universitaire de Nancy, F-54000 Nancy, France; [j]Université de Lorraine, CNRS, Laboratoire de Chimie Physique et Microbiologie pour les Matériaux et l'Environnement, F-54000 Nancy, France; [k]Normandie University, UNIROUEN Rouen, EA2656, Virology, Rouen University Hospital, F-76000 Rouen, France; [l]Virology, Pontchaillou University Hospital, F-35033 Rennes cedex, France; [m]Laboratoire de Virologie, Centre Hospitalier-Universitaire de Bretonneau, F-37044 Tours, France; [n]INSERM UMR 1259, Université de Tours, F-37044 Tours, France; [o]Laboratoire de Virologie, Centre Hospitalier-Universitaire de Montpellier, F-34295 Montpellier, France; [p]Infectious and Tropical Disease Department, Besancon University Hospital, F-25000 Besancon, France; [q]UMR CNRS 6249, Chrono Environnement, University of Bourgogne Franche-Comté, F-25000 Besancon, France; [r]AP-HP, Hôpital Bichat, Service de Réanimation Médicale et Infectieuse, F-75018 Paris, France; [s]Centre Hospitalier-Universitaire de Lille, Univ. Lille, Infectious Disease Department, CNRS, Inserm, U1019-UMR9017-CIIL, F-59000 Lille, France; [t]Université de Lille, INSERM U1285, Centre Hospitalier-Universitaire de Lille, Pôle de réanimation, CNRS, UMR 8576-UGSF-Unité de Glycobiologie Structurale et Fonctionnelle, F-59000 Lille, France; [u]Infectious and Tropical Disease Department, Croix-Rousse Hospital, University Hospital of Lyon, F-69004 Lyon, France; [v]Service de Maladies Infectieuses et Tropicales, Centre Hospitalier-Universitaire de Nantes, F-44093 Nantes, France; [w]Centre d'Investigation Clinique Unité d'Investigation Clinique 1413 INSERM, Centre Hospitalier-Universitaire de Nantes, F-44093 Nantes, France; [x]Université de Lorraine, Centre Hospitalier Régional Universitaire de Nancy, INSERM U1116, F-CRIN INICRCT, Service de Médecine Intensive et Réanimation Brabois, F-54000 Nancy, France; [y]Infectious Diseases Department, Rouen University Hospital, F-76000 Rouen, France; [z]Lyon University, CREATIS, CNRS UMR5220, INSERM U1044, INSA, F-69000 Lyon, France; [aa]Intensive Care Unit, Hospices Civils de Lyon, F-69002 Lyon, France; [bb]Infectious Diseases and Intensive Care Unit, Pontchaillou University Hospital, F-35000 Rennes, France; [cc]Centre Hospitalier Régional Universitaire de Tours, Service de Médecine Intensive Réanimation, F-37044 Tours Cedex 9, France; [dd]Tropical and Infectious Diseases, Saint Eloi Hospital, Université de Montpellier, Medical School, Montpellier University Hospital, F-34295 Montpellier Cedex 5, France; [ee]AP-HP, Hôpital Bichat, Department of Epidemiology Biostatistics and Clinical Research, F-75018 Paris, France; and [ff]AP-HP, Hôpital Bichat, Centre d'Investigation Clinique, INSERM CIC-1425, F-75018 Paris, France

Edited by Alan Hastings, University of California, Davis, CA, and approved December 22, 2020 (received for review August 25, 2020)

The characterization of severe acute respiratory syndrome coronavirus 2 (SARS-CoV-2) viral kinetics in hospitalized patients and its association with mortality is unknown. We analyzed death and nasopharyngeal viral kinetics in 655 hospitalized patients from the prospective French COVID cohort. The model predicted a median peak viral load that coincided with symptom onset. Patients with age ≥65 y had a smaller loss rate of infected cells, leading to a delayed median time to viral clearance occurring 16 d after symptom onset as compared to 13 d in younger patients ($P < 10^{-4}$). In multivariate analysis, the risk factors associated with mortality were age ≥65 y, male gender, and presence of chronic pulmonary disease (hazard ratio [HR] > 2.0). Using a joint model, viral dynamics after hospital admission was an independent predictor of mortality (HR = 1.31, $P < 10^{-3}$). Finally, we used our model to simulate the effects of effective pharmacological interventions on time to viral clearance and mortality. A treatment able to reduce viral production by 90% upon hospital admission would shorten the time to viral clearance by 2.0 and 2.9 d in patients of age <65 y and ≥65 y, respectively. Assuming that the association between viral dynamics and mortality would remain similar to that observed in our population, this could translate into a reduction of mortality from 19 to 14% in patients of age ≥65 y with risk factors. Our results show that viral dynamics is associated with mortality in hospitalized patients. Strategies aiming to reduce viral load could have an effect on mortality rate in this population.

SARS-CoV-2 | viral dynamics | mortality

The severe acute respiratory syndrome coronavirus 2 (SARS-CoV-2) which originated in Wuhan, China, at the end of December 2019, has spread rapidly around the world, resulting, in November 2020, in over 60 million confirmed cases and more than 1.4 million deaths worldwide (1). Dozens of studies have evaluated risk factors or comorbidities associated with death (2–7), in particular, male gender, older age, diabetes, severe asthma, obesity, or chronic kidney diseases (7).

In other acute or chronic viral diseases (influenza, HIV, hepatitis C virus in particular), the characterization of viral load kinetics has played an important role in understanding the pathogenesis of the virus, identifying most at risks patients, and designing antiviral drugs (8–11). In the case of SARS-CoV-2, viral kinetics remain poorly characterized, and its association with disease evolution is controversial. This is due to the fact that

Author contributions: F.M., C.L., B.V., and J. Guedj designed research; N.N., G.L., Q.L.H., J. Ghosn, I.E., Q.L., A.G., V.F., C.H., J.-C.P., V.T., J.M., B.M., K.B., F.-X.L., J.-F.T., E.F., J.P., C.C., F.R., A.K., M.E., J.-C.R., P.T., D.G., V.L.M., D.B., C.T., X.D., and Y.Y. performed research; Q.L.H. and B.V. contributed new reagents/analytic tools; N.N., G.L., Q.L.H., D.B., and C.T. analyzed data; N.N., G.L., B.V., and J. Guedj wrote the paper; and C.L., B.V., J. Guedj, J. Ghosn, I.E., Q.L., A.G., V.F., C.H., J.-C.P., V.T., J.M., B.M., K.B., F.-X.L., J.-F.T., E.F., J.P., C.C., F.R., A.K., M.E., J.-C.R., P.T., D.G., V.L.M., X.D., Y.Y., and F.M. acquired data.

Competing interest statement: J. Guedj has worked as a consultant for ROCHE Company.

This article is a PNAS Direct Submission.

Complete lists of the French Cohort Study group and the French Cohort Investigators group can be found in *SI Appendix*.

[1]N.N., G.L., Q.L.H., C.L., B.V., and J. Guedj contributed equally to this work.

[2]To whom correspondence may be addressed. Email: nadege.neant@inserm.fr.

This article contains supporting information online at https://www.pnas.org/lookup/suppl/doi:10.1073/pnas.2017962118/-/DCSupplemental.

Published February 3, 2021.

Significance

A detailed characterization of viral load kinetics and its association with disease evolution is key to understand the virus pathogenesis, identify high-risk patients, and design better treatment strategies. We here analyze the mortality and the virological information collected in 655 hospitalized patients, including 284 with longitudinal measurements, and we build a mathematical model of virus dynamics and survival. We predict that peak viral load occurs 1 d before symptom onset, on average, and that dynamics of decline after peak is slower in older patients. Viral load dynamics after hospital admission is an independent predictor of the risk of death, suggesting that prolonged viral shedding of high quantities of virus is associated with poor outcome in this population.

many studies rely either on large cross-sectional analyses with few patients having serial data points or, conversely, on detailed but small series of patients, often with a mild disease (12, 13). Moreover, the discrepancies in the time of samplings, the definition of disease severity, and the populations analyzed make it difficult to get a clear picture of viral kinetics. Despite these heterogeneous data, pieces of evidence accumulate to suggest that the incubation period is about 5 d, and that the peak viral load occurs in the early phase of illness, close to the time of symptom onset (14, 15). The time to viral clearance is variable across studies, but viral shedding could persist for several weeks after symptom onset, even months in some individuals (16), and may be shorter in young and/or asymptomatic individuals (17). Among hospitalized patients, some observational studies suggest a higher viral load in severe patients compared to nonsevere patients (18, 19), and a recent study found that higher viral load value at hospital admission was independently associated with mortality (20). However, there exist contradictory findings on the impact of disease severity on the duration of virus shedding (15, 21, 22). Besides disease severity, it has been suggested that older age may be associated with a delayed time to viral clearance (23, 24), but this, again, was not found in other studies (15). All together, these elements suggest that viral kinetics could be associated, to some extent, with disease severity. However, the precise assessment of the association between patient's characteristics, viral kinetics, and survival is unknown and subject to multiple biases emerging from observational studies.

As done for other viral diseases (25, 26), we here used the techniques of mathematical modeling to characterize, in detail, the viral dynamics in the French COVID multicenter prospective cohort of 655 patients admitted to the hospital before April 1, 2020, for which longitudinal data and mortality were collected. We developed a joint model of host/pathogen interaction and survival that captures the heterogeneity of viral patterns observed, reconstructs individual trajectories, and evaluates the association between viral kinetics and death. Finally, we use the model to anticipate the effects of antiviral treatments on viral dynamics and survival.

Results

Baseline Characteristics and Virological Data at Admission. A total of 655 patients were included in this study (Table 1); 478 (77%) were hospitalized in a conventional unit upon admission, and 144 (23%) were admitted in an intensive care unit. The delay between symptom onset and admission ranged from 0 d to 14 d, with a median time of 7 d (interquartile range [IQR]: 3 to 9 d). The majority of patients were male (59%) and under the age of 65 y (59%). Hypertension (39%), obesity (23%), chronic cardiac disease (20%), and diabetes (17%) were the most common comorbidities. Forty percent of patients received oxygen therapy upon admission, with an initial oxygen saturation median value of 95% (IQR: 93 to 97%). Nearly 40% of patients received at least one antiviral treatment during their hospitalization, essentially lopinavir/ritonavir ($n = 136$), hydroxychloroquine ($n = 62$), or remdesivir ($n = 8$); nearly 20% of patients received corticosteroid therapy.

A total of 587 nasopharyngeal swabs were performed within the two first days after admission, and the median viral load value was 6.3 $\log_{10}$ copies per mL (IQR: 4.1 to 8.4 $\log_{10}$ copies/mL) (Fig. 1*A*). In multivariate regression analysis, viral load at admission was associated with chronic cardiac disease ($P = 0.009$) and a shorter number of days between symptom onset and admission ($P < 10^{-5}$), suggesting that patients admitted early after symptom onset had higher viral load than patients arriving later on (Fig. 1*C*) (*SI Appendix*, Table S1).

Virological Follow-up and Clinical Outcome. In 284 patients, at least two viral load data were available (i.e., one at hospital admission and at least one during follow-up; *SI Appendix*, Table S2). The median follow-up time was 10 d after admission (ranging from 1 d to 55 d). A total of 78 patients (12%) died during the study follow-up, with a median time to death of 17 d after symptom onset (IQR: 9 to 25 d) (Fig. 1*D*). Overall, only four (5%) deaths occurred later than 35 d after symptom onset; 231 patients were lost to follow-up before that time, essentially due to hospital discharge or transfer to other hospitals, and were then analyzed as censored in survival analyses (see *Materials and Methods*). High levels of viral load (≥6 $\log_{10}$ copies per mL) at days 7 and 14 post symptom onset were significantly associated with mortality (*SI Appendix*, Fig. S1).

Viral Dynamic Modeling. The best model describing the virological data in terms of Bayesian information criterion (BIC) and residual error incorporated an antigen-dependent stimulation in the elimination of infected cells (*SI Appendix*, Fig. S2 and Tables S3 and S4). In this model, the equation governing the productively infected cells (see *Materials and Methods*) was given by

$$\frac{dI_2}{dt} = kI_1 - \delta I_2 - \phi \frac{F}{F+\theta} I_2. \quad [1]$$

By construction, the minimal and the maximal loss rates of infected cells are given by δ and $\delta + \phi$, respectively. Following the procedure of covariate selection, only age ≥65 y was associated with a viral kinetic parameter, namely, the maximal decline rate after peak viral load, $\phi (P < 10^{-4})$. Viral dynamic parameters and their variability were estimated with good precision (Table 2). Our model well recapitulated individual viral kinetics (Fig. 2), and the visual predictive check (VPC) showed that the central trend and the variability predicted by the model were consistent with those observed in the data (*SI Appendix*, Figs. S3 and S4). We also evaluated the result obtained with the target cell-limited model for the sake of comparison (Table 2 and Fig. 2).

Viral dynamic parameters predicted that viral load peaked, on average, 1.1 d before symptom onset, with values of ~9.8 $\log_{10}$ copies per mL, with no difference between patients aged ≥65 y and those aged <65 y. In this model, the effective loss rate of productively infected cells was further enhanced by model-predicted differences in the action of immune effector F. Maximal effect of this immune response, ϕ, was estimated to be 0.92 d^{-1} for patients aged <65 y and 0.65 d^{-1} for patients aged ≥65 y. Therefore, the loss rate of infected cells varied from $\delta = 0.33$ d^{-1} at the beginning of the infection to $\delta + \phi = 1.25$ d^{-1} and 0.98 d^{-1} in patients <65 y and ≥65 y, respectively, at the peak of the infection, when the effect of the immune response was maximal, as illustrated in Fig. 3 *A* and *B*. This allowed us to capture a biphasic decline of the virus after peak viral load,

Table 1. Demographic, clinical, and biologic characteristics of the 655 patients analyzed

Characteristics	Median (IQR or *n* %)	Missing data (%)
Male gender*	386 (59%)	0 (0%)
Age*	60 (48 to 72)	0 (0%)
Age < 65 y	387 (59%)	0 (0%)
Age ≥ 65 y	268 (41%)	0 (0%)
Time since symptom onset (days)	7 (3 to 9)	6 (1%)
Viral load at admission† (log_{10} copies per mL)	6.3 (4.1 to 8.4)	68 (10%)
Comorbidities		
Hypertension	255 (39%)	9 (1%)
Obesity*	145 (23%)	13 (2%)
Chronic cardiac disease (not hypertension)*	126 (20%)	9 (0%)
Diabetes	111 (17%)	12 (2%)
Chronic pulmonary disease (not asthma)*	72 (11%)	9 (1%)
Asthma	54 (8%)	9 (1%)
Chronic kidney disease	44 (7%)	10 (2%)
Malignant neoplasm	47 (7%)	9 (1%)
Rheumatologic disorder	36 (6%)	12 (2%)
Chronic neurological disorder	30 (5%)	10 (2%)
Chronic hematologic disease	29 (4%)	9 (1%)
Solid organ transplant	16 (3%)	23 (4%)
Chronic liver disease	7 (1%)	9 (1%)
Inflammatory bowel disease	7 (1%)	20 (3%)
Dementia	7 (1%)	10 (2%)
Malnutrition	4 (1%)	12 (2%)
Sickle cell disease	4 (1%)	124 (19%)
AIDS/HIV	0 (0%)	553 (84%)
Splenectomy	3 (0%)	24 (4%)
Clinical characteristics at admission		
Heart rate (beats per minute)	87 (77 to 100)	75 (11)
Respiratory rate (breaths per minute)	21 (18 to 27)	270 (41)
Systolic blood pressure (mmHg)	130 (113 to 145)	74 (11)
Diastolic blood pressure (mmHg)	76 (65 to 85)	74 (11)
Oxygenation on room air	328 (60%)	112 (17)
Oxygen saturation on room air (%)	96 (94 to 98)	0 (0)
Oxygenation on oxygen therapy	215 (40%)	112 (17)
Oxygen saturation on oxygen therapy (%)	95 (93 to 97)	0 (0)
Biological and virological data within the first 2 d after admission		
Haemoglobin (g/dL)		
Platelet count ($\times 10^9$ cells per L)	13.2 (11.8 to 14.4)	209 (32)
WBC count ($\times 10^9$ cells per L)	189 (151 to 244)	209 (32)
Lymphocyte count ($\times 10^9$ cells per L)	5.52 (4.26 to 7.28)	215 (33)
C-reactive protein (mg/L)	0.96 (0.7 to 1.36)	277 (42)
Treatment		
At least one antiviral	240 (39%)	43 (7)
Antibiotic	387 (63%)	40 (6)
Antifungic	32 (5%)	48 (7)
Corticosteroid	108 (18%)	47 (7)

*Baseline risk factors of mortality assessed in our cohort were those identified in the ISARIC international cohort (2), with a prevalence larger than 10% and less than 10% of missing data.
†±2 d.

where a rapid age-dependent decline was followed by a slower decline rate due to lower antigen stimulation. This corresponded to a half-life of infected cells decreasing from 50 h (IQR: 30 to 52 h) in all patients to 13 h (age <65 y; IQR: 11 to 14 h) and 17 h (age ≥65 y; IQR: 14 to 17 h) (Fig. 3*B*). The predictions obtained by the target cell-limited model gave close estimates, with a mean half-life of infected cells of 15 and 20 h in patients aged <65 y and those aged ≥65 y, respectively (Table 2). As a consequence, the predicted time to viral clearance occurred earlier in patients aged <65 y, with a median time of 13 d after symptom onset (IQR: 10 to 15 d) as compared to 16 d (IQR: 12 to 20 d) in patients aged ≥65 y ($P < 10^{-4}$) (Fig. 3*C*).

In the samples where virus was cultured, extended viral shedding was not associated with culture positivity, with all cultures of viral load assessed more than 10 d after symptom onset being negative (Fig. 1*B*). As an exploratory analysis, we evaluated the association between antiviral or corticosteroid treatment and viral load decay. No significant association was found between antiviral treatment and time to viral clearance. Corticosteroid had no effects on the time to viral clearance in aged patients; however, younger patients treated with corticosteroids had a longer time to viral clearance as compared to young untreated patients ($P = 0.01$; *SI Appendix*, Fig. S5; see *Discussion*).

Alternative Models and Sensitivity Analyses. Alternative models of the immune response did not improve the data fitting, and parameter estimates were close to those obtained with the final model (*SI Appendix*, Tables S5 and S6). In the subset of 76

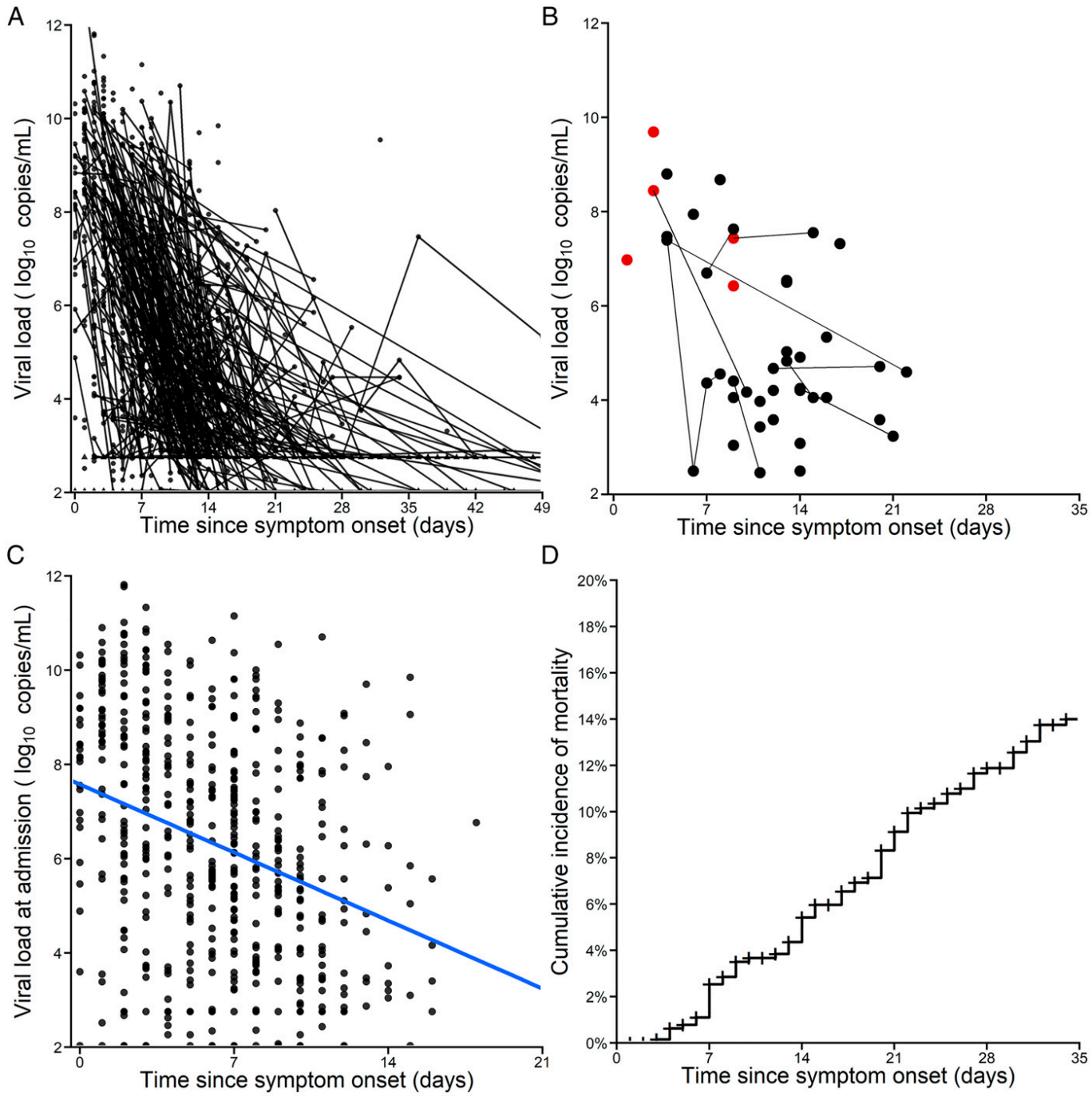

Fig. 1. Nasopharyngeal viral load data in 655 patients from the French COVID cohort. (*A*) Longitudinal viral load data expressed in time since symptom onset. (*B*) Viral load data in samples where virus culture was done. Red, positive culture; black, negative culture. The connective lines indicate serial samples from the same patients (44 samples from 37 patients) (*C*) Viral load at admission according to the time since symptom onset; the blue line is the regression line of viral load vs. time. (*D*) Kaplan–Meier curve of cumulative incidence of mortality. Patients lost to follow-up were censored at the last time point where they were known to be alive.

individuals where antibody could be measured, the median time to seroconversion was 12 d (*SI Appendix*, Fig. S6). We therefore also tested models assuming an increase in the loss rate of productively infected cells after 12 d, but these models did not lead to any improvement of the fitting criterion (*SI Appendix*, Table S6).

To evaluate reliability of our final model predictions, we also performed sensitivity analyses, varying fixed parameters k between 1 and 5 d^{-1} and c between 5 and 20 d^{-1}. The parameter estimates and the BIC were stable in all tested values, except when k was lower than 3 d^{-1} (*SI Appendix*, Fig. S7).

Association between Viral Dynamics and Mortality. In the 74 individuals who died within 35 d from symptom onset, the model predicted that the viral load was below the limit of quantification/detection in 23% (17/74) of the cases (*SI Appendix*, Fig. S8). In 39% of individuals (29/74), the viral load predicted by the model was higher than 6 $\log_{10}$ copies per mL at time of death. In multivariate analyses, the risk factors associated with survival were chronic pulmonary disease, age ≥65 y, and male gender (*SI Appendix*, Table S7). Using a joint model adjusting for these risk factors, the viral load was significantly associated with survival

Table 2. Population parameters of the final joint model of viral dynamics and survival

	Parameter estimates (RSE, %)			
	Final model		Target-cell limited model	
Longitudinal model	Fixed effect	Random effect SD	Fixed effect	Random effect SD
β(mL.virus^{-1}. d^{-1})	1.46×10^{-5} (23.4)	0.65 (26.1)	4.93×10^{-5} (39.8)	0.95 (26.1)
pT_0(virus.mL^{-1}.d^{-1})	1.48×10^{11} (26.8)	1.82 (7.7)	8.09×10^{10} (33.5)	1.74 (7.7)
δ (d^{-1})	0.33 (30.0)	0.93 (22.3)	–	–
δ_{age}(<65)(d^{-1})	–	–	1.09 (7.8)	0.39 (8.7)
δ_{age}(≥65)(d^{-1})	–	–	0.84 (22.8)	–
ϕ_{age}(<65)(d^{-1})	0.92 (8.7)	0.20 (31.2)	–	–
ϕ_{age}(≥65)(d^{-1})	0.65 (23.3)	–	–	–
θ(F.mL^{-1})	70 (80.8)	–	–	–
T_{inf}(d)	4.8 (3.2)	0.12 (14.7)	5.4 (9.0)	0.16 (14.7)
σ(virus.mL^{-1})	1.49 (4.0)	–	1.58 (4.7)	–
Male gender	2.55 (25.2)	-	2.54 (28.5)	-
Age ≥65 y	2.58 (37.9)	-	2.59 (24.6)	-
Chronic pulmonary disease	2.31 (36.8)	-	2.27 (38.7)	-
Viral load (log$_{10}$ virus.mL^{-1})	1.31 (17.0)	-	1.30 (17.1)	-

β, infection rate; δ, loss rate of infected cells; p, rate of viral production; ϕ, maximal rate of immune cell clearance; θ, F concentration giving 50% of ϕ; T_{inf}, time to infection; σ, residual variability; RSE, relative SE.

(hazard ratio [HR] = 1.31, $P < 0.001$), showing that viral load dynamics was an independent predictor of death. In the final joint model, the hazard ratios associated with age ≥65 y, male gender, and chronic pulmonary diseases were equal to 2.58, 2.55, and 2.31, respectively, showing that the presence of any of these risk factors were associated with a large increase in the risk of death (all $P < 0.01$). The joint model could well recapitulate the impact of viral load and risk factors on survival rate, with patients characterized by older age and a prolonged viral shedding showing a rapid decline of their predicted survival rate, in particular when there was another risk factor (i.e., male gender or chronic pulmonary disease; Fig. 4 and *SI Appendix*, Fig. S9).

Here, as well, we tested alternative models to test the robustness of our predictions. Assuming that the hazard function, $h(t)$, only increased after a fixed time of 7 d or 10 d after infection worsened the fitting criterion, but predicted a similar association between viral load dynamics and survival. Similar results were obtained with alternative models where $h(t)$ could increase upon infection or symptom onset, consistent with the interpretation that late, but not early, viral load may be associated with outcome (*SI Appendix*, Table S8).

Antiviral Treatment Simulation. To get a better sense of the specific impact of viral load, we further stratified our population according to age and presence of at least one risk factor. Then we evaluated the model predictions with a putative potent antiviral therapy capable of reducing viral production,p, by 90% or 99%, that would be initiated upon hospital admission. A treatment inhibiting 90% of the viral production could shorten the median time to viral clearance by 2 d (IQR: 1.5 to 2.2 d) in patients aged <65 y and by 2.9 d (IQR: 1.9 to 3.8 d) in patients aged ≥65 y (Fig. 4*A*). Considering a treatment blocking 99% of viral production, the effects would be further improved in patients aged ≥65 y, with a median reduction in time to viral clearance of 5.4 d (IQR: 3.7 to 6.9 d).

To calculate the impact of reduced viral load levels on mortality, we assumed that viral dynamics was on the causal pathway for mortality, and thus the association between viral load and mortality was fixed to the value found in our original cohort of patients that did not receive any effective antiviral therapy. With a treatment blocking 90% of viral production, the accelerated viral decline would translate, in this model, into mortality rates reduced from 2.2 to 1.9% in patients below the age of 65 y with no additional risk factor, and from 6.0 to 4.8% in those with at least one risk factor (i.e., either being male or having a chronic pulmonary disease). The effects of treatment would be more sensible in patients above the age of 65 y, with a mortality reduced from 6.4 to 5.0% for those without additional risk factor and from 19 to 14% in those having at least one other risk factor. With a treatment efficacy of 99%, the effects would be even larger, with a decrease in mortality from 19 to 12% in patients above the age of 65 y having one additional risk factor (Fig. 4*C*).

Discussion

To the best of our knowledge, this is the largest analysis of prospective nasopharyngeal SARS-CoV-2 viral dynamic data in hospitalized patients. A mathematical model of viral dynamics accounting for age- and time-dependent effects in the loss rate of infected cells could well reproduce the variability of the patterns observed, and found that older patients had a slower decline of virus after peak viral load. Using joint modeling, a statistical approach to assess the effect of a time-dependent covariate on the hazard function, we could show that the viral load was associated with death, even after adjustment of risk factors such as chronic pulmonary disease, older age, and male gender. This result was robust to various changes in model assumptions, including the parameterization of the second-phase decline. This shows that viral load kinetics could, in addition to other established risk factors, help identify most-at-risk patients during hospitalization. Accordingly, it suggests that approaches reducing viral load levels could reduce mortality, and our model can be used to quantify the magnitude of such an effect.

Our population was in line with previous series of hospitalized patients, with a population predominantly male (59%), aged 65 y and more (41%), with comorbidities that were mostly hypertension (39%), obesity (23%), and diabetes (17%) (2, 6, 7). The first striking observation in our series, as previously suggested (20), was the strong correlation between the viral load at admission and the time since symptom onset, suggesting that the peak viral load was close to the time of symptom onset. To explore this possibility in greater detail, we used a mathematical model of viral kinetics. The model providing the best fit to the data was a target cell-limited model in which the loss rate of infected cells was antigen dependent. Although only a few viral

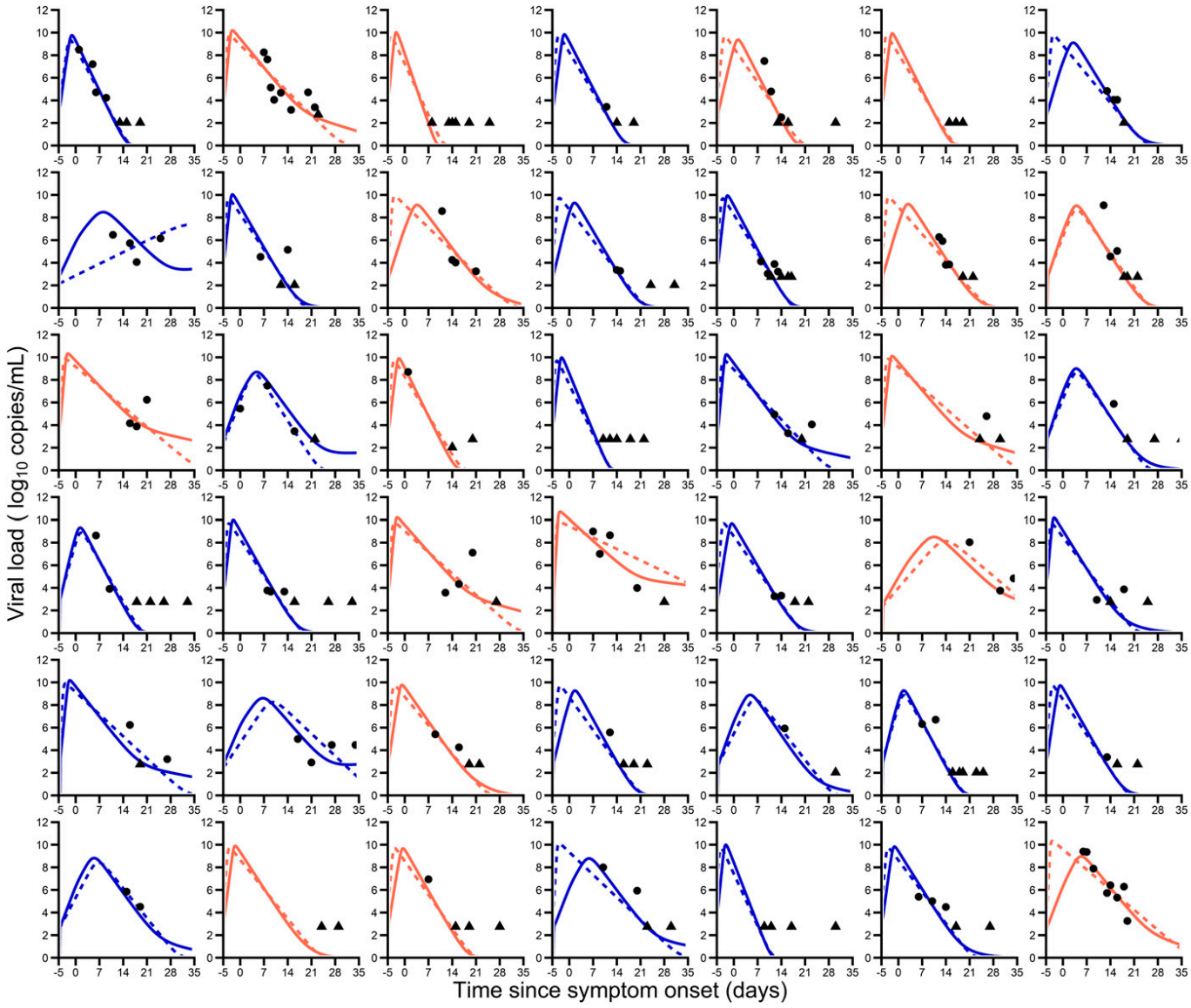

Fig. 2. Individual predictions of nasopharyngeal viral kinetics in the 42 patients for which more than three serial samples were available after day 14. The solid and dotted lines (blue, age <65 y; orange, age ≥65 y) are the individual predictions of viral load with the final model and target cell-limited model, respectively (Table 2). The circles are the observed data according to age, and triangles are data below the limit of quantification.

load data were available in the first 7 d after symptom onset, and the exact time of peak viral load could not be precisely observed, our modeling predictions suggested that the mean peak viral load was close to symptom onset (15, 27). It is noteworthy that only limited information was available in the first days from symptom onset (*SI Appendix*, Table S2), which means that these estimates represent a typical trajectory in our population, and may hide variability in the early kinetics that could not be observed in our data. Using the target cell-limited model, results also nonetheless indicated a high within-host reproduction, with a mean R_0 of 36. Results obtained in previous reports suggested lower levels of R_0, in a range 5 to 15 (28–30). In nonhuman primates, which do not show severe infection, we estimated R_0 in the nasopharynx to be about 5.6 (95% CI: 1.3 to 21) (31). Whether the high value found here is a consequence of the disease severity of our population as compared to other reports or is artifactual due to the limited information in the very early phase of the disease will require more investigation. Whatever the exact value of R_0, the fact that the viral load observed in early admitted patients was very high and could be above 10 $\log_{10}$ copies/mL is consistent with an intense replication rate of the virus that coincides with symptom onset.

The viral load after peak declined in a biphasic manner, consistent with observations made by He et al. (15). The first phase of viral decline was rapid and age dependent, with a rate equal to 1.25 and 0.98 d^{-1} in patients aged <65 y and ≥65 y, respectively, when the effect of the immune response was maximal (Fig. 3*B*). This corresponded to half-life of infected cells decreasing from 50 h to 13 h (age <65 y) and 17 h (age ≥65 y). After this first decline, a second phase of viral decline ensued that was slower, with rate δ. As we relied only on viral data and did not have access to immunological data, we could not assess which component of the immune response was most likely involved in the time-dependent clearance rate of infected cells. In the subset of individuals in which antibody could be measured, the median time to seroconversion was 12 d after symptom onset (*SI Appendix*, Fig. S6). However, models that assumed an increase in the loss rate of infected cells after day 12 did not improve data fitting (*SI Appendix*, Table S6). The reduced loss rate of infected cells could stem from a lower antigen stimulation, as

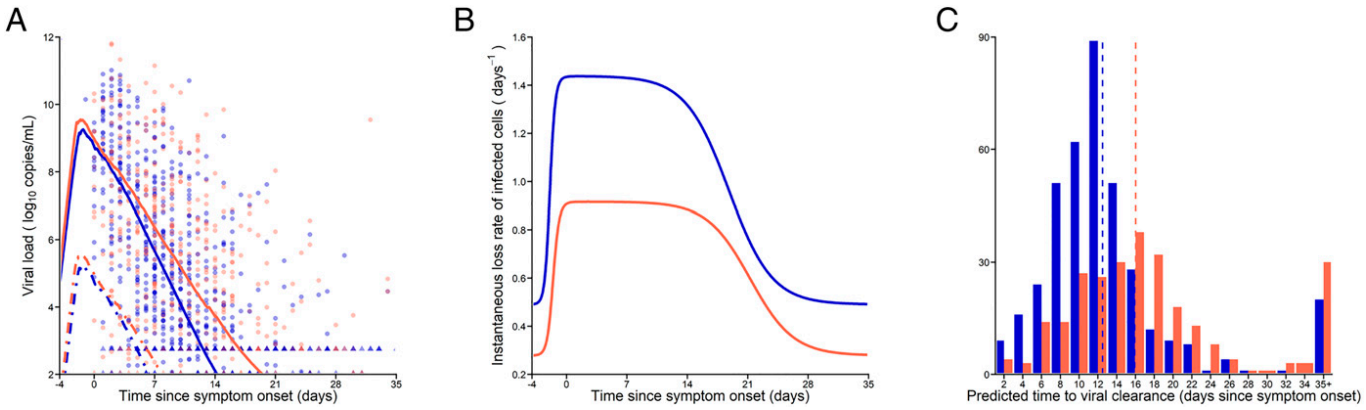

Fig. 3. Description of the individual viral load kinetic profiles. (*A*) Median of the individual predicted viral load kinetics. Solid lines, total viral load levels; dashed lines, infectious virus. Dots represents the observed data, and triangles are data below the limit of quantification. (*B*) Median of the predicted instantaneous loss rate of productively infected cells. (*C*) Distribution of the predicted time to viral clearance in the patients. Dashed lines represent the predicted median of time to viral clearance. Viral kinetic parameters were obtained by using the EBE (see *Materials and Methods*). Blue, patients aged <65 y; orange, patients aged ≥65 y.

proposed in our model, or from other immunological features, such as immune exhaustion, and suggests that seroconversion does not lead to a dramatic acceleration of viral clearance in these patients. Here we did not identify complex patterns of viral dynamics such as described in refs. 32–34; however, this may also be due to the fact that such models require intensive sampling measurements, which can hardly be done outside the context of small specific clinical or preclinical studies. Antiviral treatment and corticosteroids could, in theory, play a role in this viral decay, but could not be properly estimated in this observational study. However, we now know that hydroxychloroquine and lopinavir/ritonavir are highly unlikely to have any antiviral activity in SARS-CoV-2–infected patients (35–37). Regarding corticosteroids, a small effect toward delayed time to viral clearance in young treated as compared to young untreated patients was found.

As a consequence of their faster viral decline rate, the predicted time to viral clearance occurred earlier in patients aged <65 y, with a median time of 13 d postsymptom onset as compared to 16 d in patients aged ≥65 y ($P < 10^{-4}$). These median values nonetheless mask important heterogeneity across patients. For instance, 25% of patients aged <65 y had detectable viral loads 15 d after symptom onset, while this increased to 20 d in patients aged ≥65 y. These results show the importance of younger age, probably reflective of a more effective immune response, and are in line with previous reports (19, 38). It is important to note that a longer period of viral excretion may not necessarily translate into a similarly long infectiousness period. In our data, all viral cultures from samples collected more than 10 d after symptom onset or associated with viral load lower than 6 $\log_{10}$ copies per mL were negative (Fig. 1*B*). Even if culture results are not a direct measure of the infectiousness, they nonetheless suggest that the period during which an individual is contagious is probably short, even if virus continues to be excreted (16, 39, 40). In fact, our model predicted that the median time to achieve 6 $\log_{10}$ copies/mL was 6.5 and 8.3 d in patients aged <65 y and ≥65 y, respectively ($P < 10^{-4}$).

Next, we aimed to assess the factors associated with death. In multivariate analyses, age ≥65 y, male gender, and chronic pulmonary diseases were strongly associated with survival (all HR > 2). By using a joint model, a method used to capture the effects of time-dependent covariate on survival, viral kinetics was also identified as an independent predictor of death (HR = 1.31, $P < 10^{-3}$). Although the effects of viral load were probably not as a dramatic as those of risk factors, and its causality has not been yet established, our results nonetheless suggest that reducing viral dynamics could have a sensible effect on mortality. To study the effects of reducing viral load in more detail, we conducted simulations assuming that an antiviral treatment reducing 90% or 99% of viral production could be readily initiated upon hospital admission. The largest effects were obtained in patients aged ≥65 y and having at least one other risk factor, with a reduction of the time to viral clearance of 2.9 and 5.4 d, respectively. Assuming that the effects of viral dynamics on survival would remain similar to what was obtained here in patients receiving no effective antiviral treatments, this would translate to predicted mortality rates at day 35 of 14% and 12%, respectively, as compared to 19% in our cohort. In other populations of younger patients or without additional risk factors, the effects were predicted to be much less dramatic. Interestingly, we here considered, for the sake of simplicity, treatments blocking viral production, but largely similar results could be obtained with drugs that would block infection, as is the case for monoclonal antibodies. This level of 90% is not out of reach, and roughly corresponds to drug concentrations being 10 times higher than their EC_{50} (concentration for which 50% of maximum effect is obtained), which are standard for antiviral drugs in other infections [e.g., HIV, hepatitis B virus , hepatitis C virus, Ebola (41)]. Given the fact that peak viral load occurs early, as discussed above, it is likely that aggressive strategies that could identify patients earlier than in our study (where admission occurred, on average, 7 d after symptom onset) could have even better results. Our prediction also implicitly hypothesizes that viral load is in the causal pathway of mortality and that effective antiviral treatment, by reducing viral load, would reduce mortality rate. This assumption has been verified for other acute severe viral infections for which effective antiviral strategies exist, such as Ebola virus (8, 42). In the case of SARS-CoV-2, several antiviral drugs have been tested, but the effects on viral kinetics or even symptom evolution remain modest, even though promising results were recently found with monoclonal antibodies (43). It is also possible that viral replication in the lower respiratory tract (LRT) is a better predictor of outcome than nasopharyngeal viral load (44). Here our data showed a correlation between viral load values in both compartments (*SI Appendix*, Fig. S10). However, the predictive value of LRT could not be tested, due to the fact that patients having LRT were not representative and had a much larger mortality rate than the general population (*SI Appendix*, Fig. S10).

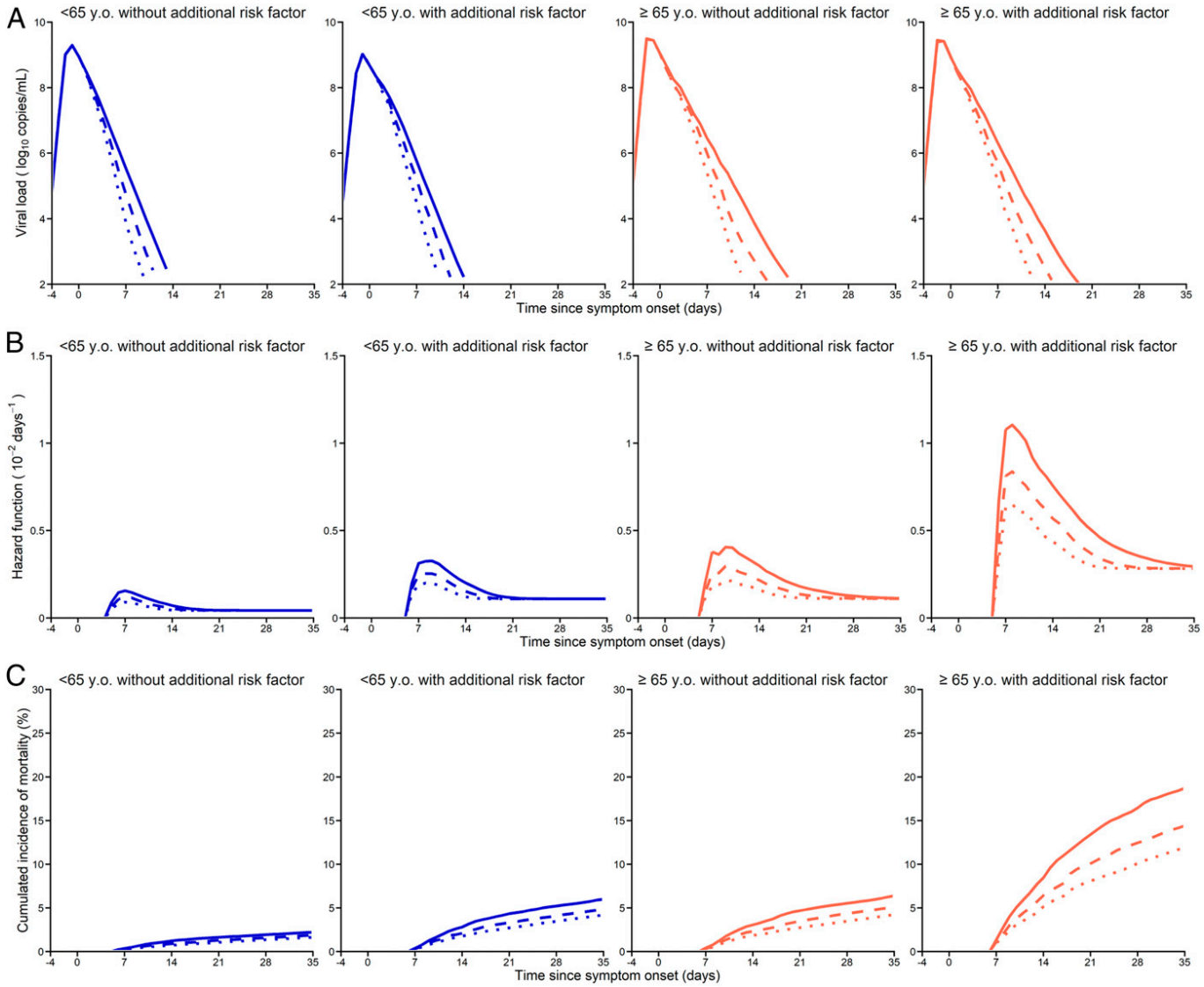

Fig. 4. Individual viral load and survival profiles and predictions according to the initiation of a putative antiviral treatment initiated at admission. (*A*) Median of the individual predicted viral load, $V(t)$ (Eqs. **1**–**3**); y.o., years old. (*B*) Median of the predicted instantaneous hazard function, $h(t)$. (*C*) Median of the predicted death rate, $1 - S(t)$ (Eq. **4**). Solid lines, predicted profile without treatment; dashed lines, treatment with 90% efficacy; dotted lines, treatment with 99% efficacy; blue, patients aged <65 y; orange, patients aged ≥65 y. The profiles are calculated in each of the following population of patients: age <65 y and absence of other significant risk factor (male gender or chronic pulmonary disease, *Left*), age <65 y and presence of at least one risk factor (*Center Left*), age ≥65 y and absence of other risk factor (*Center Right*), and age ≥65 y and presence of at least one other significant risk factor (*Right*).

To conclude, our analysis reveals that hospitalized patients are characterized by a high viral load peak close to symptom onset in a majority of patients, followed by a biphasic decline, with age being significantly associated with a delayed viral shedding. Using a joint model, we showed that viral load was an independent factor associated with death. Our results demonstrate the importance of viral dynamics to identify at-risk patients and suggest that strategies aiming to accelerate viral clearance could decrease mortality in these patients.

Materials and Methods

Ethics. Hospitalized patients with a laboratory-confirmed SARS-CoV-2 infection were enrolled in the French COVID cohort (registered in clinicaltrials.gov NCT04262921) (45). The study was conducted with the understanding and the consent of each participant or its surrogate. The study was sponsored by French National Institute of Health and Medical Research, and was supported by the Research & Action emerging infectious diseases (REACTing) consortium (46) and the French Ministry of Health. Ethics approval was given on February 5 by the French Ethics Committee CPP-Ile-de-France VI (ID RCB: 2020-A00256-33).

Patients and Data Collection. We analyzed the results obtained from patients enrolled in the cohort between February 5 and April 1, 2020, hospitalized in 18 different hospitals and for whom nasopharyngeal swabs were available. Data were collected from the French modified version of the open-access Case Report Form of the Clinical Characterization Protocol for Severe Emerging Infections of International Severe Acute Respiratory and Emerging Infection Consortium (ISARIC) (47). Data at admission time included demographic characteristics (age and gender), time since symptom onset, presence of various comorbidities, and clinical and biological markers. Survival data after hospital admission were collected up to 60 d postadmission. Patients lost to follow-up were censored at the last date of observation.

Viral Load Assessment. Nasopharyngeal swabs were collected at admission and during patient's follow-up. In a subset of patients, viral load in the LRT was also available (*SI Appendix*, Table S2). Viral load was determined by real-time semiquantitative RT-PCR, using either the Charité World Health Organization (WHO) protocol (testing E gene and RdRp) or the Pasteur institute assay (testing E gene and two other RdRp targets: IP2 and IP4) (48, 49). Results were provided in cycle threshold (Ct) and transformed into $\log_{10}$ RNA

copies per mL using the relationship assessed by Pasteur Institute for both E and IP4 genes (48) IP4 viral load value was used as a reference (Pasteur institute assay), or E gene (Charité WHO protocol). For E gene, a corrective factor was applied to correct for the differences observed between the viral load from the two genes (*SI Appendix*). Ct values above 37 (corresponding to a viral load of ~2 $\log_{10}$ for E gene and 2.7 $\log_{10}$ for IP4) were considered as below the limit of detection.

Infectious Virus. For a subset of patients, viral isolation was performed in a biosafety level 3 (BSL-3) laboratory. Briefly, for each sample, 200 μL of virus transport media containing the nasopharyngeal swab was diluted into 800 μL of Dulbecco's modified Eagle's medium (DMEM, Gibco), filtered through a 0.45-μm filter (Sartorius); then 500 μL of the filtered material was inoculated to 50,000 Vero E6 cells (reference CRL-1586, ATCC) plated in a 24-well plate. After 1 h at 37 °C, 500 μL of DMEM containing 4% of FBS (fetal bovine serum, Gibco) was added to each well. At day 6 postinfection, wells were screened for cytopathogenic effect (CPE), and, for all wells with signs of CPE, an RT-PCR targeting both E and S genes of SARS-CoV-2 (RealStar SARS-CoV-2 RT-PCR, Altona) was performed on 50 μL of supernatant to confirm the success of viral isolation.

Risk Factors Associated with Viral Load and Survival. We explored the effects of risk factors associated with higher mortality in hospital previously found by ISARIC, a consortium of large cohort studies of hospitalized patients (2), namely, age (≥65 y), male gender, chronic cardiac disease, chronic pulmonary disease, chronic kidney disease, obesity, dementia, moderate/severe liver disease, chronic neurological disease, or malignancy. Among them, only those with less than 10% of missing data and more than 10% of prevalence in our dataset were explored in our analyses. Thus, only age ≥65 y, male gender, chronic cardiac disease, chronic pulmonary disease, and obesity were evaluated in our analyses (Table 1).

Factors Associated with the Viral Load at Admission. We aimed to evaluate the factors associated with the viral load at admission (defined as the first viral load available within 2 d of admission) in a linear regression model, according to the risk factors described above and the time since symptom onset. All factors associated with $P \leq 0.1$ in univariate analyses were tested in multivariate analyses. Backward elimination was used, and $P < 0.05$ was considered statistically significant. In multivariate analyses, missing data for continuous comorbidities were imputed to the median population value. For categorical risk factors, the values were imputed randomly with a probability equal to the prevalence of each category in the population.

Viral Dynamic Model.

Model equations. We used a target cell-limited model with an eclipse phase (8, 25, 26) . The model includes three types of cell populations: target cells (T), infected cells in an eclipse phase (I_1), and productively infected cells (I_2). The model assumes that target cells are infected at a constant infection rate β (milliliters per virion per day). Once infected, cells enter an eclipse phase and become productively infected after a mean time $1/k$ (d). We assume that productively infected cells have a constant loss rate, noted $\delta(\mathrm{d}^{-1})$. Infected cells produce p viral particles per day (virus per day), but only a fraction of them, μ, is infectious, and the virus particles can either be infectious, noted V_i, or noninfectious, noted V_{ni}. We assumed that viral load, as measured by RNA copies, is the sum of infectious and noninfectious viral particles, both cleared at the same rate, c. The model can be written as

$$\begin{aligned}\frac{dT}{dt} &= -\beta V_i T\\ \frac{dI_1}{dt} &= \beta V_i T - kI_1\\ \frac{dI_2}{dt} &= kI_1 - \delta I_2\\ \frac{dV_i}{dt} &= p\mu I_2 - cV_i\\ \frac{dV_{ni}}{dt} &= p(1-\mu)I_2 - cV_{ni}.\end{aligned} \quad [2]$$

The basic reproductive number R_0, defined by the number of secondary infected cells resulting from one infected cell in a population of fully susceptible cells, T_0, is defined by $R_0 = \beta p T_0 \mu / c\delta$.

In order to evaluate the role of an immune response, we added to the model a dimensionless compartment F representing an immune response stimulated by viral antigens (50), defined as follows:

$$\frac{dF}{dt} = I_2 - d_f F. \quad [3]$$

We considered several scenarios where F either acts by reducing viral infectivity and leads to cells refractory to infection (51–53), decreases the rate of viral production (54, 55), decreases the infection rate (25), or increases the viral clearance or the loss rate of infected cells (55–57) (*SI Appendix*, Fig. S2). Following the class of models that we evaluated in previous works (30), we used similar parameterizations for the different models (*SI Appendix*), with a nonlinear and saturable effect for F defined by $\phi(F/F+\theta)$. Thus, in this model, ϕ represents the maximal potential effect of the immune response, and θ is the level of F required to achieve 50% of this maximal effect.

Assumptions on parameter values. To ensure parameter identifiability, a number of parameters had to be fixed. Virion clearance rate, c, was fixed to 10 d^{-1} similar to what has been performed in ref. 30. We assumed that the loss rate of immune effectors was slower than viral clearance, and we fixed d_f = 0.4 d^{-1} (8). As only the product $p \times T_0$ is identifiable, we fixed the density of susceptible epithelial cells, T_0, to 1.33×10^5 cells per mL. This assumption stems from the fact that there are $\sim 4 \times 10^8$ epithelial cells in the upper respiratory tract (URT), that the URT has a volume of 30 mL, and that 1% of cells express ACE2 and TMPSS receptor (58), which are used by the virus to bind target cells. The proportion μ of infectious viruses was fixed to 10^{-4} of the total RNA viral load, which was the upper bound found in animal models (31).

Initial conditions at infection. In each patient, we estimated the time of infection, noted t_{inf}. To ensure identifiability, we assumed that, at $t = t_{\mathrm{inf}}$, there was exactly one productively infected cell in the entire URT. Thus, for $t \leq t_{\mathrm{inf}}$, $T = T_0$; $I_1 = 0$; $I_2 = 1/30$; and $V = 0$. We assumed a maximal duration of 14 d between the infection and the onset of symptoms, and thus t_{inf} was bounded between 0 and 14 d before symptom onset (14).

Parameter estimation and fitting assessment. The structural model used to describe the observed $\log_{10}$ viral loads Y_{ij} of the ith subject at time t_{ij} is

$$Y_{ij} = log_{10} V(t_{ij},\ \psi_i) + e_{ij},$$

where $V(t_{ij},\ \psi_i)$ is the viral load predicted by the model at time t_{ij}, ψ_i is the vector of parameters of subject i, and e_{ij} is an additive residual Gaussian error term of constant SD, σ_{ij}. Individual parameters ψ_i follow a log-normal distribution,

$$\psi_i = \gamma \times exp(\eta_i),$$

where γ indicates the fixed effects and η_i are the random effects following a normal centered distribution with a diagonal variance–covariance matrix Ω.

Parameters were estimated by computing the maximum likelihood estimator using the stochastic approximation expectation–maximization (SAEM) algorithm implemented in Monolix Software 2018R2 (http://www.lixoft.eu/). Goodness-of-fit was assessed by visual inspection of VPC (see more details in *SI Appendix, Supplementary Information Text*) (59).

Model building strategy for viral dynamics. We used only viral load data to construct the viral dynamic model following the strategy below:

1) The target cell-limited model (Eq. **2**) was used to estimate the parameters.
2) The five models with immune effects (models B through F; *SI Appendix* and Eqs. **2** and **3**) were tested. The model providing both the lowest BIC and the lowest residual errors was retained, provided that the SEs were not worsened and the goodness-of-fit graphics were adequate.
3) The impact of risk factors was then assessed (see above). Covariates were screened using empirical Bayes estimates (EBE) of individual parameters using nonparametric tests, and those with $P < 0.1$ were included in the model. Backward elimination was used, and $P < 0.05$ was considered statistically significant.
4) Random effects with an SD < 0.1 or associated with a relative SE of greater than 100% were deleted by using a backward procedure and were kept out if the resulting BIC did not increase by more than two points.

Joint Model to Evaluate the Impact of Viral Dynamics on Survival.

Baseline risk factors associated with survival. Let X_i and C_i denote survival and censoring times for patient i, respectively, and T_i denote the last time of

observation: $T_i = \min(X_i, C_i)$, $\delta_i = 1_{\{X_i \leq C_i\}}$. We used a parametric exponential survival model to characterize the baseline hazard function, with constant rate λ. Consistent with what was done above, the risk factors associated with a $P \leq 0.1$ in univariate analyses were tested in multivariate analyses. Backward elimination was used, and variables were removed one by one until no improvement of BIC was obtained.

Assessing the impact of viral load on survival. Finally, we aimed to assess the impact of viral dynamics on survival using a joint model, where the parameters of both viral load dynamic and survival are analyzed simultaneously to limit the bias due to dropout (8, 59, 60). In this model, the hazard function for patient i at time t, $h_i(t|\psi_i)$is the instantaneous hazard function in patient i at time t,

$$h_i(t|\psi_i) = \lambda \times \exp\left(\sum_{j=1}^{r} \gamma_j \times z_i^j + \nu \times log_{10} V(t, \psi_i)\right),$$

where r are the significant risk factors found in the survival analysis above, z_i^j denotes the presence or the absence of the risk factor j in patient i, and $\exp(\gamma_j)$ denotes the hazard ratio associated with the risk factor j. Finally, ν denotes the impact of the current (log) viral load value in patient on the hazard function, with $\nu = 0$ implying that viral load has no impact on the hazard function and $\nu > 0$ implying that the current viral load value increases the hazard function. Using the same notation as before, $\exp(\nu)$ is the hazard ratio of the current viral load value.

For the sake of identifiability, we assumed that $h_i(t|\psi_i)$ was equal to 0 up until time of admission, and the survival rate up to time t in patient i, noted $S_i(t|\psi_i)$, was then obtained using the following formula:

$$S_i(t|\psi_i) = \exp\left[-\int_0^t h_i(u|\psi_i)du\right]. \quad [4]$$

The joint likelihood of the longitudinal and the survival data is then maximized using the SAEM algorithm following the methodology developed in refs. 8, 59, 60.

Predicting the impact of an effective antiviral treatment on viral kinetics and survival. The joint model was also used to simulate the effect of an antiviral treatment on viral kinetics and survival. We simulated this impact on the patients from the cohort, using their individual parameters previously estimated. We considered the effect of a treatment that would be initiated at the time of admission, with an antiviral efficacy, noted ε, in blocking viral production, p, equal to 90% or 99%. For each scenario, we plotted the median viral load and the median survival value, and the results were stratified according to the presence or absence of significant risk factors.

Sensitivity analyses and robustness. Because some parameters were not estimated, we also reestimated parameter values of the final model assuming different values of k and c ranging from 1 d^{-1} to 5 d^{-1}, and from 5 d^{-1} to 20 d^{-1}, respectively. We also tested a number of other parameterizations of the loss rate of infected cells. In particular, as the median date of antibody apparition was equal to 12 d after symptom onset in the subset of individuals where antibody had been measured (*SI Appendix*, Fig. S6), we tested models where the loss rate of infected cells could increase after day 12 (*SI Appendix*, Table S5).

We also considered different assumptions for the change in the instantaneous hazard rate for the survival component of the model, with models assuming that the hazard function could be different from 0 as early as the predicted time of infection, the onset of symptom, or after a fixed period of 7 d or 10 d after symptom onset (*SI Appendix*, Table S8).

To facilitate model comparisons, we also gave the results of the target cell-limited model assuming no change in the loss rate of infected cells over time and an effect of age on the loss rate of infected cells.

Data Availability. Anonymized spreadsheet of data has been deposited in Figshare (https://doi.org/10.6084/m9.figshare.13365398.v1).

ACKNOWLEDGMENTS. We thank all investigators for the French COVID cohort (see study groups in *SI Appendix*). The study has received financial support from the National Research Agency (ANR) through the ANR-Flash call for COVID-19 (Grant ANR-20-COVI-0018) and the Bill and Melinda Gates Foundation under Grant Agreement INV-017335. The French cohort was supported by the REACTing consortium and by a grant from the French Ministry of Health (Grant PHRC 20-0424). The funders had no role in the study design; in the collection, analysis, and interpretation of data; in the writing of the report; and in the decision to submit the article for publication.

1. World Health Organization, Coronavirus disease (COVID-19) outbreak situation: Situation report. https://www.who.int/docs/default-source/coronaviruse/situation-reports/20201012-weekly-epi-update-9.pdf. Accessed 25 January 2021.
2. A. B. Docherty *et al.*; ISARIC4C investigators, Features of 20 133 UK patients in hospital with covid-19 using the ISARIC WHO clinical characterisation protocol: Prospective observational cohort study. *BMJ* **369**, m1985 (2020).
3. C. Huang *et al.*, Clinical features of patients infected with 2019 novel coronavirus in Wuhan, China. *Lancet* **395**, 497–506 (2020).
4. N. Chen *et al.*, Epidemiological and clinical characteristics of 99 cases of 2019 novel coronavirus pneumonia in Wuhan, China: A descriptive study. *Lancet* **395**, 507–513 (2020).
5. G. Onder, G. Rezza, S. Brusaferro, Case-fatality rate and characteristics of patients dying in relation to COVID-19 in Italy. *JAMA* **323**, 1775–1776 (2020).
6. S. Richardson *et al.*; the Northwell COVID-19 Research Consortium, Presenting characteristics, comorbidities, and outcomes among 5700 patients hospitalized with COVID-19 in the New York City area. *JAMA* **323**, 2052–2059 (2020).
7. E. J. Williamson *et al.*, Factors associated with COVID-19-related death using OpenSAFELY. *Nature* **584**, 430–436 (2020).
8. V. Madelain *et al.*, Ebola viral dynamics in nonhuman primates provides insights into virus immuno-pathogenesis and antiviral strategies. *Nat. Commun.* **9**, 4013 (2018).
9. C.-C. Li *et al.*, Correlation of pandemic (H1N1) 2009 viral load with disease severity and prolonged viral shedding in children. *Emerg. Infect. Dis.* **16**, 1265–1272 (2010).
10. A. S. Perelson, A. U. Neumann, M. Markowitz, J. M. Leonard, D. D. Ho, HIV-1 dynamics in vivo: Virion clearance rate, infected cell life-span, and viral generation time. *Science* **271**, 1582–1586 (1996).
11. A. U. Neumann *et al.*, Hepatitis C viral dynamics in vivo and the antiviral efficacy of interferon-alpha therapy. *Science* **282**, 103–107 (1998).
12. L. Zou *et al.*, SARS-CoV-2 viral load in upper respiratory specimens of infected patients. *N. Engl. J. Med.* **382**, 1177–1179 (2020).
13. B. E. Young *et al.*; Singapore 2019 Novel Coronavirus Outbreak Research Team, Epidemiologic features and clinical course of patients infected with SARS-CoV-2 in Singapore. *JAMA* **323**, 1488–1494 (2020).
14. S. A. Lauer *et al.*, The incubation period of coronavirus disease 2019 (COVID-19) from publicly reported confirmed cases: Estimation and application. *Ann. Intern. Med.* **172**, 577–582 (2020).
15. X. He *et al.*, Temporal dynamics in viral shedding and transmissibility of COVID-19. *Nat. Med.* **26**, 672–675 (2020).
16. M. Cevik *et al.*, SARS-CoV-2, SARS-CoV, and MERS-CoV viral load dynamics, duration of viral shedding, and infectiousness: A systematic review and meta-analysis. *Lancet Microbe* **2**, e13–e22 (2021).
17. I. F.-N. Hung *et al.*, SARS-CoV-2 shedding and seroconversion among passengers quarantined after disembarking a cruise ship: A case series. *Lancet Infect. Dis.* **20**, 1051–1060 (2020).
18. Y. Liu *et al.*, Viral dynamics in mild and severe cases of COVID-19. *Lancet Infect. Dis.* **20**, 656–657 (2020).
19. S. Zheng *et al.*, Viral load dynamics and disease severity in patients infected with SARS-CoV-2 in Zhejiang province, China, January-March 2020: Retrospective cohort study. *BMJ* **369**, m1443 (2020).
20. R. Magleby *et al.*, Impact of SARS-CoV-2 viral load on risk of intubation and mortality among hospitalized patients with coronavirus disease 2019. *Clin. Infect. Dis.*, 10.1093/cid/ciaa851 (2020).
21. K. K.-W. To *et al.*, Temporal profiles of viral load in posterior oropharyngeal saliva samples and serum antibody responses during infection by SARS-CoV-2: An observational cohort study. *Lancet Infect. Dis.* **20**, 565–574 (2020).
22. Q.-X. Long *et al.*, Clinical and immunological assessment of asymptomatic SARS-CoV-2 infections. *Nat. Med.* **26**, 1200–1204 (2020).
23. K. Wang *et al.*, Differences of severe acute respiratory syndrome coronavirus 2 shedding duration in sputum and nasopharyngeal swab specimens among adult inpatients with coronavirus disease 2019. *Chest* **158**, 1876–1884 (2020).
24. D. Yan *et al.*, Factors associated with prolonged viral shedding and impact of lopinavir/ritonavir treatment in hospitalised non-critically ill patients with SARS-CoV-2 infection. *Eur. Respir. J.* **56**, 2000799 (2020).
25. P. Baccam, C. Beauchemin, C. A. Macken, F. G. Hayden, A. S. Perelson, Kinetics of influenza a virus infection in humans. *J. Virol.* **80**, 7590–7599 (2006).
26. A. M. Smith, A. S. Perelson, Influenza A virus infection kinetics: Quantitative data and models. *Wiley Interdiscip. Rev. Syst. Biol. Med.* **3**, 429–445 (2011).
27. S. Tubiana *et al.*, High-risk exposure without personal protective equipment and infection with SARS-CoV-2 in healthcare workers: Results of the CoV-CONTACT prospective cohort. *medRxiv* [Preprint] (2020). https://doi.org/10.1101/2020.09.17.20194860 (Accessed 14 October 2020).
28. A. Goyal, E. R. Duke, E. F. Cardozo-Ojeda, J. T. Schiffer, Mathematical modeling explains differential SARS CoV-2 kinetics in lung and nasal passages in remdesivir treated rhesus macaques. *bioRxiv* [Preprint] (2020). https://doi.org/10.1101/2020.06.21.163550 (Accessed 14 October 2020).
29. R. Ke, C. Zitzmann, R. M. Ribeiro, A. S. Perelson, Kinetics of SARS-CoV-2 infection in the human upper and lower respiratory tracts and their relationship with infectiousness. *medRxiv* [Preprint] (2020). https://doi.org/10.1101/2020.09.25.20201772 (Accessed 14 October 2020).
30. A. Gonçalves *et al.*, Timing of antiviral treatment initiation is critical to reduce SARS-CoV-2 viral load. *CPT Pharmacometrics Syst. Pharmacol.* **9**, 509–514 (2020).

31. A. Gonçalves *et al*., Viral dynamic modeling of SARS-CoV-2 in non-human primates. *Research Square* [Preprint] (2020). https://doi.org/10.21203/rs.3.rs-50301/v1 (Accessed 21 October 2020).
32. S. Wang *et al*., Modeling the viral dynamics of SARS-CoV-2 infection. *Math. Biosci.* **328**, 108438 (2020).
33. A. Goyal, E. F. Cardozo-Ojeda, J. T. Schiffer, Potency and timing of antiviral therapy as determinants of duration of SARS-CoV-2 shedding and intensity of inflammatory response. *Sci. Adv.* **6**, eabc7112 (2020).
34. A. M. Smith, Host-pathogen kinetics during influenza infection and coinfection: Insights from predictive modeling. *Immunol. Rev.* **285**, 97–112 (2018).
35. P. Maisonnasse *et al*., Hydroxychloroquine use against SARS-CoV-2 infection in non-human primates. *Nature* **585**, 584–587 (2020).
36. P. Horby *et al*., Effect of hydroxychloroquine in hospitalized patients with COVID-19: Preliminary results from a multi-centre, randomized, controlled trial. *medRxiv* [Preprint] (2020). https://doi.org/10.1101/2020.07.15.20151852 (Accessed 25 August 2020).
37. H. Pan *et al*.; WHO Solidarity Trial Consortium, Repurposed antiviral drugs for Covid-19 - Interim WHO solidarity trial results. *N. Engl. J. Med.*, 10.1056/NEJMoa2023184 (2020).
38. A. Sakurai *et al*., Natural history of asymptomatic SARS-CoV-2 infection. *N. Engl. J. Med.* **383**, 885–886 (2020).
39. B. La Scola *et al*., Viral RNA load as determined by cell culture as a management tool for discharge of SARS-CoV-2 patients from infectious disease wards. *Eur. J. Clin. Microbiol. Infect. Dis.* **39**, 1059–1061 (2020).
40. J. Bullard *et al*., Predicting infectious SARS-CoV-2 from diagnostic samples. *Clin. Infect. Dis.* **71**, 2663–2666 (2020).
41. V. Madelain *et al*., Modeling favipiravir antiviral efficacy against emerging viruses: From animal studies to clinical trials. *CPT Pharmacometrics Syst. Pharmacol.* **9**, 258–271 (2020).
42. J. Guedj *et al*., Antiviral efficacy of favipiravir against Ebola virus: A translational study in cynomolgus macaques. *PLoS Med.* **15**, e1002535 (2018).
43. P. Chen *et al*.; BLAZE-1 Investigators, SARS-CoV-2 neutralizing antibody LY-CoV555 in outpatients with covid-19. *N. Engl. J. Med.* **384**, 229–237 (2020).
44. N. Buetti *et al*., SARS-CoV-2 detection in the lower respiratory tract of invasively ventilated ARDS patients. *Crit. Care* **24**, 610 (2020).
45. Y. Yazdanpanah; French COVID cohort investigators and study group, Impact on disease mortality of clinical, biological and virological characteristics at hospital admission and over time in COVID-19 patients. *J. Med. Virol.* 10.1002/jmv.26601 (2020).
46. J.-F. Delfraissy, Y. Yazdanpanah, Y. Levy, REACTing: The French response to infectious disease crises. *Lancet* **387**, 2183–2185 (2016).
47. J. W. Dunning *et al*.; ISARIC Working Group 3, ISARIC Council, Open source clinical science for emerging infections. *Lancet Infect. Dis.* **14**, 8–9 (2014).
48. Institut Pasteur, Protocol: Real-time RT-PCR assays for the detection of SARS CoV-2. https://www.who.int/docs/default-source/coronaviruse/real-time-rt-pcr-assays-for-the-detection-of-sars-cov-2-institut-pasteur-paris.pdf?sfvrsn=3662fcb6_2. Accessed 18 October 2020.
49. V. M. Corman *et al*., Detection of 2019 novel coronavirus (2019-nCoV) by real-time RT-PCR. *Euro Surveill.* **25**, 1–8 (2020).
50. A. Gonçalves, F. Mentré, A. Lemenuel-Diot, J. Guedj, Model averaging in viral dynamic models. *AAPS J.* **22**, 48 (2020).
51. X. Wu *et al*., Intrinsic immunity shapes viral resistance of stem cells. *Cell* **172**, 423–438.e25 (2018).
52. D. B. Stetson, R. Medzhitov, Type I interferons in host defense. *Immunity* **25**, 373–381 (2006).
53. J. Bekisz, H. Schmeisser, J. Hernandez, N. D. Goldman, K. C. Zoon, Human interferons alpha, beta and omega. *Growth Factors* **22**, 243–251 (2004).
54. P. Ahlquist, A. O. Noueiry, W.-M. Lee, D. B. Kushner, B. T. Dye, Host factors in positive-strand RNA virus genome replication. *J. Virol.* **77**, 8181–8186 (2003).
55. S. Koyama, K. J. Ishii, C. Coban, S. Akira, Innate immune response to viral infection. *Cytokine* **43**, 336–341 (2008).
56. S. Jegaskanda *et al*., Influenza virus infection enhances antibody-mediated NK cell functions via type I interferon-dependent pathways. *J. Virol.* **93**, e02090–e18 (2019).
57. R. Blair, Hantavirus pulmonary syndrome acquired in New York State. *J. Hosp. Med.* **6**, S159 (2011).
58. W. Sungnak *et al*.; HCA Lung Biological Network, SARS-CoV-2 entry factors are highly expressed in nasal epithelial cells together with innate immune genes. *Nat. Med.* **26**, 681–687 (2020).
59. C. Tardivon *et al*., Association between tumor size kinetics and survival in patients with urothelial carcinoma treated with atezolizumab: Implication for patient follow-up. *Clin. Pharmacol. Ther.* **106**, 810–820 (2019).
60. S. Desmée, F. Mentré, C. Veyrat-Follet, J. Guedj, Nonlinear mixed-effect models for prostate-specific antigen kinetics and link with survival in the context of metastatic prostate cancer: A comparison by simulation of two-stage and joint approaches. *AAPS J.* **17**, 691–699 (2015).

Chapitre 6

Dynamique virale du patient hospitalisé en présence d'un traitement antiviral

6.1 Résumé

L'essai European DisCoVeRy (NCT04315948) été lancé en mars 2020 en tant qu'essai fille de l'OMS Solidarity (NCT04647669). Ces essais avaient pour objectifs d'évaluer l'efficacité clinique d'un certain nombre de médicaments redirigés selon les recommandations initiales de l'OMS chez le patient hospitalisé. L'utilité des traitements antiviraux, dont fait partie le remdesivir, a été critiquée, étant donné qu'à l'admission à l'hôpital, la réponse immunitaire déréglée ou tempête de cytokines était considérée comme le principal moteur de la dégradation clinique. A la différence des grands essais cliniques comme Solidarity ou RECOVERY (NCT04381936) qui visaient uniquement à évaluer des traitements, cet essai avait en plus de l'évaluation thérapeutique, un objectif scientifique de compréhension de la maladie. En ce sens, cet essai recrutait moins de patients que ceux sus-cités, mais a pu se procurer un grand nombre de données. En particulier, l'essai a collecté des données centralisées et normalisées de charge virale collectées séquentiellement à des temps précis après la randomisation afin d'enrichir l'analyse de l'efficacité clinique des traitements avec une analyse de l'efficacité virologique. Son critère de jugement principal était l'amélioration clinique

du patient à J15 post-randomisation, mesurée sur l'échelle clinique ordinale en 7 points définie par l'OMS. Cet essai comprenait 5 bras, Standard of Care (SoC), hydroxychloroquine, lopinavir/ritonavir, lopinavir/ritonavir+IFNβ-1a et enfin remdesivir. Les bras de l'hydroxychloroquine et ceux contenant du lopinavir/ritonavir ont été arrêtés rapidement pour futilité (respectivement le 25 mai et le 29 juin 2020) [144], pour ne garder que le bras SoC seul vs SoC + Remdesivir, arrêté le 20 janvier 2021 et qui n'a pas montré d'efficacités clinique ou antivirale dans cet essai [61].

En utilisant les connaissances acquises précédemment sur l'évolution virale naturelle, nous avons évalué tout d'abord l'impact des bras hydroxychloroquine et ceux contenant de l'IFN sur cette dernière [145]. Cependant, suite à de l'absence de signal chez le primate non-humain quant à leurs efficacités antivirales, nous n'avons pas poursuivi notre approche sur ces bras. Le remdesivir quant à lui avait montré des signaux d'efficacité antivirale chez le même modèle animal, ainsi qu'une efficacité clinique chez l'Homme, controversée, mais qui a mené à son approbation quant à l'utilisation chez le patient hospitalisé. Afin d'explorer plus précisément la question de l'efficacité antivirale, nous avons modélisé la dynamique virale de patients hospitalisés traités soit par le Standard of Care (N=329) soit par le Standard of Care + Remdesivir (N=336). En nous appuyant sur le modèle développé au chapitre précédent, nous avons incorporé l'effet du traitement par remdesivir comme paramètre inhibant la production virale. En raison de la latence nécessaire pour atteindre sa forme active, nous avons ajouté plusieurs délais pharmacologiques possibles, allant de 0 à 5 jours après le début du traitement, et nous avons effectué une approche de *Model Averaging* prenant en compte ces différents délais. Enfin, nous avons mené une analyse exploratoire en stratifiant notre population en fonction de la charge virale au moment de la randomisation, afin d'identifier la catégorie d'individus la plus susceptible de répondre au traitement.

Nous avons estimé une faible réduction de la production virale induite par le remdesivir de 52 %

(IC%95 :35-69). Les simulations avec cet effet de traitement prévoyaient une diminution de seulement 0,7 (0-1,3) jour en termes de temps de clairance virale. Nous avons constaté que cet effet s'élevait à 80 % (IC%95 :65-96) chez les patients dont la charge virale à l'admission était supérieure au seuil d'infectiosité (3,5 log10 copies/10^4 cellules), entraînant un délai de clairance virale raccourci de 2,4 (IIQ : 0,9-4,5) jours par rapport aux patients non traités. En conclusion, nous avons identifié un effet antiviral du remdesivir sur la charge virale. Cependant, cet effet reste modeste, et bien que plus puissant chez les patients admis à l'hôpital avec une charge virale élevée, cette efficacité reste en deçà de la cible pharmacodynamique de 90% identifiée dans de précédents travaux [131], ce qui peut explique l'inefficacité clinique retrouvée dans cet essai.

6.2 Article 2

Effect of remdesivir on viral dynamics in COVID-19 hospitalized patients : a modelling analysis of the randomized, controlled, open-label DisCoVeRy trial

Guillaume Lingas, Nadège Néant, Alexandre Gaylard, Drifa Belhadi, Gilles Peytavin, Maya Hites, Thérèse Staub, Richard Greil, José-Artur Paiva, Julien Poissy, Nathan Peiffer-Smadja, Dominique Costagliola, Yazdan Yazdanpanah, Florent Wallet, Amandine Gagneux-Brunon, France Mentré, Florence Ader, Charles Burdet, Jérémue Guedj, Maude Bouscambert-Duchamp ; DisCoVeRy study Group

Journal of Antimicrobial Chemotherapy, 2022

J Antimicrob Chemother
https://doi.org/10.1093/jac/dkac048

Journal of Antimicrobial Chemotherapy

Effect of remdesivir on viral dynamics in COVID-19 hospitalized patients: a modelling analysis of the randomized, controlled, open-label DisCoVeRy trial

Guillaume Lingas [1]*†, Nadège Néant[1]†, Alexandre Gaymard[2,3], Drifa Belhadi[1,4,5], Gilles Peytavin [1,6], Maya Hites[7], Thérèse Staub[8], Richard Greil[9,10,11], Jose-Artur Paiva[12,13], Julien Poissy[14], Nathan Peiffer-Smadja [1,15,16], Dominique Costagliola[17], Yazdan Yazdanpanah[1,15], Florent Wallet[18,19], Amandine Gagneux-Brunon [20,21,22], France Mentré[1,4,5,23], Florence Ader[19,24], Charles Burdet[1,4], Jérémie Guedj [1]§ and Maude Bouscambert-Duchamp[2]§ on behalf of the DisCoVeRy study group

[1]Université de Paris, IAME, INSERM, F-75018 Paris, France; [2]Hospices Civils de Lyon, Département de Virologie, Institut des Agents Infectieux, Centre National de Référence des virus des infections respiratoires France Sud, F-69004, Lyon, France; [3]Université de Lyon, Virpath, CIRI, INSERM U1111, CNRS UMR5308, ENS Lyon, Université Claude Bernard Lyon 1, F-69372, Lyon, France; [4]AP-HP, Hôpital Bichat, Département d'Épidémiologie, Biostatistique et Recherche Clinique, F-75018, Paris, France; [5]CIC-EC 1425, INSERM, F-75018, Paris, France; [6]AP-HP, Hôpital Bichat Claude Bernard, Laboratoire de Pharmacologie-toxicologie, F-75018 Paris, France; [7]Hôpital Universitaire de Bruxelles-Hôpital Erasme, Université Libre de Bruxelles, Clinique des maladies infectieuses, Brussels, Belgium; [8]Centre hospitalier de Luxembourg, Service des maladies infectieuses, L-1210 Luxembourg, Luxembourg; [9]Department of Internal Medicine III with Haematology, Medical Oncology, Haemostaseology, Infectiology and Rheumatology, Oncologic Center, Salzburg Cancer Research Institute - Laboratory for Immunological and Molecular Cancer Research (SCRI-LIMCR), Paracelsus Medical University Salzburg, 5020 Salzburg, Austria; [10]Cancer Cluster Salzburg, 5020, Salzburg, Austria; [11]AGMT, 5020 Salzburg, Austria; [12]Centro Hospitalar São João, Emergency and Intensive Care Department, Porto, Portugal; [13]Universidade do Porto, Faculty of Medicine, Porto, Portugal; [14]Université de Lille, Inserm U1285, CHU Lille, Pôle de réanimation, CNRS, UMR 8576 - UGSF - Unité de Glycobiologie Structurale et Fonctionnelle, F-59000, Lille, France; [15]AP-HP, Hôpital Bichat, Service de Maladies Infectieuses et Tropicales, F-75018 Paris, France; [16]National Institute for Health Research, Health Protection Research Unit in Healthcare Associated Infections and Antimicrobial Resistance, Imperial College London, London, UK; [17]Sorbonne Université, Inserm, Institut Pierre-Louis d'Épidémiologie et de Santé Publique, F-75013, Paris, France; [18]Service de Médecine Intensive Réanimation anesthésie, Centre Hospitalier Lyon Sud, Hospices Civils de Lyon, Pierre-Benite, France; [19]Université Claude Bernard Lyon 1, CIRI, INSERM U1111, CNRS UMR5308, ENS Lyon, F-69372, Lyon, France; [20]CHU de Saint-Etienne, Service d'Infectiologie, F-42055 Saint-Etienne, France; [21]Université Jean Monnet, Université Claude Bernard Lyon 1, GIMAP, CIRI, INSERM U1111, CNRS UMR5308, ENS Lyon, F-42023 Saint-Etienne, France; [22]CIC 1408, INSERM, F-42055 Saint-Etienne, France; [23]AP-HP, Hôpital Bichat, Unité de Recherche Clinique, F-75018, Paris, France; [24]Hospices Civils de Lyon, Département des maladies infectieuses et tropicales, F-69004, Lyon, France

*Corresponding author. E-mail: guillaume.lingas@inserm.fr
†These authors contributed equally.
§These authors contributed equally.

Received 26 November 2021; accepted 3 February 2022

Background: The antiviral efficacy of remdesivir in COVID-19 hospitalized patients remains controversial.

Objectives: To estimate the effect of remdesivir in blocking viral replication.

Methods: We analysed nasopharyngeal normalized viral loads from 665 hospitalized patients included in the DisCoVeRy trial (NCT 04315948; EudraCT 2020-000936-23), randomized to either standard of care (SoC) or SoC + remdesivir. We used a mathematical model to reconstruct viral kinetic profiles and estimate the antiviral efficacy of remdesivir in blocking viral replication. Additional analyses were conducted stratified on time of treatment initiation ($\leq$7 or $>$7 days since symptom onset) or viral load at randomization ($<$ or $\geq$3.5 $\log_{10}$ copies/10^4 cells).

Results: In our model, remdesivir reduced viral production by infected cells by 2-fold on average (95% CI: 1.5–3.2-fold). Model-based simulations predict that remdesivir reduced time to viral clearance by 0.7 days compared with SoC, with large inter-individual variabilities (IQR: 0.0–1.3 days). Remdesivir had a larger impact in patients with high viral load at randomization, reducing viral production by 5-fold on average (95% CI: 2.8–25-fold) and the median time to viral clearance by 2.4 days (IQR: 0.9–4.5 days).

Conclusions: Remdesivir halved viral production, leading to a median reduction of 0.7 days in the time to viral clearance compared with SoC. The efficacy was larger in patients with high viral load at randomization.

Introduction

Remarkable progress has recently been made in finding effective antiviral treatments in SARS-CoV-2-infected patients that can prevent disease progression and hospitalization. These treatments, which can rely either on monoclonal antibodies[1,2] or small molecules,[3,4] need to be administered early in the infection, typically in the first week after symptom onset, to be fully effective. Although the use of monoclonal antibodies has shown some encouraging results in the Recovery trial,[5] the role of antiviral treatments in hospitalized patients to prevent mechanical ventilation and death remains unclear. Among these drugs, remdesivir has received an emergency use authorization for the treatment of COVID-19 hospitalized patients in several countries, and is approved for hospitalized patients in the United States.[6] However, its clinical efficacy remains controversial, with some randomized clinical trials pointing to efficacy in preventing disease worsening, and others finding no efficacy.[7–10]

Remdesivir is a nucleoside analogue prodrug inhibiting RNA polymerase activity of several viruses[11] that has shown antiviral activity against SARS-CoV-2 both *in vitro* and in animal models.[12–14] An important element to precisely evaluate remdesivir is to analyse its effect on viral dynamics, which is likely a prerequisite to clinical efficacy. However, results from the literature are still scarce. In three randomized and controlled clinical trials, no difference in viral load levels were found between hospitalized patients receiving remdesivir and those that did not receive remdesivir.[7,10,15] In two of these studies,[7,8] the analysis of the effect was hampered by limited number of patients (with 237 and 181 patients included) and by the design of the analysis, which compared viral load at different timepoints and not the overall effect on viral dynamics.[7] Moreover, the results remained limited by the heterogeneity in the biological samples and the molecular techniques used. In the larger DisCoVeRy trial, which used normalized viral loads,[15] no effect of remdesivir on viral dynamics was found, but the variability of the time interval between the onset of symptoms and treatment initiation, which is a key factor for antiviral drug evaluation,[16,17] was not considered. One potential approach to address this issue is to use a model-based approach to reconstitute the precise effect of treatment on the course of viral dynamics, as we previously showed in a cohort of hospitalized patients.[18]

Here, we developed this approach to estimate the effect of remdesivir in inhibiting viral replication. We used normalized and centralized data on viral kinetics from the European randomized controlled DisCoVeRy trial that compared the efficacy of remdesivir plus standard of care (SoC) with SoC alone in COVID-19 hospitalized patients.[15,19]

Patients and methods

Study design and data collection

Hospitalized patients with a laboratory-confirmed SARS-CoV-2 infection were enrolled in the DisCoVeRy trial (NCT 04315948; EudraCT 2020-000936-23[15]), sponsored by the Institut national de la santé et de la recherche médicale (Inserm, France). Written informed consent was obtained from all included participants (or their legal representatives if unable to consent). We analysed the results obtained from patients allocated to receive either SoC alone or SoC plus remdesivir between March 2020 and January 2021, hospitalized at 48 different sites in France, Belgium, Portugal, Austria and Luxembourg, and for whom nasopharyngeal swabs were available. Given that patients who were reported to arrive very late in their disease could be indicative of a poor reporting of the time of symptom onset, we removed from our analysis the $N=17$ patients whose delay between the reported time of symptom onset and the randomization was larger than 20 days. Remdesivir was administered intravenously at a loading dose of 200 mg on day 1 followed by 100 mg infusions once-daily for up to 10 days. More details on study design, ethics approval and inclusion/exclusion criteria can be found in the initial trial report.[15]

Viral load measurements

Normalized viral load in samples was measured at randomization and at days 3, 5, 8, 11, 15 ± 2 and 29 ± 3 after randomization, in nasopharyngeal swabs collected through validated devices containing flocked swabs and virus transport medium.

To allow the comparison of samples of different qualities (cell richness) we followed the same methodology of normalized viral load developed previously in the context of influenza virus infection.[20] In brief, the normalized SARS-CoV-2 viral load was determined by RT-PCR blinded to treatment arm, divided by the number of cells measured (quantification of HPRT-1 housekeeping gene) and expressed in copies per 10^4 cells. All samples were centralized and analysed in the same laboratory at the National Centre for Viral Respiratory Infections (Hospices Civils de Lyon, France). We estimated the limit of detection (LoD) as 1 $\log_{10}$ copies/10^4 cells and all viral loads strictly below LoD were considered as censored.[15]

Viral load was also assessed in broncho-alveolar lavage (BAL) fluids for a subset of patients, at the clinician's discretion (see Discussion).

Viral dynamics model

We used a mathematical model to reconstruct the viral kinetics from the time of infection ($t=0$) until viral clearance. The model incorporates an effect of remdesivir, denoted as ε, that reduces viral production after a pharmacological delay, denoted as τ. The estimation of both viral kinetic and treatment parameters was obtained through fitting of the model to the virological data from both remdesivir-treated and -untreated patients from the Discovery trial.

Model equations

Given the small number of patients hospitalized in the first days after symptom onset,[15] we used a target-cell limited model with an eclipse phase to characterize viral dynamics,[18] and did not consider more complex models.[18] The model includes target cells (T) and infected cells, that are initially non-productive (I_1)during the eclipse phase and become subsequently productively infected (I_2). The model assumes that target cells are infected at a constant infection rate β, and the mean duration of the eclipse phase is noted 1/k. Productively infected cells have a constant loss rate, denoted δ, that differs between patients above or below 65 years old.[18] Each infected cell produces p viral particles per day, but only a fraction of these particles, μ are infectious. We note V the sum of infectious viral particles, V_i and of non-infectious viral particles, V_{ni} and both are cleared at rate c. The model can be written as:

$$\frac{dT}{dt} = -\beta V_i T$$
$$\frac{dI_1}{dt} = \beta V_i T - kI_1$$
$$\frac{dI_2}{dt} = kI_1 - \delta I_2$$
$$\frac{dV_i}{dt} = p\mu I_2 - cV_i$$
$$\frac{dV_{ni}}{dt} = p(1-\mu)I_2 - cV_{ni} \quad (1)$$

At the time of infection, we assumed that there is exactly one productively infected cell I_2 in the entire nasopharyngeal tract, thus: $T=T_0$; $I_1=0$; $I_2=1$; $V_i=0$; $V_{ni}=0$. The basic reproductive number R_0, defined as the number of secondary infected cells resulting from one infected cell in a population of fully susceptible cells, is equal to $\beta p T_0 \mu/c\delta$ where T_0, the total number of susceptible cells, is equal to 4×10^6 cells.[21] We used a scaling factor, f, to convert V into a normalized viral load and we note $V_{obs}=f\times V$. As only the parameter $p\times f$ can be estimated, we assumed without loss of generality that the proportion of susceptible cells in the biological sample was on average 10-fold lower than in the nasopharyngeal compartment, i.e. 0.1%.[21] Thus, we fixed f to $10^{-3}\times10^4/4\times10^6 = 2.5\times10^{-6}$. Changing the value of the scaling factor would affect the estimate of p, but not the value of the other parameters, including the estimation of R_0 and the treatment efficacy (see below).

We fixed c to 10 days^{-1}, k to 4 days^{-1} and μ to 10^{-4} as previously published.[16,18,22] Further we fixed the time of infection to 5 days prior to symptom onset in all individuals, which corresponds to the mean duration of the incubation phase.[18] We estimated p and δ as well as their interindividual variabilities. Given the lack of data on the viral upslope, we also fixed the standard deviation of the random effect associated to R_0, denoted ω_{R0} to 0.5 (which corresponds to assuming a coefficient of variation of ∼50% for this parameter).

Modelling remdesivir effect and pharmacological delay

The initiation of remdesivir reduces viral production p by a factor ε, a parameter comprised between 0 (no activity) and 1 (full viral suppression), leading to:

$$\frac{dV_i}{dt} = (1-\varepsilon)p\mu I_2 - cV_i$$
$$\frac{dV_{ni}}{dt} = (1-\varepsilon)p(1-\mu)I_2 - cV_{ni} \quad (2)$$

Active forms of remdesivir have a long mean terminal elimination half-life ($t_{½}$) of about 24 h, and in non-human primates reaches steady-state concentrations at day 4.[23] Therefore, we assumed that treatment was only effective after a certain delay after treatment initiation τ, and we considered different possible values for τ, ranging from $\tau=0$ (model M_0) to $\tau=5$ (model M_5).

We used a model averaging approach[24] to account for the uncertainty in τ. Thus, the median parameter estimates and their 95% CIs were obtained by sampling in the mixture of the parameter estimate asymptotic distribution of each model, with weights of model M_i calculated as follows:

$$w_i = \frac{e^{-\frac{AIC_i}{2}}}{\sum e^{-\frac{AIC_i}{2}}} \quad (3)$$

where AIC_i is the Akaike Information Criterion (AIC) of model M_i. We computed the model averaged likelihood using weights M_i and tested the significance of the effect of remdesivir in both models M_i and model averaging using Likelihood Ratio Test (LRT).[25]

To quantify and visualize the effect of remdesivir on the time to viral clearance, 5000 individual profiles were sampled for each candidate model M_i using the population parameters estimated in Table S1, and each potential trajectory was selected with a probability w_i. Times of treatment initiation were sampled from the fitted Gamma distribution of observed times of randomization in the population. For each simulated individual, we calculated the AUC of viral load and time to reach viral clearance, and computed the cumulated incidence of viral clearance. The same individual parameters were used assuming a null treatment efficacy ε, to simulate 5000 untreated individuals and compute the difference between a treated individual and its own control. Finally, we evaluated the effects of earlier treatment initiation, assuming a fixed time to treatment initiation of 3, 5, 7 or 9 days after symptom onset.

Sub-analyses according to viral load at admission and time since symptom onset

We used the same modelling strategy in two distinct populations, i.e. in patients in whom treatment was initiated early (≤7 days since symptom onset) and those initiating the treatment >7 days since symptom onset. We chose the cutoff of 7 days from symptom onset, consistent with the initial analysis.[15] Similarly, we conducted the same analysis in patients with high or low viral load at admission, taking the cutoff of 3.5 $\log_{10}$ copies/10^4 cells, which is the threshold level below which the virus cannot be cultured.[26]

Parameter estimation

Parameters were estimated by maximum likelihood estimation using the stochastic approximation expectation–maximization (SAEM) algorithm implemented in Monolix2020R1 (http://www.lixoft.eu), which provides estimations of the fixed effects and the standard deviation of their random effect (see Supplementary data, available at *JAC* Online). These estimates were then used to perform model averaging and results were reported as the median and 95% CI of these parameters.

Results

Baseline characteristics and viral load data of analysed population

A total of 832 patients were evaluable for the primary intention-to-treat analysis,[15] among whom 684 had at least one nasopharyngeal viral load available (Figure 1 and Figure S1). Two patients randomized in the remdesivir arm who did not receive treatment were excluded, as well as 17 patients who were randomized more than 20 days after onset of symptoms (see Methods), leaving a total of 665 patients (SoC alone, $N=329$; SoC + remdesivir, $N=336$) (Table 1; Figures S1 and S2). Patients were mostly male ($N=457$, 68.7%), younger than 65 years ($N=349$, 52.5%) and randomized more than 7 days after symptom onset ($N=455$, 68.4%). The median viral load at randomization was 3.2 $\log_{10}$ copies/10^4 cells. Overall, 15% (61/420) of patients had undetectable viral load at symptom onset; this proportion was equal to 18% (49/272) in patients randomized >7 days after symptom onset, and it was equal to 8% (12/148) in patients randomized ≤7 days after symptom onset.

Viral dynamics parameters

We used a target-cell limited model with an effect of age on the loss rate of infected cells, δ, (see Methods) which was estimated to 0.88 days^{-1} (95% CI: 0.80–0.96) in individuals aged <65 years and 0.75 days^{-1} (95% CI: 0.67–0.84) in those ≥65 years, respectively

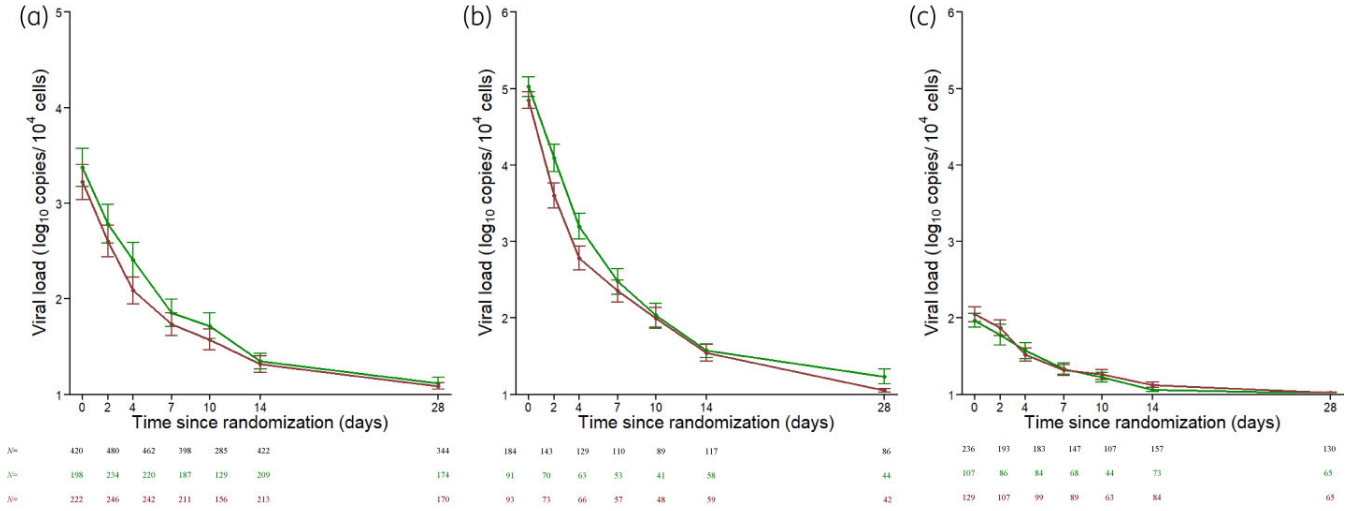

Figure 1. Nasopharyngeal normalized viral load data in 665 patients from DisCoVeRy trial analysed in the present study. (a) SARS-CoV-2 nasopharyngeal viral load according to the time since randomization. (b and c) SARS-CoV-2 nasopharyngeal viral load according to the time since randomization in patients ($N=184$) with ≥ 3.5 $\log_{10}$ copies/10^4 cells (b) and patients ($N=236$) with <3.5 $\log_{10}$ copies/10^4 cells (c). Data are presented as means (95% CI). Red lines, patients receiving remdesivir + SoC; green lines, patients receiving SoC only. Tables below show the number of samples available at each time.

(P value $<10^{-3}$; Table 2). R_0 was estimated at 10.6 (95% CI: 8.53–12.7; Table 2). The viral production p was estimated at 1.20×10^6 viruses per day (95% CI: 0.66×10^6–1.7×10^6), leading to a burst size of infectious viruses, given by $p\times\mu/\delta$ of 136 and 160 in individuals aged <65 years and those aged ≥65 years, respectively.

Table 1. Baseline characteristics of the analysed population at randomization

Characteristics	Standard of care ($N=329$)	Standard of care + remdesivir ($N=336$)
Male gender	222 (67.5%)	235 (69.9%)
Age (years)	64 (53–72)	63 (55–73)
Age ≥65 years	160 (48.6%)	156 (46.4%)
Time from symptom onset to hospitalization (days)	9 (7–11)	9 (7–11)
Patients admitted within 7 days of symptom onset	109 (33%)	101 (30%)
Duration of hospital stay (days)	12 (8–24)	13 (10–25)
Deaths	30 (9%)	30 (9%)
Normalized viral load at randomization ($\log_{10}$ copies/10^4 cells)[a]	3.2 (1.9–4.5)	3.2 (1.8–4.5)
Number of viral samples under LOQ at randomization (% of available samples)	24 (12%)	37 (17%)

Results shown are median (IQR) or *n* (%) depending on the data type.
[a]Viral load data at randomization was not available in 39.8% and 33.9% of untreated and treated patients, respectively.

Estimation of remdesivir effect on viral dynamics

Remdesivir effect, ε, was estimated for different putative values of the pharmacological delay ranging from 0 to 5 days (see Methods). Using model averaging, we estimated remdesivir to decrease the viral production p by a factor of 2 ($\varepsilon=52\%$, 95% CI: 35%–69%; Table 2) and this effect was statistically significant in model averaging (P value = 0.0031). The antiviral effect of remdesivir, ε, was statistically significant for $\tau=0$ to $\tau=3$, with values equal to 49%, 50%, 53% and 52%, respectively (P value = 0.020, 0.033, 0.0026, 0.0024, respectively, Figure 2; Table S1).

To get a sense of the effect size, we simulated 5000 *in silico* virological profiles using the estimated parameter distributions and we calculated the exact time to viral clearance for each

Table 2. Parameter distribution using model averaging

Parameter	Parameter estimates, median (95% CI)	
	Fixed effects	SD of the random effect ω
R_0	10.60 (8.53–12.68)	0.50
$\delta_{<65}$ (days^{-1})	0.88 (0.80–0.96)	0.46 (0.41–0.51)
$\delta_{\geq65}$ (days^{-1})	0.75 (0.67–0.84)	
p (10^6 virus cell^{-1} days^{-1})[a]	1.20 (0.66–1.72)	0.38 (0.14–0.63)
ε (%)	52 (35–69)	0.77 (0.18–1.37)
σ ($\log_{10}$ RNA copies/10^4 cells)	1.14 (1.09–1.19)	–

R_0, basic reproductive number; δ, loss rate of infected cells; p, rate of viral production; ε, remdesivir effect; σ, residual variability.
[a]The value of p depends on the normalization factor used to quantify viral load (see Methods).

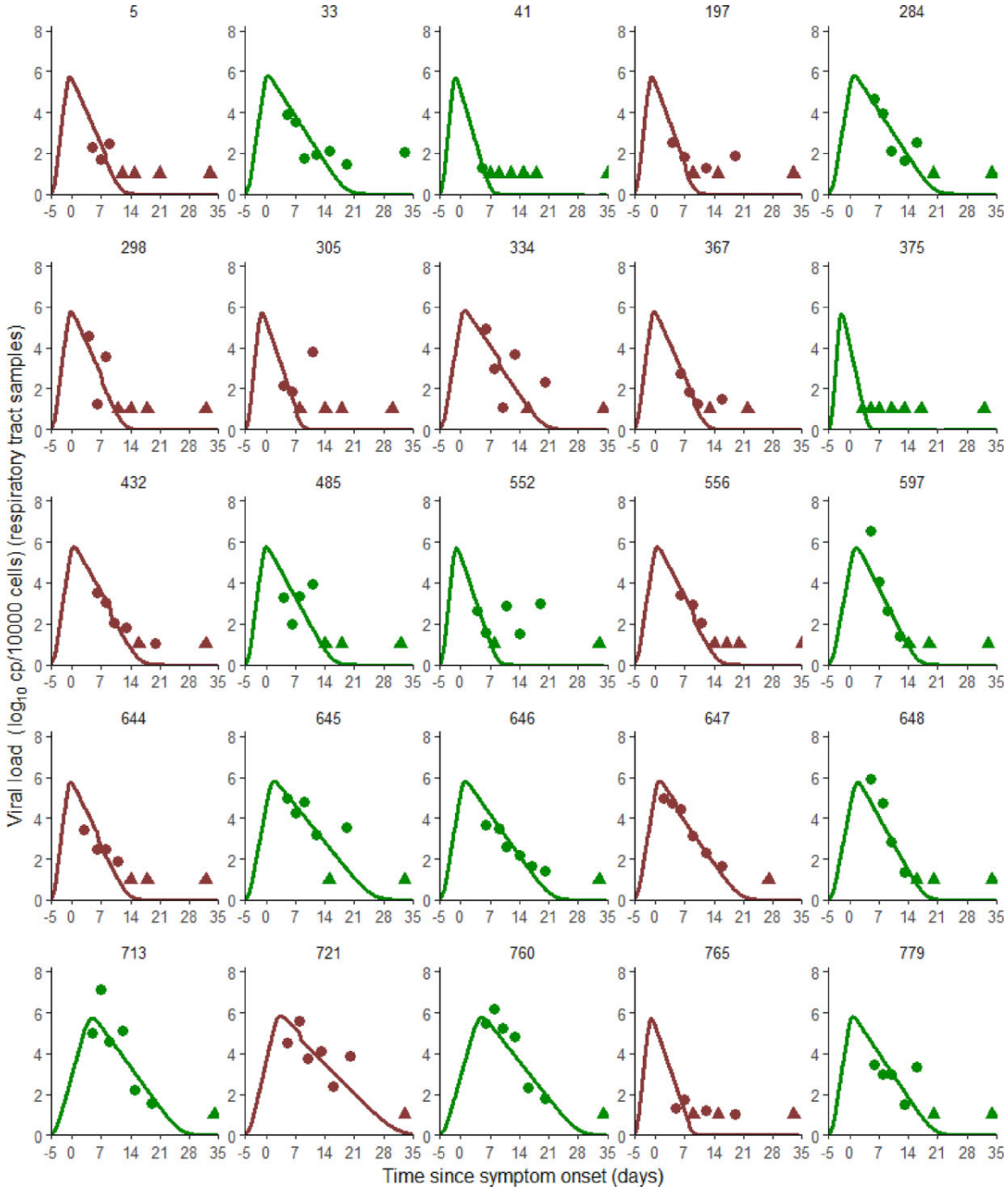

Figure 2. Model-based individual fits for $\tau = 3$. Patients represented here are the patients with seven data points collected within one week of symptom onset. Circles represent detectable viral load, triangles represent data below the limit of quantification. Results obtained by using the individual predictions of the model $\tau = 3$. Red lines and symbols, patients receiving remdesivir + SoC; green lines and symbols, patients receiving SoC only.

simulated individual. Remdesivir shortened the time to viral clearance by 0.7 days (IQR: 0.0–1.3), with a median time to viral clearance of 14.5 days (IQR: 10.4–20.2 days) and 15.3 days since symptom onset (IQR: 10.6–21.5 days) in treated and untreated individuals, respectively (Figure 3a and b). Because patients older than 65 years had a slower clearance of infected cells (P value $<10^{-3}$), they cleared virus less rapidly (15.6 versus 16.6 days in treated and untreated individuals, respectively, for patients ≥65 years and 13.3 versus 14.1 days in treated and untreated individuals, respectively, for patients <65 years). In terms of time since

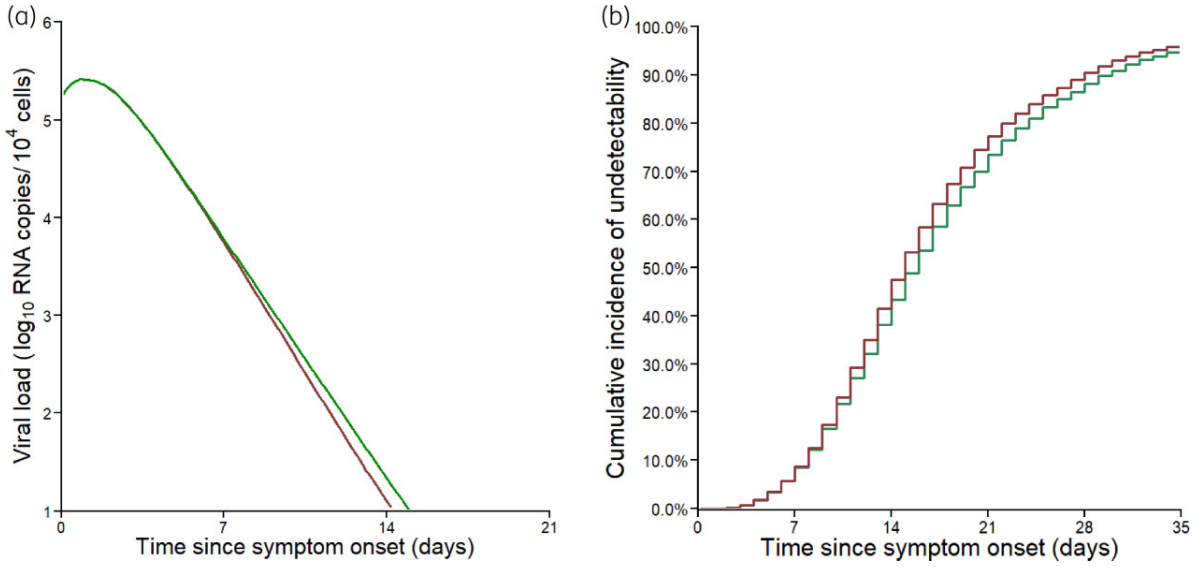

Figure 3. Viral dynamics predicted by the model. (a) Median predicted nasopharyngeal viral dynamics according to the time since symptom onset. (b) Cumulative incidence of the predicted time to viral clearance. Red line, patients receiving remdesivir + SoC; green lines, patients receiving SoC only. Results obtained by sampling 5000 individuals in the estimated parameter distributions.

randomization, remdesivir led to a time of viral clearance also reduced by 1 day, with a median time equal to 5.5 days (IQR: 1.0–12.0 days) and 6.5 days (IQR: 1.0–13.0 days) in treated and untreated individuals, respectively (Figure S3a and c), with initial undetectability at time of randomization slightly overestimated as compared with the observations (Table 1). Overall, the maximum difference in median viral loads between treated and untreated individuals was obtained at day 11.5 post symptom onset, and equal to 0.24 log_{10} copies/10^4 cells (IQR: 0.06–0.39), corresponding to a 2-fold reduction in viral load levels (Figure 3a).

We repeated the same estimation procedure in subpopulations stratified by the delay since symptom onset (Figure S4) and by the viral load at admission. In patients initiating treatment in the first 7 days following symptom onset, remdesivir effect was larger than 0 only for $\tau = 3$ (ε=36%; *P* value = 0.041, Table S2a), but it was not statistically significant by model averaging approach (*P* value = 0.07, Table S2b). In patients initiating treatment >7 days after symptom onset, remdesivir effect was no greater than 0 for any of the models considered (Tables S3a and S3b). In patients with a high viral load at admission (see Methods, $N = 184$, median time of admission = 8 days since symptom onset, IQR: 6–10, Figure 1b), remdesivir reduced viral production by 80% (95% CI: 65%–96%), i.e. a reduction by 5-fold compared with SoC, and this effect was statistically significant in model averaging (*P* value $<10^{-5}$, see Methods, Table S4a). In line with the analysis on the whole population, remdesivir effect was statistically significant for values of τ ranging from 0 to 3 days after treatment initiation, with values equal to 80%, 82%, 50% and 55%, respectively (*P* value $<10^{-3}$ for all values of τ, Table S4b). In patients admitted with a low viral load ($N = 236$, median time of admission = 9 days since symptom onset, IQR: 7–12, Figure 1c), remdesivir effect was lower and was estimated at 49%, with a poor precision of the estimation (95% CI: 0–100, *P* value = 0.013, Table S5a).

Using parameter distributions estimated in the population with high viral load at randomization, simulations showed that remdesivir led to a time to viral clearance shortened by 2.4 days (IQR: 0.9–4.5, Figure 4). Further, remdesivir led to a maximum difference between median viral loads of treated and untreated patients of 0.7 log_{10} copies/10^4 cells, reached at 12 days after symptom onset. Similar effects were obtained when looking at data in terms of time since randomization, with a median time equal to 10.5 days (IQR: 6.5–14.6 days) and 13.5 days (IQR: 10.0–18.0 days) in treated and untreated individuals, respectively (Figure S3b and d).

Discussion

We found that remdesivir had a statistically significant antiviral efficacy, reducing viral production from infected cells by 52% (95% CI: 35%–69%), which corresponds to a 2-fold reduction in viral production. The impact on viral dynamics remained modest, with an average 0.7 days reduction in the time to viral clearance and large interindividual variability. This explains why less sophisticated approaches did not find any effect of remdesivir on viral dynamics.[7,10,15]

The overall limited antiviral effect of remdesivir may be due to factors that mitigate a potential effect, in particular the heterogeneity in the time between infection and treatment initiation, as well as variability in viral load levels at the time of treatment initiation. To explore this question, we here relied on a very rich dataset of 665 patients, for which viral loads were centralized and normalized, and we used a model previously developed on a large cohort of hospitalized patients to disentangle the effects of remdesivir from the natural clearance of viral load. To identify factors associated with the effects of remdesivir on viral kinetics, we performed exploratory analyses by stratifying the population on timing of treatment initiation in days since symptom onset and on viral load at randomization, the latter being an

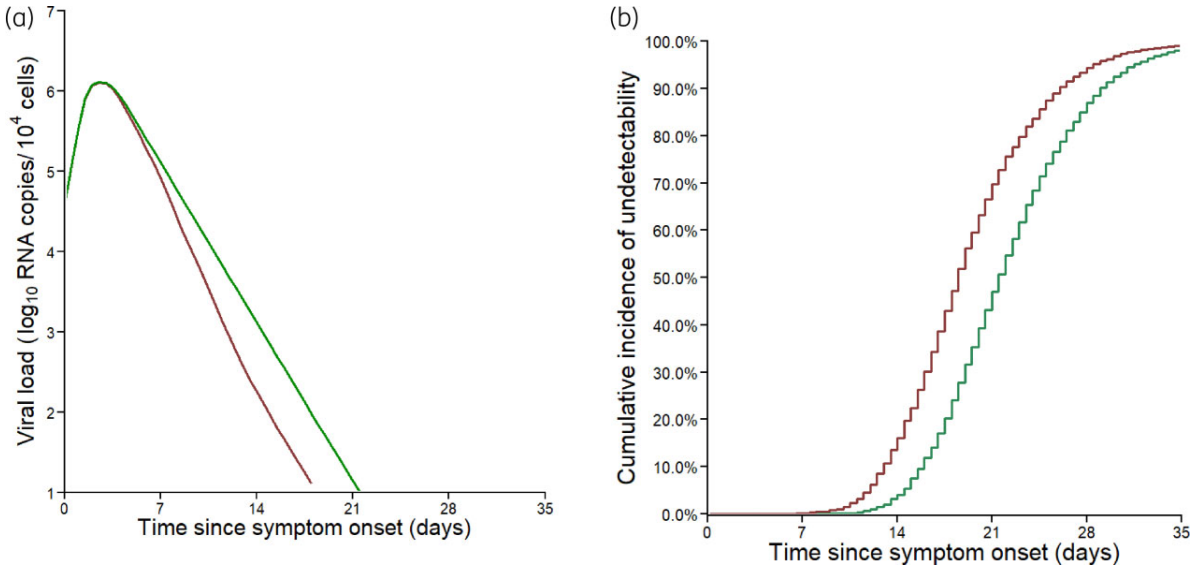

Figure 4. Viral dynamics predicted by the model in the subpopulation of viral load at admission ≥3.5 log_{10} copies/10^4 cells. (a) Median predicted nasopharyngeal viral dynamics according to the time since symptom onset. (b) Cumulative incidence of the predicted time to viral clearance. Red lines, patients receiving remdesivir + SoC; green lines patients receiving SoC only. Results obtained by sampling 5000 individuals in the estimated parameter distributions.

exploratory analysis not included in the initial trial protocol. We did not identify a significant effect of remdesivir in patients treated early, consistent with the results from descriptive models.[15] This may be due to the fact that symptom onset may not be a very good proxy of active viral replication and/or to the lack of statistical power due to the fact that viral load at admission was missing in about 40% of individuals arriving within 7 days of symptom onset (Table 1). However, remdesivir effect in reducing viral production was larger in patients with a high viral load at admission, leading to a median reduction of 2.4 days (IQR: 0.9–4.5) in the time to viral clearance compared with untreated patients. These results therefore suggest that remdesivir could be more effective in patients with high viral load, at a stage of the infection where viral replication is very active. This hypothesis is consistent with the results of the Recovery trial,[5] which identified a significant effect of monoclonal antibody combination REGN-CoV-2 on clinical outcome in hospitalized patients with a seronegative status at baseline, a factor associated with high viral load.[2,27] The relationship between treatment effect and viral load was also reported in outpatients receiving monoclonal antibodies within 7 days of symptom onset.[2,27] Simulations conducted with our model suggested no dramatic difference in viral shedding when administration is initiated between 3–7 days (Figure S5), but our model did not account for immune mechanisms that could act, in concert with early antiviral treatment, to accelerate viral clearance.[22] Consistent with the interpretation that it could be beneficial to administrate remdesivir as early as possible, results from the Pinetree study showed that administration of remdesivir in outpatients within 7 days of symptom onset led to a significant reduction of the risk of hospitalization.[3] However there was no effect of remdesivir on the average change in nasopharyngeal viral load, but more detailed analyses taking into account interpatient variability will be needed to estimate the precise effect of remdesivir on viral dynamics.

How does remdesivir antiviral efficacy compare with other antiviral drugs now available? Our estimated effect of 52% in the whole population is below the pharmacodynamic target of 90% that we determined previously to achieve clinical efficacy in hospitalized patients and/or to prevent disease acquisition in prophylactic setting.[16,18,28] It is also probably lower than what has been shown in outpatients treated with monoclonal antibodies. For instance, 7 days after treatment initiation, the viral load in ambulatory individuals receiving casirivimab + imdevimab or bamlanivimab + etesevimab was reduced by 5–10-fold compared with patients receiving placebo, as compared to 2-fold in our hospitalized population here.[2,29] The lower efficacy of remdesivir could nonetheless be relevant in a combination setting to increase the genetic barrier to resistance due to the emergence of variants of concern.[30,31] This could be even more relevant in patients with high viral load, to reduce the risk of mutation emergence in a context where huge quantities of viral progeny are still produced upon treatment initiation.

We acknowledge some important limitations to our study. First a more complete evaluation of remdesivir would involve analysing viral dynamics in the lower respiratory tract, as was done in non-human primates.[13,14] In our study, viral loads in lower respiratory tracts were available in a subset of 120 individuals. However, the number of samples was limited and these individuals had very severe disease (Table S6), making it impossible to provide an unbiased and precise estimate for remdesivir. Also, our model did not incorporate any time-dependent effects of the immune response and underestimates the response of the host in clearing the virus. Further, this model predicts that a modest antiviral effect reduces the growth rate of virus and therefore requires more time to deplete all target cells. Consequently, in this basic model treatment may have the paradoxical effect of lowering the viral load but extending the period

of shedding and the time to viral clearance.[3] This phenomenon explains why our model predicts that nearly 25% of patients would have no benefit of remdesivir in terms of viral clearance. Second, we could not evaluate the association between remdesivir drug concentration and viral decay, which would be important to obtain more definitive evidence on remdesivir antiviral activity. Here, drug concentrations were available for only a limited number of patients ($N=61$), and no significant association between drug concentrations and the time to viral clearance (Figure S6) could be found. Moreover, given that symptom onset is often after the peak viral load,[18,32] a potential bias in the estimation of early viral dynamic parameters cannot be ruled out (see a discussion on this aspect[18]). Finally, the use of adjuvant drugs such as corticosteroids or any immunosuppressive treatment that might promote viral replication, as well as the intrinsic immune competency of each treated individual have not been considered.

In conclusion, the use of a within-host model of the infection allowed us to estimate the *in vivo* antiviral efficacy of remdesivir using the nasopharyngeal swabs of hospitalized patients. Overall, we showed that remdesivir had a modest antiviral activity in reducing viral production, leading to a reduction by 0.7 days of the time to viral clearance. In exploratory analyses, remdesivir had a higher antiviral efficacy in patients with high viral load at randomization ($\geq$3.5 log copies/10^4 cells), leading to a reduction of time to viral clearance of 2.4 (IQR: 0.9–4.5) days between treated and untreated patients. The limited effect of remdesivir is consistent with the lack of clinical efficacy in hospitalized patients reported by the DisCoVeRy trial.[15]

Acknowledgements

Members of the DisCoVeRy Study Group

Sponsor: Sandrine Couffin-Cadièrgues, Christelle Delmas, Hélène Esperou (Pôle de Recherche Clinique, Inserm, Paris, France).

Investigators

Austria: Bernd Lamprecht (Kepler Universitätsklinikum Linz, Linz), Michael Joannidis (Medizinische Universität Innsbruck, Innsbruck), Alexander Egle, Richard Greil (Paracelsus Medical University Salzburg, SCRI-CCCI and AGMT). ***Belgium***: Antoine Altdorfer, Vincent Fraipont (Centre Hospitalier Régional de la Citadelle, Liège), Leila Belkhir (Cliniques Universitaires de Saint Luc, Bruxelles), Maya Hites, Gil Verschelden (Hôpital Erasme, Cliniques Universitaires de Bruxelles). ***France***: Violaine Tolsma, David Bougon (Centre Hospitalier Annecy-Genevois); Agathe Delbove, Marie Gousseff (Centre Hospitalier Bretagne-Atlantique, Vannes); Nadia Saidani, Guilhem Wattecamps (Centre Hospitalier Cornouaille, Quimper); Félix Djossou, Loïc Epelboin (Centre Hospitalier de Cayenne Andrée Rosemon); Jean-Philippe Lanoix, Pierre-Alexandre Roger, Claire Andrejak, Yoann Zerbib (Centre Hospitalier Universitaire de Amiens); Kevin Bouiller, Catherine Chirouze, Jean-Christophe Navellou (Centre Hospitalier Universitaire de Besançon); Alexandre Boyer, Charles Cazanave, Alexandre Duvignaud, Didier Gruson, Denis Malvy (Centre Hospitalier Universitaire de Bordeaux); Henry Lessire, Martin Martinot (Hospices Civils de Colmar); Pascal Andreu, Mathieu Blot, Lionel Piroth, Jean Pierre Quenot (Centre Hospitalier Universitaire de Dijon); Olivier Epaulard, Nicolas Terzi (Centre Hospitalier Universitaire de Grenoble-Alpes); Karine Faure, Emmanuel Faure, Julien Poissy, Saad Nseir (Centre Hospitalier Régional Universitaire de Lille); Florence Ader, Laurent Argaud, Tristan Ferry, Thomas Perpoint, Vincent Piriou, Jean-Christophe Richard, Julien Textoris, Florent Valour, Florent Wallet (Hospices Civils de Lyon); André Cabié, Jean- Marie Turmel, Cyrille Chabartier (Centre Hospitalier Universitaire de Martinique, Fort-de-France); Rostane Gaci, Céline Robert (Centre Hospitalier Régional de Metz-Thionville); Alain Makinson, Vincent Le Moing, Kada Klouche (Centre Hospitalier Universitaire de Montpellier); Olivier Hinschberger, Joy Mootien (Centre Hospitalier de Mulhouse Sud-Alsace); Sébastien Gibot, François Goehringer, Antoine Kimmoun, Benjamin Lefevre (Centre Hospitalier Régional Universitaire de Nancy); David Boutoille, Emmanuel Canet, Benjamin Gaborit, Paul Le Turnier, François Raffi, Jean Reignier (Centre Hospitalier Universitaire de Nantes); Johan Courjon, Jean Dellamonica, Sylvie Leroy, Charles-Hugo Marquette (Centre Hospitalier Universitaire de Nice), Paul Loubet, Claire Roger, Albert Sotto (Centre Hospitalier Universitaire de Nîmes); Cédric Bruel, Benoît Pilmis (Groupe Hospitalier de Paris Saint-Joseph); Guillaume Geri, Elisabeth Rouveix-Nordon (Hôpital Ambroise Paré, Assistance Publique - Hôpitaux de Paris); Olivier Bouchaud (Hôpital Avicenne, Assistance Publique - Hôpitaux de Paris); Samy Figueiredo, Stéphane Jaureguiberry, Xavier Monnet (Hôpital Bicêtre, Assistance Publique - Hôpitaux de Paris); Lila Bouadma, François-Xavier Lescure, Nathan Peiffer-Smadja, Jean-François Timsit, Yazdan Yazdanpanah (Hôpital Bichat - Claude Bernard, Assistance Publique - Hôpitaux de Paris); Solen Kernéis, Marie Lachâtre, Odile Launay, Jean-Paul Mira (Hôpital Cochin, Assistance Publique - Hôpitaux de Paris); Julien Mayaux, Valérie Pourcher (Hôpital de la Pitié-Salpêtrière, Assistance Publique - Hôpitaux de Paris); Jérôme Aboab, Flora Crockett, Naomi Sayre (Hôpital Delafontaine, Saint-Denis), Clément Dubost, Cécile Ficko (Hôpital d'Instruction des Armées Bégin, Saint Mandé); David Lebeaux (Hôpital Européen Georges-Pompidou, Assistance Publique - Hôpitaux de Paris); Sébastien Gallien, Armand Mekontso-Dessap (Hôpital Henri-Mondor, Assistance Publique - Hôpitaux de Paris); Jérôme Le Pavec, Francois Stefan (Hôpital Marie Lannelongue, Le Plessis-Robinson); Hafid Ait-Oufella, Karine Lacombe (Hôpital Saint-Antoine, Assistance Publique - Hôpitaux de Paris); Jean-Michel Molina (Hôpital Saint-Louis, Assistance Publique - Hôpitaux de Paris); Murielle Fartoukh, Gilles Pialoux (Hôpital Tenon, Assistance Publique - Hôpitaux de Paris); Firouzé Bani-Sadr, Bruno Mourvillier (Centre Hospitalier Universitaire de Reims); François Benezit, Fabrice Laine, Bruno Laviolle, Yves Le Tulzo, Matthieu Revest (Centre Hospitalier Universitaire de Rennes); Elisabeth Botelho-Nevers, Amandine Gagneux-Brunon, Guillaume Thiery (Centre Hospitalier Universitaire de Saint-Étienne); Raphaël Clere-Jehl, François Danion, Yves Hansmann, Ferhat Meziani, Walid Oulehri, Yvon Ruch, Charles Tacquard (Centre Hospitalier Universitaire de Strasbourg); Fanny Bounes-Vardon, Guillaume Martin-Blondel, Marlène Murris-Espin, Béatrice Riu-Poulenc (Centre Hospitalier Universitaire de Toulouse); Vanessa Jean-Michel, Eric Senneville (Centre Hospitalier de Tourcoing); Louis Bernard, Denis Garot (Centre Hospitalier Universitaire de Tours). ***Luxembourg***: Jean Reuter, Thérèse Staub (Centre Hospitalier de Luxembourg); Marc Berna (Hôpitaux Robert Schuman). ***Portugal***: Sandra Braz, Joao Miguel Ferreira Ribeiro (Centro Hospital Universitário de Lisboa Norte, Hospital de Santa Maria); José-Artur Paiva, Roberto Roncon-Albuquerque (Centro Hospitalar Universitário São João de Porto).

Laboratory support: Maude Bouscambert-Duchamp, Alexandre Gaymard, Benjamin Leveau, Bruno Lina (Hospices Civils de Lyon); Minh-Patrick Lê, Gilles Peytavin, Sarah Tubiana (Hôpital Bichat - Claude Bernard, Assistance Publique - Hôpitaux de Paris).

Trial management: Aline Dechanet (Hôpital Bichat - Claude Bernard, Assistance Publique - Hôpitaux de Paris); Juliette Saillard (ANRS-MIE), Marina Dumousseaux, Assia Ferrane (Pôle de Recherche Clinique, Inserm), Claire Fougerou-Leurent (Centre Hospitalier Universitaire de Rennes); Marion Noret (Réseau national de recherche clinique en infectiologie).

Pharmacovigilance: Alpha Diallo, Noémie Mercier, Vida Terzić (ANRS-MIE).

Statistics and data management: Drifa Belhadi, Charles Burdet, Jérémie Guedj, France Mentré, Priyanka Velou (Hôpital Bichat - Claude Bernard, Assistance Publique - Hôpitaux de Paris); Dominique Costagliola (Institut Pierre-Louis d'Épidémiologie et de Santé Publique).

Funding

This work was supported by: European Commission (EU-Response, Grant 101015736); Programme Hospitalier de Recherche Clinique (PHRC-20-0351, Ministry of Health); Domaine d'intérêt majeur One Health Île-de-France (R20117HD); REACTing, a French multi-disciplinary collaborative network working on emerging infectious diseases; Fonds Erasme-COVID-Université Libre de Bruxelles; Belgian Health Care Knowledge Centre; Austrian Group Medical Tumor; European Regional Development Fund; Portugal Ministry of Health; Portugal Agency for Clinical Research and Biomedical Innovation.

Transparency declarations

None to declare.

Supplementary data

Additional Methods, Tables S1 to S6 and Figures S1 to S6 are available as Supplementary data at *JAC* Online.

References

1 Gottlieb RL, Nirula A, Chen P *et al*. Effect of bamlanivimab as monotherapy or in combination with etesevimab on viral load in patients with mild to moderate COVID-19: A randomized clinical trial. *JAMA* 2021; **325**: 632–44.

2 Weinreich DM, Sivapalasingam S, Norton T *et al*. REGN-COV2, a neutralizing antibody cocktail, in outpatients with Covid-19. *N Engl J Med* 2021; **384**: 238–51.

3 Gottlieb RL, Vaca CE, Paredes R *et al*. Early remdesivir to prevent progression to severe Covid-19 in outpatients. *N Engl J Med* 2021; **386**: 305–15.

4 Owen DR, Allerton CMN, Anderson AS *et al*. An oral SARS-CoV-2 M pro inhibitor clinical candidate for the treatment of COVID-19. *Science* 2021; **374**: 1586–93.

5 Group RC, Horby PW, Mafham M *et al*. Casirivimab and imdevimab in patients admitted to hospital with COVID-19 (RECOVERY): a randomised, controlled, open-label, platform trial. *medRxiv* 2021; 2021.06.15.21258542.

6 NIH. Therapeutic Management. COVID-19 Treatment Guidelines. https://www.covid19treatmentguidelines.nih.gov/management/therapeutic-management/.

7 Wang Y, Zhang D, Du G *et al*. Remdesivir in adults with severe COVID-19: a randomised, double-blind, placebo-controlled, multicentre trial. *Lancet* 2020; **395**: 1569–78.

8 Beigel JH, Tomashek KM, Dodd LE *et al*. Remdesivir for the Treatment of Covid-19 — Final Report. *N Engl J Med* 2020; **383**: 1813–26.

9 WHO Solidarity Trial Consortium. Repurposed Antiviral Drugs for Covid-19 — Interim WHO Solidarity Trial Results. *N Engl J Med* 2021; **384**: 497–511.

10 Barratt-Due A, Olsen IC, Nezvalova-Henriksen K *et al*. Evaluation of the Effects of Remdesivir and Hydroxychloroquine on Viral Clearance in COVID-19. *Ann Intern Med* 2021; **174**: 1261–9.

11 Sheahan TP, Sims AC, Leist SR *et al*. Comparative therapeutic efficacy of remdesivir and combination lopinavir, ritonavir, and interferon beta against MERS-CoV. *Nat Commun* 2020; **11**: 222.

12 Wang M, Cao R, Zhang L *et al*. Remdesivir and chloroquine effectively inhibit the recently emerged novel coronavirus (2019-nCoV) in vitro. *Cell Res* 2020; **30**: 269–71.

13 Williamson BN, Feldmann F, Schwarz B *et al*. Clinical benefit of remdesivir in rhesus macaques infected with SARS-CoV-2. *Nature* 2020; **585**: 273–6.

14 Goyal A, Duke ER, Cardozo-Ojeda EF *et al*. Mathematical modeling explains differential SARS CoV-2 kinetics in lung and nasal passages in remdesivir treated rhesus macaques. *bioRxiv* 2020; 2020.06.21.163550.

15 Ader F, Bouscambert-Duchamp M, Hites M *et al*. Remdesivir plus standard of care versus standard of care alone for the treatment of patients admitted to hospital with COVID-19 (DisCoVeRy): a phase 3, randomised, controlled, open-label trial. *Lancet Infect Dis* 2021; **22**: 209–21.

16 Gonçalves A, Bertrand J, Ke R *et al*. Timing of antiviral treatment initiation is critical to reduce SARS-CoV-2 viral load. *CPT Pharmacometrics Syst Pharmacol* 2020; **9**: 509–14.

17 Gastine S, Pang J, Boshier FAT *et al*. Systematic review and patient-level meta-analysis of SARS-CoV-2 viral dynamics to model response to antiviral therapies. *Clin Pharmacol Ther* 2021; **110**: 321–33.

18 Néant N, Lingas G, Le Hingrat Q *et al*. Modeling SARS-CoV-2 viral kinetics and association with mortality in hospitalized patients from the French COVID cohort. *Proc Natl Acad Sci U S A* 2021; **118**: e2017962118.

19 Ader F. Protocol for the DisCoVeRy trial: multicentre, adaptive, randomised trial of the safety and efficacy of treatments for COVID-19 in hospitalised adults. *BMJ Open* 2020; **10**: e041437.

20 Duval X, van der Werf S, Blanchon T *et al*. Efficacy of oseltamivir-zanamivir combination compared to each monotherapy for seasonal influenza: A randomized placebo-controlled trial. *PLoS Med* 2010; **7**: e1000362.

21 Ke R, Zitzmann C, Ribeiro RM *et al*. Kinetics of SARS-CoV-2 infection in the human upper and lower respiratory tracts and their relationship with infectiousness. *medRxiv* 2020; 2020.09.25.20201772v1.

22 Ke R, Zitzmann C, Ho DD *et al*. In vivo kinetics of SARS-CoV-2 infection and its relationship with a person's infectiousness. *Proc Natl Acad Sci U S A* 2021; **118**: e2111477118.

23 EMA. Summary on compassionate use, Remdesivir, Gilead. https://www.ema.europa.eu/en/documents/other/summary-compassionate-use-remdesivir-gilead_en.pdf.

24 Gonçalves A, Mentré F, Lemenuel-Diot A *et al*. Model Averaging in Viral Dynamic Models. *AAPS J* 2020; **22**: 48.

25 Aoki Y, Röshammar D, Hamrén B *et al*. Model selection and averaging of nonlinear mixed-effect models for robust phase III dose selection. *J Pharmacokinet Pharmacodyn* 2017; **44**: 581–97.

26 Bal A, Brengel-Pesce K, Gaymard A *et al*. Clinical and laboratory characteristics of symptomatic healthcare workers with suspected COVID-19: a prospective cohort study. *Sci Rep* 2021; **11**: 14977.

27 Ratcliff J, Nguyen D, Fish M *et al*. Virological characterization of critically Ill patients with COVID-19 in the United Kingdom: Interactions of viral load, antibody status, and B.1.1.7 infection. *J Infect Dis* 2021; **224**: 595–605.

28 Czuppon P, Débarre F, Gonçalves A *et al*. Success of prophylactic antiviral therapy for SARS-CoV-2: Predicted critical efficacies and impact of different drug-specific mechanisms of action. *PLoS Comput Biol* 2021; **17**: e1008752.

29 Dougan M, Nirula A, Gottlieb RL *et al*. Bamlanivimab + etesevimab for treatment of COVID-19 in high-risk ambulatory patients. *Top Antivir Med* 2021: 33.

30 Martinez DR, Schaefer A, Leist SR *et al*. Prevention and therapy of SARS-CoV-2 and the B.1.351 variant in mice. *bioRxiv* 2021; 2021.01.27.428478.

31 Rosales R, Mcgovern BL, Luis Rodriguez M *et al*. Nirmatrelvir, Molnupiravir, and Remdesivir maintain potent in vitro activity against the SARS-CoV-2 Omicron variant. *bioRxiv* 2022; 2022.01.17.476685.

32 Jones TC, Biele G, Mühlemann B *et al*. Estimating infectiousness throughout SARS-CoV-2 infection course. *Science* 2021; **373**: 1–21.

Chapitre 7

Les thérapeutiques dans les études précliniques

Dans le cadre de ce projet de thèse, nous avons également été impliqué dans le développement pharmacologique précoce chez l'animal.

Les études précliniques d'abord *in vitro* puis suivies d'études sur les animaux sont partie du pipeline nécessaire pour faire approuver une molécule. Plus précisément, dans le cadre du SARS-CoV-2, les hamsters dorés syriens *Mesocricetus auratus* sont des modèles rongeurs largement utilisés, ayant été étudié précédemment pour plusieurs virus respiratoires dont le SARS-CoV-1 et la grippe [146]. L'infection par le virus provoque des symptômes légers à modérés, pouvant même aller jusqu'à la détresse respiratoire, cependant la maladie reste non-létale. Nous avons ainsi pu étudier différents traitements chez ce modèle (annexe 2) en collaboration avec l'Unité des Virus Emergents (UVE, INSERM U1207, Université d'Aix-Marseille). Le primate non-humain est quant à lui le *gold standard* dans les maladies virales, étant le modèle se rapprochant le plus de l'Homme en terme de physiopathologies et de réponse immunologique [147]. Dans le SARS-CoV-2, trois types de primates non-humains sont utilisés couramment : les macaques rhésus (*Macaca mulatta*, les macaques cynomolgus (*Macaca fascicularis*) et enfin les singes verts africains (*Chlorocebus aethiops*). L'avantage

de ces modèles est que bien qu'ils ne fassent pas de forme grave, ils reproduisent adéquatement la physiopathologie du virus observée chez l'Homme, notamment l'induction d'une réplication virale élevée pendant deux semaines, une forte réponse immunitaire qui empêche une réinfection, une pneumonie et une excrétion virale prolongée chez les macaques âgés de la race rhésus ou cynomolgus [146]. Ces derniers ont été utilisés par l'infrastructure Infectious Diseases Models for Innovative Therapies (IDMIT) avec qui nous avons collaboré pour évaluer des traitements, notamment l'hydroxychloroquine [145] et le Lopinavir/Ritonavir (non publié) et enfin le favipiravir.

7.1 Favipiravir

Dans le cadre de cette thèse, le favipiravir (molécule d'intérêt du projet initial de la thèse) a tout d'abord été étudié en tant que traitement du virus de Lassa chez des primates non-humains. L'objectif de ce travail était de modéliser la dynamique virale de ce virus et l'impact de l'effet antiviral du traitement sur cette dernière. Nous avons pu identifier son mode d'action en tant qu'agent mutagène qui rend les virus produits non infectieux. Nous avons pu ensuite estimer son efficacité antivirale, et réaliser des prédictions quant à son efficacité lors de l'utilisation chez l'Homme à des doses déjà connues. Cet article a été publié le 7 janvier 2021 dans le journal *PLoS Computational Biology* (Annexe 1). Le favipiravir ayant eu des résultats prometteurs *in vitro* dans le SARS-CoV-2, nous l'avons étudié tout d'abord chez le hamster syrien. Notre objectif a été de déterminer les doses efficaces qui induisaient une réduction de 90 ou 99% des titres infectieux. Des hamsters syriens ont été infectés par différentes doses de virus infectieux ($10^4; 10^5; 10^6$ $TCID_{50}$) et traités par favipiravir (1340±36, 670±42 and 1390±126 mg/kg/day) ou non-traités. Les données récupérées à différents temps post-infection consistaient en titres infectieux de virus, ARN viral et concentration

plasmatiques de favipiravir. Nous avons pu constater une réduction significative de la concentration de titres infectieux et d'ARN quel que soit l'inoculum lorsque les hamsters étaient traités par 1400 mg/kg/jour de favipiravir. Utilisant une régression non linéaire, nous avons pu calculer les doses nécessaires pour réduire de 90% et 99% la charge virale infectieuse (article publié, voir annexe 2).

Devant ces signes encourageants du favipiravir, nous l'avons ensuite ré-étudié chez le primate non-humain (*cynomolgus macaques*) en collaboration avec l'IDMIT, en utilisant la même approche que pour l'hydroxychloroquine [145]. Les régimes de doses utilisés ont été déterminé en utilisant une relation allométrique [148], ce qui a donné des doses proches de ce que nous connaissions de précédentes études sur les virus Ebola [73] et Zika. Malheureusement, suite à l'absence de signal quant à son efficacité antivirale, nous n'avons pas réalisé de modélisation plus complexe sur ce modèle animal. Dans cette étude, des macaques cynomolgus ont été infectés soit par le virus Zika, soit par le SARS-CoV-2 puis traités par favipiravir ou non-traités. Nous avons pu montrer que le traitement n'avait malheureusement aucun effet sur la cinétique virale du SARS-CoV-2, et 4 animaux traités ont dû être euthanasiés en raison d'une détérioration clinique rapide, ce qui suggère un rôle potentiel du favipiravir dans l'aggravation de la maladie chez les animaux infectés par le SARS-CoV-2.

Ce résultat préclinique peut être mis en relation avec celui d'Holubar et al., qui ne trouvent pas d'améliorations clinique ni virologique [81], et compromettent donc son utilisation future quelle que soit le type de patient considéré.

7.2 Article 3

Antiviral efficacy of favipiravir against Zika and SARS-CoV-2 viruses in non-human primates

Romain Marlin, Delphine Desjardins, Vanessa Contreras, Guillaume Lingas, Caroline Solas, Pierre Roques ; Thibaut Naninck, Quentin Pascal, Sylvie Behillil, Pauline Maissonnasse, Julien Lemaitre, Nidhal Kahlaoui, Benoit Delache, Andrés Pizzorno, Antoine Nougairede, Camille Ludot, Olivier Terrier, Nathalie Deruddre-Bosque, Francis Relouzat, Catherine Chapon, Raphael Ho Tsong Fang, Sylvie Van Der Werf, Manuel Rosa Calatravas, Denis Malvy, Xavier de Lamballerie, Jeremie Guedj, Roger Le Grand

Nature Communications, 2022.

nature communications

Article

https://doi.org/10.1038/s41467-022-32565-w

Antiviral efficacy of favipiravir against Zika and SARS-CoV-2 viruses in non-human primates

Received: 17 March 2022

Accepted: 5 August 2022

Published online: 30 August 2022

Check for updates

Romain Marlin[1,11], Delphine Desjardins[1,11], Vanessa Contreras[1,11], Guillaume Lingas[2,11], Caroline Solas[3,11], Pierre Roques[1,10,11], Thibaut Naninck[1], Quentin Pascal[1], Sylvie Behillil[4,5], Pauline Maisonnasse[1], Julien Lemaitre[1], Nidhal Kahlaoui[1], Benoit Delache[1], Andrés Pizzorno[6], Antoine Nougairede[7], Camille Ludot[1], Olivier Terrier[6], Nathalie Dereuddre-Bosquet[1], Francis Relouzat[1], Catherine Chapon[1], Raphael Ho Tsong Fang[1], Sylvie van der Werf[4,5], Manuel Rosa Calatrava[6,8], Denis Malvy[9], Xavier de Lamballerie[7], Jeremie Guedj[2,11] ✉ & Roger Le Grand[1,11] ✉

The COVID-19 pandemic has exemplified that rigorous evaluation in large animal models is key for translation from promising in vitro results to successful clinical implementation. Among the drugs that have been largely tested in clinical trials but failed so far to bring clear evidence of clinical efficacy is favipiravir, a nucleoside analogue with large spectrum activity against several RNA viruses in vitro and in small animal models. Here, we evaluate the antiviral activity of favipiravir against Zika or SARS-CoV-2 virus in cynomolgus macaques. In both models, high doses of favipiravir are initiated before infection and viral kinetics are evaluated during 7 to 15 days after infection. Favipiravir leads to a statistically significant reduction in plasma Zika viral load compared to untreated animals. However, favipiravir has no effects on SARS-CoV-2 viral kinetics, and 4 treated animals have to be euthanized due to rapid clinical deterioration, suggesting a potential role of favipiravir in disease worsening in SARS-CoV-2 infected animals. To summarize, favipiravir has an antiviral activity against Zika virus but not against SARS-CoV-2 infection in the cynomolgus macaque model. Our results support the clinical evaluation of favipiravir against Zika virus but they advocate against its use against SARS-CoV-2 infection.

Favipiravir (T-705) is an RNA polymerase inhibitor approved in Japan for the treatment of noncomplicated influenza infections and in clinical development in the United States. The drug has shown a strong antiviral activity against several RNA viruses in vitro[1] and in macaque models, including Ebola virus[2], Lassa virus[3], and Marburg[4] virus, making it an attractive candidate against emergent RNA viruses. During the 2013–2016 Ebola outbreak, the drug was evaluated in a clinical trial in Guinea[5], with no significant or definite effect on mortality, possibly due to suboptimal dosing regimens[6]. Few months later, favipiravir was also evaluated against Zika virus (ZIKV). It showed a strong antiviral activity in vitro[7], but its clinical impact could not be evaluated, due among others to the rapid decline of the epidemic. Results from mathematical modeling provided evidence that favipiravir could have a strong antiviral efficacy against ZIKV in cynomolgus macaques (CM)[7].

A list of author affiliations appears at the end of the paper. ✉e-mail: jeremie.guedj@inserm.fr; roger.le-grand@cea.fr

Favipiravir has also naturally been considered as a drug candidate against SARS-CoV-2. In vitro evaluation showed mixed results, with an antiviral activity of favipiravir, as measured by the 50% effective concentrations (EC50), ranging from 62 to >500 µM (10 to >78 µg/mL)[8–11]. The results were more encouraging in vivo, with favipiravir leading to reduction of infectious titers in lungs and clinical alleviation of the disease in the hamster model[12–14]. Given the complexity of the drug pharmacokinetics[15,16], an important finding of these studies was that the antiviral efficacy was achieved with plasma trough concentrations that were comparable or lower to those found during human clinical trials[6]. However toxicity signals were observed in some animals at the largest doses[12], and the translation to humans doses is made difficult by the rapid metabolic activity of rodents. Nonetheless, these results prompted a large interest due to the lack of *per os* antiviral drugs available, and favipiravir is currently being evaluated in more than 72 clinical trials registered in February 2022[17], both in ambulatory and hospitalized patients, making it the third largest evaluated antiviral drug administered to COVID-19 patients. Although some preliminary studies suggested that favipiravir could decrease the time to viral clearance in mild or moderate COVID-19 patients[18] or the time to clinical improvement[19], the retrospective aspect or the absence of randomization of most studies precludes solid conclusion on favipiravir efficacy.

In order to support ongoing and future clinical evaluations of favipiravir against SARS-CoV-2 and Zika infections, and more generally against future emerging RNA viruses, we designed three successive experiments in cynomolgus macaques (Fig. 1). We first provided a detailed description of favipiravir pharmacokinetic in uninfected animals over a 14 days repeated-dose experiments to define relevant dosing regimens. In a second experiment, we evaluated the antiviral efficacy of favipiravir in a CM model of Zika infection. In a third experiment, we evaluated the antiviral efficacy of favipiravir against SARS-CoV-2 infection in a CM model that reproduces human infection and makes possible the evaluation of drug efficacy in a well-controlled setting. We discuss the implications of our findings for favipiravir clinical evaluation against emerging or re-emerging RNA viruses.

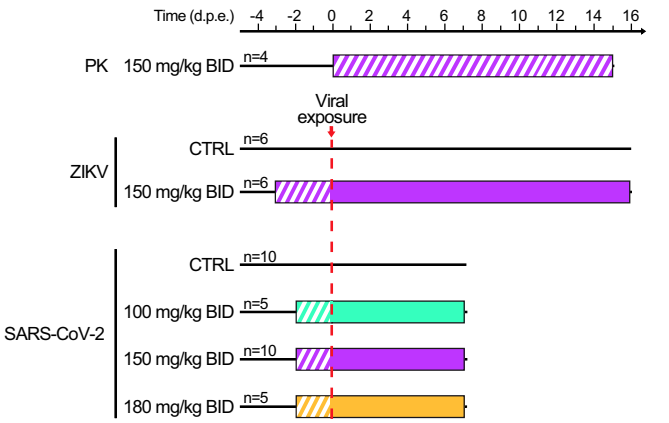

Fig. 1 | Study design of the 3 experiments. In the first experiment of pharmacokinetic (PK), $n = 4$ animals were treated with favipiravir (FPV) for 14 days. In the second experiment, $n = 12$ were either treated or received placebo, and were challenged with 10^6 PFU of Zika virus (ZIKV) three days after treatment initiation. In the third experiment, $n = 30$ animals were either treated or received a placebo, and were challenged with 10^6 PFU of SARS-CoV-2 two days after treatment initiation. Hatched area indicates FPV treatment without viral exposure. Colored areas indicate FPV dosing regimens; cyan: 200 mg/kg twice a day (BID) administered intravenously (i.v) on day −2 followed by 100 mg/kg BID administered subcutaneously (s.c); magenta: 250 mg/kg BID i.v. on day −3 (ZIKV) or −2 (SARS-CoV-2) followed by 150 mg/kg BID s.c.; yellow: 250 mg/kg BID i.v. on day −2 followed by 180 mg/kg BID sc. Untreated animals received NaCl 0.9% solution as placebo.

a

	D0	D7	D14
Cmax (µg/mL)	309	292	323
Tmax (h)	0.5	5.0	0.4
Ctrough (µg/mL)	75.2	79.1	131.6
Half life (h)	4.7	5.2	2.8
$AUC_{0\to12}$ (µg.h/mL)	1287	1512	554
$AUC_{0\to\infty}$ (µg.h/mL)	2477	1939	1452

b

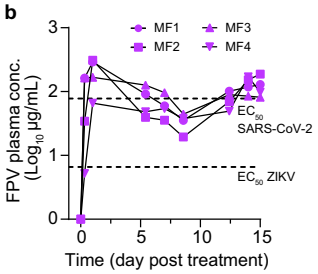

Fig. 2 | Plasma FPV concentration of four uninfected NHPs. a Favipiravir pharmacokinetic parameters during treatment with 250 mg/kg BID i.v. on day 0 followed by 150 mg/kg BID s.c. for 14 days. **b** Longitudinal evolution of plasma FPV concentrations with respect to EC_{50} values obtained on ZIKV and SARS-CoV-2 given in refs. 7, 12. Source data are provided as a Source Data file.

Results

Selection of dosing regimen against Zika and SARS-CoV-2 virus infections

We first evaluated the pharmacokinetics of favipiravir in non-infected CM, using a loading dose of 250 mg/kg twice a day (BID) administered intravenously (IV), followed by repeated subcutaneous administrations of 150 mg/kg BID. In the four animals, the drug concentrations rapidly increased to achieve a median maximal (C_{max}) and trough (C_{trough}) concentrations of 309.1 and 75.2 µg/mL, respectively, after the loading dose (Fig. 2). Interestingly, favipiravir concentrations were maintained at high levels over the 14 days of the experiment, with trough concentrations of 79.1 and 131.6 µg/mL at day 7 and day 14, respectively (Fig. 2). These values are larger than the drug EC_{50} of favipiravir against ZIKV, that ranges between 2.2 and 6.6 µg/mL, supporting the choice of this dosing regimen in challenge experiments. In the case of SARS-CoV-2, the uncertainty in the exact value of EC_{50} (see "Discussion") led us to consider a larger spectrum of doses. Consistent with our previous studies[2], we used doses of 100/150/180 mg/kg BID to evaluate the full spectrum of efficacy and toxicity of favipiravir.

Favipiravir pre-exposure prophylaxis reduces Zika virus replication

In a second experiment, we analyzed the antiviral efficacy of favipiravir against Zika virus. In this experiment, 6 control animals were untreated and infected by ZIKV (strain H/PF/2013), and 6 animals initiated favipiravir treatment 3 days before infection (pre-exposure prophylaxis), using the same dosing regimen than in the PK experiment (Fig. 1). Animals treated with favipiravir had lower levels of viral load than untreated animals (Fig. 3a, b). Their viral kinetic profile was nonetheless less consistent than control animals, with some individuals experiencing longer duration of viral shedding. Overall, favipiravir had a significant effect on the peak viral replication, with median peak viral load of 5.6 and 6.5 $\log_{10}$ copies/mL in treated and untreated animals, respectively ($p = 0.026$, Fig. 3c). The overall viral shedding, as measured by the Area Under the Curve (AUC) from 0 to 7 days post exposure (dpe), was also significantly different between untreated and treated animals, with median values of 6.5 vs 5.9 $\log_{10}$ copies.day/mL in untreated and treated animals, respectively ($p = 0.041$, Fig. 3d). We also investigated a concentration-dependent effect of favipiravir, taking the geometric mean of plasma trough concentrations between 0 and 5 dpe as a surrogate of drug exposure (see "Methods"). Drug concentration showed a trend towards an effect on peak viral load and on AUC viral load ($p = 0.056$ and $p = 0.074$, respectively, Fig. 3e, f), suggesting that high concentrations could be associated with a reduction of viral load, with a nonlinear relationship.

Beside drug concentrations, several treated animals exhibited distinctive cytokine dynamics compared to control animals (Figs. 3g and S2). Indeed, levels of IL-1RA and CCL2 peaked at 1 dpe and went

https://doi.org/10.1038/s41467-022-32565-w

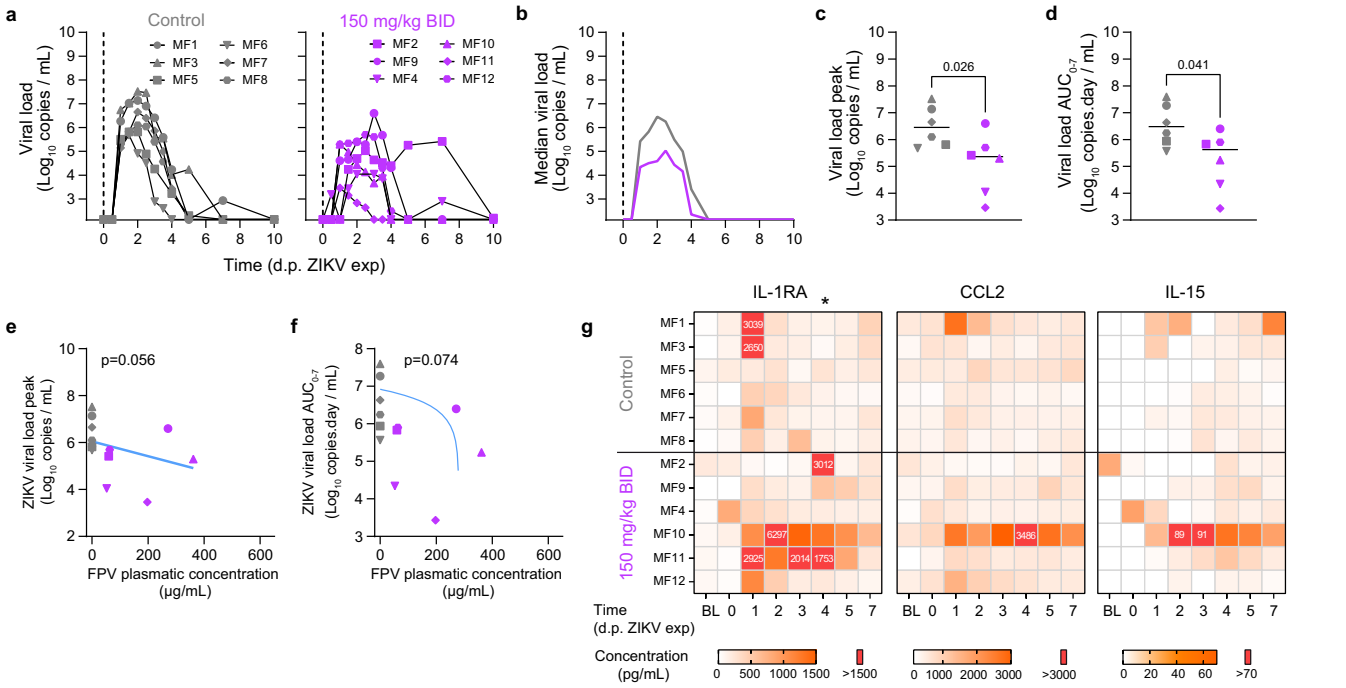

Fig. 3 | Viral kinetic and pharmacokinetic in ZIKV infected cynomolgus macaques treated with FPV. a Individual plasma viral loads determined by RT-PCR in all animals; **b** Median plasma viral load values observed in each treatment group; **c**, **d** Viral kinetic parameters (peak and AUC viral load) during the first 7 days of infection. Median value is indicated by horizontal bar. Parameters were compared between groups using the two-tailed non-parametric Mann–Whitney test. **e**, **f** Viral kinetic parameters (peak and AUC viral load between 0 and 7 dpi) according to geometric mean FPV plasma trough concentration. Grey: untreated; Purple: 150 mg/kg BID. A Spearman correlation test was performed to assess the association between drug concentration and viral kinetic parameters. Two-tailed *p* values are indicated. **g** Heatmaps of the concentrations of IL-1RA, CCL2, and IL-15 measured in plasma ZIKV infected animals. The asterisk indicates a significant difference in the concentration of IL-1RA at 4 d.p.e. between the control group and the FPV group. Parameters were compared between groups using the two-tailed non-parametric Mann–Whitney test. The color scale (in pg.mL^{-1}) is shown at the bottom. Source data are provided as a Source Data file.

back to basal level at 2/3 dpe for most animals, whereas the pro-inflammatory factors were sustained at high concentration until 5-7 dpe for treated animals, suggesting that they could be causally related to favipiravir administration (Fig. 3g).

Overall the treatment was well tolerated, even if the median loss weight at day 7 post treatment initiation was more elevated in treated (6.71%) than control (2.96%) animals ($p = 0.093$, Figs. S1b and S1d). Biochemistry parameters tended to be impacted in treated animals, especially with alteration of liver function and metabolism. In fact, the treated animals, which exhibited sustained inflammation, showed also markers of hepatic cytolysis (ASAT elevation), slight cholestasis (GGT elevation) associated with increase uremia and lipidaemia after ZIKV exposure, whereas these parameters remained unchanged in untreated animals (Fig. S3).

Favipiravir pre-exposure prophylaxis does not reduce SARS-CoV-2 virus replication

Following what was done for hydroxychloroquine[20], we studied in vitro antiviral activity of favipiravir against SARS-CoV-2 infection in the reconstituted human airway epithelium MucilAir™ model (HAE). Doses of 200–600 µM failing to reduce significantly SARS-CoV-2 apical viral titers at 48 h post infection, and did not protect the epithelial integrity during infection (Fig. S4).

We next tested the efficacy of favipiravir in the CM model of SARS-CoV-2 infection following exposure to 1×10^6 pfu of SARS-CoV-2 (hCoV-19/France/IDF0372/2020) by combined nasopharyngeal and tracheal routes as we previously reported[20–22] (Fig. S10). Ten control animals were left untreated and infected by SARS-CoV-2 virus, and 20 animals initiated favipiravir treatment 2 days before infection (pre-exposure prophylaxis), with a loading dose followed by maintenance doses of 100 ($n = 5$), 150 ($n = 10$) and 180 ($n = 5$) mg/kg BID. Viral kinetics in nasopharyngeal compartment were similar between untreated and treated animals, irrespective of the dose (Fig. 4a, b). Peak viral load in nasal fluid was largely similar in all groups, with median values of 8.2, 7.2, 8.3, and 8.1 $\log_{10}$ copies/mL in untreated, 100 mg, 150 mg, and 180 mg/kg BID groups respectively (Fig. 4c). Similar results were obtained for the AUC viral load in the nasal fluid, with median values of 8.5, 7.4, 8.6, and 8.4 $\log_{10}$ copies day/mL in untreated, 100 mg, 150 mg and 180 mg/kg BID groups, respectively (Fig. 4d). Results were largely similar in the tracheal fluid (Fig. S5), although a larger peak viral load was observed in animals treated with 180 mg/kg BID as compared to untreated (median values of 8.0 and 7.4 $\log_{10}$ copies/mL, respectively, $p = 0.003$, Fig. S5c). There was no effect of drug concentration on nasopharyngeal peak viral load ($p = 0.64$ Fig. 4f), but there was a trend towards an effect of favipiravir concentration in increasing AUC viral load ($p = 0.084$, Fig. 4g). The same results were observed in tracheal fluid, with a trend towards tracheal peak viral loads ($p = 0.087$) and AUC viral load (Supplementary Fig. S5e, f).

Viral load was also measured in BAL at 3 dpe (Fig. 4e). There was a trend towards larger viral loads in treated animals, in particular at the larger doses. While control animals had a median peak viral load at 6.39 $\log_{10}$ copies/mL, these values were equal to 6.32, 7.08, and 7.80 $\log_{10}$ copies/mL in treated animals at the dose of 100, 150, and 180 mg/kg BID, respectively (p-value to controls of 0.768, 0.143, and 0.005, respectively). The favipiravir concentrations determined in the epithelial lining fluid (ELF) were also correlated with the BAL viral load ($p < 0.0001$, Fig. 4h). Similar trends were observed in lung tissues at euthanasia (Fig. S5g, h).

Untreated infected animals exhibited mild clinical signs, consistent with a disease being often asymptomatic or mildly symptomatic in humans, with coughing or sneezing without dyspnea in SARS-CoV-2 infected animals (Fig. S6). Slight weight loss was observed in all

https://doi.org/10.1038/s41467-022-32565-w

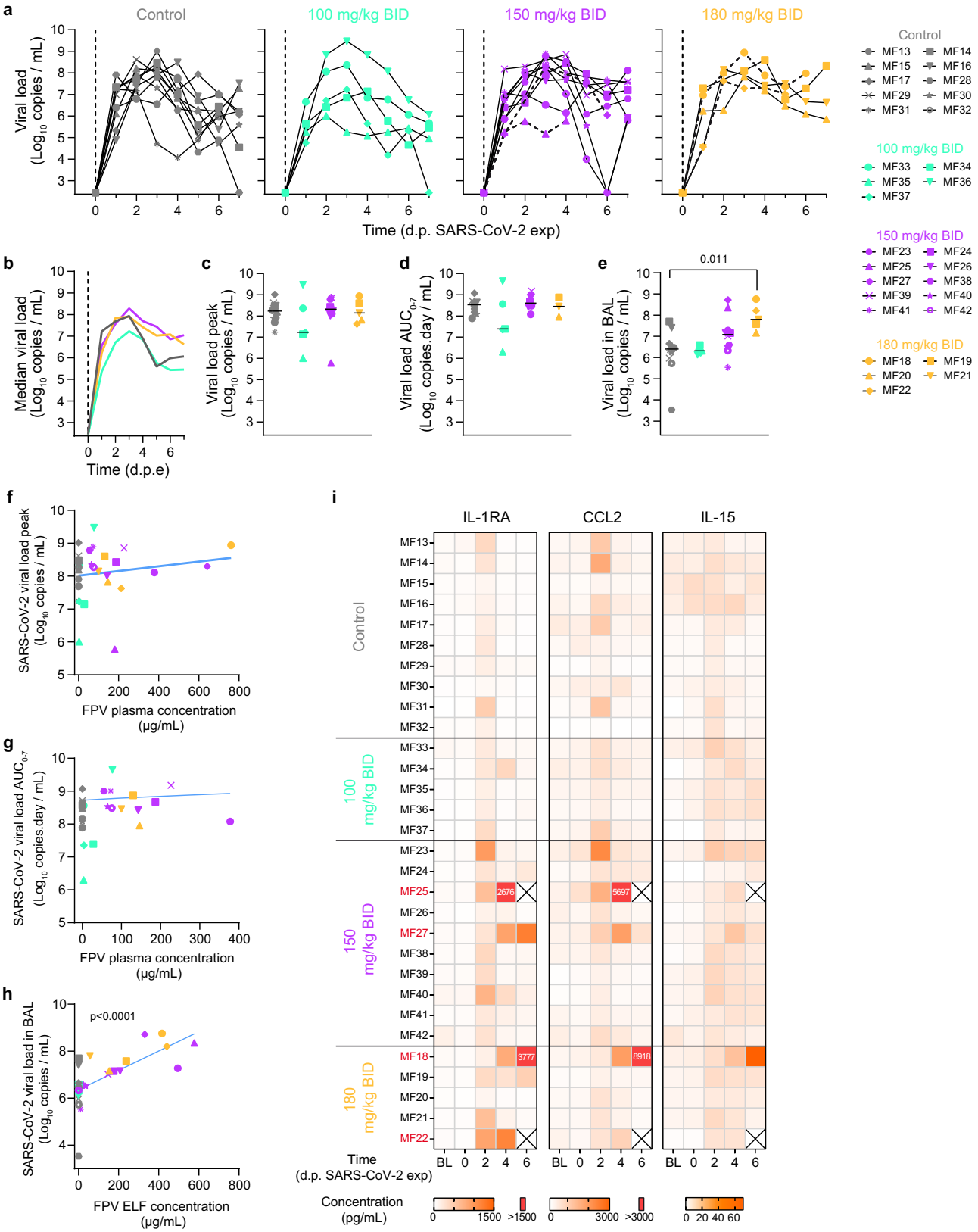

untreated infected animals that could be due to either infection and/or repeated anesthesia (Fig. S1c). Treatment led to weight loss, with a median weight loss after 7 days of treatment equal to 2.78, 6.23, 4.87, and 6.44% in untreated, 100 mg, 150 mg, and 180 mg/kg BID groups, respectively (p-value to controls of 0.001, 0.006, and 0.055, respectively) (Fig. S1d).

Exacerbation of SARS-CoV-2 disease in favipiravir treated macaques

Similar to previous observations[20,23] animals infected by SARS-CoV-2 showed transient elevated levels of IL-1RA, CCL2, and IL15, that peaked at 2 dpe. As observed during ZIKV infection, levels of these pro-inflammatory factors were sustained or continued to increase after 2

Fig. 4 | Viral kinetic and pharmacokinetic in the respiratory tract of SARS-CoV-2-infected cynomolgus macaques treated with FPV. a Individual nasopharyngeal viral loads determined by RT-PCR in all animals; **b** Median nasopharyngeal viral load values observed in each treatment group; **c**, **d** Viral kinetic parameters (peak and AUC viral load) during the first 7 days of infection. **e** Viral load in bronchoalveolar lavages (BAL) at 3 dpe. Median value is indicated by horizontal bar. Parameters were compared between groups using Kruskal-Wallis test following Dunn's multiple comparisons. **f**, **g** Viral kinetic parameters (peak and AUC viral load between 0 and 7 dpi) according to geometric mean FPV plasma trough concentration. **h** Viral load in BAL according to FPV concentration in the epithelial lining fluid (ELF). A Spearman correlation test was performed to assess the association between drug concentration and viral kinetic parameters. Two-tailed *p* value is indicated. Grey: untreated; cyan: 100 mg/kg BID; purple: 150 mg/kg BID; yellow: 180 mg/kg BID. **i** Heatmaps of the concentrations of IL-1RA, CCL2 and IL-15 measured in plasma SARS-CoV-2 infected animals. The color scale (in $pg.mL^{-1}$) is shown at the bottom. Source data are provided as a Source Data file.

dpe in treated animals, suggesting that they could be exacerbated by the administration of favipiravir. Consistent with this interpretation, there was a dose-dependent effect on cytokines, with larger levels observed in SARS-CoV-2 infected animals treated with 150 or 180 mg/kg BID than those untreated or treated with 100 mg/kg BID (Fig. 4i). In treated animals, 4/20 animals (MF18, MF22, MF25, and MF27) had to be euthanized due to rapid deterioration of their clinical score, and all these animals were infected with SARS-CoV-2 (2 receiving 150 mg/kg BID and 2 receiving 180 mg/kg BID). In these 4 animals, the levels of IL-1RA and CCL2 remained large at all times, and similar observations could be made on other cytokines (Fig. S7). Veterinary examination showed a shock in these four animals with severe hypothermia, bradycardia, with or without electrocardiographic abnormalities, hypoxemia, discordance, tachypnea, hypotension neutrophilia, and lymphopenia. Blood chemistry showed an increase of transaminases (ASAT and ALAT) without change in PAL or GGT suggesting hepatocellular necrosis (Fig. 5a and Fig. S8). In these animals, metabolism impairment was observed with an increase of plasma triglycerides and decrease of fructosamine and cholesterol levels with a similar kinetic than clinical score (Figs. S8 and S6). This interpretation is also corroborated by an increased levels of plasma creatinine in two animals from high dose group suggesting acute kidney failure. Moreover, metabolism alteration was confirmed by the continued increase of favipiravir plasma concentration, the reduction of M1 metabolite/favipiravir plasma ratio over time (Fig. 5b) and an accumulation of favipiravir in tissues (Fig. S9a). Ultrasounds and CT imaging performed 5 dpe and histological analyses showed typical feature of severe form of SARS-CoV-2 infection such as acute interstitial pneumonia with significant pleural effusion and left ventricle dilatation along with hepatomegaly with severe liver steatosis (Fig. 5c–e and Fig. S9c). Lesions on tissues were also noticed on other animals at a lower extent (Fig. S9b). Furthermore, high amount of virus was found in lung tissues of these four animals (Fig. 5f and Fig. S9d). Altogether, this suggest that animals had a multiple organs dysfunction syndrome (MODS) with liver and cardiac failure, associated with an acute kidney failure in two animals. This is consistent with the elevated levels of CCL2 and IL-1RA observed in all four animals, showing an immune activation which part of MODS physiopathology.

Discussion

Here we showed the results of experiments in cynomolgus macaques to evaluate the antiviral effect of favipiravir against Zika and SARS-CoV-2 viruses. We determined dosing regimens that achieved relevant drug concentrations with respect to drug EC_{50} and we evaluated the effects of pre-exposure favipiravir treatment on viral kinetics. Favipiravir significantly reduced Zika viral replication while being well tolerated at 150 mg/mL BID. However, it had no antiviral effect against SARS-CoV-2 at any of the doses tested (ranging 100–180 mg/kg BID), and 4/20 treated animals had a rapid clinical deterioration which required premature euthanasia during the study.

The effects of favipiravir on Zika virus viremia in macaques unambiguously demonstrate for the first time in vivo antiviral activity of favipiravir. As mentioned for other viral diseases, favipiravir can penetrate the sexual compartments and cross the blood brain barrier, facilitating the purge of the reservoirs of the virus[24]. In addition to mono-therapy, favipiravir may represent a good candidate for combined therapies with antiviral drugs such as galidesivir, which was also reported highly active in the NHP model[25]. Although the probable teratogenicity of favipiravir prevents its use in pregnant women, its ease of storage and its oral administration make it particularly relevant as a first line of protection to administer to suspect or contact cases.

The results obtained against SARS-CoV-2 infection are in contradiction with those in the hamster model[12–14]. This may stem from several factors, that are not mutually exclusive. First, the drug pharmacokinetics in NHPs differ from that in hamsters that was characterized by rapid drug metabolism, reducing its toxic effects and offering the possibility to administer large doses in hamsters[26]. For instance, we estimated previously that the effective dose to reduce viral replication by 90% (ED_{90}) in hamster in preventive therapy was 35 mg/day, which corresponds to about 600 mg/kg BID. Using the classical allometric rules, this would correspond to a dose of 200 mg/kg BID in NHPs, which is higher than the 100–180 mg/kg BID range tested here. However, the results found in HAE system, with no viral activity observed at doses up to 600 μM (Fig. S4) suggest that concentrations may need to be very high to generate a strong antiviral effect. In fact, our results even suggested an enhanced viral replication effect, with larger viral load levels in highest dosing group regimens than in untreated animals, despite mean plasma favipiravir concentrations well above the highest EC_{50} value and good diffusion into lung tissue (mean lung/plasma ratio 86%). Whether this is a genuine effect or is simply coincidental is unknown, but it is noteworthy that similar results were also reported in previous ex vivo models[27]. Regardless of the origin of this difference between the hamster and the NHP models, the dosing regimens used here in NHPs correspond to doses in humans that are already larger than 1200 mg BID (see refs. 2, 24 for a detailed analysis of the correspondence between NHP and human pharmacokinetics). This is to be compared with the dose of 600–800 mg BID favipiravir usually administered, and is consistent with the lack of antiviral activity that has been reported in randomized clinical trials[28,29]. In fact our results show that even larger doses are unlikely to generate an antiviral activity, and therefore do not support the use of favipiravir against SARS-CoV-2 infection.

SARS-CoV-2 infection results in several extrapulmonary manifestations, including kidney and liver injury[30]. Angiotensin-converting enzyme 2 (ACE2), the entry receptor for SARS-CoV-2, is expressed in the liver and kidney[31–33] but viral replication in these organs remains controversial[34,35]. Both kidney and liver injury are likely multifactorial involving direct effects of the virus with inflammation and tissue damages, but also indirect effects resulting from systemic inflammation, dysregulated immune responses, endothelial dysfunction, and impaired organ crosstalk[32,35,36]. Elevation of liver enzymes have been reported during SARS-CoV-2 infection, however, liver injury may be a reflection of a severe form of the disease[32]. Hepatic injury associated with COVID-19 seems due to systemic inflammation and multi-organ dysfunction[36]. Our results showed also an exacerbation of SARS-CoV-2 disease in four animals treated with favipiravir, with an impact on liver and kidney functions. Importantly this effect had not been seen in previous experiments involving favipiravir and repeated anesthesia nor in infected untreated animals[15], suggesting that this effect was causally related to the dual effects of favipiravir administration and SARS-CoV-2 infection. Effects on liver functions and liver enzyme levels were reported as main adverse effects in COVID-19 patients

https://doi.org/10.1038/s41467-022-32565-w

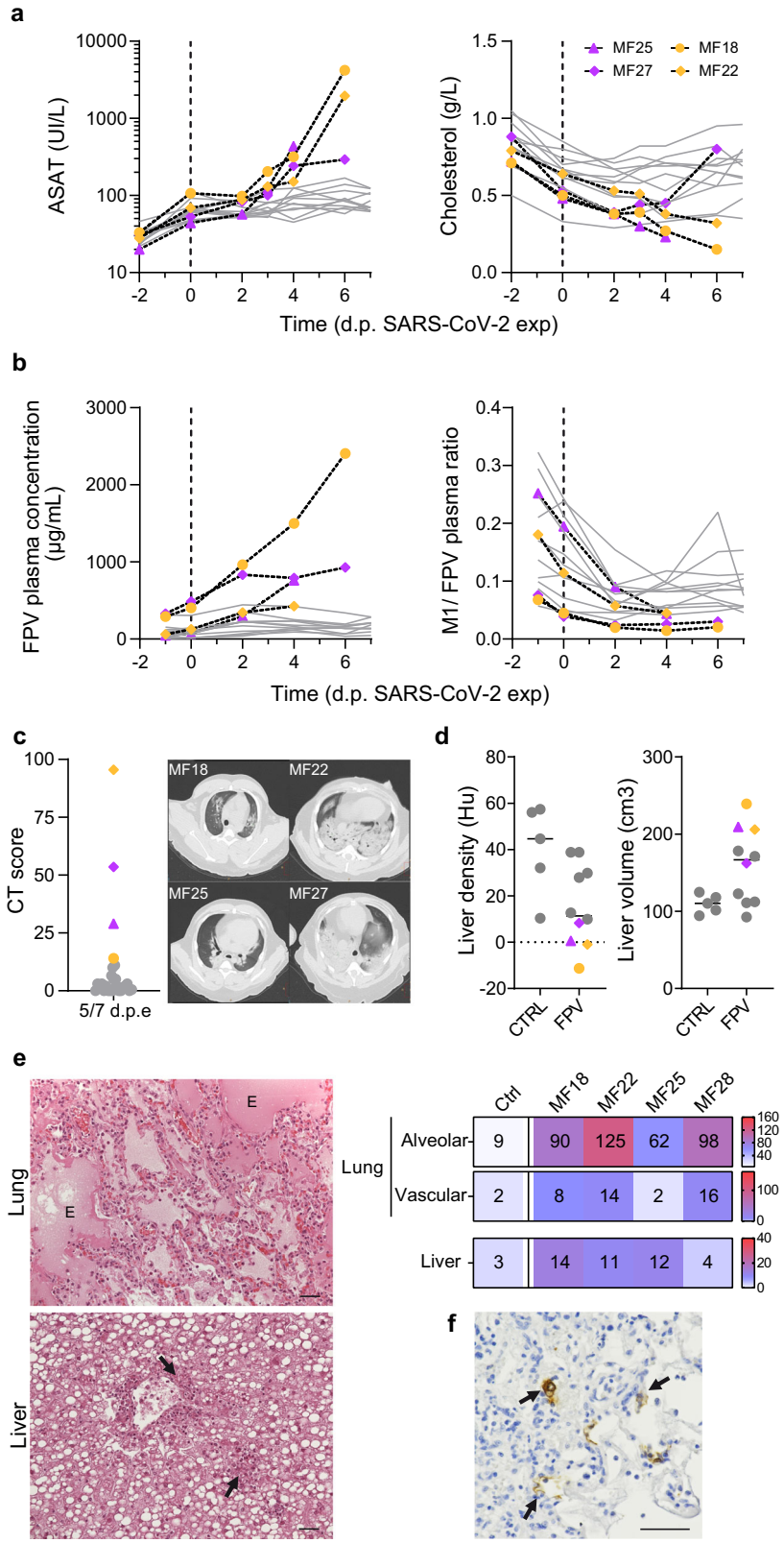

that received favipiravir treatment[29]. Favipiravir metabolization by the liver may increase the susceptibility to liver injury with SARS-CoV-2 infection and thus revealed liver pathogenicity.

To summarize, our results show that favipiravir has an antiviral activity against Zika virus but not against SARS-CoV-2 infection in the cynomolgus macaque model. They do not support the use of favipiravir in humans against SARS-CoV-2 infection.

Methods

Ethics and biosafety statement

Cynomolgus macaques (*Macaca fascicularis*), aged 44-86 months (20 females and 22 males, Table S1) and originating from Mauritian AAALAC certified breeding centers were used in this study. All animals were housed in IDMIT facilities (CEA, Fontenay-aux-roses), under BSL-2 and BSL-3 containment when necessary (Animal facility authorization #D92-

Fig. 5 | Exacerbation of SARS-CoV-2 induced disease in four FPV-treated macaques. Four infected animals treated with FPV were early euthanized after reach of humane endpoint. **a** Analyze of ASAT and Cholesterol levels in plasma of treated infected animals. **b** Longitudinal evolution of FPV concentration and M1/FPV ratio in plasma. **c** Lung lesions were assessed by chest CT at 5 dpe. Overall CT score are indicated, historical untreated animal were showed in grey. Representative images of lung lesions in the four NHPs. **d** Liver density and volume was assessed by CT scan at 5 dpe. Values for MF18, MF22, MF25, and MF27 are indicated in color according to the FPV dose (pink: 150 mg/kg BID and yellow: 180 mg/kg BID), and other FPV treated animals were indicated in grey. Median value is indicated by horizontal bar. Source data are provided as a Source Data file. **e** Tissue lesions and cell infiltrates were analyzed at necropsy and histological score for lung (alveolar and vascular areas) and liver were shown for the 4 NHPs in comparison with control animals (median of $n = 5$). Representative images of lung (top) and liver (down) were shown. The letter E indicates presence of edema and black arrows show the neutrophilic infiltration. **f** Presence of SARS-CoV-2 infected cells in lung tissue was exhibited anti-Nucleocapsid antibody. Black arrows indicated infected cells. The black bars indicate 50 µm.

032-02, Prefecture des Hauts de Seine, France) and in compliance with European Directive 2010/63/EU, the French regulations and the Standards for Human Care and Use of Laboratory Animals, of the Office for Laboratory Animal Welfare (OLAW, assurance number #A5826-01, US). The protocols were approved by the institutional ethical committee "Comité d'Ethique en Expérimentation Animale du Commissariat à l'Energie Atomique et aux Energies Alternatives" (CEtEA #44) under statement numbers A16-013 and A20-011. These studies were authorized by the "Research, Innovation and Education Ministry" under registration numbers APAFIS#4079-2016021212132792v3 and APAFIS#24434-2020030216532863v1.

Design of the experiments

In the first experiment, the pharmacokinetics of FPV was assessed in 4 uninfected animals, that received a loading dose (250 mg/kg) BID by intravenous route on the first day and a maintenance dose (150 mg/kg) BID for 14 days by subcutaneous route (simply called "150 mg/kg BID" in the following).

In the second experiment, 12 animals (including the four animals from the first experiment) were randomly assigned to the same dosing regimen or received NaCl 0.9% solution as control (simply called "untreated" in the following). Three days after treatment initiation, animals were exposed to 10^6 pfu of H/PF/13 Zika strain via subcutaneous route. All animals were followed for at least 14 days post exposure. Blood sampling was performed all along the study to quantify circulating levels of ZIKV, to determine the concentrations of favipiravir and cytokines in plasma. Animals were euthanized between 14 and 16 dpe.

In the third experiment, favipiravir was evaluated for the treatment of SARS-CoV-2. In our animal model, SARS-CoV-2 infection is similar in male and female cynomolgus macaques (Fig. S10). Animals were randomized to the same dosing regimen or were left untreated, as well as a larger maintenance dose of 180 mg/kg BID (called "180 mg/kg BID" in the following) or a lower dosing regimen group with a loading dose of 200 mg/kg BID on day 0 followed by a maintenance dose of 100 mg/kg BID (called "100 mg/kg BID" in the following). Two days after treatment initiation, all animals were exposed to 10^6 pfu of SARS-CoV-2 (hCoV-19/France/IDF0372/2020 strain; GISAID EpiCoV platform under accession number EPI_ISL_406596) via the combination of intranasal and intra-tracheal routes (Day 0), using atropine (0.04 mg/kg) for pre-medication and ketamine (5 mg/kg) with medetomidine (0.05 mg/kg) for anesthesia. All animals were euthanized at day 7 post exposure.

In all experiments, animals were observed daily and clinical exams were performed at baseline, daily on anaesthetized animals using ketamine (5 mg/kg) and medetomidine (0.05 mg/kg). During SARS-CoV-2 infection follow-up, body weight, rectal temperature, food/water consumption, activity, dehydration, respiration, heart rates, and oxygen saturation were recorded in a scoring grid. If animals reached the humane end point score, euthanasia was performed. Blood, as well as nasopharyngeal, tracheal, and rectal swabs, were collected among time. Broncho-alveolar lavages (BAL) were performed using 50 mL sterile saline on 3 and 6 dpi. Chest CT was performed on 5 dpi in anesthetized animals using tiletamine (5 mg/kg) and zolazepam (5 mg/kg). Blood cell counts, haemoglobin and haematocrit were determined from EDTA blood using a DXH800 analyzer (Beckman Coulter). Biochemistry parameters were analyzed with standard kits (Siemens) and with a canine kit (Randox) in lithium heparin plasma, inactivated with Triton X-100, using ADVIA1800 analyzer (Siemens). Cytokines were quantified in EDTA-treated plasma using NHP Milliplex (Millipore) and a Bioplex 200 analyser (Bio-Rad) according to the manufacturer's instructions.

Virus quantification in cynomolgus macaque samples

Plasma samples were collected from EDTA blood. Analysis by RT-qPCR using primers and probes derived from[37] (ZIKV_F, and ZIKV_R) encompassing a small segment coding for the E protein. Briefly, RNA was purified from 100 µL of plasma, using the Nucleospin 96 Virus Kit (Macherey Nagel, Düren, Germany, ref: 740452.4) according to the manufacturer's instructions. RNA was eluted in 100 µL of nuclease-free water and stored at −80 °C until analysis. ZIKV viral stock, diluted in an EDTA-plasma sample from ZIKV-non-infected macaques was used to generate a standard curve by serial 10-fold dilutions. Three aliquots of the ZIKV stock and two EDTA-plasma samples from ZIKV-negative macaques were used as positive and negative RT-qPCR controls, respectively. Then, 10 µL of the extracted RNA was mixed with the QRT-PCR medium containing primers, probes, enzyme and buffer (Supersript III platinum one step qPCR system from Invitrogen, Villebon-sur-Yvette, France) in a 96 well plate and ran on a Bio-Rad CFX thermocycler (Bio-Rad Lab., Marnes-la-Coquette, France). Results were quantified relative to ZIKV Vero supernatant diluted from 10^7 copies/mL to 330 copies/mL that was previously calibrated as described in ref. 38. Lower limit of quantification (LOQ) = 2.70 $\log_{10}$ copies of ZIKV RNA per mL; Lower limit of detection (LOD) = 2 $\log_{10}$ copies/mL. Data were analysed with CFX Maestro (V2.2)

Upper respiratory (nasopharyngeal and tracheal) and rectal specimens were collected with swabs (Viral Transport Medium, CDC, DSR-052-01). Tracheal swabs were performed by insertion of the swab above the tip of the epiglottis into the upper trachea at approximately 1.5 cm of the epiglottis. All specimens were stored between 2 and 8 °C until analysis by RT-qPCR with a plasmid standard concentration range containing an *RdRp* gene fragment including the *RdRp-IP4* RT-PCR target sequence (Supplementary Table II). The limit of detection was estimated to be 2.67 $\log_{10}$ copies of SARS-CoV-2 gRNA per mL and the limit of quantification was estimated to be 3.67 $\log_{10}$ copies/mL. The protocol describing the procedure for the detection of SARS-CoV-2 is available on the WHO website (https://www.who.int/docs/default-source/coronaviruse/real-time-rt-pcr-assays-for-the-detection-of-sars-cov-2-institut-pasteur-paris.pdf?sfvrsn=3662fcb6_2).

CT scan imaging of SARS-CoV-2 infected animals

CT acquisitions were performed under breath-hold using the Digital Photon Counting (DPC) PET-CT system (Vereos-Ingenuity, Philips) implemented in a BSL-3 laboratory. The CT detector collimation used was 64 × 0.6 mm, the tube voltage was 120 kV, and the intensity was approximately 150 mAs. The intensity was regulated by automatic dose optimization tools. CT images were reconstructed with a slice thickness of 1.25 mm and an interval of 0.63 mm. Images were analyzed using INTELLISPACE PORTAL (V8, Philips Healthcare) and 3DSlicer (open-source tool; Version 5). All lung images had the same window

level of −300 and a window width of 1600. Pulmonary lesions were defined as ground-glass opacity, crazy-paving pattern, or consolidations, as previously described[20–23,39]. Two to three individuals assessed the lesion features detected by CT imaging independently and the final CT score results were determined by consensus. Pre-existing background lesions or lesions induced by experimental atelectasis were scored 0. Liver volume and average density were assessed following organ segmentation in 3DSlicer software.

Pharmacokinetic assessment

Quantification of favipiravir, in plasma, BAL and tissues was performed by a validated sensitive and selective validated high-performance liquid chromatography coupled with tandem mass spectrometry (HPLC-MS/MS) method (UPLC-TQD, Waters, USA) with a lower limit of quantification of 0.1 μg/mL as previously described (12). Its major circulating metabolite M1 was quantified in plasma and tissues using to the same validated LC-MS/MS method. Lung biopsies collected after euthanasia were thoroughly rinsed with cold 0.9% NaCl to remove blood contamination and blotted with filter paper. Then, each lung biopsy was weighed and homogenized with 1 ml of 0.9% NaCl using a Mixer mill MM200 (Retsch, Germany). Cellular debris was removed by centrifugation, and the supernatant was stored at −80 °C. Favipiravir and M1 were extracted by a simple protein precipitation method, using acetonitrile for plasma and ice-cold acetonitrile for clarified tissue homogenates. Briefly, 50 μL of samples matrix was added to 500 μL of acetonitrile solution containing the internal standard (favipiravir-13C,15N, Alsachim), then vortexed for 2 min followed by centrifugation for 10 min at 4 °C. The supernatant medium was evaporated and the dry residues were then transferred to 96-well plates and 50 μL was injected.

Drug accumulation in lung was assessed by calculating a tissue to plasma concentration ratio. The favipiravir concentration in the epithelial lining fluid (ELF) were obtained from measured BAL fluid concentrations (C_{BAL}) after correction using the urea dilution method: $C_{ELF} = C_{BAL} \times (Urea_{plasma}/Urea_{BAL})$, where $Urea_{BAL}$ and $Urea_{plasma}$ correspond to the concentrations of urea determined in BAL fluid and plasma, respectively. Urea was determined in BAL by LC-MS/MS with a limit of quantification of 1.25 μg/mL as previously described[40].

Favipiravir pharmacokinetics and effects on viral kinetic parameters

The following pharmacokinetic parameters of plasma favipiravir were calculated in the 4 treated uninfected animals through non-compartimental analysis (NCA) and are presented as median: C_{max}, T_{max}, half-life, C_{min}, areas under curve (AUC): $AUC_{0\to12}$ and $AUC_{0\to\infty}$. C_{min} are the concentrations extrapolated 10 h after treatment administration using λ_z regression determined with PkAnalix.

The following viral kinetic parameters were calculated in all infected animals: peak viral load, logarithm of the AUC of viral load between 0 and 7 dpe. In treated infected animals, we used the geometric mean concentrations of pre-dose favipiravir observed between 0 and 5 dpe (ZIKV), and 0 and 7 dpe (SARS-CoV-2) as a pharmacokinetic parameter reflecting the exposure to favipiravir.

In vitro efficacy of favipiravir against SARS-CoV-2 infection in the HAE system

MucilAir™ HAE reconstituted from human primary cells obtained from bronchial biopsies, were provided by Epithelix SARL (Ref. EP01MD, Geneva, Switzerland) and maintained in air–liquid interphase with specific culture medium in Costar Transwell inserts (Corning, NY, USA) according to the manufacturer's instructions. For infection experiments, apical poles were infected with a 150 μl dilution of virus in OptiMEM medium (Gibco, ThermoFisher Scientific), at a multiplicity of infection (MOI) of 0.1. Treatments with FPV were applied through basolateral poles. FPV treatments were performed on days -2, -1, 0 (1 h after viral infection), and 1 post infection. Samples were collected at 48 hpi. Variations in transepithelial electrical resistance (Δ TEER) were measured using a dedicated volt-ohm meter (EVOM2, Epithelial Volt/Ohm Meter for TEER) and expressed as Ohm.cm2.

Statistical analysis. Data were collected using classical Excel files (Microsoft Excel 2016). Differences between unmatched groups were compared using the Mann–Whitney U test and Kruskal–Wallis test following Dunn's multiple comparisons (Graphpad Prism 8.0). The following viral kinetic parameters were calculated in each experimental group as medians: viral load peak, logarithm of the area under the curve of the viral load. To evaluate a potential effect of drug exposure on viral dynamics, we further evaluated the correlation of the viral kinetic parameters with the plasma concentrations of FPV, taking the geometric mean trough concentrations observed in each infected macaque between 0 and 7 days after infection as a marker of drug exposure (Spearman test).

Reporting summary

Further information on research design is available in the Nature Research Reporting Summary linked to this article.

Data availability

Source data are provided with this paper. The data generated in this study are provided in the Source Data file. Source data are provided with this paper.

References

1. Madelain, V. et al. Ebola virus infection: Review of the pharmacokinetic and pharmacodynamic properties of drugs considered for testing in human efficacy trials. *Clin. Pharmacokinet.* **55**, 907–923 (2016).
2. Guedj, J. et al. Antiviral efficacy of favipiravir against Ebola virus: A translational study in cynomolgus macaques. *PLoS Med.* **15**, e1002535 (2018).
3. Lingas, G., Rosenke, K., Safronetz, D. & Guedj, J. Lassa viral dynamics in non-human primates treated with favipiravir or ribavirin. *PLoS Comput. Biol.* **17**, e1008535 (2021).
4. Bixler, S. L. et al. Efficacy of favipiravir (T-705) in nonhuman primates infected with Ebola virus or Marburg virus. *Antivir. Res.* **151**, 97–104 (2018).
5. Sissoko, D. et al. Experimental treatment with favipiravir for ebola virus disease (the JIKI Trial): A historically controlled, single-arm proof-of-concept trial in guinea. *PLoS Med.* **13**, e1001967 (2016).
6. Nguyen, T. H. et al. Favipiravir pharmacokinetics in Ebola-Infected patients of the JIKI trial reveals concentrations lower than targeted. *PLoS Neglected Trop. Dis.* **11**, e0005389 (2017).
7. Best, K. et al. Zika plasma viral dynamics in nonhuman primates provides insights into early infection and antiviral strategies. *Proc. Natl Acad. Sci. USA* **114**, 8847–8852 (2017).
8. Wang, M. et al. Remdesivir and chloroquine effectively inhibit the recently emerged novel coronavirus (2019-nCoV) in vitro. *Cell Res.* **30**, 269–271 (2020).
9. Jeon, S. et al. Identification of antiviral drug candidates against SARS-CoV-2 from FDA-approved drugs. *Antimicrob. Agents Chemother.* **64**, e00819–20 (2020).
10. Shannon, A. et al. Rapid incorporation of Favipiravir by the fast and permissive viral RNA polymerase complex results in SARS-CoV-2 lethal mutagenesis. *Nat. Commun.* **11**, 1–9 (2020).
11. Pizzorno, A. et al. In vitro evaluation of antiviral activity of single and combined repurposable drugs against SARS-CoV-2. *Antivir. Res.* **181**, 104878 (2020).
12. Driouich, J.-S. et al. Favipiravir antiviral efficacy against SARS-CoV-2 in a hamster model. *Nat. Commun.* **12**, 1–13 (2021).

13. Kaptein, S. J. et al. Favipiravir at high doses has potent antiviral activity in SARS-CoV-2- infected hamsters, whereas hydroxychloroquine lacks activity. *Proc. Natl Acad. Sci. USA* **117**, 26955–26965 (2020).
14. Abdelnabi, R. et al. The combined treatment of Molnupiravir and Favipiravir results in a potentiation of antiviral efficacy in a SARS-CoV-2 hamster infection model. *EBioMedicine* **72**, 103595 (2021).
15. Madelain, V. et al. Favipiravir pharmacokinetics in nonhuman primates and insights for future efficacy studies of hemorrhagic fever viruses. *Antimicrob. Agents Chemother.* **61**, e01305–16 (2017).
16. Ison, M. G. & Scheetz, M. H. Understanding the pharmacokinetics of favipiravir: Implications for treatment of influenza and COVID-19. *EBioMedicine* **63**, 103204 (2021).
17. Thu, V. N. et al. RCT studies on preventive measures and treatments for COVID-19 [Data set]. *Zenodo*. https://doi.org/10.5281/zenodo.4266528 (2020)
18. Ivashchenko, A. A. et al. AVIFAVIR for treatment of patients with moderate coronavirus disease 2019 (COVID-19): Interim results of a phase II/III multicenter randomized clinical trial. *Clin. Infect. Dis.* **73**, 531–534 (2021).
19. Shinkai, M. et al. Efficacy and safety of favipiravir in moderate COVID-19 pneumonia patients without oxygen therapy: A randomized, phase III clinical trial. *Infect. Dis. Ther.* https://doi.org/10.1007/s40121-021-00517-4 (2021).
20. Maisonnasse, P. et al. Hydroxychloroquine use against SARS-CoV-2 infection in non-human primates. *Nature* **585**, 584–587 (2020).
21. Brouwer, P. J. et al. Two-component spike nanoparticle vaccine protects macaques from SARS-CoV-2 infection. *Cell* **184**, 1188–1200 (2021).
22. Maisonnasse, P. et al. COVA1-18 neutralizing antibody protects against SARS-CoV-2 in three preclinical models. *Nat. Commun.* **12**, 6097 (2021).
23. Marlin, R. et al. Targeting SARS-CoV-2 receptor-binding domain to cells expressing CD40 improves protection to infection in convalescent macaques. *Nat. Commun.* **12**, 5215 (2021).
24. Madelain, V. et al. Modeling favipiravir antiviral efficacy against emerging viruses: From animal studies to clinical trials. *CPT Pharmacomet. Syst. Pharm.* **9**, 258–271 (2020).
25. Lim, S.-Y. et al. Galidesivir, a direct-acting antiviral drug, abrogates viremia in rhesus macaques challenged with Zika virus. *Open Forum Infect. Dis.* **4**, S55 (2017).
26. Litterst, C. L., Mimnaugh, E. G., Reagan, R. L. & Gram, T. E. Comparison of in vitro drug metabolism by lung, liver, and kidney of several common laboratory species. *Drug Metab. Dispos.* **3**, 259–265 (1975).
27. Tomita, Y., Takeda, M. & Matsuyama, S. The anti-influenza virus drug favipiravir has little effect on replication of SARS-CoV-2 in cultured cells. *Antimicrob. Agents Chemother.* **65**, e00020–21 (2021).
28. Holubar, M. et al. Favipiravir for treatment of outpatients with asymptomatic or uncomplicated coronavirus disease 2019 (COVID-19): A double-blind, randomized, placebo-controlled, phase 2 trial. *Clin. Infect. Dis.* https://doi.org/10.1093/cid/ciac312 (2022).
29. Bosaeed, M. et al. Efficacy of favipiravir in adults with mild COVID-19: A randomized, double-blind, multicentre, placebo-controlled clinical trial. *Clin. Microbiol. Infect.* **28**, 602–608 (2022).
30. Gupta, A. et al. Extrapulmonary manifestations of COVID-19. *Nat. Med.* **26**, 1017–1032 (2020).
31. Zou, X. et al. Single-cell RNA-seq data analysis on the receptor ACE2 expression reveals the potential risk of different human organs vulnerable to 2019-nCoV infection. *Front. Med.* **14**, 185–192 (2020).
32. Luo, M., Ballester, M. P., Soffientini, U., Jalan, R. & Mehta, G. SARS-CoV-2 infection and liver involvement. *Hepatol. Int.* https://doi.org/10.1007/s12072-022-10364-1 (2022).
33. Hamming, I. et al. Tissue distribution of ACE2 protein, the functional receptor for SARS coronavirus. A first step in understanding SARS pathogenesis. *J. Pathol.* **203**, 631–637 (2004).
34. Tarik Aslan, A. & Yasemin Balaban, H. An overview of SARS-COV-2-related hepatic injury. *Hepatol. Forum* **2**, 122–127 (2021).
35. He, W. et al. Mechanisms of SARS-CoV-2 infection-induced kidney injury: A literature review. *Front. Cell Infect. Microbiol.* **12**, 838213 (2022).
36. Dufour, J.-F., Marjot, T., Becchetti, C. & Tilg, H. COVID-19 and liver disease. *Gut*. https://doi.org/10.1136/gutjnl-2021-326792 (2022).
37. Lanciotti, R. S. et al. Genetic and serologic properties of Zika virus associated with an epidemic, Yap State, Micronesia, 2007. *Emerg. Infect. Dis.* **14**, 1232–1239 (2008).
38. Hamel, R. et al. Biology of Zika virus infection in human skin cells. *J. Virol.* **89**, 8880–8896 (2015).
39. Zabaleta, N. et al. An AAV-based, room-temperature-stable, single-dose COVID-19 vaccine provides durable immunogenicity and protection in non-human primates. *Cell Host Microbe* **29**, 1437–1453.e8 (2021).
40. Gontijo, A. V. L. et al. Biopharmaceutical characterization of nebulized antimicrobial agents in rats: 2. Colistin. *Antimicrob. Agents Chemother.* **58**, 3950–3956 (2014).

Acknowledgements

We thank Sebastien Langlois, Quentin Sconosciuti, Victor Magneron, Claire-Maelle Fovet, Johana Demilly, Nina Dhooge, Pauline Le Calvez, Maxime Potier, Jen-Marie Robert, Orianne Lacroix, Christophe Joubert, Thierry Prot and Cristina Dodan for the NHP experiments; Laetitia Bossevot, Marco Leonec and Julie Morin for the RT-qPCR and Luminex assays, and for the preparation of reagents; Sophie Luccantoni, Céline Mayet, Camille Mabillon for the NHP tissue processing and histology staining; Anne-Sophie Gallouët, Mathilde Galhaut, Cécile Hérate for the help in NHP experiments and tissue processing; Blanche Fert for the CT experiments; Mylinda Barendji, Julien Dinh and Elodie Guyon for the NHP sample processing; Karine Barthelemy for drug concentration analysis; Sylvie Keyser for the transports organization; Frederic Ducancel and Yann Gorin for their help with the logistics and safety management; Isabelle Mangeot for here help with resources management and Brice Targat contributed to data management. The Infectious Disease Models and Innovative Therapies (IDMIT) research infrastructure is supported by the "Programme Investissements d'Avenir", managed by the ANR under reference ANR-11-INBS-0008. The Fondation Bettencourt Schueller and the Region Ile-de-France contributed to the implementation of IDMIT's facilities and imaging technologies. The NHP study received financial support from REACTing, the Fondation pour la Recherche Medicale (FRM; AM-CoV-Path), the "Agence Nationale de Recherche sur le SIDA et les hépatites virales – Maladies infectieuses émergentes" (ANRS-MIE), the ZIKAlliance project which received funding from the European Union's Horizon 2020 Research and Innovation Programme under Grant Agreement N.734548, and the European Infrastructure TRANSVAC2 (730964) for implementation of in vivo imaging technologies an NHP immuno assays. The European Union IMI2 program CARE (101005077) supports the development of the models. The HAE study received financial support from REACTing, the Fondation pour la Recherche Medicale (FRM; AM-CoV-Path) and the Région Auvergne-Rhône-Alpes. The virus stocks used in NHPs were obtained through the EVAg platform (https://www.european-virus-archive.com/), funded by H2020 (653316).

Author contributions

R.M. contributed to the project conception and design of the study, contributed to animal work, the coordination of the experiments, data analysis, figures design, and the writing of the paper. D.D. contributed to project conception and design of the study, the coordination of the experiments, data analysis, and the writing of the paper. V.C. contributed to project conception and design of the study, contributed to

animal work, data analysis, and figures design. G.L. contributed to data analysis and statistical analysis. C.S. supervised and coordinated the FPV pharmacokinetics analysis, contributed to data analysis and the writing of the paper. P.M. contributed to project conception and design of the study, contributed to animal work. Julien LEMAITRE contributed to clinical follow-up of macaques, to animal work, data analysis, and the writing of the paper. T.N. performed CT scans and quantification, contributed to the data analysis and the writing of the paper. N.K. performed CT scans and acquisition parameter design, and contributed to data analysis. Q.P. contributed to animal work, supervised and coordinated histological analysis, performed tissue lesion scoring, and contributed to the writing of the paper. C.L. contributed to animal work, set up and performed histological staining. N.D.-B. contributed to the animal work and cytokine measurements, analyzed the data, and coordinated IDMIT core activities. B.D. contributed to coordination of animal experiment, contributed to animal work, and acquisition on animal data. C.C. coordinated the imaging facility. R.H.T.F. coordinated the animal core facility, and contributed to study design and data analysis. Francis Relouzat contributed to animal work. A.N. performed RT–qPCR viral quantification and analyzed the data. S.B. performed RT–qPCR viral quantification and analyzed the data. S.v.d.W. provided the viral challenge stock, coordinated the viral load quantification, and analyzed the data. O.T. and A.P. designed the in vitro evaluation of FPV (HAE), performed in vitro work, and analyzed the data. M.R. Calatrava designed the in vitro evaluation of FPV (HAE), supervised and coordinated the work, analyzed the data. D.M. contributed to data analysis and the writing of the paper. P.R. contributed to the project conception and design of the study, the coordination of the experiments, data analysis, and the writing of the paper. X.d.L. contributed to study design, pharmacokinetics/pharmacodynamics analysis, and the writing of the paper. R.L.G. conceived the project, designed the study, coordinated the work, analyzed the data, and wrote the article. J.G. contributed to project conception and study design, to data analysis, the pharmacokinetics/pharmacodynamics study, and wrote the article.

Competing interests

The funders had no role in study design, data collection, data analysis, data interpretation, or data reporting. The authors D.M., C.S., J.G., and X.d.L. report ongoing collaborations between their institution, INSERM, and Toyama, the manufacturer of Favipiravir. The remaining authors declare no competing interests.

Additional information

Supplementary information The online version contains supplementary material available at https://doi.org/10.1038/s41467-022-32565-w.

Correspondence and requests for materials should be addressed to Jeremie Guedj or Roger Le Grand.

Peer review information *Nature Communications* thanks and the other anonymous reviewer(s) for their contribution to the peer review of this work. Peer review reports are available.

Reprints and permission information is available at http://www.nature.com/reprints

Publisher's note Springer Nature remains neutral with regard to jurisdictional claims in published maps and institutional affiliations.

[1]Université Paris-Saclay, Inserm, CEA, Center for Immunology of Viral, Auto-immune, Hematological and Bacterial diseases » (IMVA-HB/IDMIT), Fontenay-aux-Roses & Le Kremlin-Bicêtre, France. [2]Université de Paris, INSERM, IAME, F-75018 Paris, France. [3]Aix-Marseille Univ, APHM, Unité des Virus Emergents (UVE) IRD 190, INSERM 1207, Laboratoire de Pharmacocinétique et Toxicologie, Hôpital La Timone, 13005 Marseille, France. [4]Unité de Génétique Moléculaire des Virus à ARN, GMVR, Institut Pasteur, UMR CNRS 3569, Université de Paris, Paris, France. [5]Centre National de Référence des Virus des infections respiratoires (dont la grippe), Institut Pasteur, Paris, France. [6]CIRI, Centre International de Recherche en Infectiologie, (Team VirPath), Univ Lyon, Inserm, U1111, Université Claude Bernard Lyon 1, CNRS, UMR5308, ENS de Lyon, F-69007 Lyon, France. [7]Unité des Virus Emergents, UVE: Aix Marseille Univ, IRD 190, INSERM 1207, IHU Méditerranée Infection, 13005 Marseille, France. [8]VirNext, Université Claude Bernard Lyon 1, Faculté de Médecine Laennec, Lyon, France. [9]Department of infectious ad tropical diseases, University hopsital, Bordeaux & Inserm 1219/IRD, Bordeaux University, Bordeaux, France. [10]Present address: Virology Unit, Institut Pasteur de Guinée, Conakry, Guinée. [11]These authors contributed equally: Romain Marlin, Delphine Desjardins, Vanessa Contreras, Guillaume Lingas, Caroline Solas, Pierre Roques, Jeremie Guedj, Roger Le Grand. ✉e-mail: jeremie.guedj@inserm.fr; roger.le-grand@cea.fr

Chapitre 8

Discussion

L'objectif principal de ce travail de thèse était de modéliser la dynamique virale intra-hôte du SARS-CoV-2 depuis l'infection jusqu'à la clairance virale chez le patient hospitalisé à l'aide de modèles mathématiques. Dans notre premier travail, nous nous sommes appuyés sur des données de cohorte issues des patients de la première vague de la pandémie. A l'aide d'un modèle conjoint liant dynamique virale et risque de décès, nous avons pu quantifier le lien entre ces deux composantes et prédire l'impact de traitements antiviraux efficaces. Le second projet visait quant à lui à évaluer l'efficacité du remdesivir sur la réduction de la charge virale. Nous avons modélisé la dynamique virale des patients des bras Standard of Care et Standard of Care + Remdesivir de l'essai DisCoVeRy. Grâce à ce modèle, nous avons ainsi pallié aux biais liés aux hétérogénéités inter-patients non prises en compte dans l'analyse initiale des mêmes données qui n'avaient pas trouvé d'effet significatif du remdesivir. Nous avons ainsi cherché à différencier et quantifier cette différence entre les dynamiques virales des patients traités et non traités et enfin à identifier les patients les plus susceptibles de répondre à ce traitement.

Nous avons pu identifier grâce à nos modèles que le début des symptômes coïncidait avec le pic

de charge virale, mettant en exergue l'importance de la transmission asymptomatique. De plus, nous avons pu quantifier le lien entre charge virale et risque de décès, démontrant ainsi l'importance de la composante virale de la maladie chez le patient hospitalisé. En couplant cette information avec notre résultat montrant que parmi ces patients, les plus âgés ont une excrétion virale prolongée, nous avons démontré ainsi l'importance de faire baisser la charge virale nasopharyngée chez le patient hospitalisé. Cependant l'efficacité d'un traitement à réduire la production virale se doit d'être élevée (>90%) afin d'avoir un effet clinique, seuil non atteint par le remdesivir.

Une première limite de nos modélisations concerne les données, limitées à des charges virales génomiques éparses, qui nous a poussé à utiliser un modèle simple "Target-Cell-Limited", sans possibilité de modéliser la charge virale infectieuse ou la réponse immunitaire. Compte tenu des effectifs importants, la fréquence de nos prélèvements ne permettait pas une description précise de chaque trajectoire individuelle. Cependant, modéliser la dynamique virale au niveau populationnel sur un grand nombre de patients a permis dans ces travaux d'obtenir des résultats fiables, évitant les phénomènes de régression vers la moyenne et de shrinkage. Néanmoins, nous avons pu dans notre premier travail identifier un modèle plus complexe incorporant une réponse immunitaire qui décrivait tout aussi bien nos données. Ce type de réponse immunitaire a notamment été utilisé par la suite par Ke et al. qui ont modélisé des données individuelles plus détaillées [83]. Cependant, l'absence de donnée concernant la réponse immunitaire nous a empêché de confirmer ou d'infirmer ce résultat. De plus, nos prédictions quant à la réduction de la mortalité suite à la baisse de la charge virale reposent sur l'hypothèse selon laquelle la dynamique virale nasopharyngée est directement liée au risque de décès. Or, ne disposant pas d'information sur la réponse inflammatoire, nous n'avons pu quantifier le lien entre cette dernière et la probabilité de décès. Or ces deux composantes ont été montrées comme étroitement imbriquées dans de nombreux travaux [33, 43-46]. De plus, la maladie, à l'hôpital, est no-

tamment accompagnée d'une pneumonie, donc dans le compartiment pulmonaire. Les données dont nous disposions dans ce compartiment étaient biaisées par la population dans laquelle elles avaient été collectées (voir discussion du chapitre 5). Cependant, la charge virale pulmonaire pourrait potentiellement représenter un biomarqueur reflétant de manière plus réaliste l'évolution clinique de la maladie. En ce sens, il pourrait être intéressant de questionner la cible pharmacodynamique de 90% décrite par Gonçalves et al. [131], qui a été identifiée sur la charge virale nasopharyngée.

Parienti et al. chez le patient ambulatoire [103], montrent que la réduction de la charge virale nasopharyngée induite par des traitements va de pair avec la diminution du risque d'hospitalisation et de décès. Dans notre second projet, la modélisation nous a permis d'identifier et de quantifier l'efficacité antivirale du remdesivir à réduire la production virale, ce qui n'avait pas été retrouvée dans l'analyse principale [61]. Malheureusement, celle-ci se trouve être en deçà des cibles pharmacodynamiques de 90 et 99% utilisées pour les prédictions de traitement antiviral de notre premier projet. Cela est donc cohérent avec le résultat clinique retrouvé, et ajoute donc un élément compromettant son utilisation hospitalière. Cependant, il est intéressant de noter que l'efficacité antivirale du remdesivir est fortement augmentée chez les patients ayant une charge virale élevée. Ce résultat est en concordance avec ceux concernant d'autres traitements. En particulier, la combinaison casirivimab+imdevimab a montré une efficacité croissante avec les niveaux de charge virale chez le sujet ambulatoire [58]. L'essai RECOVERY a quant à lui retrouvé une efficacité clinique du même traitement chez les patients hospitalisés séronégatifs à l'admission [65], signe d'une charge virale plus élevée que chez ceux ayant déjà monté une réponse anticorps à l'infection [149]. Enfin, cette combinaison d'anticorps a montré une efficacité de plus de 99% pour bloquer les infections *de novo* des cellules cibles [150].

Un autre traitement qui a montré des signaux prometteurs est notamment la combinaison tixagevi-

mab+cilgavimab, qui cible la protéine Spike du virus. En effet, nous avons pu chez le hamster syrien évaluer et comparer les efficacités de ce traitement entre les souches ancestrale, Omicron BA.1 et Omicron BA.2. Nous avons constaté une forte réduction de la concentration de titres infectieux et d'ARN quelle que soit la souche lorsque les hamsters étaient traités par dose élevée de tixagevimab+cilgavimab. De la même manière que pour le favipiravir (voir chapitre 7), nous avons pu calculer la concentration nécessaire pour réduire de 90% la charge virale infectieuse (EC90), soit notre cible pharmacodynamique (article accepté, voir annexe 2). Ce traitement est actuellement évalué dans la seconde partie de l'essai DisCoVeRy. Au vu des données pharmacocinétiques de ce traitement [151], et des doses administrées dans cet essai [152], il est raisonnable de penser que l'EC90 de ce traitement, tout du moins contre le variant BA.2, puisse être atteinte. Également, les patients enrôlés ont notamment pour critère de recrutement un test antigénique positif à l'admission, synonyme d'une charge virale élevée [153].

Tous ces résultats nous poussent donc à croire que les molécules faisant baisser fortement la charge virale, sous condition d'une efficacité >90%, ont leur place dans l'arsenal thérapeutique du patient hospitalisé [65]. Parmi celles-ci, les petites molécules n'ayant pas pour cible la protéine Spike ont un intérêt particulier. En effet, celles-ci, telles que le molnupiravir ou le nirmatrelvir, gardent leur activités antivirales face aux variants émergents [154, 155], là où les anticorps monoclonaux voient leurs efficacités grandement diminuées [154, 156-159], notamment contre le variant Omicron. Notamment, dans le cadre de cette thèse, nous avons estimé que la concentration de tixagevimab+cilgavimab nécessaire pour obtenir une réduction de 90% de la charge virale infectieuse concentration était multipliée par 14 pour le variant BA.1 et par 5 pour le variant BA.2. par rapport à la souche ancestrale (Annexe 3).

Perspectives

Dans ces travaux, la modélisation de la dynamique virale du patient hospitalisé a permis la quantification de l'impact de la charge virale sur le risque de mortalité et celui du remdesivir sur la dynamique virale. Cependant, ce dernier n'a pas eu d'effet conséquent et aucun effet sur l'amélioration clinique des patients. Il conviendrait ainsi d'étudier l'efficacité antivirale de traitements ayant une efficacité clinique chez le patient hospitalisé. De plus, nos travaux n'ont pas permis de caractériser de manière fine les trajectoires individuelles, dû à des données éparses. Il conviendrait ainsi de modéliser de manière plus précise l'histoire naturelle de la dynamique virale, par exemple pour caractériser le rebond viral qui a pu être observé sous traitement par nirmatrelvir+ritonavir [160].

Notre modélisation ne s'est concentrée que sur un seul biomarqueur, à savoir l'ARN génomique nasopharyngé. Cependant d'autres marqueurs virologiques existent, tels que l'antigénémie, qui présente de nombreux avantages par rapport à la charge virale nasopharyngée. Obtenue par une simple prise de sang, elle procure un marqueur plus global de l'infection. En effet, celui-ci reflète la progression de l'infection au niveau nasopharyngé mais également dans les autres compartiments, dont pulmonaire. De plus, il permettrait d'obtenir un biomarqueur virologique dans le même compartiment que les biomarqueurs immunitaires, évitant des extrapolations. Ces derniers ont d'autant plus d'importance que la couverture vaccinale, qui impacte de manière très conséquente la dynamique virale [161], est maintenant largement étendue. Un marqueur pouvant permettre de prendre en compte la protection immunitaire globale, naturelle ou vaccinale, est notamment l'ED50, obtenu *in vitro*, qui mesure la capacité des anticorps à neutraliser le virus/les cellules infectées. Celui-ci est d'autant plus intéressant qu'il permet de tester l'immunité globale d'un individu contre d'autres VoC [162]. Enfin, nos modèles pourraient également s'appliquer aux patients ambulatoires, afin de quantifier le lien entre dynamique virale et probabilité d'évolution vers une forme grave. Plus finement, il serait inté-

ressant de modéliser conjointement la dynamique virale et la dynamique de la symptomatologie, à l'instar de Canini et al. [123] dans le cadre de la grippe. En couplant la neutralisation des anticorps présents suite à une infection ou à une vaccination ou l'efficacité antivirale d'une molécule à nos connaissances sur la dynamique virale, il serait donc possible d'anticiper la protection conférée par notre système immunitaire ou un traitement contre l'acquisition de l'infection ou l'évolution vers des formes graves causées par de nouveaux variants.

Bibliographie

[1] Huang et al. "Clinical features of patients infected with 2019 novel coronavirus in Wuhan, China". In : *Lancet* 395.10223 (2020), p. 497-506. ISSN : 1474547X. DOI : 10.1016/S0140-6736(20)30183-5/ATTACHMENT/D5332CA1-83D8-4C4C-BC57-00A390BF0396/MMC1.PDF.

[2] Zhou et al. "A pneumonia outbreak associated with a new coronavirus of probable bat origin". In : *Nat. 2020 5797798* 579.7798 (2020), p. 270-273. ISSN : 1476-4687. DOI : 10.1038/s41586-020-2012-7.

[3] *COVID-19 Map - Johns Hopkins Coronavirus Resource Center.*

[4] Haidong Wang et al. "Estimating excess mortality due to the COVID-19 pandemic: a systematic analysis of COVID-19-related mortality, 2020–21". In : *Lancet* 399.10334 (2022), p. 1513-1536. ISSN : 01406736. DOI : 10.1016/S0140-6736(21)02796-3/ATTACHMENT/FF5628FC-BF52-40E6-9395-0EB70E16DE99/MMC1.PDF.

[5] Eskild Petersen et al. "Comparing SARS-CoV-2 with SARS-CoV and influenza pandemics". In : *Lancet. Infect. Dis.* 20.9 (2020), e238. ISSN : 14744457. DOI : 10.1016/S1473-3099(20)30484-9.

[6] Cordelia E.M. Coltart et al. "The Ebola outbreak, 2013–2016: old lessons for new epidemics". In : *Philos. Trans. R. Soc. B Biol. Sci.* 372.1721 (2017), p. 2013-2016. ISSN : 14712970. DOI : 10.1098/RSTB.2016.0297.

[7] *Allocution liminaire du Directeur général de l'OMS lors du point presse sur la COVID-19 - 11 mars 2020.*

[8] Henrik Salje et al. "Estimating the burden of SARS-CoV-2 in France". In : *Science (New York, N.Y.)* 369 (6500 juill. 2020), p. 208-211. ISSN : 1095-9203. DOI : 10.1126/SCIENCE.ABC3517.

[9] Derek K. Chu et al. "Physical distancing, face masks, and eye protection to prevent person-to-person transmission of SARS-CoV-2 and COVID-19: a systematic review and meta-analysis". In : *Lancet (London, England)* 395.10242 (2020), p. 1973-1987. ISSN : 1474-547X. DOI : 10.1016/S0140-6736(20)31142-9.

[10] Katherine A. Auger et al. "Association Between Statewide School Closure and COVID-19 Incidence and Mortality in the US". In : *JAMA* 324.9 (2020), p. 859-870. ISSN : 0098-7484. DOI : 10.1001/JAMA.2020.14348.

[11] Laura Di Domenico et al. "Impact of lockdown on COVID-19 epidemic in Île-de-France and possible exit strategies". In : *BMC Med.* 18.1 (2020), p. 1-13. ISSN : 17417015. DOI : 10.1186/S12916-020-01698-4/FIGURES/7.

[12] Alessio Andronico et al. "Evaluating the impact of curfews and other measures on SARS-CoV-2 transmission in French Guiana". In : *Nat. Commun.* 12.1 (2021). ISSN : 20411723. DOI : 10.1038/S41467-021-21944-4.

[13] Tiffany Charmet et al. “Impact of original, B.1.1.7, and B.1.351/P.1 SARS-CoV-2 lineages on vaccine effectiveness of two doses of COVID-19 mRNA vaccines: Results from a nationwide case-control study in France”. In : *Lancet Reg. Heal. - Eur.* 8 (2021), p. 100171. issn : 2666-7762. doi : 10.1016/J.LANEPE.2021.100171.

[14] Koen B. Pouwels et al. “Effect of Delta variant on viral burden and vaccine effectiveness against new SARS-CoV-2 infections in the UK”. In : *Nat. Med.* 27.12 (2021), p. 2127-2135. issn : 1546170X. doi : 10.1038/S41591-021-01548-7.

[15] Sara Y. Tartof et al. “Effectiveness of mRNA BNT162b2 COVID-19 vaccine up to 6 months in a large integrated health system in the USA: a retrospective cohort study”. In : *Lancet (London, England)* 398.10309 (2021), p. 1407-1416. issn : 1474-547X. doi : 10.1016/S0140-6736(21)02183-8.

[16] Daniel R. Feikin et al. “Duration of effectiveness of vaccines against SARS-CoV-2 infection and COVID-19 disease: results of a systematic review and meta-regression”. In : *The Lancet* 399 (10328 mars 2022), p. 924-944. issn : 1474547X. doi : 10.1016/S0140-6736(22)00152-0/ATTACHMENT/4664DFD4-ED73-4B26-8AEA-E5C6A4B600BA/MMC1.PDF.

[17] Alexander E. Gorbalenya et al. “The species Severe acute respiratory syndrome-related coronavirus: classifying 2019-nCoV and naming it SARS-CoV-2”. In : *Nat. Microbiol. 2020 54* 5.4 (2020), p. 536-544. issn : 2058-5276. doi : 10.1038/s41564-020-0695-z.

[18] Na Zhu. “A Novel Coronavirus from Patients with Pneumonia in China, 2019”. In : *N. Engl. J. Med.* 382.8 (2020), p. 727-733. issn : 0028-4793. doi : 10.1056/NEJMOA2001017/SUPPL_FILE/NEJMOA2001017_DISCLOSURES.PDF.

[19] Roujian Lu et al. “Genomic characterisation and epidemiology of 2019 novel coronavirus: implications for virus origins and receptor binding”. In : *Lancet* 395.10224 (2020), p. 565-574. issn : 1474547X. doi : 10.1016/S0140-6736(20)30251-8/ATTACHMENT/1686D69B-3F2C-44B2-A8A5-C648EF9D1C2B/MMC1.PDF.

[20] Yaara Finkel et al. “The coding capacity of SARS-CoV-2”. In : *Nat. 2020 5897840* 589.7840 (2020), p. 125-130. issn : 1476-4687. doi : 10.1038/s41586-020-2739-1.

[21] Jian Shang et al. “Structural basis of receptor recognition by SARS-CoV-2”. In : *Nature* 581.7807 (2020), p. 221-224. issn : 1476-4687. doi : 10.1038/S41586-020-2179-Y.

[22] Alexandra C. Walls et al. “Structure, Function, and Antigenicity of the SARS-CoV-2 Spike Glycoprotein”. In : *Cell* 181.2 (2020), 281-292.e6. issn : 1097-4172. doi : 10.1016/J.CELL.2020.02.058.

[23] Jun Lan et al. “Structure of the SARS-CoV-2 spike receptor-binding domain bound to the ACE2 receptor”. In : *Nat. 2020 5817807* 581.7807 (2020), p. 215-220. issn : 1476-4687. doi : 10.1038/s41586-020-2180-5.

[24] Thomas P. Peacock et al. “The furin cleavage site in the SARS-CoV-2 spike protein is required for transmission in ferrets”. In : *Nat. Microbiol. 2021 67* 6.7 (2021), p. 899-909. issn : 2058-5276. doi : 10.1038/s41564-021-00908-w.

[25] Ben Hu et al. “Characteristics of SARS-CoV-2 and COVID-19”. In : *Nat. Rev. Microbiol.* 19.3 (2021), p. 1. ISSN : 17401534. DOI : 10.1038/S41579-020-00459-7.

[26] Armin Bayati et al. “SARS-CoV-2 infects cells after viral entry via clathrin-mediated endocytosis”. In : *J. Biol. Chem.* 296 (2021). ISSN : 1083351X. DOI : 10.1016/J.JBC.2021.100306/ATTACHMENT/E72AE184-2A33-4DF7-89B5-D1F6F6CD5CC8/MMC1.PDF.

[27] Cody B. Jackson et al. “Mechanisms of SARS-CoV-2 entry into cells”. In : *Nat. Rev. Mol. Cell Biol.* 23.1 (2022), p. 3. ISSN : 14710080. DOI : 10.1038/S41580-021-00418-X.

[28] Adam L. Bailey et Michael S. Diamond. “A Crisp(r) New Perspective on SARS-CoV-2 Biology”. In : *Cell* 184 (1 jan. 2021), p. 15-17. ISSN : 1097-4172. DOI : 10.1016/J.CELL.2020.12.003.

[29] Yixuan J. Hou et al. “SARS-CoV-2 Reverse Genetics Reveals a Variable Infection Gradient in the Respiratory Tract”. In : *Cell* 182.2 (2020), 429-446.e14. ISSN : 1097-4172. DOI : 10.1016/J.CELL.2020.05.042.

[30] Ji Hoon Ahn et al. “Nasal ciliated cells are primary targets for SARS-CoV-2 replication in the early stage of COVID-19”. In : *J. Clin. Invest.* 131.13 (2021). ISSN : 15588238. DOI : 10.1172/JCI148517.

[31] Robert P. Dickson et al. “The Microbiome and the Respiratory Tract”. In : *Annual review of physiology* 78 (fév. 2016), p. 481. ISSN : 15451585. DOI : 10.1146/ANNUREV-PHYSIOL-021115-105238.

[32] Roman Wölfel et al. “Virological assessment of hospitalized patients with COVID-2019”. In : *Nat. 2020 5817809* 581.7809 (2020), p. 465-469. ISSN : 1476-4687. DOI : 10.1038/s41586-020-2196-x.

[33] Stefanie Deinhardt-Emmer et al. “Early postmortem mapping of sars-cov-2 rna in patients with covid-19 and the correlation with tissue damage”. In : *Elife* 10 (2021). ISSN : 2050084X. DOI : 10.7554/ELIFE.60361.

[34] Carly G.K. Ziegler et al. “SARS-CoV-2 Receptor ACE2 Is an Interferon-Stimulated Gene in Human Airway Epithelial Cells and Is Detected in Specific Cell Subsets across Tissues”. In : *Cell* 181.5 (2020), p. 1016. ISSN : 10974172. DOI : 10.1016/J.CELL.2020.04.035.

[35] Wenling Wang et al. “Detection of SARS-CoV-2 in Different Types of Clinical Specimens”. In : *JAMA* 323.18 (2020), p. 1843-1844. ISSN : 0098-7484. DOI : 10.1001/JAMA.2020.3786.

[36] David L. Jones et al. “Shedding of SARS-CoV-2 in feces and urine and its potential role in person-to-person transmission and the environment-based spread of COVID-19”. In : *Sci. Total Environ.* 749 (2020), p. 141364. ISSN : 0048-9697. DOI : 10.1016/J.SCITOTENV.2020.141364.

[37] Dickson W.L. Wong et al. “Multisystemic Cellular Tropism of SARS-CoV-2 in Autopsies of COVID-19 Patients”. In : *Cells 2021, Vol. 10, Page 1900* 10.8 (2021), p. 1900. ISSN : 2073-4409. DOI : 10.3390/CELLS10081900.

[38] WHO. “Traitements contre la COVID-19”. In : Mars (2022).

[39] OMS. “Orientations évolutives concernant la prise en charge clinique de la COVID-19 : orientations évolutives, 23 novembre 2021”. In : (2021).

[40] Ludovico Cantuti-Castelvetri et al. “Neuropilin-1 facilitates SARS-CoV-2 cell entry and infectivity”. In : *Science* 370.6518 (2020). issn : 1095-9203. doi : 10.1126/SCIENCE.ABD2985.

[41] Guilherme Dias de Melo et al. “COVID-19-related anosmia is associated with viral persistence and inflammation in human olfactory epithelium and brain infection in hamsters”. In : *Sci. Transl. Med.* 13.596 (2021), p. 8396. issn : 19466242. doi : 10.1126/SCITRANSLMED.ABF8396/SUPPL_FILE/ABF8396_SM.PDF.

[42] Helen M. Lazear, John W. Schoggins et Michael S. Diamond. “Shared and Distinct Functions of Type I and Type III Interferons”. In : *Immunity* 50.4 (2019), p. 907-923. issn : 1074-7613. doi : 10.1016/J.IMMUNI.2019.03.025.

[43] Alessandro Sette et Shane Crotty. “Adaptive immunity to SARS-CoV-2 and COVID-19”. In : *Cell* 184.4 (2021), p. 861. issn : 10974172. doi : 10.1016/J.CELL.2021.01.007.

[44] Chuan Qin et al. “Dysregulation of immune response in patients with COVID-19 in Wuhan, China”. In : *Clin. Infect. Dis. An Off. Publ. Infect. Dis. Soc. Am.* 71.15 (2020), p. 762-768. issn : 15376591. doi : 10.1093/CID/CIAA248.

[45] Xuetao Cao. “COVID-19: immunopathology and its implications for therapy”. In : *Nat. Rev. Immunol. 2020 205* 20.5 (2020), p. 269-270. issn : 1474-1741. doi : 10.1038/s41577-020-0308-3.

[46] Mingfeng Liao et al. “Single-cell landscape of bronchoalveolar immune cells in patients with COVID-19”. In : *Nat. Med. 2020 266* 26.6 (2020), p. 842-844. issn : 1546-170X. doi : 10.1038/s41591-020-0901-9.

[47] Bin Ju et al. “Human neutralizing antibodies elicited by SARS-CoV-2 infection”. In : *Nature* 584 (7819 août 2020), p. 115-119. issn : 1476-4687. doi : 10.1038/S41586-020-2380-Z.

[48] Louis Grandjean et al. “Long-Term Persistence of Spike Protein Antibody and Predictive Modeling of Antibody Dynamics After Infection With Severe Acute Respiratory Syndrome Coronavirus 2”. In : *Clinical infectious diseases : an official publication of the Infectious Diseases Society of America* 74 (7 avr. 2022), p. 1220-1229. issn : 1537-6591. doi : 10.1093/CID/CIAB607.

[49] David Alfego et al. “A population-based analysis of the longevity of SARS-CoV-2 antibody seropositivity in the United States”. In : *EClinicalMedicine* 36 (2021). issn : 25895370. doi : 10.1016/J.ECLINM.2021.100902/ATTACHMENT/CC25B47A-F545-4555-A8C8-0D1C061C4460/MMC2.PDF.

[50] Raymond A. Harvey et al. “Association of SARS-CoV-2 Seropositive Antibody Test With Risk of Future Infection”. In : *JAMA Internal Medicine* 181 (5 mai 2021), p. 672-679. issn : 2168-6106. doi : 10.1001/JAMAINTERNMED.2021.0366.

[51] Fernando P. Polack et al. “Safety and Efficacy of the BNT162b2 mRNA Covid-19 Vaccine”. In : *The New England journal of medicine* 383 (27 déc. 2020), p. 2603-2615. ISSN : 1533-4406. DOI : 10.1056/NEJMOA2034577.

[52] Lindsey R. Baden et al. “Efficacy and Safety of the mRNA-1273 SARS-CoV-2 Vaccine”. In : *The New England journal of medicine* 384 (5 fév. 2021), p. 403-416. ISSN : 1533-4406. DOI : 10.1056/NEJMOA2035389.

[53] Merryn Voysey et al. “Safety and efficacy of the ChAdOx1 nCoV-19 vaccine (AZD1222) against SARS-CoV-2: an interim analysis of four randomised controlled trials in Brazil, South Africa, and the UK”. In : *The Lancet* 397 (10269 jan. 2021), p. 99-111. ISSN : 1474547X. DOI : 10.1016/S0140-6736(20)32661-1/ATTACHMENT/BD910DFE-2C8A-4512-A277-6B1DBA6322EE/MMC2.PDF.

[54] Nick Andrews et al. “Covid-19 Vaccine Effectiveness against the Omicron (B.1.1.529) Variant”. In : *New England Journal of Medicine* 386 (16 avr. 2022), p. 1532-1546. ISSN : 0028-4793. DOI : 10.1056/NEJMOA2119451/SUPPL_FILE/NEJMOA2119451_DISCLOSURES.PDF.

[55] Michael Dougan et al. “Bamlanivimab plus Etesevimab in Mild or Moderate Covid-19”. In : *N. Engl. J. Med.* 385.15 (2021), p. 1382-1392. ISSN : 1533-4406. DOI : 10.1056/NEJMOA2102685.

[56] Robert L. Gottlieb et al. “Early Remdesivir to Prevent Progression to Severe Covid-19 in Outpatients”. In : *N. Engl. J. Med.* 386.4 (2022), p. 305-315. ISSN : 0028-4793. DOI : 10.1056/NEJMOA2116846/SUPPL_FILE/NEJMOA2116846_DATA-SHARING.PDF.

[57] Anil Gupta et al. “Effect of Sotrovimab on Hospitalization or Death Among High-risk Patients With Mild to Moderate COVID-19: A Randomized Clinical Trial”. In : *JAMA* 327.13 (2022), p. 1236-1246. ISSN : 0098-7484. DOI : 10.1001/JAMA.2022.2832.

[58] David M. Weinreich et al. “REGEN-COV Antibody Combination and Outcomes in Outpatients with Covid-19”. In : *N. Engl. J. Med.* 385.23 (2021), e81. ISSN : 0028-4793. DOI : 10.1056/NEJMOA2108163/SUPPL_FILE/NEJMOA2108163_DATA-SHARING.PDF.

[59] Myron J. Levin et al. “Intramuscular AZD7442 (Tixagevimab–Cilgavimab) for Prevention of Covid-19”. In : *N. Engl. J. Med.* 386.23 (2022), p. 2188-2200. ISSN : 0028-4793. DOI : 10.1056/NEJMOA2116620/SUPPL_FILE/NEJMOA2116620_DATA-SHARING.PDF.

[60] Who Solidarity Trial Consortium. “Remdesivir and three other drugs for hospitalised patients with COVID-19: final results of the WHO Solidarity randomised trial and updated meta-analyses”. In : *The Lancet* 399 (10339 mai 2022), p. 1941-1953. ISSN : 1474547X. DOI : 10.1016/S0140-6736(22)00519-0/ATTACHMENT/C1772ABE-CCEE-4B89-A469-1C16F93184AE/MMC1.PDF.

[61] Florence Ader et al. “Remdesivir plus standard of care versus standard of care alone for the treatment of patients admitted to hospital with COVID-19 (DisCoVeRy): a phase 3, randomised, controlled, open-label trial”. In : *Lancet Infect. Dis.* 0.0 (2021). ISSN : 1473-3099. DOI : 10.1016/S1473-3099(21)00485-0.

[62] J D et al. Lundgren. “A Neutralizing Monoclonal Antibody for Hospitalized Patients with Covid-19”. In : *N. Engl. J. Med.* 384.10 (2021), p. 905-914. issn : 0028-4793. doi : 10.1056/NEJMOA2033130/SUPPL_FILE/NEJMOA2033130_DATA-SHARING.PDF.

[63] ACTIV-3/TICO LY-CoV555 Study Group. “Efficacy and safety of two neutralising monoclonal antibody therapies, sotrovimab and BRII-196 plus BRII-198, for adults hospitalised with COVID-19 (TICO): a randomised controlled trial”. In : *The Lancet. Infectious diseases* 22 (5 mai 2022), p. 622-635. issn : 1474-4457. doi : 10.1016/S1473-3099(21)00751-9.

[64] ACTIV-3/TICO LY-CoV555 Study Group. “A Neutralizing Monoclonal Antibody for Hospitalized Patients with Covid-19”. In : *New England Journal of Medicine* 384 (10 mars 2021), p. 905-914. issn : 0028-4793. doi : 10.1056/NEJMOA2033130/SUPPL_FILE/NEJMOA2033130_DATA-SHARING.PDF.

[65] RECOVERY Collaborative Group. “Casirivimab and imdevimab in patients admitted to hospital with COVID-19 (RECOVERY): a randomised, controlled, open-label, platform trial”. In : *Lancet* 399.10325 (2022), p. 665-676. issn : 0140-6736. doi : 10.1016/S0140-6736(22)00163-5.

[66] Eva Konkolova et al. “Remdesivir triphosphate can efficiently inhibit the RNA-dependent RNA polymerase from various flaviviruses”. In : *Antiviral research* 182 (oct. 2020). issn : 1872-9096. doi : 10.1016/J.ANTIVIRAL.2020.104899.

[67] Brandi N. Williamson et al. “Clinical benefit of remdesivir in rhesus macaques infected with SARS-CoV-2”. In : *Nature* 585 (7824 sept. 2020), p. 273-276. issn : 14764687. doi : 10.1038/s41586-020-2423-5.

[68] Brandi N. Williamson et al. “Subcutaneous remdesivir administration prevents interstitial pneumonia in rhesus macaques inoculated with SARS-CoV-2”. In : *Antiviral Research* 198 (fév. 2022). issn : 18729096. doi : 10.1016/j.antiviral.2022.105246.

[69] Jonathan Grein et al. “Compassionate Use of Remdesivir for Patients with Severe Covid-19”. In : *New England Journal of Medicine* 382 (24 juin 2020), p. 2327-2336. issn : 0028-4793. doi : 10.1056/nejmoa2007016.

[70] Yeming Wang et al. “Remdesivir in adults with severe COVID-19: a randomised, double-blind, placebo-controlled, multicentre trial”. In : *The Lancet* 395 (10236 mai 2020), p. 1569-1578. issn : 1474547X. doi : 10.1016/S0140-6736(20)31022-9.

[71] Andreas Barratt-Due et al. “Evaluation of the effects of remdesivir and hydroxychloroquine on viral clearance in covid-19: A randomized trial”. In : *Annals of Internal Medicine* 174 (9 sept. 2021), p. 1261-1269. issn : 15393704. doi : 10.7326/M21-0653.

[72] Daouda Sissoko et al. “Experimental Treatment with Favipiravir for Ebola Virus Disease (the JIKI Trial): A Historically Controlled, Single-Arm Proof-of-Concept Trial in Guinea”. In : *PLoS Med.* 13.3 (2016). issn : 1549-1676. doi : 10.1371/JOURNAL.PMED.1001967.

[73] Vincent Madelain et al. “Ebola viral dynamics in nonhuman primates provides insights into virus immuno-pathogenesis and antiviral strategies”. In : *Nat. Commun. 2018 91* 9.1 (2018), p. 1-11. issn : 2041-1723. doi : 10.1038/s41467-018-06215-z.

[74] Guillaume Lingas et al. “Lassa viral dynamics in non-human primates treated with favipiravir or ribavirin”. In : *PLOS Comput. Biol.* 17.1 (2021), e1008535. issn : 1553-7358. doi : 10.1371/JOURNAL.PCBI.1008535.

[75] Manli Wang et al. “Remdesivir and chloroquine effectively inhibit the recently emerged novel coronavirus (2019-nCoV) in vitro”. In : *Cell Research 2020 30:3* 30 (3 fév. 2020), p. 269-271. issn : 1748-7838. doi : 10.1038/s41422-020-0282-0.

[76] *ICTRP Search Portal.*

[77] Chuan Huan Chuah et al. “Efficacy of Early Treatment with Favipiravir on Disease Progression among High Risk COVID-19 Patients: A Randomized, Open-Label Clinical Trial”. In : *Clinical infectious diseases : an official publication of the Infectious Diseases Society of America* (nov. 2021). issn : 1537-6591. doi : 10.1093/CID/CIAB962.

[78] Chang Chen et al. “Favipiravir Versus Arbidol for Clinical Recovery Rate in Moderate and Severe Adult COVID-19 Patients: A Prospective, Multicenter, Open-Label, Randomized Controlled Clinical Trial”. In : *Frontiers in pharmacology* 12 (sept. 2021). issn : 1663-9812. doi : 10.3389/FPHAR.2021.683296.

[79] Yohei Doi et al. “A Prospective, Randomized, Open-Label Trial of Early versus Late Favipiravir Therapy in Hospitalized Patients with COVID-19”. In : *Antimicrobial agents and chemotherapy* 64 (12 déc. 2020). issn : 1098-6596. doi : 10.1128/AAC.01897-20.

[80] Mohammad Bosaeed et al. “Efficacy of favipiravir in adults with mild COVID-19: a randomized, double-blind, multicentre, placebo-controlled clinical trial”. In : *Clinical Microbiology and Infection* 28 (4 avr. 2022), p. 602. issn : 14690691. doi : 10.1016/J.CMI.2021.12.026.

[81] Marisa Holubar et al. “Favipiravir for treatment of outpatients with asymptomatic or uncomplicated COVID-19: a double-blind randomized, placebo-controlled, phase 2 trial”. In : *Clinical Infectious Diseases: An Official Publication of the Infectious Diseases Society of America* (avr. 2022). issn : 1058-4838. doi : 10.1093/CID/CIAC312.

[82] Yannis Michalakis et al. “SARS-CoV-2 viral RNA levels are not ’viral load’”. In : *Trends Microbiol.* 29.11 (2021), p. 970. issn : 18784380. doi : 10.1016/J.TIM.2021.08.008.

[83] Ruian Ke et al. “Daily longitudinal sampling of SARS-CoV-2 infection reveals substantial heterogeneity in infectiousness”. In : *Nat. Microbiol. 2022 75* 7.5 (2022), p. 640-652. issn : 2058-5276. doi : 10.1038/s41564-022-01105-z.

[84] Nadège Néant et al. “Modeling SARS-CoV-2 viral kinetics and association with mortality in hospitalized patients from the French COVID cohort”. In : *Proc. Natl. Acad. Sci. U. S. A.* 118.8 (2021), e2017962118. doi : 10.1073/PNAS.2017962118.

[85] Lirong Zou et al. “SARS-CoV-2 Viral Load in Upper Respiratory Specimens of Infected Patients”. In : *N. Engl. J. Med.* 382.12 (2020), p. 1177-1179. issn : 1533-4406. doi : 10.1056/NEJMC2001737.

[86] Stephen A. Lauer et al. “The Incubation Period of Coronavirus Disease 2019 (COVID-19) From Publicly Reported Confirmed Cases: Estimation and Application”. In : *https://doi.org/10.7326/M20-0504* 172.9 (2020), p. 577-582. issn : 15393704. doi : 10.7326/M20-0504.

[87] Ben Killingley et al. “Safety, tolerability and viral kinetics during SARS-CoV-2 human challenge in young adults”. In : *Nat. Med. 2022 285* 28.5 (2022), p. 1031-1041. issn : 1546-170X. doi : 10.1038/s41591-022-01780-9.

[88] Muge Cevik et al. “SARS-CoV-2, SARS-CoV, and MERS-CoV viral load dynamics, duration of viral shedding, and infectiousness: a systematic review and meta-analysis”. In : *The Lancet Microbe* 2.1 (2021), e13-e22. issn : 26665247. doi : 10.1016/S2666-5247(20)30172-5/ATTACHMENT/870A676D-E584-4EC8-B33D-9119177DD6F5/MMC1.PDF.

[89] Sjoerd Euser et al. “SARS-CoV-2 viral-load distribution reveals that viral loads increase with age: a retrospective cross-sectional cohort study”. In : *Int. J. Epidemiol.* 50.6 (2021), p. 1795-1803. issn : 14643685. doi : 10.1093/IJE/DYAB145.

[90] Helena C. Maltezou et al. “Association between Upper Respiratory Tract Viral Load, Comorbidities, Disease Severity, and Outcome of Patients with SARS-CoV-2 Infection”. In : *J. Infect. Dis.* 223.7 (2021), p. 1132-1138. issn : 15376613. doi : 10.1093/INFDIS/JIAA804.

[91] Hooman Parhizkar et al. “Quantifying environmental mitigation of aerosol viral load in a controlled chamber with participants diagnosed with COVID-19”. In : *Clin. Infect. Dis. An Off. Publ. Infect. Dis. Soc. Am.* (2022). issn : 1058-4838. doi : 10.1093/CID/CIAC006.

[92] Michael Marks et al. “Transmission of COVID-19 in 282 clusters in Catalonia, Spain: a cohort study”. In : *Lancet Infect. Dis.* 21.5 (2021), p. 629-636. issn : 14744457. doi : 10.1016/S1473-3099(20)30985-3.

[93] Aurélien Marc et al. “Quantifying the relationship between SARS-CoV-2 viral load and infectiousness”. In : *Elife* 10 (2021). issn : 2050-084X. doi : 10.7554/ELIFE.69302.

[94] Ashish Goyal et al. “Viral load and contact heterogeneity predict SARS-CoV-2 transmission and super-spreading events”. In : *Elife* 10 (2021), p. 1-63. issn : 2050084X. doi : 10.7554/ELIFE.63537.

[95] Ruian Ke et al. “In vivo kinetics of SARS-CoV-2 infection and its relationship with a person’s infectiousness”. In : *Proc. Natl. Acad. Sci. U. S. A.* 118.49 (2021). issn : 10916490. doi : 10.1073/PNAS.2111477118/SUPPL_FILE/PNAS.2111477118.SAPP.PDF.

[96] Xi He et al. “Temporal dynamics in viral shedding and transmissibility of COVID-19”. In : *Nat. Med.* 26.5 (2020), p. 672-675. issn : 1546170X. doi : 10.1038/S41591-020-0869-5.

[97] Baptiste Elie et al. “Variant-specific SARS-CoV-2 within-host kinetics”. In : *J. Med. Virol.* (2022). issn : 0146-6615. doi : 10.1002/JMV.27757.

[98] N.G. Davies et al. “Estimated transmissibility and impact of SARS-CoV-2 lineage B.1.1.7 in England”. In : *Science (80-.).* 372 (2021).

[99] Stephen M. Kissler et al. “Viral Dynamics of SARS-CoV-2 Variants in Vaccinated and Unvaccinated Persons”. In : *N. Engl. J. Med.* 385.26 (2021), p. 2489-2491. issn : 0028-4793. doi : 10.1056/NEJMC2102507/SUPPL_FILE/NEJMC2102507_DISCLOSURES.PDF.

[100] Francois Blanquart et al. “Characterisation of vaccine breakthrough infections of sars-cov-2 delta and alpha variants and within-host viral load dynamics in the community, france, june to july 2021”. In : *Eurosurveillance* 26.37 (2021), p. 2100824. issn : 15607917. doi : 10.2807/1560-7917.ES.2021.26.37.2100824/CITE/PLAINTEXT.

[101] Hannah W. Despres et al. “Measuring infectious SARS-CoV-2 in clinical samples reveals a higher viral titer:RNA ratio for Delta and Epsilon vs. Alpha variants”. In : *Proc. Natl. Acad. Sci. U. S. A.* 119.5 (2022). issn : 1091-6490. doi : 10.1073/PNAS.2116518119.

[102] Stephen M. Kissler et al. “Viral dynamics of acute SARS-CoV-2 infection and applications to diagnostic and public health strategies”. In : *PLoS Biol.* 19.7 (2021), p. 1-17. issn : 15457885. doi : 10.1371/journal.pbio.3001333.

[103] Jean-Jacques Parienti et Harm-Jan de Grooth. “Clinical relevance of nasopharyngeal SARS-CoV-2 viral load reduction in outpatients with COVID-19”. In : *Journal of Antimicrobial Chemotherapy* (avr. 2022). issn : 0305-7453. doi : 10.1093/JAC/DKAC104.

[104] Felipe Erez-Garcia et al. “High SARS-CoV-2 Viral Load and Low CCL5 Expression Levels in the Upper Respiratory Tract Are Associated With COVID-19 Severity”. In : *J. Infect. Dis.* 225.6 (2022), p. 977. issn : 15376613. doi : 10.1093/INFDIS/JIAB604.

[105] Kirsten Alexandra Eberhardt et al. “RNAemia Corresponds to Disease Severity and Antibody Response in Hospitalized COVID-19 Patients”. In : *Viruses 2020, Vol. 12, Page 1045* 12.9 (2020), p. 1045. issn : 1999-4915. doi : 10.3390/V12091045.

[106] Jesse Fajnzylber et al. “SARS-CoV-2 viral load is associated with increased disease severity and mortality”. In : *Nat. Commun. 2020 111* 11.1 (2020), p. 1-9. issn : 2041-1723. doi : 10.1038/s41467-020-19057-5.

[107] Lars F. Westblade et al. “SARS-CoV-2 Viral Load Predicts Mortality in Patients with and without Cancer Who Are Hospitalized with COVID-19”. In : *Cancer Cell* 38.5 (2020), 661-671.e2. issn : 18783686. doi : 10.1016/J.CCELL.2020.09.007.

[108] Chiara Piubelli et al. “Overall decrease in SARS-CoV-2 viral load and reduction in clinical burden: the experience of a hospital in northern Italy”. In : *Clin. Microbiol. Infect.* 27.1 (2021), 131.e1. issn : 14690691. doi : 10.1016/J.CMI.2020.10.006.

[109] Mathieu Blot et al. “Alveolar SARS-CoV-2 Viral Load Is Tightly Correlated With Severity in COVID-19 ARDS”. In : *Clin. Infect. Dis.* 72.9 (2021), E446-E447. issn : 1537-6591. doi : 10.1093/CID/CIAA1172.

[110] Shufa Zheng et al. “Viral load dynamics and disease severity in patients infected with SARS-CoV-2 in Zhejiang province, China, January-March 2020: retrospective cohort study”. In : *BMJ* 369 (2020). issn : 1756-1833. doi : 10.1136/BMJ.M1443.

[111] Nicholas G. Davies et al. “Increased mortality in community-tested cases of SARS-CoV-2 lineage B.1.1.7”. In : *Nature* 593.7858 (2021), p. 270-274. issn : 14764687. doi : 10.1038/s41586-021-03426-1.

[112] Mark G. Thompson et al. “Prevention and Attenuation of Covid-19 with the BNT162b2 and mRNA-1273 Vaccines”. In : *New England Journal of Medicine* 385 (4 juill. 2021), p. 320-329. issn : 0028-4793. doi : 10.1056/NEJMOA2107058.

[113] Matan Levine-Tiefenbrun et al. “Viral loads of Delta-variant SARS-CoV-2 breakthrough infections after vaccination and booster with BNT162b2”. In : *Nat. Med.* 27.12 (2021), p. 2108-2110. issn : 1546170X. doi : 10.1038/S41591-021-01575-4.

[114] Anika Singanayagam et al. “Community transmission and viral load kinetics of the SARS-CoV-2 delta (B.1.617.2) variant in vaccinated and unvaccinated individuals in the UK: a prospective, longitudinal, cohort study”. In : *Lancet Infect. Dis.* 22.2 (2022), p. 183-195. issn : 14744457. doi : 10.1016/S1473-3099(21)00648-4.

[115] Olha Puhach et al. “Infectious viral load in unvaccinated and vaccinated individuals infected with ancestral, Delta or Omicron SARS-CoV-2”. In : *Nat. Med. 2022* (2022), p. 1-10. issn : 1546-170X. doi : 10.1038/s41591-022-01816-0.

[116] Anne L. Wyllie et al. “Saliva or Nasopharyngeal Swab Specimens for Detection of SARS-CoV-2”. In : *New England Journal of Medicine* 383 (13 sept. 2020), p. 1283-1286. issn : 0028-4793. doi : 10.1056/NEJMC2016359/SUPPL_FILE/NEJMC2016359_DISCLOSURES.PDF.

[117] Mohan Rao et al. “Comparing Nasopharyngeal Swab and Early Morning Saliva for the Identification of Severe Acute Respiratory Syndrome Coronavirus 2 (SARS-CoV-2)”. In : *Clinical Infectious Diseases* 72 (9 mai 2021), e352-e356. issn : 1058-4838. doi : 10.1093/CID/CIAA1156.

[118] Abbas Mohammadi et al. “SARS-CoV-2 detection in different respiratory sites: A systematic review and meta-analysis”. In : *EBioMedicine* 59 (sept. 2020), p. 102903. issn : 23523964. doi : 10.1016/J.EBIOM.2020.102903/ATTACHMENT/57C5FDAF-640E-4028-BEF9-DDE2F4CE3851/MMC1.PDF.

[119] Quentin Le Hingrat et al. “Detection of SARS-CoV-2 N-antigen in blood during acute COVID-19 provides a sensitive new marker and new testing alternatives”. In : *Clinical Microbiology and Infection* 27 (5 mai 2021), 789.e1-789.e5. issn : 14690691. doi : 10.1016/J.CMI.2020.11.025/ATTACHMENT/11860D04-46DB-4BE7-BBD6-070BF442CD6B/MMC1.PDF.

[120] Alan S. Perelson et al. “HIV-1 dynamics in vivo: virion clearance rate, infected cell life-span, and viral generation time”. In : *Science* 271.5255 (1996), p. 1582-1586. issn : 0036-8075. doi : 10.1126/SCIENCE.271.5255.1582.

[121] Avidan U. Neumann et al. “Hepatitis C viral dynamics in vivo and the antiviral efficacy of interferon-alpha therapy”. In : *Science* 282.5386 (1998), p. 103-107. issn : 0036-8075. doi : 10.1126/SCIENCE.282.5386.103.

[122] Baccam et al. “Kinetics of Influenza A Virus Infection in Humans”. In : *J. Virol.* 80.15 (2006), 7590 LP -7599. doi : 10.1128/JVI.01623-05.

[123] Laetitia Canini et Fabrice Carrat. “Population modeling of influenza A/H1N1 virus kinetics and symptom dynamics”. In : *J. Virol.* 85.6 (2011), p. 2764-2770. issn : 1098-5514. doi : 10.1128/JVI.01318-10.

[124] Katharine Best et al. “Zika plasma viral dynamics in nonhuman primates provides insights into early infection and antiviral strategies”. In : *Proc. Natl. Acad. Sci. U. S. A.* 114.33 (2017), p. 8847-8852. issn : 1091-6490. doi : 10.1073/PNAS.1704011114.

[125] Xianfang Wu et al. “Intrinsic Immunity Shapes Viral Resistance of Stem Cells”. In : *Cell* 172.3 (2018), 423-438.e25. issn : 0092-8674. doi : 10.1016/J.CELL.2017.11.018.

[126] Sinthujan Jegaskanda et al. “Influenza Virus Infection Enhances Antibody-Mediated NK Cell Functions via Type I Interferon-Dependent Pathways”. In : *J. Virol.* 93.5 (2019). issn : 0022-538X. doi : 10.1128/JVI.02090-18/SUPPL_FILE/JVI.02090-18-S0001.PDF.

[127] Sunpeng Wang et al. “Modeling the viral dynamics of SARS-CoV-2 infection”. In : *Math. Biosci.* 328 (2020), p. 108438. issn : 0025-5564. doi : 10.1016/J.MBS.2020.108438.

[128] Ashish Goyal, E. Fabian Cardozo-Ojeda et Joshua T. Schiffer. “Potency and timing of antiviral therapy as determinants of duration of SARS-CoV-2 shedding and intensity of inflammatory response”. In : *Sci. Adv.* 6.47 (2020). issn : 23752548. doi : 10.1126/SCIADV.ABC7112.

[129] Shohei Koyama et al. “Innate immune response to viral infection”. In : *Cytokine* 43.3 (2008), p. 336-341. issn : 1096-0023. doi : 10.1016/J.CYTO.2008.07.009.

[130] Peter C. Taylor et al. “Neutralizing monoclonal antibodies for treatment of COVID-19”. In : *Nature Reviews Immunology 2021 21:6* 21 (6 avr. 2021), p. 382-393. issn : 1474-1741. doi : 10.1038/s41577-021-00542-x.

[131] Antonio Gonçalves et al. “Timing of Antiviral Treatment Initiation is Critical to Reduce SARS-CoV-2 Viral Load”. In : *CPT Pharmacometrics Syst. Pharmacol.* 9.9 (2020), p. 509-514. issn : 2163-8306. doi : 10.1002/PSP4.12543.

[132] Peter Czuppon et al. “Success of prophylactic antiviral therapy for SARS-CoV-2: Predicted critical efficacies and impact of different drug-specific mechanisms of action”. In : *PLOS Computational Biology* 17 (3 mars 2021), e1008752. issn : 1553-7358. doi : 10.1371/JOURNAL.PCBI.1008752.

[133] Ashish Goyal et al. “Slight reduction in SARS-CoV-2 exposure viral load due to masking results in a significant reduction in transmission with widespread implementation”. In : *Sci. Rep.* 11.1 (2021), p. 11838. issn : 20452322. doi : 10.1038/S41598-021-91338-5.

[134] Silke Gastine et al. “Systematic Review and Patient-Level Meta-Analysis of SARS-CoV-2 Viral Dynamics to Model Response to Antiviral Therapies”. In : *Clin. Pharmacol. Ther.* 110.2 (2021), p. 321-333. issn : 1532-6535. doi : 10.1002/CPT.2223.

[135] Marion Kerioui et al. “Modelling the association between biomarkers and clinical outcome: An introduction to nonlinear joint models”. In : *Br. J. Clin. Pharmacol.* 88.4 (2022), p. 1452-1463. issn : 1365-2125. doi : 10.1111/BCP.15200.

[136] Russ Wolfinger. “Laplace’s approximation for nonlinear mixed models”. In : *Biometrika* 80.4 (1993), p. 791-795. issn : 0006-3444. doi : 10.1093/BIOMET/80.4.791.

[137] Arthur P Dempster, Nan M Laird et Donald B Rubin. “Maximum likelihood from incomplete data via the EM algorithm”. In : *Journal of the Royal Statistical Society: Series B (Methodological)* 39.1 (1977), p. 1-22.

[138] Bernard Delyon, Marc Lavielle et Eric Moulines. “Convergence of a stochastic approximation version of the EM algorithm”. In : *Annals of statistics* (1999), p. 94-128.

[139] Estelle Kuhn et Marc Lavielle. “Coupling a stochastic approximation version of EM with an MCMC procedure”. In : *ESAIM Probab. Stat.* 8 (2004), p. 115-131. issn : 1292-8100. doi : 10.1051/PS:2004007.

[140] Elodie L. Plan et al. “Performance comparison of various maximum likelihood nonlinear mixed-effects estimation methods for dose-response models”. In : *AAPS J.* 14.3 (2012), p. 420-432. issn : 1550-7416. doi : 10.1208/S12248-012-9349-2.

[141] S T Buckland, K P Burnham et N H Augustin. *Model Selection: An Integral Part of Inference*. 1997, p. 603-618.

[142] Antonio Gonçalves et al. “Model Averaging in Viral Dynamic Models”. In : *AAPS J.* 22.2 (2020), p. 48. issn : 15507416. doi : 10.1208/S12248-020-0426-7.

[143] Kenneth P. Burnham et David R. Anderson. *Multimodel inference: Understanding AIC and BIC in model selection*. Nov. 2004. doi : 10.1177/0049124104268644.

[144] Florence Ader et al. “An open-label randomized controlled trial of the effect of lopinavir/ritonavir, lopinavir/ritonavir plus IFN-β-1a and hydroxychloroquine in hospitalized patients with COVID-19”. In : *Clin. Microbiol. Infect.* (2021). doi : 10.1016/J.CMI.2021.05.020.

[145] Pauline Maisonnasse et al. “Hydroxychloroquine use against SARS-CoV-2 infection in non-human primates”. In : *Nature* 585 (7826 sept. 2020), p. 584-587. issn : 1476-4687. doi : 10.1038/S41586-020-2558-4.

[146] César Muñoz-Fontela et al. “Animal models for COVID-19”. In : *Nature 2020 586:7830* 586 (7830 sept. 2020), p. 509-515. issn : 1476-4687. doi : 10.1038/s41586-020-2787-6.

[147] Bert A. T Hart et al. “The translational value of non-human primates in preclinical research on infection and immunopathology”. In : *European journal of pharmacology* 759 (juill. 2015), p. 69-83. issn : 1879-0712. doi : 10.1016/J.EJPHAR.2015.03.023.

[148] FDA. *Guidance for Industry Estimating the Maximum Safe Starting Dose in Initial Clinical Trials for Therapeutics in Adult Healthy Volunteers Pharmacology and Toxicology Guidance for Industry Estimating the Maximum Safe Starting Dose in Initial Clinical Trials for Therapeutics in Adult Healthy Volunteers*. 2005.

[149] Andrew G. Letizia et al. “SARS-CoV-2 seropositivity and subsequent infection risk in healthy young adults: a prospective cohort study”. In : *The Lancet Respiratory Medicine* 9 (7 juill. 2021), p. 712-720. issn : 2213-2600. doi : 10.1016/S2213-2600(21)00158-2.

[150] Daniela Conrado. *VIRAL KINETICS IN COVID-19 OUTPATIENTS TREATED WITH CASIRIVIMAB+IMDEVIMAB COMBINATION*. 2022.

[151] FDA. *FACT SHEET FOR HEALTHCARE PROVIDERS: EMERGENCY USE AUTHORIZATION FOR EVUSHELD™ (tixagevimab co-packaged with cilgavimab)*.

[152] *Trial of Treatments for COVID-19 in Hospitalized Adults - Full Text View - ClinicalTrials.gov*.

[153] Lukas Lanser et al. "Evaluating the clinical utility and sensitivity of SARS-CoV-2 antigen testing in relation to RT-PCR Ct values". In : *Infection* 49 (3 juin 2021), p. 555-557. issn : 14390973. doi : 10.1007/S15010-020-01542-0/TABLES/1.

[154] Ryuta Uraki et al. "Therapeutic efficacy of monoclonal antibodies and antivirals against SARS-CoV-2 Omicron BA.1 in Syrian hamsters". In : *Nat. Microbiol. 2022* (2022), p. 1-7. issn : 2058-5276. doi : 10.1038/s41564-022-01170-4.

[155] Louis D Saravolatz, Shawn Depcinski et Mamta Sharma. "Molnupiravir and Nirmatrelvir-Ritonavir: Oral COVID Antiviral Drugs". In : *Clinical Infectious Diseases* (mars 2022). issn : 1058-4838. doi : 10.1093/CID/CIAC180.

[156] Pengfei Wang et al. "Antibody resistance of SARS-CoV-2 variants B.1.351 and B.1.1.7". In : *Nature* 593 (7857 mai 2021), p. 130-135. issn : 14764687. doi : 10.1038/s41586-021-03398-2.

[157] Delphine Planas et al. "Reduced sensitivity of SARS-CoV-2 variant Delta to antibody neutralization". In : *Nature* 596 (7871 août 2021), p. 276-280. issn : 14764687. doi : 10.1038/s41586-021-03777-9.

[158] Timothée Bruel et al. "Serum neutralization of SARS-CoV-2 Omicron sublineages BA.1 and BA.2 in patients receiving monoclonal antibodies". In : *Nature Medicine* 28 (6 juin 2022), p. 1297-1302. issn : 1546170X. doi : 10.1038/s41591-022-01792-5.

[159] Franck Touret et al. "In vitro evaluation of therapeutic antibodies against a SARS-CoV-2 Omicron B.1.1.529 isolate". In : *Scientific Reports 2022 12:1* 12 (1 mars 2022), p. 1-5. issn : 2045-2322. doi : 10.1038/s41598-022-08559-5.

[160] Holly Soares et al. "Viral Load Rebound in Placebo and Nirmatrelvir-Ritonavir Treated COVID-19 Patients is not Associated with Recurrence of Severe Disease or Mutations". In : (juin 2022). doi : 10.21203/RS.3.RS-1720472/V1.

[161] Rolando Pajon et al. "Initial analysis of viral dynamics and circulating viral variants during the mRNA-1273 Phase 3 COVE trial." In : *Nature medicine* 28 (4 avr. 2022), p. 823-830. issn : 1546-170X (Electronic). doi : 10.1038/s41591-022-01679-5.

[162] Delphine Planas et al. "Reduced sensitivity of SARS-CoV-2 variant Delta to antibody neutralization". In : *Nature 2021 596:7871* 596 (7871 juill. 2021), p. 276-280. issn : 1476-4687. doi : 10.1038/s41586-021-03777-9.

Chapitre 9

Annexes

Annexe 1 : Lassa viral dynamics in non-human primates treated with favipiravir or ribavirin, *PLoS Computational Biology*, 2021

PLOS COMPUTATIONAL BIOLOGY

RESEARCH ARTICLE

Lassa viral dynamics in non-human primates treated with favipiravir or ribavirin

Guillaume Lingas[1]*, **Kyle Rosenke**[2], **David Safronetz**[3,4], **Jérémie Guedj**[1]

1 Université de Paris, IAME, INSERM, Paris, France, **2** Laboratory of Virology, National Institute of Allergy and Infectious Diseases, National Institutes of Health, Rocky Mountain Laboratories, Hamilton, Montana, USA, **3** Department of Medical Microbiology, University of Manitoba, Winnipeg, Manitoba, Canada, **4** Zoonotic Diseases and Special Pathogens, Public Health Agency of Canada, Winnipeg, Manitoba, Canada

* guillaume.lingas@inserm.fr

OPEN ACCESS

Citation: Lingas G, Rosenke K, Safronetz D, Guedj J (2021) Lassa viral dynamics in non-human primates treated with favipiravir or ribavirin. PLoS Comput Biol 17(1): e1008535. https://doi.org/10.1371/journal.pcbi.1008535

Editor: Rustom Antia, Emory University, UNITED STATES

Received: April 9, 2020

Accepted: November 13, 2020

Published: January 7, 2021

Peer Review History: PLOS recognizes the benefits of transparency in the peer review process; therefore, we enable the publication of all of the content of peer review and author responses alongside final, published articles. The editorial history of this article is available here: https://doi.org/10.1371/journal.pcbi.1008535

Data Availability Statement: Data is available at FigShare, at this DOI: 10.6084/m9.figshare.13061501 (https://figshare.com/search?q=10.6084%2Fm9.figshare.13061501). The model used in Monolix 2018R2 software to fit the data using

Abstract

Lassa fever is an haemorrhagic fever caused by Lassa virus (LASV). There is no vaccine approved against LASV and the only recommended antiviral treatment relies on ribavirin, despite limited evidence of efficacy. Recently, the nucleotide analogue favipiravir showed a high antiviral efficacy, with 100% survival obtained in an otherwise fully lethal non-human primate (NHP) model of Lassa fever. However the mechanism of action of the drug is not known and the absence of pharmacokinetic data limits the translation of these results to the human setting. Here we aimed to better understand the antiviral effect of favipiravir by developping the first mathematical model recapitulating Lassa viral dynamics and treatment. We analyzed the viral dynamics in 24 NHPs left untreated or treated with ribavirin or favipiravir, and we put the results in perspective with those obtained with the same drugs in the context of Ebola infection. Our model estimates favipiravir EC_{50} *in vivo* to 2.89 $\mu g.mL^{-1}$, which is much lower than what was found against Ebola virus. The main mechanism of action of favipiravir was to decrease virus infectivity, with an efficacy of 91% at the highest dose. Based on our knowledge acquired on the drug pharmacokinetics in humans, our model predicts that favipiravir doses larger than 1200 mg twice a day should have the capability to strongly reduce the production infectious virus and provide a milestone towards a future use in humans.

Author summary

Lassa virus is the etiological agent of Lassa fever, an haemorrhagic fever endemic that cause nearly 5000 deaths every year in West Africa. Here, we provide the first within-host mathematical model of the infection by Lassa virus in a macaque model and we analyze the antiviral effect of two candidate drugs, favipiravir or ribavirin. We show that both drugs act primarily by increasing mutagenesis in vivo. Both drugs had a strong antiviral efficacy in reducing the proportion of non infectious virus produced by infected cells, up to 91 and 40% for favipiravir and ribavirin, respectively. We bridge these predictions with our knowledge of the drugs pharmacokinetics to identify target concentrations having the capability to rapidly clear infectious virus from infected individuals.

non-linear mixed effect model is available at FigShare, using the following DOI: 10.6084/m9.figshare.13061588 (https://figshare.com/search?q=10.6084%2Fm9.figshare.13061588).

Funding: The authors received no specific funding for this work.

Competing interests: The authors have declared that no competing interests exist.

Introduction

Lassa Virus (LASV; family *Arenaviridae*, genus *Mammarenavirus*) is the etiological agent of Lassa Fever (LF), a severe haemorrhagic fever. LF is endemic in West Africa, with 100,000-300,000 individuals infected with LASV every year resulting in an estimated 5,000 deaths [1] due to haemorrhage and multi-organ failure, while about 20% of survivors present long-term complications, such as hearing deficit [2]. In 2015/16, a particularly severe outbreak of LF occurred in Nigeria, associated with a mortality rate exceeding 50% and several nosocomial transmission events to health care providers, posing a serious threat to public health and resulting in a state of emergency being declared [3]. Further, the circulation of LASV is extending, with human cases detected recently in previously unaffected countries such as Mali, Burkina Faso or Ghana, leading to increasingly frequent outbreaks and leaving about 200 million people at risk for the disease [4]. Therefore treatment of LF is essentially supportive. WHO recommends high doses of ribavirin administered intravenously for severe cases, as ribavirin showed efficacy in macaques [5, 6]; however there is no clear evidence of efficacy in humans and the treatment is associated with potential side effects [7].

In the last years, several research groups were involved in the evaluation of the antiviral activity of favipiravir, an anti-influenza drug approved in Japan, against a variety of emerging RNA viruses, in particular Ebola, Lassa and Marburg viruses [8, 9]. In 2018, Guedj et al. [10] showed that early administration of favipiravir was associated with a strong antiviral activity in cynomolgus macaques infected by Ebola virus, with a 50% survival obtained at daily doses of 300 mg/kg and 360 mg/kg. The same year, Rosenke et al. [11] showed 100% survival in cynomolgus macaques infected with Lassa virus and treated up to 4 days post infection using daily doses of 300 mg/kg.

Although these results obtained in the "gold standard animal model" [12] may support the evaluation of favipiravir in clinical trials, we need to better understand how favipiravir acts *in vivo* against the virus and to better characterize its dose-concentration-antiviral activity relationship. Given the difficulty to access detailed data with BSL4 agents, it is crucial to leverage information by bridging the data collected in the different experiments. For instance the experiments performed in Ebola infected macaques provided a detailed understanding of favipiravir pharmacokinetics [13]. This information can be used to calculate the drug EC_{50} *in vivo* in LASV-infected animals. Likewise the comparison of viral dynamics obtained during treatment with favipiravir in different infections can be used to better understand the drug's mechanism of action. Previous results suggested that favipiravir could increase mutagenesis but also reduce specific infectivity [14–16].

Here, our goal was to reanalyze the viral dynamics in macaques infected with LASV and treated with favipiravir or ribavirin. Using our experience acquired on drug's PK/PD gained in previous experiments of macaques infected with Ebola virus [8], we aimed to build a mathematical model that could recapitulate the viral dynamics in LASV infected animals. We used this model to provide a better understanding on favipiravir and ribavirin mode of action and antiviral activity *in vivo*. We discuss how these results could be relevant for future clinical use of favipiravir in humans.

Materials and methods

Study design and data provided

We reanalyzed the data provided by Rosenke et al. in two successive experiments [11]. In brief the data involve $N = 24$ female cynomolgus macaques (*Macaca fascicularis*) that received either ribavirin (RBV, $N = 8$), favipiravir (FPV, $N = 8$) or were left untreated (controls, $N = 8$). Each animal was injected intramuscularly with a lethal dose of LASV strain Josiah (10^4 50% tissue

culture infective dose $TCID_{50}$). In all treated animals, treatment was initiated at D4 post-infection and was continued during 14 consecutive days. Animals treated with favipiravir received a loading dose of 300 mg/kg intravenously the first day of treatment, followed by subcutaneous injection of 50 mg/kg every 8 hours (TID, i.e., a daily dose of 150 mg/kg, $N = 4$) or 300 mg/kg once a day (QD, $N = 4$). Animals treated with ribavirin received a loading dose of 30 mg/kg the first day of treatment, followed by subcutaneous injections of 10 mg/kg TID (daily dose 30 mg/kg, $N = 4$) or 30 mg/kg QD ($N = 4$). Animals were euthanized when the clinical score was greater than 35 and surviving animals were otherwise euthanized at day 56. Animals were sampled for RNA viral load (copies/mL) and $TCID_{50}$ per mL (thereafter referred to as titers). Blood samples were collected at days 0, 3, 6, 9, 12, 15, 18, 24, 31, 42, 49 and 56, and at the time of death for euthanized animals. In 12 animals (4 controls as well as those receiving FPV TID or RBV TID), no data were available for viral titers at D3 and the qPCR limit of quantification was 2.75 $\log_{10}$ RNA copies per mL. The other animals had a qPCR limit of quantification of 3.26 $\log_{10}$ RNA copies per mL. In 4 animals (receiving RBV QD), viral titers were available only at the time of death. Limit of quantification for titers was 2 $\log_{10}$ $TCID_{50}$ per mL. For the sake of the descriptive analysis, all ribavirin treated animals were considered as a single treatment group and we analyzed the RNA and titers kinetics at the time of peak RNA viral load, comparing each treatment group to the controls.

Viral dynamic model

Our goal was to build a within-host model of Lassa viral infection in order to unravel the host-pathogen-drug interactions and determine ribavirin and favipiravir most likely modes of action against LASV.

Biological model. We used a target-cell limited model with a compartment for the innate immune response, F, that renders target cells, T, definitely refractory to infection [8]. The model includes four types of cell populations: target cells (T), refractory cells (R), infected cells in an eclipse phase (I_1) and productively infected cells (I_2). The model assumes that target cells are infected at a constant infection rate β (mL.RNA $copies^{-1}.day^{-1}$). Once infected, cells enter an eclipse phase and become productively infected after a mean time $1/k$ (day). We assume that productively infected cells have a constant loss rate, noted δ (day^{-1}). Infected cells produce p RNA copies per day (RNA $copies.mL^{-1}.day^{-1}$). Because both RNA viral load and infectious virus were measured, we further distinguished infectious virus, noted V_i, and non infectious virus, noted V_{ni}. We assumed that viral load, as measured by RNA copies, is the sum of infectious and non-infectious viruses, both cleared at the same rate, c. We assumed for simplification that 1 $TCID_{50}$ corresponds to 1 infectious virus. Infected cells produce proportionally as well a dimensionless immune effector, namely F, eliminated at a rate d_f. The model therefore can be written as:

$$\frac{dT}{dt} = -\beta V_i T - \phi T \frac{F}{F+\theta} \tag{1}$$

$$\frac{dI_1}{dt} = \beta V_i T - kI_1 \tag{2}$$

$$\frac{dI_2}{dt} = kI_1 - \delta I_2 \tag{3}$$

$$\frac{dV_i}{dt} = \frac{a}{vol} De^{-(a+c_t)t} + p\mu I_2 - cV_i \tag{4}$$

$$\frac{dV_{ni}}{dt} = p(1-\mu)I_2 - cV_{ni} \quad (5)$$

$$\frac{dF}{dt} = I_2 - d_f F \quad (6)$$

where β is the rate of infection of target cells and c is the clearance rate of RNA copies in the circulation. Once productively infected, cells produce p RNA copies per day, but only a fraction of them, μ, is infectious. One can derive the basic reproduction number, $R_0 = \frac{\beta\mu p T_0}{c\delta}$ that corresponds to the numbers of cells infected by an infected cell in a population of fully susceptible cells (T_0). The effect of the immune response is therefore represented by the term $\phi T \frac{F}{F+\theta}$. In this model, the presence of viral antigen stimulates the innate immune response, represented by the compartment F, which activates and renders uninfected cells refractory to infection at a rate noted ϕ, while θ represents the concentration of F required to achieve 50% of the maximal effect.

As an initial infectious viral load is required to model the start of the infection, we used a model proposed by Best et al. [17] to model the progressive arrival of the viral inoculum to the infection site after intramuscular injection. In this model the initial inoculum dose, D (equal to 10^4 $TCID_{50}$), is diluted into the plasmatic volume, *vol* (equal to 300 mL in macaques [18]) and is transported to the site of infection with rate a. During the transport, the virus can also be eliminated, with a clearance rate c_t.

Further, as some animals did not show any viral load rebound after treatment cessation, we modeled the possibility that animals could be cured from virus. Following what has been done in other curable viral infection (such as Hepatitis C virus), we assumed that the infection was cured if there was less than one infectious virus in the plasmatic volume, *vol* [19]. This corresponds to having a concentration of $V_i < 0.003$ $TCID_{50}.mL^{-1}$.

Favipiravir and ribavirin pharmacokinetic models. We used published pharmacokinetic models to predict plasma drug concentrations of favipiravir and ribavirin, noted C_{FPV} and C_{RBV}, respectively. Ribavirin pharmacokinetics was described by a one-compartment model [20] while complex favipiravir pharmacokinetics was described by a one-compartment model with an enzyme-dependent elimination rate [13] (S1 Text). Given the absence of pharmacokinetic data in the experiment, we fixed all individual parameters to the mean values found in the literature [13, 20] (see S1 Table and predictions in S1 Fig).

Favipiravir and ribavirin modes of action. We studied the possibility that FPV and RBV could either reduce the viral production, p, or decrease the proportion of infectious virus, μ. We noted ϵ_{drug} the antiviral efficacy of the considered drug (i.e. ϵ_{FPV} or ϵ_{RBV}) and we assumed an E_{max} model to relate drug concentration to efficacy:

$$\epsilon_{FPV}(t) = \frac{C_{FPV}^{\kappa}(t)}{C_{FPV}^{\kappa}(t) + EC_{50_{FPV}}^{\kappa}} \quad (7)$$

$$\epsilon_{RBV}(t) = \frac{C_{RBV}(t)}{C_{RBV}(t) + EC_{50_{RBV}}} \quad (8)$$

where $EC_{50_{FPV}}$ and $EC_{50_{RBV}}$ are the drug concentrations of FPV and RBV, respectively, needed to achieve 50% efficacy. In the case of FPV, for which 2 different doses were used, we further considered the possibility of a sigmoidicity parameter (Hill coefficient, noted κ) in the concentration-effect relationship, ranging from 1 to 5 (close to an "on-off" effect). We did not consider a Hill coefficient for RBV different than 1 since only one dose was used. During

treatment the model equations given by Eqs (4) and (5) become:

$$\frac{dV_i}{dt} = \frac{a}{vol} De^{-(a+c_t)t} + p\mu(1-\epsilon_{drug})I_2 - cV_i \tag{9}$$

$$\begin{cases} \frac{dV_{ni}}{dt} = p(1-\mu)(1-\epsilon_{drug})I_2 - cV_{ni} \\ \text{(if treatment blocks production)} \end{cases} \tag{10a}$$

$$\begin{cases} \frac{dV_{ni}}{dt} = p(1-(\mu(1-\epsilon_{drug})))I_2 - cV_{ni} \\ \text{(if treatment makes virus non infectious)} \end{cases} \tag{10b}$$

Parameter estimation & model building

Assumptions on fixed parameter values. To ensure parameter identifiability, a number of parameters had to be fixed. Viral clearance in plasma, noted c, respectively, was fixed to 20 d^{-1}, similar to what has been performed in Zika and Ebola viruses [8, 18]. For simplification, we fixed viral clearance in the tissues c_t to the same value. Clearance rate of immune effector, d_f, was fixed to 0.4 d^{-1} [8]. As only the product pT_0 is identifiable, we fixed T_0 to 10^7 cells.mL^{-1}, as it is an approximation of the liver size, which is the main target of LASV [18].

Algorithm for inference. Parameter estimation was performed in a non-linear mixed effect model framework and the likelihood was maximized using the SAEM [21](Stochastic Approximation Expectation-Maximization) algorithm implemented in Monolix software (http://lixoft.com). Information brought by data under limit of quantification was taken into account in parameter estimation [22, 23]. Statistical criterion used for model discrimination was the BIC.

Model building strategy. Our model building strategy was the following (S2 Fig).

1) We considered 4 models assuming that favipiravir or ribavirin could either block viral production or viral infectivity (Eq 10a or Eq 10b). All 4 candidate models were fitted assuming different fixed values for k and a ranging from 4 to 20 d^{-1} and 0.005 to 0.1 d^{-1}, respectively. At this stage, we assumed no sigmoidicity for FPV and $\kappa = 1$.

2) We considered other modes of action of the immune response, using the same parametrization that was used in previous works. We tested several scenarios where F either acted by reducing viral infectivity, decreasing the rate of viral production, increasing viral clearance or the loss rate of infected cells through a cytotoxic effect (S2 Text).

3) The selected model was then reduced to limit the number of random effects. Random effects with a standard deviation <0.1 or associated with a relative standard error of +100% were deleted by using a backward procedure and were kept out if the resulting BIC did not significantly increase by more than 2 points.

4) Finally, we aimed to account for uncertainty on the sigmoidicity parameter, κ. We considered values of κ ranging from 1 to 5 and we estimated the model parameters in each scenario. We then used the model averaging approach proposed in Gonçalves et al. [24] to take into account model uncertainty. Thus, we calculated the weight associated to each value of κ, given by $\omega_\kappa = \frac{e^{-\frac{BIC_\kappa}{2}}}{\sum e^{-\frac{BIC_\kappa}{2}}}$. Then the parameter estimate and its confidence interval was obtained by sampling parameters in the mixture of the asymptotic distribution of the estimators of each model, with weights ω_κ.

Simulations studies and extrapolation

Predicting the effects of drug human exposure. Using the same approach of model averaging to account for model uncertainty on κ, we simulated viral dynamic profiles that could be obtained with clinically relevant residual concentrations. We assumed a fixed treatment duration of 14 days, with treatment initiation at D4, D6 or D8 post infection. We assumed constant favipiravir concentrations equal to 46.1 or 25.9 μg.mL^{-1}, which correspond to the mean residual concentrations obtained respectively 2 and 4 days after treatment initiation in Ebola-infected patients of the JIKI trial [25]. We also considered a larger value of 80 μg.mL^{-1}, which corresponds to the residual value showing efficacy in NHPs infected with Ebola virus [10]. For ribavirin, we assumed constant drug concentration of 15 μg.mL^{-1}, which corresponds to the mean value reported in individuals receiving the recommended dosing regimen in Lassa infection (1000 mg every 6 h) [26].

Results

Descriptive analysis of viral kinetics

Survival at D56 was achieved in 100% of animals receiving 300 mg/kg/day of favipiravir, whereas all other animals died within 23 days post-infection (Fig 1). Although all animals treated with ribavirin died, the survival was extended over control animals (P<0.001), showing the benefit of ribavirin. Finally, low dose favipiravir of 150 mg/kg/day showed no benefit on survival compared to untreated animals (P = 0.4).

Ribavirin and favipiravir 150 mg/kg/day had a limited effect on viral titers at peak RNA viral load with median values of 4.32 and 4.07 $\log_{10}$TCID$_{50}$.mL^{-1}, respectively, vs 5.90 $\log_{10}$TCID$_{50}$.mL^{-1} for controls, (p<0.01 to controls in both cases). In contrast all animals receiving 300 mg/kg/day favipiravir has undetectable viral titers at all times (p<0.01 vs control, Table 1).

Although viral titers remained undetectable, high levels of viral load were observed in these animals during all the course of the infection, with peak viral load of 5.03 $\log_{10}$ RNA copies.mL^{-1} compared to 7.96 $\log_{10}$ RNA copies.mL^{-1} in untreated animals (p<0.01). The effect of

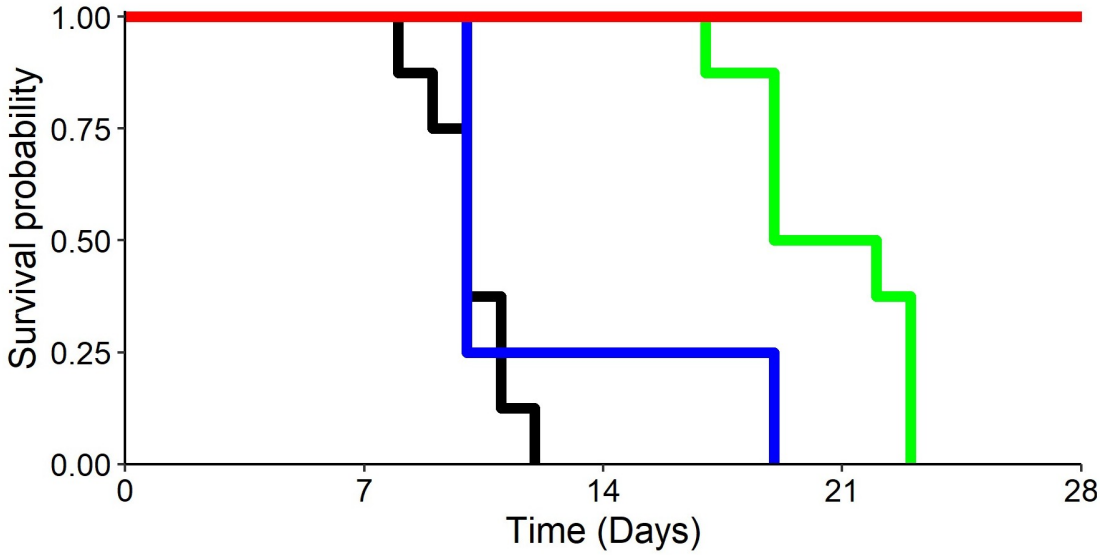

Fig 1. Observed survival according to treatment received. Black curve: animals receiving vehicle treatment; green: animals treated with RBV; blue: animals treated with FPV 150 mg/kg/day; red: animals treated with FPV 300 mg/kg/day.

https://doi.org/10.1371/journal.pcbi.1008535.g001

Table 1. Description of viral kinetics. Median (min-max). * = p <0.05 to untreated (Log-rank test for survival, Wilcoxon test for viral load and titers).

	No Treatment	RBV 30 mg/kg/day	FPV 150 mg/kg/day	FPV 300 mg/kg/day
Time to death (d)	10 (8-12)	20.5* (17-23)	10 (10-19)	NA
Time to peak viral load (d)	9 (9-12)	15* (11-15)	10 (9-15)	7.5 (6-15)
Peak viral load (log_{10} RNA copies.mL^{-1})	7.96 (7.47-8.07)	7.68 (7.21-8.57)	7.37* (7.20-7.94)	5.03* (4.68-6.65)
Viral titers at peak viral load ($log_{10}TCID_{50}.mL^{-1}$)	5.90 (5.35-6.95)	4.32* (4.20-4.44)	4.07* (3.94-5.20)	2* (2-2)

https://doi.org/10.1371/journal.pcbi.1008535.t001

favipiravir was dose dependent, with a dose of 150 mg/kg/day leading to high levels of RNA viral load at peak (7.37 log_{10} RNA copies.mL^{-1}, $p<0.05$ compared to untreated animals). In ribavirin treated animals, the peak viral load was similar to untreated animals (Table 1).

Taken together, these results suggest a greater effect of both ribavirin and favipiravir on viral titers than on viral load. To visualize that, we plotted the ratio of viral titers to viral load at the time of peak viral load, a proxy of the ratio of proportion of infectious virus (Fig 2). Interestingly there was a clear reduction of this ratio in all treated animals ($p<0.05$ for all groups compared to control). Of note, as viral titers were under the limit of detection in animals in animals treated with 300 mg/kg/day, the values were imputed to the limit of detection, i.e., 2 $log_{10}TCID_{50}.mL^{-1}$. Hence this ratio represents a minimal estimate for these animals. We compared these observations with those obtained in other cynomolgus macaques infected with Ebola virus and treated with comparable doses of favipiravir [10]. Interestingly, in these animals the ratio of viral titers to viral load remained unchanged across the different doses of favipiravir and was not lower than in untreated animals (Fig 2). This suggests that the mechanism of action of favipiravir observed here against Lassa virus could be different from what was observed in Ebola infected individuals.

Viral dynamic models

Model building and drug's most likely mechanism of action. The BIC obtained for all tested models are given in S3 Fig. The model assuming an effect of both favipiravir and ribavirin in reducing the proportion of infectious virus (Eq 10b for both drugs) systematically provided a better fit to the data than a model assuming that the favipiravir or ribavirin could block viral production (Eq 10a, S3A & S3D Fig, $\Delta BIC \approx 10$ points in all cases considered). When considering further different levels of sigmoidicity in the concentration effect curve of favipiravir, the best model was obtained with $\kappa = 5$ (Fig 3 and S3E Fig).

We also aimed to understand in more details what were the differences in model predictions according to the putative mechanisms of action of both drugs. Assuming that both drugs block viral production not only deteriorated data fitting criterion (i.e. increased BIC by 10 points) but also provided inconsistent predictions. Indeed, the ratio of infectious virus was increased during treatment and was dose dependent, and this pattern could not be reproduced by a model assuming that treatment reduces the production of virus per infected cell (Fig 2 and S4A Fig). In contrast, assuming an effect in reducing the proportion of infectious virus could recapitulate the effect of treatment on the proportion of infectious virus (S4B Fig). Further, the analysis of the individual parameter estimates showed differences across the treatment groups in the distribution of the proportion of infectious virus, μ (S5 Fig). This is at odds with the fact that μ is not related to treatment, and therefore should be similarly distributed in all groups.

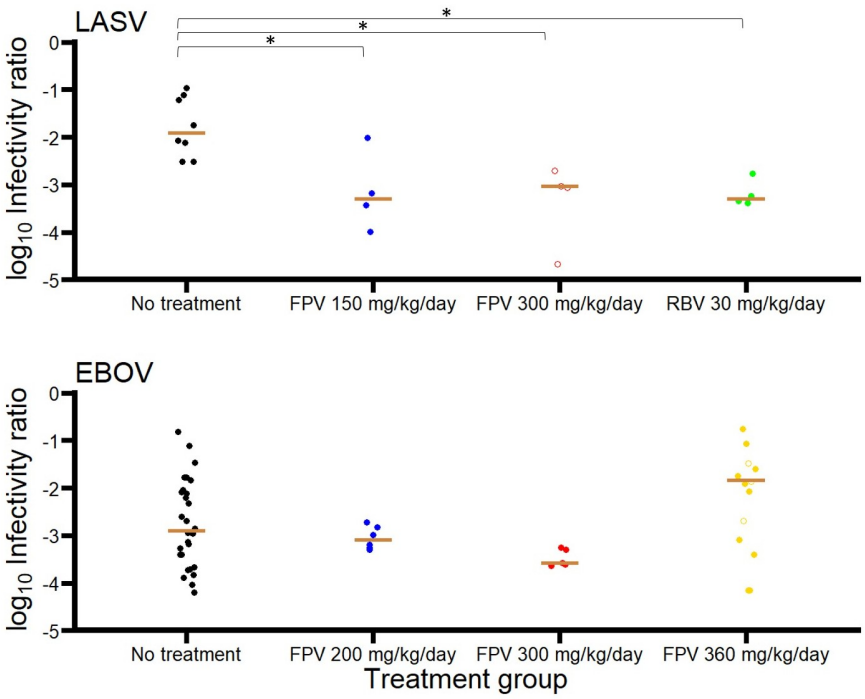

Fig 2. Ratio of titers to viral load at the time of peak viral load in cynomolgus macaques infected with Lassa (top) or Ebola (bottom) virus. The ratio of titers is given by $\log_{10}\left(\frac{TCID_{50}.mL^{-1}}{RNAcopies.mL^{-1}}\right)$. Animals infected with Lassa virus were either untreated (black), treated with FPV 150 mg/kg/day (blue) or 300 mg/kg/day (red), and treated with RBV (green). Similar ratio was calculated in animals infected with Ebola virus that were either untreated, treated with FPV 200 mg/kg/day (blue), FPV 300 mg/kg/day (red), or FPV 360 mg/kg/day. Empty circles correspond to undetectable viral titers imputed to the limit of detection (2 $\log_{10}TCID_{50}.mL^{-1}$). * = $p<0.05$ (Wilcoxon test).

https://doi.org/10.1371/journal.pcbi.1008535.g002

Challenging immune response's mode of action. The refractory model outperformed all other models of immune response (S2 Text), with BIC difference of more than 9 points (S2 Table). Moreover, we verified the necessity of this immune response as well as the effector compartment. Those models showed deteriorated statistical criteria in terms of BIC, with increase of at least 6 points, supporting the use of a refractory response with an effector compartment (S3 Table).

Parameters estimation of best model using model averaging. Next, we took into account the uncertainty on the sigmoidicity of the concentration-effect relationship of favipiravir (see Materials and methods), using the best model determined above. Indeed, the parameter estimates obtained with varying values of κ from 1 to 5 were largely similar, even when the concentration-effect curve was close to an on-off effect ($\kappa = 5$). Overall the model averaging results provided an estimate of the favipiravir and ribavirin EC_{50} of 2.89 (95% CI 1.44-4.55) and 2.97 (95% CI 2.46-3.51) $\mu g.mL^{-1}$, respectively (Table 2). With the PK profile of each drug (S1 Fig), one can calculate the average antiviral efficacy during the course of treatment. At the doses of 150 and 300 mg/kg per day, favipiravir led to average efficacy of 59% and 91% with a sigmoidicity, in reducing virus infectivity. The large level of efficacy in animals treated with 300 mg/kg was sufficient to rapidly drive the infectious virus to the cure boundary after treatment initiation and reproduce extinction of infectious viruses. For ribavirin, the predicted average drug concentration was equal to 3.6 $\mu g.mL^{-1}$ (irrespective of the dosing regimen, see S1B Fig), corresponding to an average efficacy of 40% in reducing virus infectivity. Of note,

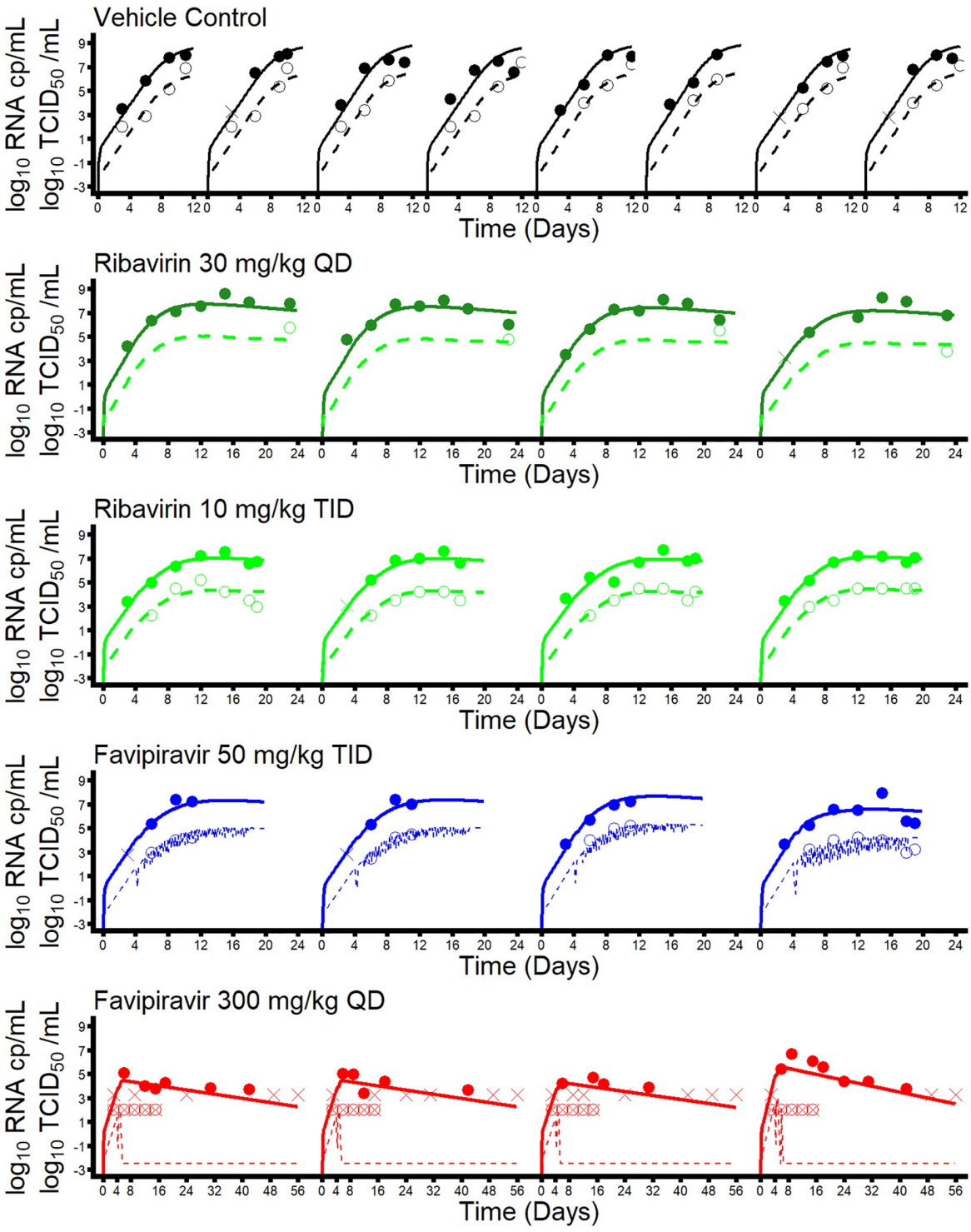

Fig 3. Individual fits of viral load (plain lines) and viral titers (dashed line) for best model considered ($\kappa = 5$). Plain circles represent observed viral loads and empty circles represent observed viral titers. Data below the limit of detection were represented by crosses (viral load) or crossed empty circles (viral titers).

https://doi.org/10.1371/journal.pcbi.1008535.g003

Table 2. Parameters distribution using model averaging (Median, 95% CI).

	Parameter estimates	
Parameter	**Fixed effects (Median, 95% CI)**	**Standard deviation of the random effect (Median, 95% CI)**
R_0	38.6 (37.9-39.3)	0
ϕ (d^{-1})	0.43 (0.31-0.54)	0
δ (10^{-1} d^{-1})	1.1 (1.05-1.12)	0.13 (0.10-0.16)
p (10^4 RNA copies/cell/d)	5.86 (2.01-12.4)	0.33 (0.01-0.65)
θ	121.8 (0-393.7)	0
$EC_{50\,RBV}$ (μg/mL)	2.97 (2.46-3.51)	0
$EC_{50\,FPV}$ (μg/mL)	2.89 (1.44-4.55)	0.95 (0.37-1.50)
μ	0.005 (0.004-0.006)	0
σ_{RNA}(log_{10}RNA copies. mL^{-1})	0.642	-
$\sigma_{TCID_{50}}$(log_{10} $TCID_{50}.mL^{-1}$)	0.571	-
	Fixed parameters	
a (d^{-1})	0.05	-
k (d^{-1})	4	-
c (d^{-1})	20	-
vol (mL)	300	-
T_0 (Cells.mL^{-1})	10^7	-
df (d^{-1})	0.4	-
κ	1-5	-

https://doi.org/10.1371/journal.pcbi.1008535.t002

this estimate of EC_{50} was robust to hypothesis on the mechanism of action and a model assuming an effect of both drugs in blocking viral production led to estimates of drug EC_{50} of 5.82 (95% CI 2.62-9.02) and 5.1 (95% CI 3.92-6.28) μg.mL^{-1} for favipiravir and ribavirin, respectively (S7 Fig).

The model included a compartment for the innate immune response, whose antigen-dependent stimulation render susceptible cells refractory to infection. We estimated that the maximal rate of conversion from susceptible to refractory, ϕ, was equal to 0.43 d^{-1} (95% CI 0.31-0.54). By depleting the compartment of susceptible cells and preventing the infection to start again by reaching the cure boundary, this mechanism explains why viral load does not increase after treatment cessation at D17 (Fig 3 and S6 Fig), even when the efficacy was modest. In all surviving animals, viral load after peak viral load declined slowly which was attributed to a loss rate of infected cells of 0.11 d^{-1} (95% CI 0.105-0.112), corresponding to a half life of 6 days.

Predictions of drug efficacy for human dosing regimens

We simulated the effect of favipiravir and ribavirin on viral dynamics for levels of drug concentrations similar to those obtained with clinical dosing regimens of favipiravir and ribavirin (Fig 4). In the JIKI trial, patients infected with Ebola virus received 1200 mg BID of favipiravir, with residual drug concentrations of 46.1 and 25.9 μg.mL^{-1} respectively 2 and 4 days after treatment initiation, respectively. These dosing regimens would both lead to antiviral efficacy against Lassa infection larger than 99%. Even in the most conservative scenario where only a sigmoidicity of 1 would be considered, these levels are sufficient to achieve an efficacy greater than 90%. For ribavirin, the recommended dosing regimen against Lassa would correspond to drug concentration of 15 μg.mL^{-1} (see Materials and methods), corresponding to an antiviral efficacy of 83%.

As predicted by viral kinetic models [27] the impact of these treatment is larger when it is initiated early in the infection. For instance initiating a treatment at D4 post infection (i.e., at the first detectable viral load) would lead to cure within a day with all concentrations of favipiravir considered. For treatment initiated at D6 or after, treatment may need to be administered for more than 2 weeks to drive the virus to the cure boundary. For ribavirin, the efficacy was sufficient to bend the course of virus and reduce peak viral load, but it was not sufficient to drive the virus towards extinction.

Discussion

We developed the first mathematical model describing LASV viral dynamics during treatment with favipiravir and ribavirin in a non-human primate model of Lassa infection. The comparative approach used to discriminate between drugs modes of action showed that the best description of the data was obtained when both favipiravir and ribavirin were assumed to act reduce the proportion of infectious virus. Our model provided an estimate of the drugs EC_{50}, equal to 2.89 and 2.97 μg.mL^{-1} for favipiravir and ribavirin, respectively. Given the viral dynamic profiles of LASV, our model predicted that favipiravir and ribavirin achieved average drug efficacy of 91 and 40% in reducing infectious virus, respectively.

One of the interest of this study was to compare with results obtained previously in the context of Ebola infection, in a similar animal model of cynomolgus macaques. The *in vivo* EC_{50} identified for favipiravir against Lassa virus was much lower than against Ebola virus (2.97 μg/mL is ribavirin EC50. the correct one is Favipiravir EC50, which is 2.89 μg/mL. vs 200 μg.mL^{-1}, respectively [8]) and was consistent with values found in vitro of 4.6 μg.mL^{-1} [28]. Another interesting observation was the difference in the drug mechanism of action in the two viral infections. Here, the data showed that favipiravir, and ribavirin to a lesser extent, had an effect in reducing the virus infectivity, as measured by the ratio of $TCID_{50}$ to RNA copies (Fig 2). In the context of Ebola and Marburg infection NHP models, favipiravir was associated with an increased virus diversity [10, 16]. A small effect on virus infectivity was reported in [16], but this was not observed in our previous study. Further studies on genomic viruses will be needed to confirm that the strong effect of favipiravir on virus infectivity is also caused by an increased in virus mutagenesis and, if so, what levels of mutagenesis might be associated with "error catastrophe". In our model, the concentration-effect relationship of favipiravir was associated with a high sigmoidicity, suggesting that error catastrophe can only be observed when the drug concentrations passes a critical threshold. Of note, mutagenesis may also increase the risk of emergence of mutations conferring resistance. Resistance to treatment were not observed in NHP models of Ebola and Marburg infections, but patterns of resistance to resistance to favipiravir were identified in in vitro models of influenza infection [29].

Another important finding of our study was the demonstration that ribavirin had an antiviral efficacy in vivo against Lassa infection. Here again the effect passed through a modulation of the infectivity rather than the viral production. In a previous mice model of Lassa infection, we identified an effect of ribavirin in reducing the loss rate of infected cells but no specific antiviral effect [30]. Interestingly and consistent with an effect of ribavirin that would not be purely antiviral, animals treated with ribavirin had a median survival of 20.5 days, as compared to 10 days in animals left untreated or receiving 150 mg/kg/day favipiravir.

To what extent these promising effects translate to clinical setting? Here as well we compared our results with those obtained in Ebola infection, where patients received high doses of favipiravir [31]. The residual drug concentrations of 46.1 or 25.9 μg.mL^{-1} obtained respectively at 2 and 4 days after treatment initiation are more than $10 \times EC_{50}$, and may therefore be sufficient to generate a high antiviral efficacy. Although the pharmacokinetics of favipiravir is

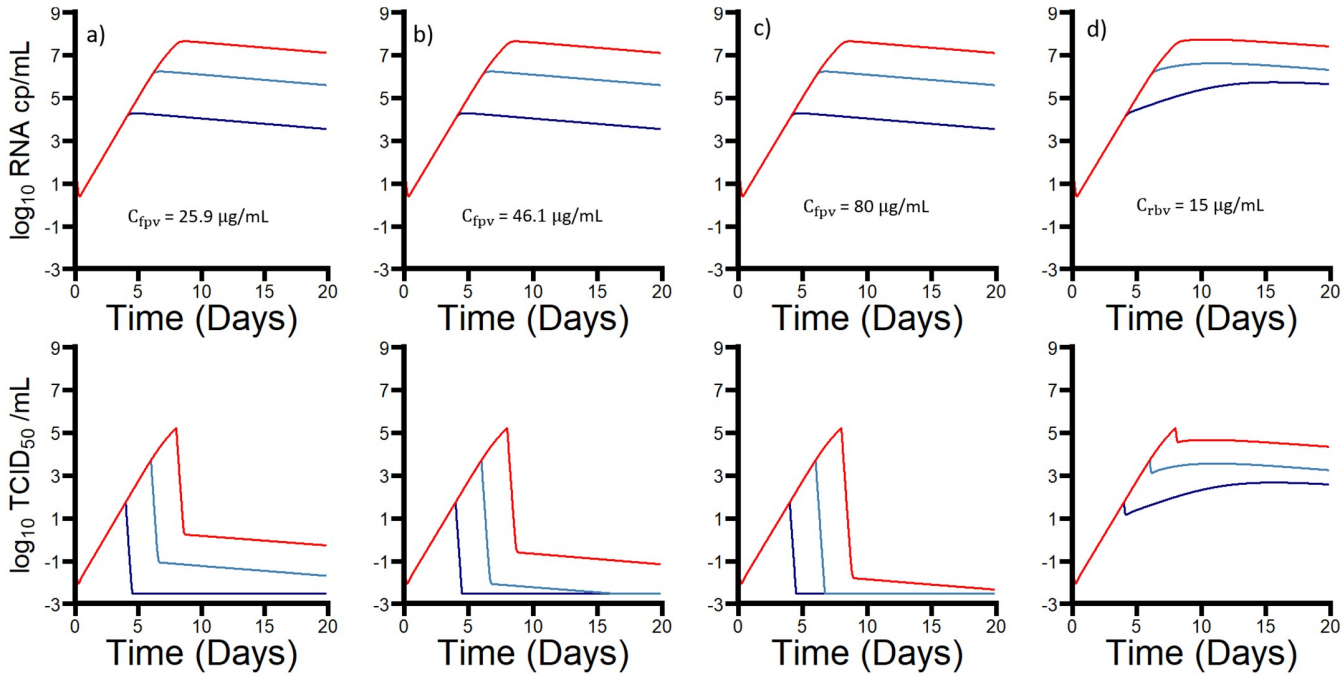

Fig 4. Mutagenesis model simulations. Constant favipiravir plasmatic concentration (a-c) or constant ribavirin plasmatic concentration (d). Treatment started at D4 (navy blue), D6 (blue), or D8 (red).

https://doi.org/10.1371/journal.pcbi.1008535.g004

challenging and that some reductions in drug concentrations may occur over time [25] these results suggest that favipiravir could have a strong antiviral efficacy against Lassa virus. As discussed by we and others, antiviral treatment needs to be initiated before most target cells have been infected (i.e., before peak viral load) to have a large efficacy [8, 24, 27, 32]. By reducing peak viral load, treatment will in addition reduce the antigen stimulation and reduce the risk of a dysregulated immune responses. In clinical setting, the implication of these findings is treatment should be initiated as early as possible [33] and before peak viral load. This is thus a limitation for the translation of our results to human. However, with these levels of efficacy it is possible that viral load may be sufficiently reduced to accelerate the time to viral negativity, as suggested by our simulations (Fig 4). Importantly, the clinical efficacy of ribavirin against Lassa virus has never been demonstrated in clinical trials. Here our results show that ribavirin has a genuine antiviral efficay; at the doses recommended by WHO guidelines (1000 mg every 6 h, [26, 34]), ribavirin may reduce virus infectivity by ≈ 80%. Given the other viral dynamic parameters, this efficacy may not be sufficient to drive the virus to error catastrophe (see Fig 4D). However it may still be relevant to reduce viral growth, lower inflammation and increase survival [8]. It is noteworthy that the mechanism of action of favipiravir may lead to a strong disconnection between the viral load kinetics, as measured by PCR, and the kinetics of infectious virus, measured by $TCID_{50}$. In that respect, the analysis of the viral dynamic should rely on both viral dynamics to precisely measure drug efficacy.

Several limitations need to be kept in mind. First, we assumed that LASV infection occurred only in one compartment. Although this may raise criticism [35], modeling multicompartmental infection will require data that do not exist at this time. We took the liver size as a proxy for the number of infected cells, which is supported by necropsy sampling showing that the liver was the organ having the highest level of viral replication (S8 Fig). Second we used a simple "cure boundary", based on concepts developed in other curable viral infections.

Although this hypothesis could well recapitulate the kinetics observed, the precise estimation of this cure boundary will require specifically designed experiment, such as studies involving shorter and repeated cure of treatments. In fact the existence of this cure boundary may be questioned, and may be more likely a virological control, as low levels of infectious virus were still detected in the liver and the cerebellum of "cured" animals long after treatment cessation (S8 Fig). Finally, and unlike what was done in Ebola infections, our model did not include an adaptive immune response [8]. This is due to the fact that we did not have any data on T or B-cell dynamics. Here our model focused primarily on the innate immune response. Following previous findings in Ebola virus [8], our model assumed an effect of the immune response in rendering cells refractory to infection, that could reflect the effects of IFNα. We also considered several alternative models where an immune compartment could reduce viral infectivity, viral production, or increase the loss rate of free virus and infected cells, and verified the necessity of this immune response as well the presence of an effector compartment (S2 Text), but all alternative models showed deteriorated statistical criteria. Our prediction of the importance of IFNα is in line with *in vitro* [36] and in NHP [37] findings. Finally, and unlike what was done in Ebola infections, we did not incorporate an adaptive immune response in the model. Although IgG and IgM may be detectable 15 days after infection [37], it is noteworthy that the viral load concentrations did not show a rapid decline after peak viral load. Even surviving animals with undetectable viral titers at all times had detectable viral load until 40 days after infection, suggesting a modest role of the adaptive immune response in viral clearance. This immune effector is also known to reduce viral production, however favipiravir and ribavirin acting on the same target probably rendered this mode of action impossible to properly evaluate. Further viral dynamics after peak was characterized by a rather slow decline, suggesting that the adaptive immune response was limited, including in animals treated with high dose favipiravir.

To summarize our results provide the first description of viral dynamics in NHPs infected with Lassa virus. They provide target drug concentrations for ribavirin and favipiravir and strongly suggest that these drugs could be effective in reducing the proportion of infectious virus at dosing regimens relevant in humans.

Supporting information

S1 Fig. Pharmacokinetic models and concentrations predictions of treatments considered. a). Favipiravir model. b). Ribavirin model.
(TIF)

S2 Fig. Model building procedure. Steps of model selection.
(TIFF)

S3 Fig. BIC of models tested throughout model building. A-D) Step 1. A) FPV and RBV blocking production. B) FPV mutagen, RBV blocking production. C) RBV mutagen, FPV blocking production. D) FPV and RBV mutagens. E) Step 2-3. Mutagenesis model after random effect selection.
(TIF)

S4 Fig. Predictions of titers/RNA at peak RNA viral load. Top: Production blockage model. Bottom: Mutagenesis model. Yellow bars represent observed medians of each group.
(TIF)

S5 Fig. Empirical Bayes estimates of parameter μ. EBEs were obtained using the production blockage model. * = $p < 0.05$. Horizontal lines represent medians by group.
(TIF)

S6 Fig. Evolution of target cells TC, productive infected cells I2, refractory cells R and immune effector F. Black curve: animals receiving vehicle treatment; green: animals treated with RBV; blue: animals treated with FPV 150 mg/kg/day; red: animals treated with FPV 300 mg/kg/day.
(TIF)

S7 Fig. Parameters estimates distributions by model averaging. Top: Production blockage model. Bottom: mutagenesis model.
(TIF)

S8 Fig. Post-mortem RNA viral load by organ. Black: Untreated. Green: Treated by ribavirin. Blue: Treated by low dose favipiravir. Red: Treated by high dose favipiravir.
(TIF)

S1 Table. Pharmacokinetic parameters of favipiravir and ribavirin. Values are estimated population values.
(PDF)

S2 Table. BIC Comparison between modes of action of the immune response. FPV and RBV mutagen agents, $\kappa = 1$.
(PDF)

S3 Table. F compartment assessment. Refractory model with FPV and RBV mutagen agents, $\kappa = 1$.
(PDF)

S1 Text. Favipiravir pharmacokinetic model. Equations for the pharmacokinetic model of favipiravir described in the litterature.
(PDF)

S2 Text. Supplementary models equations. Equations of models tested for model selection.
(PDF)

Acknowledgments

We thank Sylvain Baize (Pasteur Institute) for critical reading of an initial version of the manuscript.

Author Contributions

Formal analysis: Guillaume Lingas.

Investigation: Kyle Rosenke, David Safronetz.

Writing – original draft: Guillaume Lingas.

Writing – review & editing: Jérémie Guedj.

References

1. CDC. Estimated number of Lassa fever cases in West Africa each year Death rate from Ebola Death rate from Lassa fever. 2015.
2. Hallam HJ, Hallam S, Rodriguez SE, Barrett ADTT, Beasley DWCC, Chua A, et al. Baseline mapping of Lassa fever virology, epidemiology and vaccine research and development review-article. npj Vaccines. 2018; 3(1). https://doi.org/10.1038/s41541-018-0049-5 PMID: 29581897

3. Buba MI, Dalhat MM, Nguku PM, Waziri N, Mohammad JO, Bomoi IM, et al. Mortality Among Confirmed Lassa Fever Cases During the 2015–2016 Outbreak in Nigeria. American Journal of Public Health. 2018; 108(2):262–264. https://doi.org/10.2105/AJPH.2017.304186 PMID: 29267063

4. Fichet-Calvet E, Rogers DJ. Risk maps of lassa fever in West Africa. PLoS Neglected Tropical Diseases. 2009; 3(3). https://doi.org/10.1371/journal.pntd.0000388 PMID: 19255625

5. World Health Organization, Lassa Fever;. https://www.who.int/news-room/fact-sheets/detail/lassa-fever.

6. Jahbrlsg PB, Hesse RA, Eddy GA, Johnsotn KM, Catlls RT, Stephen EL, et al. Lassa Virus Infection of Rhesus Monkeys: Pathogenesis and Treatment with Ribavirin. 1980; 141(5):580–589.

7. Lee DU, Je SH, Yoo SJ, Kwon T, Shin JY, Byun JJ, et al. Hematological adverse effects and pharmacokinetics of ribavirin in pigs following intramuscular administration. Journal of Veterinary Pharmacology and Therapeutics. 2017; 40(5):561–568. https://doi.org/10.1111/jvp.12394 PMID: 28205288

8. Madelain V, Baize S, Jacquot F, Reynard S, Fizet A, Barron S, et al. Ebola viral dynamics in nonhuman primates provides insights into virus immuno-pathogenesis and antiviral strategies. Nature Communications. 2018; 9(1):1–11. https://doi.org/10.1038/s41467-018-06215-z PMID: 30275474

9. Bixler SL, Bocan TM, Wells J, Wetzel KS, Tongeren SAV, Dong L, et al. Efficacy of favipiravir (T-705) in nonhuman primates infected with Ebola virus or Marburg virus. Antiviral Research. 2018; 151:97–104. https://doi.org/10.1016/j.antiviral.2017.12.021 PMID: 29289666

10. Guedj J, Piorkowski G, Jacquot F, Madelain V, Nguyen THT, Rodallec A, et al. Antiviral efficacy of favipiravir against Ebola virus: A translational study in cynomolgus macaques. PLoS Medicine. 2018; 15 (3):1–21. https://doi.org/10.1371/journal.pmed.1002535 PMID: 29584730

11. Rosenke K, Feldmann H, Westover JB, Hanley PW, Martellaro C, Feldmann F, et al. Use of favipiravir to treat lassa virus infection in Macaques. Emerging Infectious Diseases. 2018; 24(9):1696–1699. https://doi.org/10.3201/eid2409.180233 PMID: 29882740

12. Shurtleff AC, Warren TK, Bavari S. Nonhuman primates as models for the discovery and development of ebolavirus therapeutics. Expert Opinion on Drug Discovery. 2011; 6(3):233–250. https://doi.org/10.1517/17460441.2011.554815 PMID: 22647202

13. Madelain V, Guedj J, Mentré F, Nguyen THT, Jacquot F, Oestereich L, et al. Favipiravir Pharmacokinetics in Nonhuman Primates and Insights for Future Efficacy Studies of Hemorrhagic Fever Viruses. Antimicrobial Agents and Chemotherapy. 2017; 61(1). https://doi.org/10.1128/AAC.01305-16 PMID: 27736754

14. Arias A, Thorne L, Goodfellow I. Favipiravir elicits antiviral mutagenesis during virus replication in vivo. eLife. 2014; 3:e03679. https://doi.org/10.7554/eLife.03679 PMID: 25333492

15. Escribano-Romero E, Jiménez de Oya N, Domingo E, Saiz JC. Extinction of West Nile Virus by Favipiravir through Lethal Mutagenesis. Antimicrobial Agents and Chemotherapy. 2017; 61(11). https://doi.org/10.1128/AAC.01400-17 PMID: 28848019

16. Espy N, Nagle E, Pfeffer B, Garcia K, Chitty AJ, Wiley M, et al. T-705 induces lethal mutagenesis in Ebola and Marburg populations in macaques. Antiviral Research. 2019; 170(May):104529. https://doi.org/10.1016/j.antiviral.2019.06.001 PMID: 31195019

17. Best K, Perelson AS. Mathematical modeling of within-host Zika virus dynamics. Immunological Reviews. 2018; 285(1):81–96. https://doi.org/10.1111/imr.12687 PMID: 30129207

18. Best K, Guedj J, Madelain V, de Lamballerie X, Lim SY, Osuna CE, et al. Zika plasma viral dynamics in nonhuman primates provides insights into early infection and antiviral strategies. Proceedings of the National Academy of Sciences. 2017; 114(33):8847–8852. https://doi.org/10.1073/pnas.1704011114 PMID: 28765371

19. Perelson AS, Guedj J. Modelling hepatitis C therapy-predicting effects of treatment. Nature Reviews Gastroenterology and Hepatology. 2015; 12(8):437–445. https://doi.org/10.1038/nrgastro.2015.97 PMID: 26122475

20. Lin Cc, Yeh Lt, Luu T, Lourenco D, Johnson JYNL. Pharmacokinetics and Metabolism of [14 C] Ribavirin in Rats and Cynomolgus Monkeys. 2003; 47(4):1395–1398.

21. Kuhn E, Lavielle M. Maximum likelihood estimation in nonlinear mixed effects models. Computational Statistics and Data Analysis. 2005; 49(4):1020–1038. https://doi.org/10.1016/j.csda.2004.07.002

22. Samson A, Lavielle M, Mentré F. Extension of the SAEM algorithm to left-censored data in nonlinear mixed-effects model: Application to HIV dynamics model. Computational Statistics & Data Analysis. 2006; 51(3):1562–1574. https://doi.org/10.1016/j.csda.2006.05.007

23. Thiébaut R, Guedj J, Jacqmin-Gadda H, Chêne G, Trimoulet P, Neau D, et al. Estimation of dynamical model parameters taking into account undetectable marker values. BMC Medical Research Methodology. 2006; 6(1):38. https://doi.org/10.1186/1471-2288-6-38 PMID: 16879756

24. Gonçalves A, Mentré F, Lemenuel-Diot A, Guedj J. Model Averaging in Viral Dynamic Models. AAPS Journal. 2020; 22(2):1–11. PMID: 32060662

25. Nguyen THT, Guedj J, Anglaret X, Laouénan C, Madelain V, Taburet AM, et al. Favipiravir pharmacokinetics in Ebola-Infected patients of the JIKI trial reveals concentrations lower than targeted. PLoS Neglected Tropical Diseases. 2017; 11(2):1–18. https://doi.org/10.1371/journal.pntd.0005389 PMID: 28231247

26. Bausch D, Hadi C, Khan S, Lertora JL. Review of the Literature and Proposed Guidelines for the Use of Oral Ribavirin as Postexposure Prophylaxis for Lassa Fever. Clinical Infectious Diseases. 2010; 51 (12):1435–1441. https://doi.org/10.1086/657315 PMID: 21058912

27. Friberg LE, Guedj J. Acute bacterial or viral infection—What's the difference? A perspective from PKPD modellers. Clinical Microbiology and Infection. 2020. https://doi.org/10.1016/j.cmi.2019.12.008

28. Oestereich L, Rieger T, Lüdtke A, Ruibal P, Wurr S, Pallasch E, et al. Efficacy of Favipiravir Alone and in Combination With Ribavirin in a Lethal, Immunocompetent Mouse Model of Lassa Fever. The Journal of Infectious Diseases. 2015; 213(6):934–938. https://doi.org/10.1093/infdis/jiv522 PMID: 26531247

29. Goldhill DH, Te Velthuis AJW, Fletcher RA, Langat P, Zambon M, Lackenby A, et al. The mechanism of resistance to favipiravir in influenza. Proceedings of the National Academy of Sciences of the United States of America. 2018; 115(45):11613–11618. https://doi.org/10.1073/pnas.1811345115 PMID: 30352857

30. Carrillo-Bustamante P, Nguyen THT, Oestereich L, Günther S, Guedj J, Graw F. Determining Ribavirin's mechanism of action against Lassa virus infection. Scientific Reports. 2017; 7(1):1–12. https://doi.org/10.1038/s41598-017-10198-0 PMID: 28916737

31. Sissoko D, Laouenan C, Folkesson E, M'Lebing AB, Beavogui AH, Baize S, et al. Experimental Treatment with Favipiravir for Ebola Virus Disease (the JIKI Trial): A Historically Controlled, Single-Arm Proof-of-Concept Trial in Guinea. PLoS Medicine. 2016; 13(3):1–36. https://doi.org/10.1371/journal.pmed.1001967

32. Hadjichrysanthou C, Cauët E, Lawrence E, Vegvari C, De Wolf F, Anderson RM. Understanding the within-host dynamics of influenza A virus: From theory to clinical implications. Journal of the Royal Society Interface. 2016; 13(119). https://doi.org/10.1098/rsif.2016.0289 PMID: 27278364

33. Okokhere P, Colubri A, Azubike C, Iruolagbe C, Osazuwa O, Tabrizi S, et al. Clinical and laboratory predictors of Lassa fever outcome in a dedicated treatment facility in Nigeria: a retrospective, observational cohort study. The Lancet Infectious Diseases. 2018; 18(6):684–695. https://doi.org/10.1016/S1473-3099(18)30121-X PMID: 29523497

34. WHO. Clincial Management of Patients with Viral Haemorrhagic Fever: A Pocket Guide for the Front-line Health Worker. World Health Organization. 2016; p. 1–191.

35. Chertow DS, Shekhtman L, Lurie Y, Davey RT, Heller T, Dahari H. Modeling Challenges of Ebola Virus–Host Dynamics during Infection and Treatment. Viruses. 2020; 12(1). https://doi.org/10.3390/v12010106 PMID: 31963118

36. Baize S, Pannetier D, Faure C, Marianneau P, Marendat I, Georges-Courbot MC, et al. Role of interferons in the control of Lassa virus replication in human dendritic cells and macrophages. Microbes and Infection. 2006; 8(5):1194–1202. https://doi.org/10.1016/j.micinf.2006.02.002 PMID: 16621649

37. Baize S, Marianneau P, Loth P, Reynard S, Journeaux A, Chevallier M, et al. Early and strong immune responses are associated with control of viral replication and recovery in lassa virus-infected cynomolgus monkeys. Journal of virology. 2009; 83(11):5890–5903. https://doi.org/10.1128/JVI.01948-08 PMID: 19297492

Annexe 2 : Favipiravir antiviral efficacy against SARS-CoV-2 in a hamster model, *Nature Communications*, 2021

nature COMMUNICATIONS

ARTICLE

https://doi.org/10.1038/s41467-021-21992-w OPEN

Favipiravir antiviral efficacy against SARS-CoV-2 in a hamster model

Jean-Sélim Driouich[1,5], Maxime Cochin[1,5], Guillaume Lingas[2], Grégory Moureau[1], Franck Touret[1], Paul-Rémi Petit[1], Géraldine Piorkowski[1], Karine Barthélémy[1], Caroline Laprie[3], Bruno Coutard[1], Jérémie Guedj[2], Xavier de Lamballerie[1], Caroline Solas[1,4] & Antoine Nougairède[1✉]

Despite no or limited pre-clinical evidence, repurposed drugs are massively evaluated in clinical trials to palliate the lack of antiviral molecules against SARS-CoV-2. Here we use a Syrian hamster model to assess the antiviral efficacy of favipiravir, understand its mechanism of action and determine its pharmacokinetics. When treatment is initiated before or simultaneously to infection, favipiravir has a strong dose effect, leading to reduction of infectious titers in lungs and clinical alleviation of the disease. Antiviral effect of favipiravir correlates with incorporation of a large number of mutations into viral genomes and decrease of viral infectivity. Antiviral efficacy is achieved with plasma drug exposure comparable with those previously found during human clinical trials. Notably, the highest dose of favipiravir tested is associated with signs of toxicity in animals. Thereby, pharmacokinetic and tolerance studies are required to determine whether similar effects can be safely achieved in humans.

[1] Unité des Virus Émergents, UVE: Aix Marseille Univ, IRD 190, INSERM 1207, Marseille, France. [2] Université de Paris, IAME, INSERM, Paris, France. [3] Laboratoire Vet-Histo, Marseille, France. [4] Laboratoire de Pharmacocinétique et Toxicologie, Hôpital La Timone, APHM, Marseille, France. [5] These authors contributed equally: Jean-Sélim Driouich, Maxime Cochin. ✉email: antoine.nougairede@univ-amu.fr

In March 2020, the World Health Organization declared coronavirus disease 2019 (COVID-19) a pandemic[1]. The COVID-19 outbreak was originally identified in Wuhan, China, in December 2019 and spread rapidly around the world within a few months. The severe acute respiratory syndrome coronavirus 2 (SARS-CoV-2), the causative agent of COVID-19, belongs to the *Coronaviridae* family and is closely related to the SARS-CoV, which emerged in China in 2002[2]. After an incubation period of about 5 days, disease onset usually begins with an influenza-like syndrome associated with high virus replication in respiratory tracts[3,4]. In some patients, a late acute respiratory distress syndrome, associated with high levels of inflammatory proteins, occurs within one to two weeks[3]. As of 11 November 2020, more than 90 million cases of COVID-19 have resulted in more than 1,936,000 deaths[5]. In the face of this ongoing pandemic and its unprecedented repercussions, not only on human health but also on society, ecology and economy, there is an urgent need for effective infection prevention and control measures.

Whilst host-directed and immune-based therapies could prove useful for the clinical management of critically ill patients, the availability of safe and effective antiviral molecules would represent an important step toward fighting the current pandemic. As conventional drug development is a slow process, repurposing of drugs already approved for any indication was extensively explored and led to the implementation of many clinical trials for the treatment of COVID-19[6]. However, the development of effective antiviral drugs for the treatment of COVID-19, should, as much as possible, rely on robust pre-clinical in vivo data, not only on efficacy generated in vitro. Accordingly, rapid implementation of rodent and non-human primate animal models should help to assess more finely the potential safety and efficacy of drug candidates and to determine appropriated dose regimens in humans[7,8].

Favipiravir (6-fluoro-3-hydroxypyrazine-2-carboxamine) is an anti-influenza drug approved in Japan that has shown broad-spectrum antiviral activity against a variety of other RNA viruses[9–15]. Favipiravir is a prodrug that is metabolized intracellularly into its active ribonucleoside 5′-triphosphate form that acts as a nucleotide analog to selectively inhibit RNA-dependent RNA polymerase and induce lethal mutagenesis[16,17]. Recently, several studies reported in vitro inhibitory activity of favipiravir against SARS-CoV-2 with 50% effective concentrations (EC_{50}) ranging from 62 to > 500 µM (10 to > 78 µg/mL)[18–20]. Based on these results, more than 20 clinical trials on the management of COVID-19 by favipiravir are ongoing (https://clinicaltrials.gov/).

In the present study, we evaluate the efficacy of favipiravir in vitro and using a Syrian hamster model (*Mesocricetus auratus*). Our results show that preventive or preemptive administration of high doses favipiravir induce significant reduction of infectious titers and histopathological damages in lungs and clinical alleviation of the disease. Analysis of genetic diversity of viral populations in lungs also confirms the mutagenic effect of favipiravir.

Results

In vitro efficacy of favipiravir. Using VeroE6 cells and an antiviral assay based on reduction of cytopathic effect (CPE), we recorded EC_{50} and EC_{90} of 204 and 334 µM using a multiplicity of infection (MOI) of 0.001, 446, and > 500 µM with an MOI of 0.01 (Table 1 and Supplementary Fig. 1) in accordance with previous studies[18–20]. Infectious titer reductions (fold change in comparison with untreated cells) were ≥ 2 with 125 µM of favipiravir and ranged between 11 and 342 with 500 µM. Using Caco-2 cells, which do not exhibit CPE with SARS-CoV-2 BavPat1 strain, infectious titer reductions were around 5 with 125 µM of favipiravir and ranged between 144 and 7721 with 500 µM of the drug. 50% cytotoxic concentrations (CC_{50}) in VeroE6 and Caco-2 cells were > 500 µM.

Infection of Syrian hamsters with SARS-CoV-2. Following Chan et al., we implemented a hamster model to study the efficacy of antiviral compounds[7]. Firstly, we intranasally infected 4-week-old female Syrian hamsters with 10^6 $TCID_{50}$ of virus. Groups of two animals were sacrificed 2, 3, 4, and 7 days post-infection (dpi). Viral replication was quantified in sacrificed animals by RT-qPCR in organs (lungs, brain, liver, small/large bowel, kidney, spleen, and heart) and plasma. Viral loads in lungs peaked at 2 dpi, remained elevated until 4 dpi and dramatically decreased at 7 dpi (Supplementary 2). Viral loads in plasma peaked at 3 dpi and viral replication was detected in the large bowel at 2 dpi (Supplementary Fig. 2 and Supplementary Data 1). No viral RNA was detected in almost all the other samples tested (Supplementary Data 1). Subsequently, we infected animals with two lower virus inocula (10^5 and 10^4 $TCID_{50}$). Viral RNA was quantified in lungs, large bowel, and plasma from sacrificed animals 2, 3, 4, and 7 dpi (Supplementary Fig. 2 and Supplementary Data 1). Viral loads in lungs peaked at 2 and 3 dpi with inocula of 10^5 and 10^4 $TCID_{50}$, respectively. Maximum viral loads in lungs of animals infected with each virus inoculum were comparable. Viral RNA yields in plasma and large bowel followed a similar trend but with more variability, with this two lower inocula. In addition, clinical monitoring of animals showed no marked symptoms of infection but normalized weights (i.e., % of initial weights) significantly lower from 3 dpi when compared to animals intranasally inoculated with sodium chloride 0.9% (Supplementary Fig. 2).

In vivo efficacy of favipiravir. To assess the efficacy of favipiravir, hamsters received the drug, intraperitoneally, three times a day (TID). We used three doses of favipiravir: 18.75, 37.5, and 75 mg/day (corresponding to 340 ± 36, 670 ± 42 and 1390 ± 126 mg/kg/day, respectively).

In a first set of experiments, treatment was initiated at the day of infection (preemptive antiviral therapy) and ended at 2 dpi. We infected groups of 6 animals intranasally with three virus inocula (10^6, 10^5, and 10^4 $TCID_{50}$) and viral replication was measured in lungs and plasma at 3 dpi (Fig. 1a). Each virus inoculum was assessed in an independent experiment. When analysis of virus replication in clarified lung homogenates was based on infectious titers (as measured using $TCID_{50}$ assay), the effect of favipiravir in reducing infectious titers was dose dependent, in particular when low virus inocula were used to infect animals (Fig. 1b). At each virus inoculum, mean infectious titers for groups of animals treated with 75 mg/day TID were significantly lower than those observed with untreated groups ($p \le 0.0001$): reduction of infectious titers ranged between 1.9 and 3.7 $\log_{10}$. For animals infected with 10^5 or 10^4 $TCID_{50}$, significant infectious titer reductions of around 0.8 $\log_{10}$ were also observed with the dose of 37.5 mg/day TID ($p \le 0.038$). Drug 90 and 99% effective doses (ED_{90} and ED_{99}) were estimated based on these results and ranged between 31–42 mg/day and 53–70 mg/day, respectively (Table 2). When analysis of virus replication in clarified lung homogenates were assessed on viral RNA yields (as measured using quantitative real-time RT-PCR assay), significant differences with groups of untreated animals, ranging between 0.7 and 2.5 $\log_{10}$, were observed only with the higher dose of favipiravir ($p \le 0.012$). Once again, this difference was more noticeable with lower virus inocula (Fig. 1c). Since we found higher reductions of infectious titers than those observed with viral RNA yields, we estimated the relative infectivity of viral particle (i.e., the ratio of

Table 1 In vitro efficacy of favipiravir.

Cell line	MOI	Drug effective concentration[a]		Infectious titer reduction[b]		
		EC_{50}	EC_{90}	125 µM	250 µM	500 µM
Vero E6	0.001	204 µM	334 µM	2.2	13.2	341.9
	0.01	446 µM	>500 µM	2.0	5.7	10.9
Caco-2	0.001	na	na	5.6	137.4	7720.8
	0.01	na	na	4.0	7.2	144.0

MOI multiplicity of infection, *na* not applicable.
[a]Estimated from dose-response curves of antiviral activity (Supplementary Fig. 1).
[b]Calculated using mean infectious titers without favipiravir (virus control).

the number of infectious particles over the number of viral RNA molecules). Decreased infectivity was observed in all treated groups of animals. These differences were always significant with the higher dose of favipiravir ($p \le 0.031$) and were significant with the dose of 37.5 mg/day TID for animals infected with 10^5 or 10^4 $TCID_{50}$ of virus ($p \le 0.041$) (Fig. 1d). We then measured plasma viral loads using quantitative real-time RT-PCR assay and found, with the higher dose of favipiravir and the groups of animals infected with 10^6 or 10^4 $TCID_{50}$, significant reductions of 2.1 and 2.62 log_{10}, respectively ($p \le 0.022$) (Fig. 1e). Finally, signs of toxicity were observed with animal treated with the dose of 75 mg/day TID: normalized weights were significantly lower than those of untreated animals (Fig. 1f).

In a second set of experiments, we assessed, over a period of 7 days, the impact of the preemptive therapy on the clinical course of the disease using weight as the primary criterion (Fig. 2a). Since signs of toxicity were noticed during the first set of experiments, we evaluated the toxicity of the three doses of favipiravir with groups of four non-infected animals treated during four days (Fig. 2b). Important toxicity was observed with the dose of 75 mg/day TID with, from the first day of treatment, normalized weights significantly lower than those of untreated animals (Supplementary Data 5). We also found a constant, but moderate, toxicity with the dose of 37.5 mg/day TID that was significant at day 4, 5, and 6 only. No toxicity was detected with the lower dose of favipiravir. To assess if the toxicity observed with the highest dose of favipiravir was exacerbated by the infection, we compared normalized weights of infected and non-infected animals treated with the dose of 75 mg/day TID. Regardless of the virus inoculum, no significant difference was observed at 1, 2, and 3 dpi (Supplementary Fig. 4). After this evaluation of favipiravir toxicity, we intranasally infected groups of 10 animals with two virus inocula (10^5 or 10^4 $TCID_{50}$). Each virus inoculum was assessed in an independent experiment. Treatment with a dose of 37.5 mg/day TID was initiated on the day of infection (preemptive antiviral therapy) and ended at 3 dpi (Fig. 2a). With both virus inocula, treatment was associated with clinical alleviation of the disease (Fig. 2c, d). With the inoculum of 10^5 $TCID_{50}$, mean weights of treated animals were significantly higher than those of untreated animals at 5 and 6 dpi ($p \le 0.031$). Similar observations were made with the inoculum of 10^4 $TCID_{50}$ at 5, 6, and 7 dpi ($p < 0.0001$).

In a third set of experiments, treatment was started 1 day before infection (preventive antiviral therapy) and ended at 2 dpi. We intranasally infected groups of 6 animals with 10^4 $TCID_{50}$ of virus and viral replication was measured in lungs and plasma at 3 dpi (Fig. 3a). Once again, an inverse relationship was observed between lung infectious titers and the dose of favipiravir (Fig. 3b). Mean infectious titers for groups of animals treated with 37.5 and 75 mg/day TID were significantly lower than those observed with untreated groups ($p \le 0.002$). Of note, undetectable infectious titers were found for all animals treated with the higher dose. Estimated ED_{90} and ED_{99} were 35 and 47 mg/day, respectively (Table 2). Significant reductions of viral RNA yields of 0.9 and 3.3 log_{10}, were observed with animals treated with 37.5 and 75 mg/day TID, respectively ($p \le 0.023$) (Fig. 3c). Resulting infectivity of viral particle was decreased, with a significant reduction only for the higher dose of favipiravir ($p = 0.005$) (Fig. 3e). Finally, we found significantly reduced plasma viral loads with animals treated with 37.5 and 75 mg/day TID ($p \le 0.005$) (Fig. 3f). Once again, signs of toxicity were observed with animal treated with the dose of 75 mg/day TID: normalized weights were significantly lower than those of untreated animals (Fig. 3d).

In a last set of experiments, we assessed the impact of favipiravir treatment on lung pathological changes induced by SARS-CoV-2. Animals were intranasally infected with 10^4 $TCID_{50}$ of virus. Treatment with two doses of favipiravir (37.5 and 75 mg/day TID) was initiated one day before infection (preventive antiviral therapy) or at day of infection (preemptive antiviral therapy) and ended at 3 dpi. For each therapeutic strategy and for each dose of favipiravir, a group of four animals was sacrificed at 3 and 5 dpi (Fig. 4a and c). As a control, we used four vehicle-treated groups of four animals (one at 3 dpi and one at 5 dpi for each therapeutic strategy). Based on the severity of inflammation, alveolar hemorrhagic necrosis and vessel lesions, a cumulative score from 0 to 10 was calculated and assigned to a grade of severity (0 = normal; 1 = mild; 2 = moderate; 3 = marked and 4 = severe; details in Supplementary Data 7). Overall, lungs of untreated animals displayed typical lesions of air-borne infection (i.e., broncho-interstitial pneumonia), with a progression between 3 dpi and 5 dpi that reflects the virus dissemination within the respiratory tree as previously demonstrated[7,21]. At 3 dpi, 7/8 untreated animals displayed mild pulmonary pathological changes (Fig. 4b and d) leading to difficulty to assess the efficacy of the treatment even if almost all mean cumulative scores of treated animals were significantly lower than those of untreated groups. In contrast, at 5 dpi all untreated animals displayed severe pulmonary impairments and we observed a dose-dependent effect of favipiravir (Fig. 4b and d). When using a preemptive antiviral strategy, all animals treated with 37.5 mg/day TID had marked histopathological damages in lungs and animals treated with 75 mg/day TID displayed mild or moderate histopathological damages (Supplementary Fig. 5). When using a preventive antiviral strategy, all animals treated with 37.5 mg/day TID had mild to marked damages in lung and animals treated with 75 mg/day TID displayed no or mild histopathological damages (Fig. 4e–h). At 5 dpi, significant cumulative score reductions were observed with both doses of favipiravir regardless the therapeutic strategy used ($p = 0.0286$, details in Supplementary Data 8).

Favipiravir pharmacokinetics (PK) in a hamster model. We first assessed the PK and lung distribution of favipiravir in a subgroup of uninfected animals. Groups of animals were treated

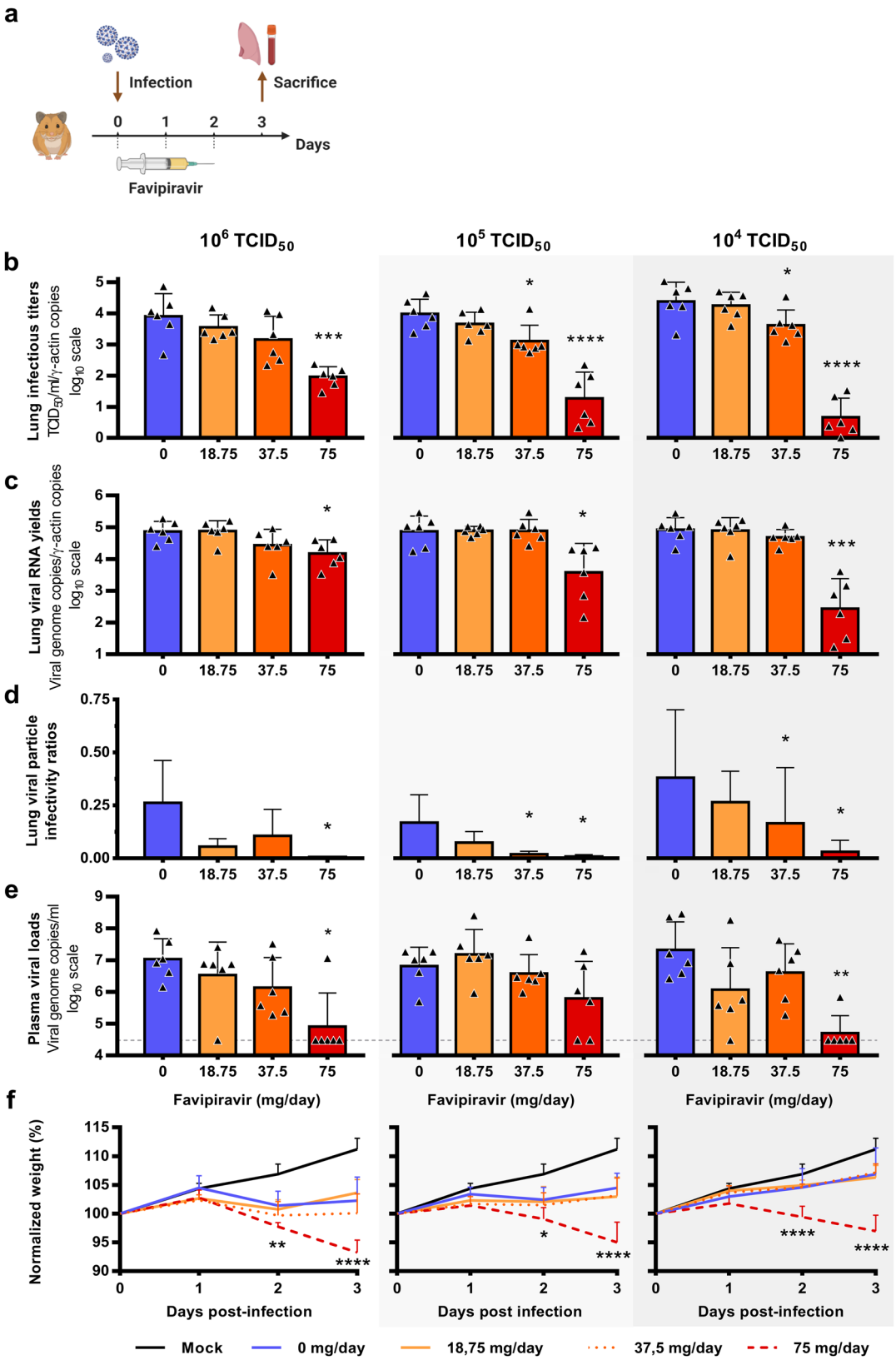

respectively with a single dose of favipiravir administrated intraperitoneally: 6.25 mg, 12.5 mg, and 25 mg. In each dose group, we sacrificed three animals at specific time points post-treatment (0.5, 1, 5 or 8 h) for determination of favipiravir in plasma. Drug concentration in lung tissue was determined at 0.5 and 5 h post-treatment. Subsequently, we assessed the favipiravir concentration after multiple dose in animals intranasally infected with 10^5 $TCID_{50}$ of virus. Groups of nine animals received the three doses evaluated for 3 days (Fig. 1): 18.75 mg/day, 37.5 mg/day or 75 mg/day TID and were sacrificed at 12-h after the last treatment dose. Favipiravir trough concentrations were quantified in plasma ($n = 9$) and lung tissue ($n = 3$).

Fig. 1 Virological results with preemptive favipiravir therapy. a Experimental timeline. Groups of 6 hamsters were intranasally infected with 10^6, 10^5 or 10^4 $TCID_{50}$ of virus. **b** Viral replication in lung based on infectious titers (measured using a $TCID_{50}$ assay) expressed in $TCID_{50}$/copy of ɣ-actine gene ($n = 6$ animals/group). **c** Viral replication in lung based on viral RNA yields (measured using an RT-qPCR assay) expressed in viral genome copies/copy of ɣ-actine gene ($n = 6$ animals/group). **d** Relative lung viral particle infectivities were calculated as follows: ratio of lung infectious titer over viral RNA yields ($n = 6$ animals/group). **e** Plasma viral loads (measured using an RT-qPCR assay) are expressed in viral genome copies/mL of plasma (the dotted line indicates the detection threshold of the assay) ($n = 6$ animals/group). **f** Clinical course of the disease ($n = 6$ animals/group). Normalized weight at day n was calculated as follows: % of initial weight of the animal at day n. Data represent mean ± SD (details in Supplementary Data 2). Two-sided statistical analysis were performed using Shapiro–Wilk normality test, Student t-test, Mann–Whitney test, Welch's test, and two-way ANOVA with Post-hoc Dunnett's multiple comparisons test (details in Supplementary Data 3 and 4). ****, ***, ** and * symbols indicate that the average value for the group is significantly lower than that of the untreated group with a p-value < 0.0001, ranging between 0.0001–0.001, 0.001–0.01, and 0.01–0.05, respectively. Source data are provided as a Source data file.

Table 2 Drug effective doses (ED) on reducing viral titers according to the level of viral inoculum.

Virus inoculum	ED_{50} mg/day (95% CI[a])	ED_{90} mg/day (95% CI[a])	ED_{99} mg/day (95% CI[a])
Preemptive therapy			
10^4 $TCID_{50}$	34 (30–37)	42 (38–46)	53 (48–58)
10^5 $TCID_{50}$	26 (21–30)	37 (31–44)	56 (46–65)
10^6 $TCID_{50}$	15 (10–20)	31 (21–41)	70 (48–93)
Preventive therapy			
10^4 $TCID_{50}$	27 (25–29)	35 (32–38)	47 (44–51)

Dose–response curves are presented in Supplementary Fig. 3.
[a]95% confidence interval.

Results are presented in Table 3 and Supplementary Fig. 7. The single dose PK analysis showed that the maximum concentration of favipiravir was observed at 0.5 h at all doses, then plasma drug concentrations decreased exponentially to reach concentrations below 10 µg/ml at 12 h. Favipiravir PK exhibited a non-linear increase in concentration between the doses. After multiple doses, trough concentrations (12 h) of favipiravir also exhibited a non-linear increase between doses. The extrapolated 12 h post-treatment concentrations after a single dose were calculated in order to determine the accumulation ratio. Accumulation ratios were respectively 6, 16, and 21 at the three doses, confirming the non-proportional increase between doses. The average concentration after single dose administration over 0–12-h intervals was calculated and the respective values obtained were 10.1 µg/mL, 38.7 µg/mL, and 100.5 µg/mL for the three favipiravir doses.

Favipiravir lung concentrations were 1.6–2.7-fold lower than in plasma for both administration of single and multiple doses. After a single dose, the mean lung to plasma ratio ranged from 0.37 to 0.62 according to the time post-treatment and was similar between the three doses of favipiravir at 0.5 h. A high ratio 5 h post-treatment was observed at the highest dose (25 mg) with an increase by a factor 1.6–1.8 compared with the lower doses. After multiple doses, the lung penetration of favipiravir was confirmed with a mean lung to plasma ratio ranging from 0.35 to 0.44. Favipiravir was not detected in the lungs at the lowest dose (18.75 mg/day).

Mutagenic effect of favipiravir. To understand which genomic modifications accompanied favipiravir treatment, direct complete genome sequencing of clarified lung homogenates from animals intranasally infected with 10^6 $TCID_{50}$ of virus and treated with the two highest doses of drug (preemptive antiviral therapy; Fig. 1) was performed. Data were generated by next-generation sequencing from lung samples of four animals per group (untreated, 37.5 mg/day TID and 75 mg/day TID). The mean sequencing coverage for each sample ranged from 10,991 to 37,991 reads per genomic position and we subjected substitutions with a frequency ≥ 1% to further analysis. The genetic variability in virus stock was also analyzed: 14 nucleotide polymorphisms were detected of which 5 recorded a mutation frequency higher than 10% (Supplementary Data 10).

In order to study the mutagenic effect of favipiravir, we used the consensus sequence from virus stock as reference and all the mutations simultaneously detected in a lung sample and in virus stock were not considered in the further analysis (1–4 mutations per sample, see Supplementary Data 10). Overall, no majority mutations were detected (mutation frequency > 50%), and almost all of the mutations occurred at a frequency lower than 10% (Fig. 5a). In addition, mutations were distributed throughout the whole genome (Fig. 5b).

Results revealed a relationship between the number of mutations detected per sample and the dose of favipiravir (Fig. 5c): the mean number of mutations increased by a factor 2 and 4.8 with groups of animals treated with 37.5 and 75 mg/day, TID respectively. The difference is significant only with a dose of 37.5 mg/day TID ($p = 0.029$). This increase of the number of mutations is mainly the consequence of the occurrence of a large number of G → A substitutions and, to a lesser extent, C → U substitutions. Consequently, regardless of the dose of favipiravir, mean frequency of G → A substitutions was significantly increased by a factor of 4.2 ($p \leq 0.009$). This rise of these transition mutations led to increased frequency of all transition mutations (significant only at dose of 37.5 mg/day TID; $p = 0.037$) and increased frequency of non-synonymous mutations (significant only at dose of 75 mg/day TID; $p = 0.009$) (Fig. 5d). We investigated whether or not effectiveness in treated animals was linked with the characteristics of the mutations detected on viral populations and found that infectious titers in lungs were negatively associated with frequency of non-synonymous and G → A mutations, and positively associated with frequency of synonymous mutations ($p < 0.03$; Fig. 5e). Finally, our experiments revealed some parallel evolution events; 32 substitutions in viral sub-populations were detected in two independent animals. Notably, 18 of these shared mutations were detected only with treated animals, 14 of them being non-synonymous (Supplementary Data 13). These mutations are located in nsp2, 3, 4, 5, 6, 14, N protein, Matrix, ORF 3a and 8. At this stage, one cannot conclude if these substitutions reflect the adaptation to the hamster model or are the result of the antiviral selection.

Discussion

In the current study, we used a hamster model to assess efficacy of the favipiravir against SARS-CoV-2. Following infection, viral RNA was mainly detected in lungs, blood, and, to a lesser extent, in the large bowel. Peak of viral replication was observed at 2–3 dpi, in line with recently reported investigations that involved 6–10-weeks-old hamsters[7]. Clinically, the main symptom was the

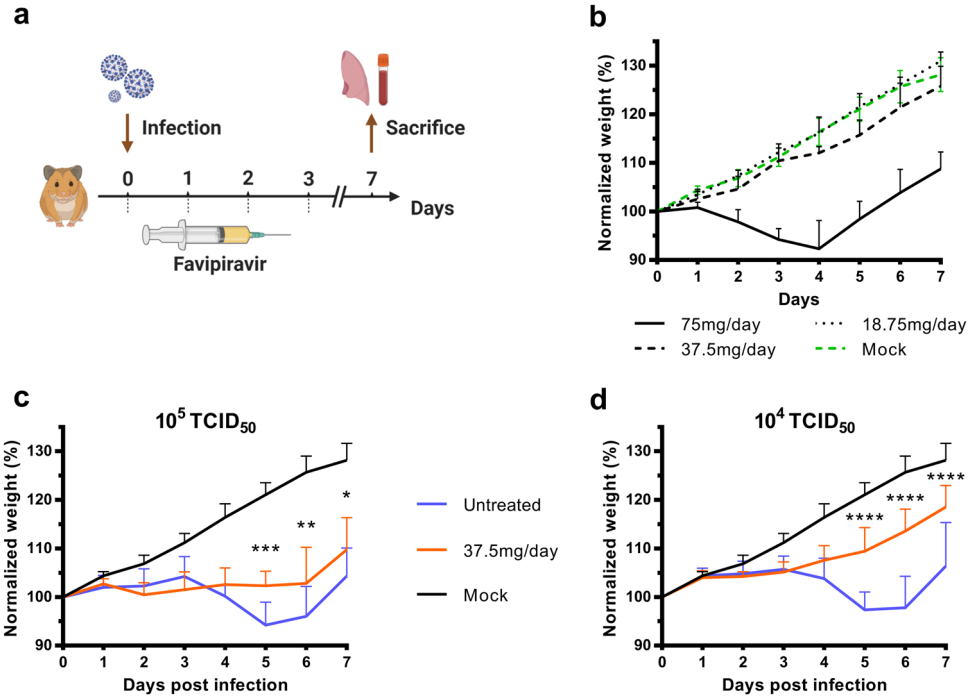

Fig. 2 Clinical follow-up of animals. a Experimental timeline. **b** Evaluation of the toxicity of the three doses of favipiravir (mg/day TID) with groups of four uninfected animals following the experimental timeline described in panel a but without infection. **c**, **d** Clinical follow-up with groups of 10 animals infected respectively with 10^5 and 10^4 $TCID_{50}$ of virus and treated with a dose of favipiravir of 37.5 mg/day TID. Normalized weight at day *n* was calculated as follows: % of initial weight of the animal at day *n*. Data represent mean ± SD (details in Supplementary Data 2). Two-sided statistical analysis were performed using two-way ANOVA with Post-hoc Dunnett's multiple comparisons test or Post-hoc Sidak's multiple comparisons test (details in Supplementary Data 5). ****, ***, ** and * symbols indicate that the average value for the group is significantly lower than that of the untreated group with a *p*-value < 0.0001, ranging between 0.0001–0.001, 0.001–0.01, and 0.01–0.05, respectively Source data are provided as a Source data file.

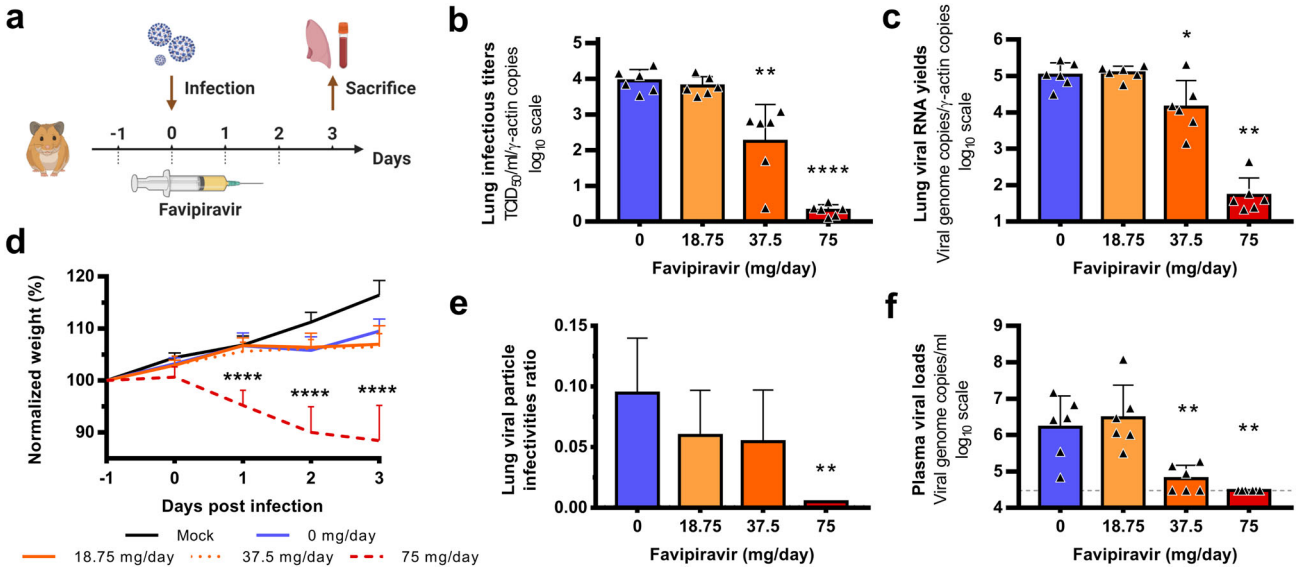

Fig. 3 Virological results with preventive favipiravir therapy. a Experimental timeline. Groups of 6 hamsters were intranasally infected with 10^4 $TCID_{50}$ of virus. **b** Viral replication in lungs based on infectious titers (measured using a $TCID_{50}$ assay) expressed in $TCID_{50}$/copy of ɣ-actine gene ($n = 6$ animals/group). **c** Viral replication in lungs based on viral RNA yields (measured using an RT-qPCR assay) expressed viral genome copies/copy of ɣ-actine gene ($n = 6$ animals/group). **d** Clinical course of the disease ($n = 6$ animals/group). Normalized weight at day *n* was calculated as follows: % of initial weight of the animal at day *n*. **e** Relative lung virus infectivities were calculated as follows: ratio of lung infectious titer over viral RNA yields ($n = 6$ animals/group). **f** Plasma viral loads (measured using an RT-qPCR assay) are expressed in viral genome copies/mL of plasma (the dotted line indicates the detection threshold of the assay) ($n = 6$ animals/group). Data represent mean ± SD (details in Supplementary Data 2). Statistical analysis were performed using Shapiro–Wilk normality test, Student *t*-test, Mann–Whitney test, One-sample *t*-test and two-way ANOVA with Post-hoc Dunnett's multiple comparisons test (details in Supplementary Data 3 and 4). ****, ** and * symbols indicate that the average value for the group is significantly different from that of the untreated group with a *p*-value < 0.0001, ranging between 0.001–0.01 and 0.01–0.05, respectively. Source data are provided as a Source data file.

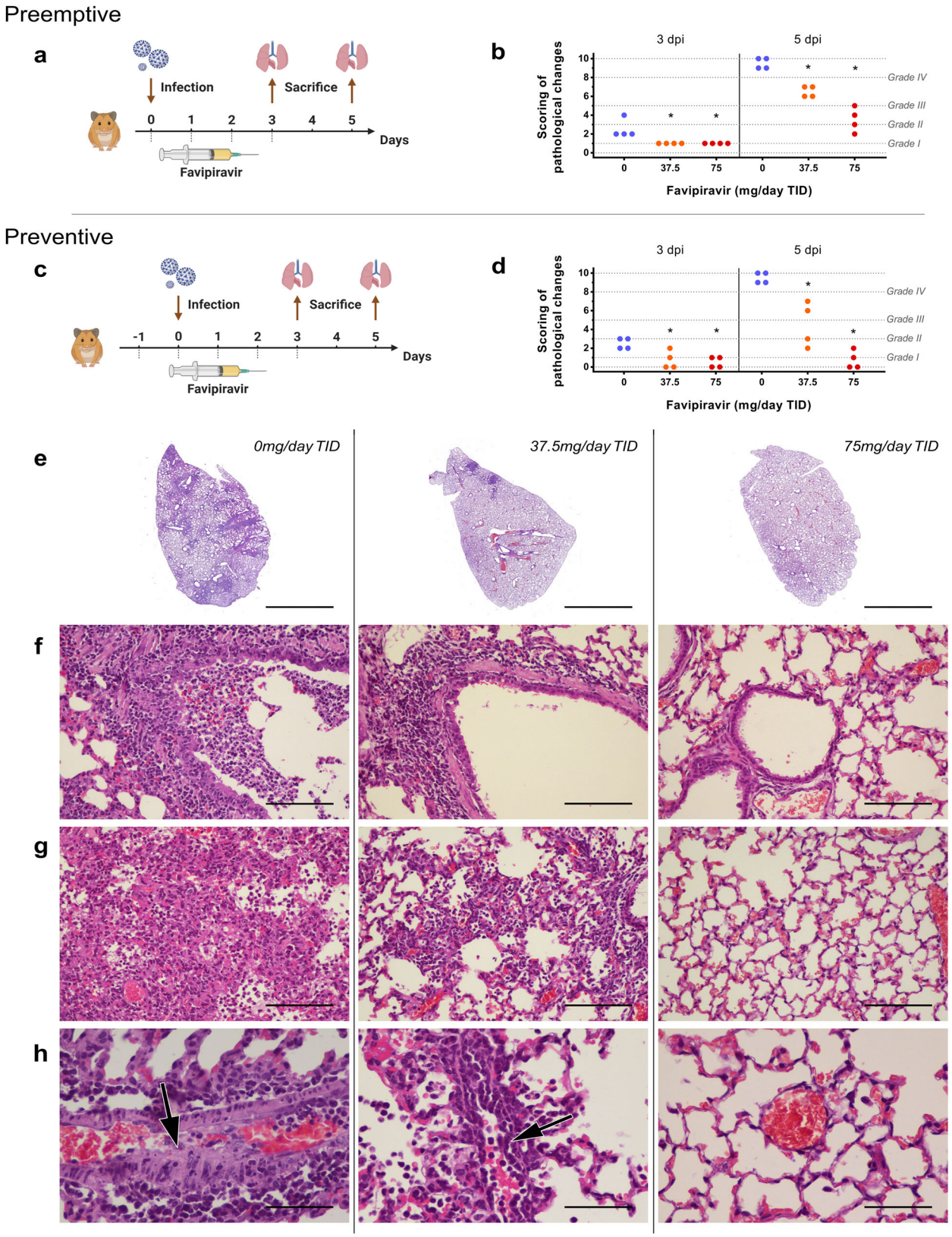

lack of weight gain, observed from the first day of infection and followed by recovery at 7 dpi. Histopathological changes are comparable to those previously described[7,21]. Notably, our results revealed that all animals with marked or severe pulmonary impairments displayed vascular lesions (endothelitis, vasculitis) as previously described in humans[22]. Overall, this confirmed that the in vivo model, with younger animals (4 weeks-old), is suitable for preclinical evaluation of antiviral compounds against SARS-CoV-2.

Using a preemptive strategy, we demonstrated that doses of favipiravir of around 700–1400 mg/kg/day TID reduced viral replication in the lungs of infected animals and allowed clinical

Fig. 4 Lung histopathological changes with preemptive or preventive favipiravir therapy. Groups of four animals were intranasally infected with 10^4 $TCID_{50}$ of virus and sacrificed at 3 and 5 dpi. Experimental timelines for preemptive (**a**) and preventive (**c**) favipiravir therapies. At day of sacrifice, lungs were collected, fixed, and embedded in paraffin. Tissue sections were stained with hematoxylin-eosin (H&E). Based on severity of inflammation, alveolar hemorrhagic necrosis, and vessel lesions, a cumulative score from 0 to 10 was calculated and assigned to a grade of severity (I, II, III, and IV). Scoring of pathological changes for preemptive (**b**) and preventive (**d**) favipiravir therapies ($n = 4$ animals/group) (details in Supplementary Data 7). Two-sided statistical analysis were performed using Shapiro–Wilk normality test, Student t-test, Mann–Whitney test, and two-way ANOVA with Post-hoc Dunnett's multiple comparisons test (details in Supplementary Data 7 and 8). * Symbol indicates that the average value for the group is significantly different from that of the untreated group with a *p*-value ranging between 0.01 and 0.05. **e** Representative images of lung tissue (left lobe) (scale bar: 4 mm): multifocal and extensive areas of inflammation for untreated animal, multifocal but limited areas of inflammation for 37.5 mg/day treated animal and normal lung for 75 mg/day treated animal ($n = 4$ samples/group). **f** Representative images of bronchial inflammation (scale bar: 100 µ): severe peribronchiolar inflammation and bronchiole filled with neutrophilic exudates for untreated animal, mild peribronchiolar inflammation for 37.5 mg/day treated animal and normal bronchi for 75 mg/day treated animal ($n = 4$ samples/group). **g** Representative images of alveolar inflammation (scale bar: 100 µ): severe infiltration of alveolar walls, alveoli filled with neutrophils/macrophages for untreated animal, moderate infiltration of alveolar walls, some alveoli filled with neutrophils/macrophages for 37.5 mg/day treated animal and normal alveoli for 75 mg/day treated animal. **h** Representative images of vessel inflammation (scale bar: 50 µ): infiltration of vascular wall with neutrophils/cell debris and endothelial damage (arrow) for untreated animal, moderate endothelial leukocytic accumulation for 37.5 mg/day treated animal and normal vessel for 75 mg/day treated animal ($n = 4$ samples/group). Clinical courses of the disease are presented in Supplementary Fig. 6. Source data are provided as a Source data file.

Table 3 Plasma and lung concentrations of favipiravir after administration of a single dose or multiple dose of favipiravir.

Time post-treatment	Single dose				Multiple dose[a] (Day 3)			
	Dose	Plasma (µg/mL)	Lung (µg/g)	L/p ratio	Dose	Plasma (µg/mL)	Lung (µg/g)	L/p ratio
0.5 h	25 mg	372 ± 47.5	216 ± 39	0.58 ± 0,04	75 mg/day TID			
1 h		279 ± 49.9						
5 h		135 ± 49.0	81.3 ± 24	0.62 ± 0.10				
8 h		5.77 ± 1.34						
12 h		1.43[b]				29.9 ± 9.83	16.0 ± 4.87	0.44 ± 0,07
0.5 h	12.5 mg	166 ± 52.0	90.7 ± 12.7	0.58 ± 0.14	37.5 mg/day TID			
1 h		155 ± 20.6						
5 h		10.7 ± 5.16	3.84 ± 1.49	0.37 ± 0.052				
8 h		1.94 ± 0.06						
12 h		0.16[b]				2.57 ± 1.22	1.36 ± 0.14	0.35 ± 0,03
0.5 h	6.25 mg	86.3 ± 4.11	50.2 ± 16.4	0.58 ± 0.17	18.75 mg/day TID			
1 h		35.2 ± 27.8						
5 h		2.90 ± 0.25	1.09 ± 0.05	0.38 ± 0.05				
8 h		0.56 ± 0.16						
12 h		0.05[b]				0.31 ± 0.14	Not detected	NA

NA not applicable.
Data represent mean ± SD; three animals for each condition except at multiple dose ($n = 9$ for plasma; $n = 3$ for lung); details in Supplementary Data 9.
[a]PK realized after 3 days of favipiravir administered three times a day, at the end of the dosing interval (trough concentrations).
[b]Extrapolated C_{12h}.

alleviation of the disease (Figs. 1 and 2). In the most favorable situation, where high doses were used as a preventive therapy, favipiravir led to undetectable viral replication in lung and plasma. These results showed that the use of high doses of favipiravir could expand its in vivo spectrum against RNA viruses. Reduction of viral replication was greater when estimated on the basis of infectious titers than on total viral RNA as previously observed in non-human primates treated with Remdesivir and in hamsters treated with favipiravir[23,24]. Furthermore, the analysis of pulmonary histopathological changes revealed that favipiravir played a protective role by reducing the severity of the lesions. However, the effective doses of favipiravir were higher than those usually used in rodent models (≈100–400 mg/kg/day)[10,12,25–28]. This can be correlated with the high favipiravir EC_{50} found in vitro for SARS-CoV-2. Moreover, effective doses were associated with significant toxicity in our hamster model (Fig. 2). This observed toxicity reflected only the adverse effects of favipiravir and was not exacerbated during SARS-CoV-2 infection. Indeed, similar weights were measured among infected and non-infected animals treated with the highest dose of favipiravir at 1, 2, and 3 dpi.

In the present study, reduction of viral replication was correlated with the dose of favipiravir administrated and inversely correlated with the virus inoculum. In a recent study, the efficacy of favipiravir intraperitoneally or orally administrated twice daily (loading dose of 900 and 1200 mg/kg/day followed by 600 and 1000 mg/kg/day, respectively) was assessed using a similar hamster model (6–10 weeks old) with high virus inocula (2×10^6 $TCID_{50}$)[24]. Treatment with the highest dose of favipiravir resulted in a moderate decrease of viral RNA yields in lung tissue and the lowest dose induced an even smaller inhibitory effect. However, significant infectious titers reduction were observed in a dose-dependent manner in lungs. Both doses were also associated with regression of pulmonary histopathological impairments. Overall, these results are in accordance with ours at the medium and the high doses of favipiravir (around 670 and 1390 mg/kg/day TID). However, in this other study, no signs of toxicity were associated with favipiravir treatment regardless the dosing regimen. This discrepancy could be due to the difference between (i) the highest daily doses used (1000 mg/kg/day in regards to 1390 mg/kg/day in our study), (ii) the dosing regimens (BID instead of TID in our

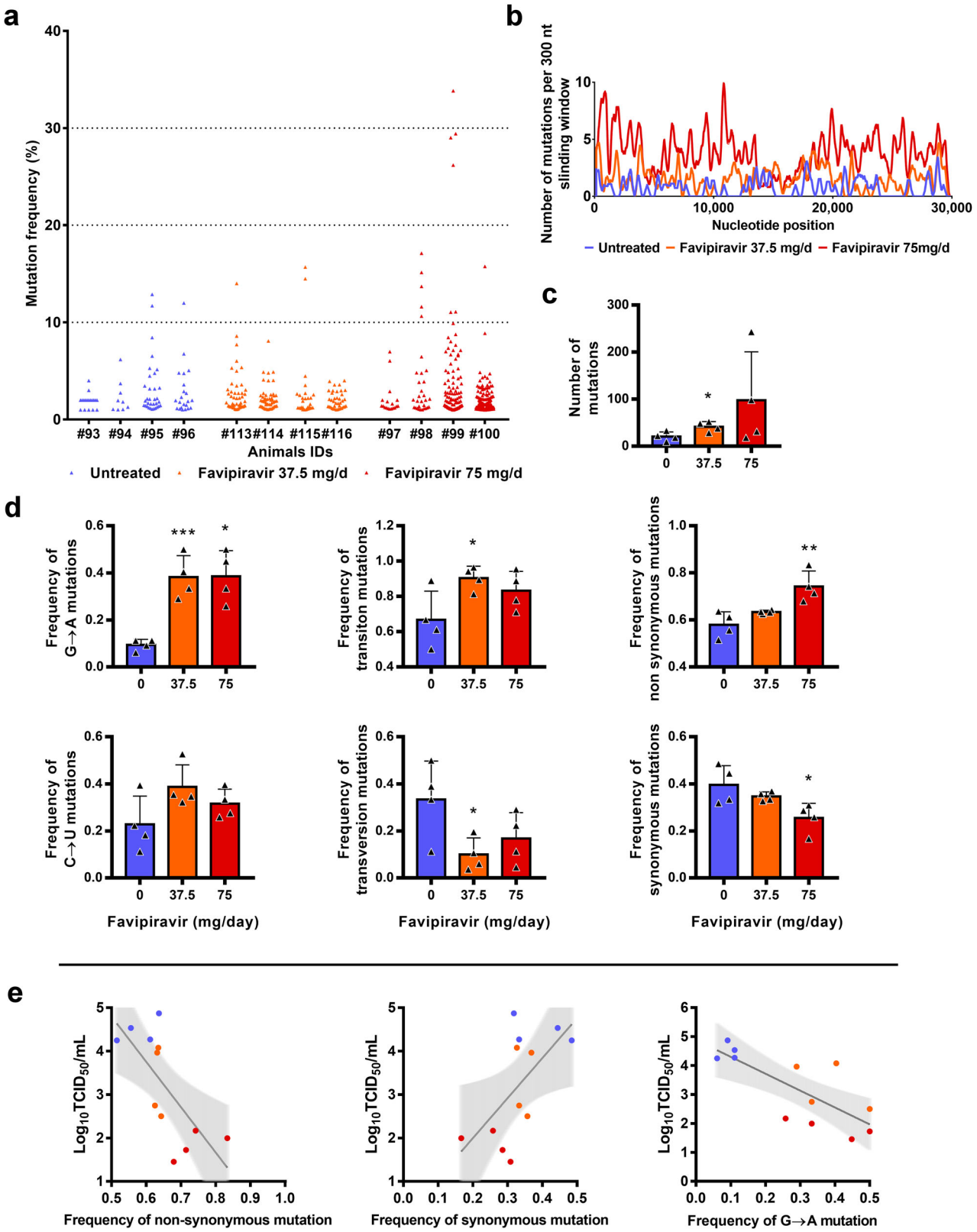

study), and/or (iii) the age of the hamsters at day of infection (6–10 weeks old in comparison to 4 weeks old in our study).

With influenza viruses, favipiravir acts as a nucleotide analog since it is recognized as a purine nucleotide by the viral RNA-dependent RNA polymerase. It is metabolized intracellularly to its active form and incorporated into nascent viral RNA strands. This inhibits RNA strand extension and induces abnormal levels of mutation accumulation into the viral genome[16,17]. Recently, it was shown in vitro that favipiravir has a similar mechanism of action with SARS-CoV-2 through a combination of chain termination, reduced RNA synthesis and lethal mutagenesis[20]. Our genomic analysis confirmed the mutagenic effect of favipiravir

Fig. 5 Mutagenic effect of favipiravir. a Viral genetic diversity in clarified lung homogenates. For each condition, four samples were analyzed. Each triangle represents a mutation (only substitutions with a frequency ≥ 1% were considered). **b** Patterns of mutation distribution on complete viral genome. Each variable nucleotide position was counted only once when found. The variability was represented using 75 nt sliding windows. For each condition, variable nucleotide positions were determined and represented using a 300 nt sliding window. **c** Mean number of mutations ($n = 4$ samples/group). Data represent mean ± SD. **d** Mutation characteristics ($n = 4$ samples/group). For each sample, the frequency of a given mutation was calculated as follows: number of this kind of mutation detected in the sample divided by the total number of mutations detected in this sample. Data represent mean ± SD (details in details in Supplementary Data 10 and 13). Two-sided statistical analysis were performed using Shapiro–Wilk normality test, Student *t*-test, Mann–Whitney test, and Welch's test (details in Supplementary Data 11 and 12). ***, ** and * symbols indicate that the average value for the group is significantly lower than that of the untreated group with a p-value ranging between 0.0001–0.001, 0.001–0.01, and 0.01–0.05, respectively. **e** Association between lung infectious titers (measured using a $TCID_{50}$ assay) and frequency of non synonymous, synonymous and G → A mutations. Each dot represent data from a given animal. Statistical analysis was performed using univariate linear regression. The error band (in gray) represent the 95% confidence interval of the regression line. Source data are provided as a Source data file.

in vivo[24]. Indeed, we found that favipiravir treatment induced appearance of a large number of G → A mutations into viral genomes (Fig. 5). This was associated to a decrease of viral infectivity probably because alteration of the genomic RNA disturb the replication capacity. Similar findings were described in vitro and in vivo with other RNA viruses[9,16,29,30]. Of note, we also observed a strong inverse association between infectious titers in lungs and the proportion of non-synonymous mutations detected in viral populations. Because random non-synonymous mutations are more deleterious than synonymous mutations[31], this suggests that they were randomly distributed over the three positions of the codons and that no compensatory mechanism was triggered by the virus to eliminate them (*i.e.* negative selection). Finally, the inverse correlation between lung infections titers and the frequency of G → A substitutions showed that an increased proportion of these mutations beyond an error threshold might be expected to cause lethal mutagenesis.

Genomic analyses revealed that 18 mutations detected in viral sub-populations were shared only with treated animals. Two of them were located in the nsp14 coding region involved in the proof-reading activity of the viral RNA polymerisation[32,33]. However, they were located in the N7 MTase domain involved in viral RNA capping[34,35]. By comparison, resistance mutations selected against Remdesivir in β-coronavirus murine hepatitis virus model were obtained in the RdRP (nsp12) coding sequence[36]. Further investigations are needed to assess the impact of these mutations on the antiviral effect of favipiravir.

Favipiravir PK in our hamster model displayed a non-linear increase in plasma exposure between the doses as already reported in non-human primates[37]. The observed favipiravir concentration versus time profiles were in agreement with previous results of a PK study performed in 7–8-week-old hamsters orally treated with a single dose of 100 mg/kg of favipiravir[38]. The maximum plasma drug concentration occurred at 0.5 h after oral administration, earlier than in humans, and then decreased rapidly in agreement with its short half-life[39]. After repeated doses, plasma exposure confirmed non-linear PK over the entire range of doses, further emphasized by accumulation ratios. The important accumulation observed at the highest dose could explain in part the toxicity observed in hamsters at this dose. Favipiravir undergoes an important hepatic metabolism mainly by aldehyde oxidase producing an inactive M1 metabolite and inhibits aldehyde oxidase activity in a concentration- and time-dependent manner. These properties explain the self-inhibition of its own metabolism as observed in our study in which the highest dose of favipiravir led to a greater increase in favipiravir concentrations[40].

A good penetration of favipiravir in lungs was observed with lung/plasma ratios ranging from 35 to 44% after repeated doses, consistent with its physicochemical properties. Lung exposure was also in accordance with the previous studies[38].

The medium dose of favipiravir used in this study (670 mg/kg/day TID) is within the range of the estimated doses required to reduce by 90% (ED_{90}) the level of infectious titers in lungs (ranging between 31 and 42 mg/day corresponding to 570–780 mg/kg/day) (Table 2) and displayed limited drug-associated toxicity (Fig. 2b). Animals infected with 10^5 and 10^4 $TCID_{50}$ of virus, and treated following a preemptive strategy with this dose displayed significant reduction of infectious titers and histopathological scores in lungs and clinical alleviation of the disease (Figs. 1, 2, and 4). Animal treated following a preventive strategy with this dose also displayed significant reduction of viral replication and histopathological scores in lungs (Figs. 3 and 4). Regarding the accumulation ratio after repeated doses and the good penetration of favipiravir in lungs, effective concentrations can be expected in lungs, throughout the course of treatment using this dose of 670 mg/kg/day TID.

How clinically realistic are these results? To address this question we compared the drug concentrations obtained in the hamster model with those obtained in patients. In 2016, a clinical trial evaluated the use of favipiravir in Ebola-infected patients[41]. The dose used in Ebola-infected patients was 6000 mg on day 0 followed by 1200 mg BID for 9 days. The median trough concentrations of favipiravir at day 2 and day 4 were 46.1 and 25.9 µg/mL, respectively. This is within the range observed here in hamsters treated with the highest dose (around 1400 mg/kg/day), with a mean trough concentration of 29.9 µg/mL. However, additional investigations are required to determine whether or not similar favipiravir plasma exposure in SARS-COV-2 infected patients are associated with antiviral activity. The major differences in PK between hamster and humans, and the toxicity observed at the highest doses in our animal model limits the extrapolation of our results. Therefore, whether safe dosing regimens in humans may achieve similar plasma exposure and recapitulate the profound effect on viral replication is unknown. Further, the intracellular concentration of the active metabolite was not determined and which parameter of the drug pharmacokinetics best drives the antiviral effect remains to be established.

In summary, this study establishes that high doses of favipiravir are associated with antiviral activity against SARS-CoV-2 infection in a hamster model. The better antiviral efficacy was observed using a preventive strategy, suggesting that favipiravir could be more appropriate for a prophylactic use. Our results should be interpreted with caution because high doses of favipiravir were associated with signs of toxicity in our model. It is required to determine if a tolerable dosing regimen could generate similar exposure in non-human primates, associated with significant antiviral activity, before testing a high dose regimen in COVID-19 patients. Furthermore, subsequent studies should determine if an increased antiviral efficacy can be reached using favipiravir in association with other effective antiviral drugs, since

this strategy may enable to reduce the dosing regimen of favipiravir. Finally, this work reinforces the need for rapid development of animal models to confirm in vivo efficacy of antiviral compounds and accordingly, to determine appropriate dose regimens in humans before starting clinical trials.

Methods

Cells. VeroE6 cells (ATCC CRL-1586) and Caco-2 cells (ATCC HTB-37) were grown at 37 °C with 5% CO_2 in minimal essential medium (MEM) supplemented with 7.5% heat-inactivated fetal bovine serum (FBS), 1% penicillin/streptomycin and 1% non-essential amino acids (all from ThermoFisher Scientific).

Virus. All experiments with infectious virus were conducted in biosafety level (BSL) 3 laboratory. SARS-CoV-2 strain BavPat1, supplied through European Virus Archive GLOBAL (https://www.european-virus-archive.com/), was provided by Christian Drosten (Berlin, Germany). Virus stocks were prepared by inoculating at MOI of 0.001 a 25 cm 2 culture flask of confluent VeroE6 cells with MEM medium supplemented with 2.5% FBS. The cell supernatant medium was replaced each 24 h and harvested at the peak of infection, supplemented with 25 mM HEPES (Sigma), aliquoted and stored at −80 °C.

In vitro determination of EC_{50}, EC_{90}, CC_{50}, and infectious titer reductions. One day prior to infection, 5×10^4 VeroE6 cells were seeded in 96-well culture plates (5×10^4 cells/well in 100 µL of 2.5% FBS medium (assay medium). The next day, seven 2-fold serial dilutions of favipiravir (Courtesy of Toyama-Chemical; 0.61 µg/mL to 78.5 µg/mL, in triplicate) were added (25 µL/well, in assay medium). Eight virus control wells were supplemented with 25 µL of assay medium and eight cell controls were supplemented with 50 µL of assay medium. After 15 min, 25 µL of virus suspension, diluted in assay medium, was added to the wells at an MOI of 0.01 or 0.001 (except for cell controls). Three days after infection, cell supernatant media were collected to perform $TCID_{50}$ assay (at concentration of 500, 250, and 125 µM), as described below, in order to calculate infectious titer reductions and cell viability was assessed using CellTiter-Blue reagent (Promega) following the manufacturer's intstructions. Fluorescence (560/590 nm) was recorded with a Tecan Infinite 200Pro machine (Tecan). The 50 and 90% effective concentrations (EC_{50}, EC_{90}) were determined using logarithmic interpolation (% of inhibition were calculated as follows: $(OD_{sample} - OD_{virus\ control})/(OD_{cell\ control} - OD_{virus\ control})$). For the evaluation of CC_{50} (the concentration that induced 50% cytoxicity), the same culture conditions were set as for the determination of the EC_{50}, without addition of the virus, then cell viability was measured using CellTiter Blue (Promega). CC_{50} was determined using logarithmic interpolation.

In vivo experiments

Approval and authorization. In vivo experiments were approved by the local ethical committee (C2EA—14) and the French 'Ministère de l'Enseignement Supérieur, de la Recherche et de l'Innovation' (APAFIS#23975) and performed in accordance with the French national guidelines and the European legislation covering the use of animals for scientific purposes. All experiments were conducted in BSL 3 laboratory.

Animal handling. Three-week-old female Syrian hamsters were provided by Janvier Labs. Animals were maintained in ISOcage P - Bioexclusion System (Techniplast) with unlimited access to water/food and 14 h/10 h light/dark cycle. Animals were weighed and monitored daily for the duration of the study to detect the appearance of any clinical signs of illness/suffering. Virus inoculation was performed under general anesthesia (isoflurane). Organs and blood were collected after euthanasia (cervical dislocation) which was also realized under general anesthesia (isoflurane).

Hamster Infection. Anesthetized animals (four-week-old) were intranasally infected with 50 µL containing 10^6, 10^5 or 10^4 $TCID_{50}$ of virus in 0.9% sodium chloride solution. The mock group was intranasally inoculated with 50 µL of 0.9% sodium chloride solution.

Favipiravir administration. Hamster were intraperitoneally inoculated with different doses of favipiravir. Control group were intraperitoneally inoculated with a 0.9% sodium chloride solution.

Organ collection. Organs were first washed in 10 mL of 0.9% sodium chloride solution and then transferred to a 2 mL or 50 mL tube containing respectively 1 mL (small/large bowel pieces, kidney, spleen, and heart) or 10 mL (lungs, brain and liver) of 0.9% sodium chloride solution and 3 mm glass beads. They were crushed using a Tissue Lyser machine (Retsch MM400) for 5 min at 30 cycles/s and then centrifuged 5 min at 16,200 × *g*. Supernatant media were transferred to a 2 mL tube, centrifuged 10 min at 16,200 × *g*, and stored at −80 °C. One milliliter of blood was harvested in a 2 mL tube containing 100 µL of 0.5 M EDTA (ThermoFischer Scientific). Blood was centrifuged for 10 min at 16,200 × *g* and stored at −80 °C.

Quantitative real-time RT-PCR (RT-qPCR) assays. To avoid contamination, all experiments were conducted in a molecular biology laboratory that is specifically designed for clinical diagnosis using molecular techniques, and which includes separate laboratories dedicated to perform each step of the procedure. Prior to PCR amplification, RNA extraction was performed using the QIAamp 96 DNA kit, and the Qiacube HT kit and the Qiacube HT (both from Qiagen) following the manufacturer's instructions. Shortly, 100 µl of organ clarified homogenates, spiked with 10 µL of internal control (bacteriophage MS2)[42], were transferred into an S-block containing the recommended volumes of VXL, proteinase K, and RNA carrier. RT-qPCR (SARS-CoV-2 and MS2 viral genome detection) were performed with the Express one step RT-qPCR Universal kit (ThermoFisher Scientific) using 3.5 µL of RNA and 6.5 µL of RT-qPCR mix that contains 250 nmol of each primer and 75 nmol of probe. Amplification was performed with the QuantStudio 12K Flex Real-Time PCR System (ThermoFisher Scientific) using the following conditions: 50 °C for 10 min, 95 °C for 20 s, followed by 40 cycles of 95 °C for 3 s, 60 °C for 30 s. qPCR (ɣ-actine gene detection) was perfomed under the same condition as RT-qPCR with the following modifications: we used the Express one step qPCR Universal kit (ThermoFisher Scientific) and the 50 °C step of the amplification cycle was removed. Data were collected using the QuantStudio 12K Flex Software v1.2.3. Primers and probes sequences used to detect SARS-CoV-2, MS2 and ɣ-actine are described in Supplementary Table 1.

Tissue-culture infectious dose 50 ($TCID_{50}$) assay. To determine infectious titers, 96-well culture plates containing confluent VeroE6 cells were inoculated with 150 µL per well of serial dilutions of each sample (four-fold or ten-fold dilutions when analyzing lung clarified homogenates or cell supernatant media, respectively). Each dilution was performed in sextuplicate. Plates were incubated for 4 days and then read for the absence or presence of cytopathic effect in each well. Infectious titers were estimated using the method described by Reed & Muench[43].

Favipiravir pharmacokinetics. Animal handling, hamster infections, and favipiravir administrations were performed as described above. A piece of left lung was first washed in 10 mL of sodium chloride 0.9% solution, blotted with filter paper, weighed and then transferred to a 2 mL tube containing 1 mL of 0.9% sodium chloride solution and 3 mm glass beads. It was crushed using the Tissue Lyser machine (Retsch MM400) during 10 min at 30 cycles/s and then centrifuged 5 min at 16,200 × *g*. Supernatant media were transferred to 2 mL tubes, centrifuged 10 min at 16,200 × *g* and stored at −80 °C. One milliliter of blood was harvested in a 2 mL tube containing 100 µL of 0.5 M EDTA (ThermoFischer Scientific). Blood was centrifuged for 10 min at 16,200 × *g* and stored at −80 °C.

Quantification of favipiravir in plasma and lung tissues was performed by a validated sensitive and selective validated high-performance liquid chromatography coupled with tandem mass spectrometry method (UPLC-TQD, Waters, USA) with a lower limit of quantification of 0.1 µg/mL. Precision and accuracy of the three quality control samples (QCs) were within 15% over the calibration range (0.5 µg/mL to 100 µg/mL) (Bekegnran et al., submitted). Favipiravir was extracted by a simple protein precipitation method, using acetonitrile for plasma and ice-cold acetonitrile for clarified lung homogenates. Briefly, 50 µL of samples matrix was added to 500 µL of acetonitrile solution containing the internal standard (favipiravir-13C,15N, Alsachim), then vortexed for 2 min followed by centrifugation for 10 min at 4 °C. The supernatant medium was evaporated and the dry residues were then transferred to 96-well plates and 50 µL was injected. To assess the selectivity and specificity of the method and matrix effect, blank plasma and tissues homogenates from 2 control animals (uninfected and untreated) were processed at each run. Moreover, the same control samples spiked with favipiravir concentration equivalent to the QCs (0.75, 50, and 80 µg/mL) were also processed and compared to the QCs samples. Data were collected using the MassLynx Mass Spectrometry Software 4.1.

Noncompartemental analysis conducted using software Pkanalix2019R2 (www.lixoft.com). Areas under the plasma concentration time curve were computed using medians of favipiravir concentrations at 0.5, 1, 5, and 8 h, and extrapolated until $T = 12$ h. C_{trough} were extrapolated at $T = 12$ h using lambda-z loglinear regression on the decreasing slope of concentrations.

Histology. Animal handling, hamster infections, and favipiravir administrations were performed as described above. Lungs were collected after intratracheal instillation of 4% (w/v) formaldehyde solution, fixed 72 h at room temperature with a 4% (w/v) formaldehyde solution and embedded in paraffin. Tissue sections of 3.5 µm, obtained following guidelines from the "global open RENI" (The standard reference for nomenclature and diagnostic criteria in toxicologic pathology; https://www.goreni.org/), were stained with hematoxylin-eosin (H&E) and blindly analyzed by a certified veterinary pathologist. Microscopic examination was done using a Nikon Eclipse E400 microscope. Different anatomic compartments were examined (see Supplementary Table 2): (1) for bronchial and alveolar walls, a score of 0 to 4 was assigned based on the severity of inflammation; (2) regarding alveoli, a score of 0 to 2 was assigned based on presence and severity of hemorrhagic necrosis; (3) regarding vessel lesions (endothelitis/vasculitis), absence or presence was scored 0 or 1 respectively. A cumulative score was then calculated and assigned to a grade of severity (see Supplementary Table 3).

Sequence analysis of the full-length genome. 200 µL of lung clarified homogenate or infectious cell supernatant (virus stock) was inactivated with an equal volume of VXL lysis buffer (Qiagen) and viral RNA was extracted using an EZ1 Advanced XL robot with the EZ1 mini virus 2.0 kit (both from Qiagen) and linear acrylamide (ThermoFisher Scientific) in place of carrier RNA. cDNA was generated in a final volume of 40 µL using 14 µL of nucleic acid extract, random hexamer and the Protoscript II First Strand cDNA Synthesis Kit (New England Biolabs). A specific set of primers (Supplementary Table 4) was used to generate thirteen amplicons covering the entire genome with the Q5 High-Fidelity DNA polymerase (New England Biolabs). PCR mixes (final volume 25 µL) contained 2.5 µL of cDNA, 2 µL of each primer (10 µM), and 12.5 µL of Q5 High-Fidelity 2X Master Mix. Amplification was performed with the following conditions: 30 s at 98 °C, then 45 cycles of 15 s at 98 °C and 5 min at 65 °C. Size of PCR products was verified by gel electrophoresis. For each sample, an equimolar pool of all amplicons was prepared and purified using Monarch PCR & DNA Cleanup Kit (New England Biolabs). After DNA quantification using Qubit dsDNA HS Assay Kit and Qubit 2.0 fluorometer (ThermoFisher Scientific), amplicons were fragmented by sonication into fragments of around 200 bp long. Libraries were built by adding barcodes, for sample identification, and primers using AB Library Builder System (ThermoFisher Scientific). To pool equimolarly the barcoded samples a quantification step by real-time PCR using Ion Library TaqMan Quantitation Kit (ThermoFisher Scientific) was performed. Then, emulsion PCR from pools and loading on 530 chip was performed using the automated Ion Chef instrument (ThermoFisher Scientific). Sequencing was performed using the S5 Ion torrent technology v5.12 (ThermoFisher Scientific) following the manufacturer's instructions. Consensus sequence was obtained after trimming of reads (reads with quality score < 0.99, and length < 100 pb were removed and the 30 first and 30 last nucleotides were removed from the reads). Mapping of the reads on a reference (determine following blast of De Novo contigs) was done using CLC genomics workbench software v.20 (Qiagen). A de novo contig was also produced to ensure that the consensus sequence was not affected by the reference sequence. Mutation frequency for each position was calculated as the number of reads with a mutation compared to the reference divided by the total number of reads at that site. Only substitutions with a frequency of at least 1% were taken into account for the analysis (Supplementary Data 10).

ED_{50}, ED_{90}, and ED_{99} determination. We conducted a nonlinear regression of infectious viral load against dose, using an E_{max} model, giving $VL = VL_0 \times \left(1 - \left(\frac{D^\gamma}{D^\gamma + D_{50}^\gamma}\right)\right)$ with VL_0 being infectious viral load of untreated animals. We estimated D_{50} the dose required to decrease viral load by 50%, using a coefficient γ to account for the high sigmoidicity of the relation between dose and titers. γ coefficient was chosen as the one maximizing likelihood of the model. We extrapolated the D_{90} and D_{99} using $D_{90} = \sqrt[\gamma]{9 \times D_{50}^\gamma}$ and $D_{99} = \sqrt[\gamma]{99 \times D_{50}^\gamma}$, as well as their 95% confidence interval using the delta method.

Graphical representations and statistical analysis. Graphical representations and statistical analyses were performed with Graphpad Prism 7 (Graphpad software) except linear/nonlinear regressions and their corresponding graphical representations that were performed using R statistical software (http://www.R-project.org). Statistical details for each experiment are described in the figure legends and in corresponding Supplementary data. When relevant, two-sided statistical tests were always used. *P*-values lower than 0.05 were considered statistically significant. Experimental timelines were created on biorender.com.

Reporting summary. Further information on research design is available in the Nature Research Reporting Summary linked to this article.

Data availability

Raw sequence reads of the virus genome analyzed in this study have been deposited in the BioProject data bank (PRJNA648821). Authors can confirm that all other relevant data are included in the paper and/or its Supplementary information files. Source data are provided with this paper.

Received: 17 July 2020; Accepted: 28 January 2021;
Published online: 19 March 2021

References

1. WHO. World Health Organization. WHO Director-General's opening remarks at the media briefing on COVID-19—11 March 2020 (https://www.who.int) (2020).
2. Zhu, N. et al. A novel coronavirus from patients with pneumonia in China, 2019. *N. Engl. J. Med.* **382**, 727–733 (2020).
3. Huang, C. et al. Clinical features of patients infected with 2019 novel coronavirus in Wuhan, China. *Lancet* **395**, 497–506 (2020).
4. He, X. et al. Temporal dynamics in viral shedding and transmissibility of COVID-19. *Nat. Med.* **26**, 672–675 (2020).
5. Dong, E., Du, H. & Gardner, L. An interactive web-based dashboard to track COVID-19 in real time. *Lancet Infect. Dis.* **20**, 533–534 (2020).
6. Mercorelli, B., Palu, G. & Loregian, A. Drug repurposing for viral infectious diseases: how far are we? *Trends Microbiol* **26**, 865–876 (2018).
7. Chan, J. F. et al. Simulation of the clinical and pathological manifestations of Coronavirus Disease 2019 (COVID-19) in golden Syrian hamster model: implications for disease pathogenesis and transmissibility. *Clin. Infect. Dis.* https://doi.org/10.1093/cid/ciaa325 (2020).
8. Rockx, B. et al. Comparative pathogenesis of COVID-19, MERS, and SARS in a nonhuman primate model. *Science* **368**, 1012–1015 (2020).
9. Guedj, J. et al. Antiviral efficacy of favipiravir against Ebola virus: a translational study in cynomolgus macaques. *PLoS Med.* **15**, e1002535 (2018).
10. Yamada, K. et al. Reevaluation of the efficacy of favipiravir against rabies virus using in vivo imaging analysis. *Antivir. Res* **172**, 104641 (2019).
11. Segura Guerrero, N. A., Sharma, S., Neyts, J. & Kaptein, S. J. F. Favipiravir inhibits in vitro Usutu virus replication and delays disease progression in an infection model in mice. *Antivir. Res* **160**, 137–142 (2018).
12. Tani, H. et al. Therapeutic effects of favipiravir against severe fever with thrombocytopenia syndrome virus infection in a lethal mouse model: dose-efficacy studies upon oral administration. *PLoS ONE* **13**, e0206416 (2018).
13. Jochmans, D. et al. Antiviral activity of favipiravir (T-705) against a broad range of paramyxoviruses in vitro and against human metapneumovirus in hamsters. *Antimicrob. Agents Chemother.* **60**, 4620–4629 (2016).
14. Takahashi, K. et al. In vitro and in vivo activities of T-705 and oseltamivir against influenza virus. *Antivir. Chem. Chemother.* **14**, 235–241 (2003).
15. Rosenke, K. et al. Use of favipiravir to treat lassa virus infection in macaques. *Emerg. Infect. Dis.* **24**, 1696–1699 (2018).
16. Baranovich, T. et al. T-705 (favipiravir) induces lethal mutagenesis in influenza A H1N1 viruses in vitro. *J. Virol.* **87**, 3741–3751 (2013).
17. Sangawa, H. et al. Mechanism of action of T-705 ribosyl triphosphate against influenza virus RNA polymerase. *Antimicrob. Agents Chemother.* **57**, 5202–5208 (2013).
18. Wang, M. et al. Remdesivir and chloroquine effectively inhibit the recently emerged novel coronavirus (2019-nCoV) in vitro. *Cell Res.* **30**, 269–271 (2020).
19. Jeon, S. et al. Identification of antiviral drug candidates against SARS-CoV-2 from FDA-approved drugs. *Antimicrob. Agents Chemother.* https://doi.org/10.1128/AAC.00819-20 (2020).
20. Shannon, A. et al. Rapid incorporation of Favipiravir by the fast and permissive viral RNA polymerase complex results in SARS-CoV-2 lethal mutagenesis. *Nat. Commun.* **11**, 4682 (2020).
21. Sia, S. F. et al. Pathogenesis and transmission of SARS-CoV-2 in golden hamsters. *Nature* **583**, 834–838 (2020).
22. Varga, Z. et al. Endothelial cell infection and endotheliitis in COVID-19. *Lancet* **395**, 1417–1418 (2020).
23. Williamson, B. N. et al. Clinical benefit of remdesivir in rhesus macaques infected with SARS-CoV-2. *Nature* **585**, 273–276 (2020).
24. Kaptein, S. J. F. et al. Favipiravir at high doses has potent antiviral activity in SARS-CoV-2-infected hamsters, whereas hydroxychloroquine lacks activity. *Proc. Natl Acad. Sci. USA* https://doi.org/10.1073/pnas.2014441117 (2020).
25. Sidwell, R. W. et al. Efficacy of orally administered T-705 on lethal avian influenza A (H5N1) virus infections in mice. *Antimicrob. Agents Chemother.* **51**, 845–851 (2007).
26. Smither, S. J. et al. Post-exposure efficacy of oral T-705 (Favipiravir) against inhalational Ebola virus infection in a mouse model. *Antivir. Res.* **104**, 153–155 (2014).
27. Julander, J. G., Shafer, K., Smee, D. F., Morrey, J. D. & Furuta, Y. Activity of T-705 in a hamster model of yellow fever virus infection in comparison with that of a chemically related compound, T-1106. *Antimicrob. Agents Chemother.* **53**, 202–209 (2009).
28. Oestereich, L. et al. Efficacy of favipiravir alone and in combination with ribavirin in a lethal, immunocompetent mouse model of lassa fever. *J. Infect. Dis.* **213**, 934–938 (2016).
29. Escribano-Romero, E., Jimenez de Oya, N., Domingo, E. & Saiz, J. C. Extinction of West Nile virus by favipiravir through lethal mutagenesis. *Antimicrob. Agents Chemother.* https://doi.org/10.1128/AAC.01400-17 (2017).
30. Arias, A., Thorne, L. & Goodfellow, I. Favipiravir elicits antiviral mutagenesis during virus replication in vivo. *Elife* **3**, e03679 (2014).
31. Cuevas, J. M., Domingo-Calap, P. & Sanjuan, R. The fitness effects of synonymous mutations in DNA and RNA viruses. *Mol. Biol. Evol.* **29**, 17–20 (2012).
32. Eckerle, L. D., Lu, X., Sperry, S. M., Choi, L. & Denison, M. R. High fidelity of murine hepatitis virus replication is decreased in nsp14 exoribonuclease mutants. *J. Virol.* **81**, 12135–12144 (2007).
33. Ferron, F. et al. Structural and molecular basis of mismatch correction and ribavirin excision from coronavirus RNA. *Proc. Natl Acad. Sci. USA* **115**, E162–E171 (2018).

34. Chen, Y. et al. Structure-function analysis of severe acute respiratory syndrome coronavirus RNA cap guanine-N7-methyltransferase. *J. Virol.* **87**, 6296–6305 (2013).
35. Ma, Y. et al. Structural basis and functional analysis of the SARS coronavirus nsp14-nsp10 complex. *Proc. Natl Acad. Sci. USA* **112**, 9436–9441 (2015).
36. Agostini, M. L. et al. Coronavirus susceptibility to the antiviral remdesivir (GS-5734) is mediated by the viral polymerase and the proofreading exoribonuclease. *mBio* https://doi.org/10.1128/mBio.00221-18 (2018).
37. Madelain, V. et al. Favipiravir pharmacokinetics in nonhuman primates and insights for future efficacy studies of hemorrhagic fever viruses. *Antimicrob. Agents Chemother.* https://doi.org/10.1128/AAC.01305-16 (2017).
38. Gowen, B. B. et al. Alterations in favipiravir (T-705) pharmacokinetics and biodistribution in a hamster model of viral hemorrhagic fever. *Antivir. Res.* **121**, 132–137 (2015).
39. Madelain, V. et al. Ebola virus infection: review of the pharmacokinetic and pharmacodynamic properties of drugs considered for testing in human efficacy trials. *Clin. Pharmacokinet.* **55**, 907–923 (2016).
40. Madelain, V. et al. Modeling favipiravir antiviral efficacy against emerging viruses: from animal studies to clinical trials. *CPT Pharmacomet. Syst. Pharm.* **9**, 258–271 (2020).
41. Sissoko, D. et al. Experimental treatment with favipiravir for Ebola virus disease (the JIKI Trial): a historically controlled, single-arm proof-of-concept trial in Guinea. *PLos Med.* https://doi.org/10.1371/journal.pmed.1001967 (2016).
42. Ninove, L. et al. RNA and DNA bacteriophages as molecular diagnosis controls in clinical virology: a comprehensive study of more than 45,000 routine PCR tests. *PLoS ONE* **6**, e16142 (2011).
43. Reed, L. J. & Muench, H. A simple method of estimating fifty per cent endpoints. *Am. J. Epidemiol.* **27**, 493–497 (1938).

Acknowledgements

We thank Laurence Thirion (UVE; Marseille) for providing RT-qPCR systems. We thank Camille Placidi (UVE; Marseille) for her technical contribution. We thank Lionel Chasson (CIML; Marseille) for helping to generate low magnification pictures. We also thank Pr. Ernest A. Gould (UVE; Marseille) for his careful reading of the manuscript and English language editing. We thank Pr. Drosten and Pr. Drexler for providing the SARS-CoV-2 strain through the European Research infrastructure EVA GLOBAL. This work was supported by the Fondation de France "call FLASH COVID-19", project TAMAC, by "Institut national de la santé et de la recherche médicale" through the REACTing (REsearch and ACTion targeting emerging infectious diseases) initiative ("Preuve de concept pour la production rapide de virus recombinant SARS-CoV-2"), and by European Virus Archive Global (EVA 213 GLOBAL) funded by the European Union's Horizon 2020 research and innovation program under grant agreement No. 871029. A part of the work was done on the Aix Marseille University antivirals platform "AD2P".

Author contributions

Conceptualization, J.S.D., M.C., G.M., and A.N.; methodology, J.S.D., M.C., G.L., G.M., C.L., and A.N.; formal analysis, J.S.D., M.C., and G.L.; investigation, J.S.D., M.C., G.M., F.T., P.R.P., G.P., K.B., C.L., and A.N.; resources, F.T., B.C., J.G., X.d.L., C.S., and A.N.; writing—original draft, J.S.D., M.C., C.L., J.G., C.S., and A.N.; writing—review & editing, J.G., X.d.L., C.S., and A.N.; visualization, J.S.D., M.C., G.L., F.T., P.R.P., and A.N.; supervision, A.N.; funding acquisition, F.T., B.C., X.d.L., and A.N.

Competing interests

J.G. has consulted for F. Hoffman-La Roche. C.S. has consulted for ViiV Healthcare, MSD and Gilead. The remaining authors declare no competing interests.

Additional information

Supplementary information The online version contains supplementary material available at https://doi.org/10.1038/s41467-021-21992-w.

Correspondence and requests for materials should be addressed to A.N.

Peer review information *Nature Communications* thanks Nikolaus Osterrieder and the other, anonymous, reviewer(s) for their contribution to the peer review of this work. Peer reviewer reports are available.

Reprints and permission information is available at http://www.nature.com/reprints

Publisher's note Springer Nature remains neutral with regard to jurisdictional claims in published maps and institutional affiliations.

Annexe 3 : Activity of Tixagevimab/Cilgavimab against the Omicron variant of SARS-CoV-2 in a hamster model, en révision dans *Ebiomedicine*

Activity of Tixagevimab/Cilgavimab against the Omicron variant of SARS-CoV-2 in a hamster model

Brief title: Tixagevimab/Cilgavimab activity in hamster model

Jean-Sélim Driouich[1], Guillaume Lingas[2], Léa Luciani[1], Maxime Cochin[1], Paola Mariela Saba Villarroel[1], Grégory Moureau[1], Paul-Rémi Petit[1], Franck Touret[1], Jérémie Guedj[2], Xavier de Lamballerie[1#] & Antoine Nougairède[1#]

[1]: Unité des Virus Émergents, UVE: Aix Marseille Univ, IRD 190, INSERM 1207, Marseille, France.

[2]: Université de Paris, IAME, INSERM, F-75018 Paris, France

[#]: These authors contributed equally

Corresponding author: Antoine NOUGAIREDE, antoine.nougairede@univ-amu.fr

Key words: SARS-CoV2, Omicron variant, hamster model, monoclonal antibody, clinical therapeutics

Abstract

The efficacy of pre-exposure prophylaxis by the Tixagevimab/Cilgavimab cocktail (AZD7442) was evaluated in hamsters against a clinical BA.1 strain of SARS-CoV-2 variant Omicron. AZD7442 retains inhibitory activity against Omicron despite a substantial loss of efficacy. We estimate that Omicron virus requires about 20-times more antibodies in plasma than the ancestral B.1 strain (G614) virus to achieve a similar drug efficacy in reducing lung infectious titers.

Research in context

The recent emergence of Omicron SARS-CoV-2 variants carrying mutations on the spike protein raises the question of a possible escape to therapeutic antibodies. Here we evaluated *in vivo* the efficacy of the Tixagevimab/Cilgavimab cocktail (AZD7442) on a clinical strain of the Omicron BA.1 variant using the hamster model. Our results indicate that AZD7442 retains inhibitory activity in vivo against this variant, although this activity is less than against an ancestral SARS-CoV2 strain.

Introduction

Since its emergence in 2019, the severe acute respiratory syndrome coronavirus 2 (SARS-CoV-2), the causative agent of the coronavirus disease 2019 (COVID-19), has evolved rapidly, leading to the successive emergence of variants carrying mutations on the spike protein. Assessing the degree of escape of circulating variants from naturally produced antibodies (previous infections or after vaccination) or therapeutic antibodies is crucial to inform public health policies (1).

The Omicron variant (lineage B.1.1.529) comprises several sublineages. The original BA.1 sublineage emerged in South Africa in late 2021 and has rapidly spread worldwide with very high incidence levels (2). This variant contains a large number of mutations, including over 30 in the spike protein (Fig.1-A). Some of these mutations are associated with potential escape from humoral immunity and higher transmissibility (3, 4). Soon after the emergence of this first variant, another sublineage, BA.2, has begun outcompeting BA.1. In March 2022, BA.2 was the dominant sublineage in many countries(5). BA.2 differs from BA.1 notably by the presence of 21 mutations in the spike protein (Fig.1-A), which may impact the susceptibility of the variant to different monoclonal antibodies (mABs). Several *in vitro* studies have shown that mABs already used against SARS-COV-2 during the pandemic have reduced or no efficacy against these variants (6-14). In one of these live-virus assays, the activity against BA.1 sublineage of the combination of Cilgavimab/Tixagevimab (AZD7442) that targets the SARS-CoV-2 spike receptor binding domain (RBD)(15) and marketed by AstraZeneca as Evusheld, was drastically reduced (6). In contrast the Omicron BA.2 contains fewer spike mutations than BA.1 among these some are shared and others are original (Fig 1-A). Various *in vitro* assay against BA.2 have shown a restored activity of Cilgavimab resulting in a significant improvement of the Evusheld neutralizing activity In patients treated with the C/T combination, several studies also described a reduced efficacy against these variants, since their sera have a low neutralization capacity against various Omicron sublineages (16-18).

Here, we present *in vitro* experiment assessing the neutralizing activity of Evusheld against differrents Omicron sub variants and the evaluation of the efficacy of pre-exposure prophylaxis by AZD7442 in Syrian hamsters (*Mesocricetus auratus*), against the two sublineages BA.1 and BA.2 of SARS-CoV-2 variant Omicron.

Methods

Cells

VeroE6 cells (ATCC CRL-1586) were cultured at 37°C with 5% CO2 in minimal essential medium (MEM) supplemented with 1% Penicillin/Streptomycin, 1% non-essential amino acids and 7% of heat-inactivated fetal bovine serum (FBS) (all from ThermoFisher Scientific). VeroE6/TMPRSS2 cells (NIBSC 100978) were cultured in the same medium supplemented with 2% of G-418 (ThermoFisher Scientific).

Viruses

The B.1 BavPat1 SARS-CoV-2 strain (G614 strain) was obtained from Pr. C. Drosten through EVA GLOBAL (https://www.european-virus-archive.com/) and contains the D614G mutation. Virus stocks of this strain was produced using VeroE6 cells (passage history: 2 for in vivo studies). The clinical strains of the SARS-CoV-2 BA.1 and BA.2 Omicron variants used here are respectively named 2021/FR/1514 and 2022/FR/TCO and are available through EVA GLOBAL (www.european-virus-archive.com, ref: 001V-04653, GISAID: EPI_ISL_7899754; ref: 001V-04663, GISAID: EPI_ISL_ 11926922; respectively). The clinical strains of the SARS-CoV-2 BA.1.1 was provided by Pr B. Lina and is named hCoV-19/France/ARA-HCL021232176201/2021 and have been deposited on GISAID : EPI_ISL_8544750.

Virus stocks of this strain was produced using VeroE6/TMPRSS2 cells (passage history: 1 for in vivo studies). All virus stocks were characterized by whole-genome sequencing (Ion Torrent) in order to verify the absence of additional mutations, especially in the spike-coding region. All experiments with infectious viruses were performed in a biosafety level 3 laboratory.

Antibodies

The combination Cilgavimab/Tixagevimab (AZD7442, Evusheld, AstraZeneca) were obtained from pharmacy of the University hospital of La Timone, Marseille, France.

In vitro experiments

In vitro 50% effective concentrations (EC_{50} compound concentration required to inhibit viral RNA replication by 50%) were determined as previously described (19). Briefly, one day prior to infection, VeroE6/TMPRSS2 cells were seeded in 96 well culture plates. The next day, antibodies were diluted in PBS with ½ dilutions from 5000 to 2.4 ng/mL. Twelve twofold serial dilutions of antibodies in triplicate were added to the cells (25 µL/well). Then, 25 µL of a virus mix diluted in medium was added to the wells. The amount of virus working stock used was calibrated prior to the assay so that the viral replication was still in the exponential growth phase for the readout (19-22). Plates were incubated 15 min at room temperature and then 2 days at 37 °C prior to quantification of the viral genome by real-time RT-PCR as previously described (19-22). RT-qPCR reactions were performed on QuantStudio 12K Flex Real-Time PCR System (Applied Biosystems) and analyzed using QuantStudio 12K Flex Applied Biosystems software v1.2.3. Primers and probe sequences, which target SARS-CoV-2N gene, are described in Touret et al, 2022 (19). Viral inhibition was calculated as follow: 100 * (quantity mean “virus control” − sample quantity)/quantity mean “virus control”. The EC_{50} were determined using logarithmic interpolation after performing a nonlinear regression as previously described (19-21, 23-25).

In vivo experiments

All experiments were approved by the local ethical committee (C2EA—14) and the French 'Ministère de l'Enseignement Supérieur, de la Recherche et de l'Innovation' (APAFIS#23975).

Three-week-old female Syrian hamsters, provided by Janvier Labs (SPF status), were housed in ISOcage P - Bioexclusion System (Techniplast) with unlimited access to food/water and 14h/10h light/dark cycle. Wooden gnawing blocks and extra bedding materials were provided as cage enrichment. The animals were monitored and weighed daily to detect the appearance of clinical signs of pain, suffering or distress. Infection, nasal washes and intramuscular administrations were performed under general anesthesia (isoflurane). Animals were infected with 3.10^4 $TCID_{50}$ of virus (virus diluted in 0.9% sodium chloride solution, intranasal infection with 50µL). Organs and blood were collected after euthanasia (cervical dislocation under general anesthesia (isoflurane)).

Study design

Group size was calculated with an effect size of 2 and a power of 80%, resulting in 5 to 9 animals/group. Sample sizes were maximized within the capacity of the BSL3 housing, and compound and virus stock availability. A total of 146 animals were used in this study. Animals were randomly assigned to groups but confounders were not controlled. Since, the same experimenters carried out infection/treatment/clinical follow-up, it was impossible to perform a blind trial. Predefined humane endpoints (>20% weight loss, moribund and a scoring >10 calculated according to a clinical evaluation scale) were set as exclusion criteria. No animals were excluded from the study.

Organ and blood collection

Nasal washes were performed with 150µl of 0.9% sodium chloride solution and transferred into 1.5mL tubes containing 0.5mL of 0.9% sodium chloride solution, centrifuged at 16,200g for 10 minutes and stored at -80°C. Lung and blood samples were taken just after the animals were sacrificed. Left pulmonary lobes were washed with 10mL of 0.9% sodium chloride solution, blotted with filter paper, weighed, transferred into 2mL tubes containing 1mL of 0.9% sodium chloride solution and 3mm glass beads, crushed using a Tissue Lyser machine (Retsch MM400) for 20min at 30 cycles/s and centrifuged 10 min at 16,200g. Supernatant media were transferred into 1.5mL tubes, centrifuged 10 min at 16,200g and stored at -80°C. Recovery of plasma: One milliliter of blood was harvested in a 2mL tube containing 100µL of 0.5M EDTA (ThermoFischer Scientific) and centrifuged 10 min at 16,200g.

$TCID_{50}$ assay

Virus titration was performed with 96-well culture plates containing confluent VeroE6/TMPRSS2 cells inoculated with 150µL per well of four-fold dilutions of crushed lung supernatant samples (dilutions with medium supplemented with 2.5% FBS). After 6 days of incubation the absence/presence of cytopathic effect in each well was read and infectious titers were estimated using the Reed & Muench calculation method.

Real time quantitative RT-PCR (RT-qPCR) assays

For viral quantification in lungs clarified homogenates and nasal washes, nucleic acids from each sample were extracted using QIAamp 96 DNA kit and Qiacube HT robot (both from Qiagen). Viral RNA yields were measured using a real time RT-qPCR assay targeting the rdrp gene as previously described (26).

Quantification of Cilgavimab/Tixagevimab monoclonal antibodies in blood samples

To estimate the exposure of animals to Cilgavimab/Tixagevimab monoclonal antibodies (AZD7442), we measured the level of human IgG antibodies directed against the S1 domain of the spike protein of the SARS-CoV-2 using a commercial enzyme-linked immunosorbent assay (ELISA) kit (Euroimmun). Results were expressed in binding antibody units per mL (BAU/mL) following manufacturer instructions and converted to µg/mL using blank plasma from untreated/infected animals spiked with known quantities of AZD7442.

EC_{90} determination

We used the following non-linear function to determine the concentration/effect relationship:

$$\mathrm{VL} = \mathrm{VL}_0 \times \left(1 - \frac{\mathrm{C}_{\mathrm{AZD7442}}^{\gamma}}{\mathrm{EC}_{50}^{\gamma} + \mathrm{C}_{\mathrm{AZD7442}}^{\gamma}}\right)$$

Where VL_0 is the lung viral load in untreated animals, $\mathrm{C}_{\mathrm{AZD7442}}$ is the plasma concentration of AZD-7442, EC_{50} is the drug concentration required to decrease viral load by 50% compared to untreated animals, and γ is a sigmoidicity parameter, chosen as the one maximizing likelihood of the model. We extrapolated the EC_{90} using $\mathrm{EC}_{90} = \sqrt[\gamma]{9 \times \mathrm{EC}_{50}^{\gamma}}$. Parameters were estimated separately according to strain, using non-linear regression. Values under the limit of detection (LoD) for lung infectious titers or AZD7442 concentrations were imputed to this LoD, respectively 2.43 $TCID_{50}$/g and 0.54 µg/mL.

Graphical representations and statistical analysis

Experimental timelines were generated on biorender.com. Graphical representations and statistical analyses) were realized using Graphpad Prism 7 software, except nonlinear regressions and their corresponding graphical representations that were performed using the package *nlreg*, implemented in *R* statistical software *(http://www.R-project.org)*. Statistical details for each experiment are provided in the figure legends. P values less than 0.05 were considered statistically significant.

Results

AZD7442 *in vitro* evaluation against Omicron sub variants

First we evaluated, *in vitro*, the neutralization ability of the Evusheld cocktail against the Omicron sub variant BA.1, BA.1.1 and BA.2 using the B.1 ancestral strain as reference. We evaluated the variants sensibility to Evusheld with a standardized dose-response experiment developed for SARS-Cov-2 antivirals evaluation and applied to therapeutic antibodies (Fig 1-b). Among all three sub-variants, the BA.1.1 is less susceptible to Evusheld neutralization than BA.1 with fold change (f.c) of 91.7 and 21.5 respectively (Fig 1-c). This result is in line with a recent publication exploring Omicron sub variants antibody escape using pseudo particles. Regarding BA.2 we confirmed the restoration of Evusheld neutralizing ability with an EC_{50} of 98.9 $ng.ml^{-1}$ resulting in a smaller fold change (f.c~3.7) when compared to BA.1 and BA.1.1 (Fig 1-c). Observing that BA.1 has been totally replaced by BA.2 making BA.1.1 not epidemiologically relevant we decided to evaluate Evusheld *in vivo* only with BA.1 and BA.2.

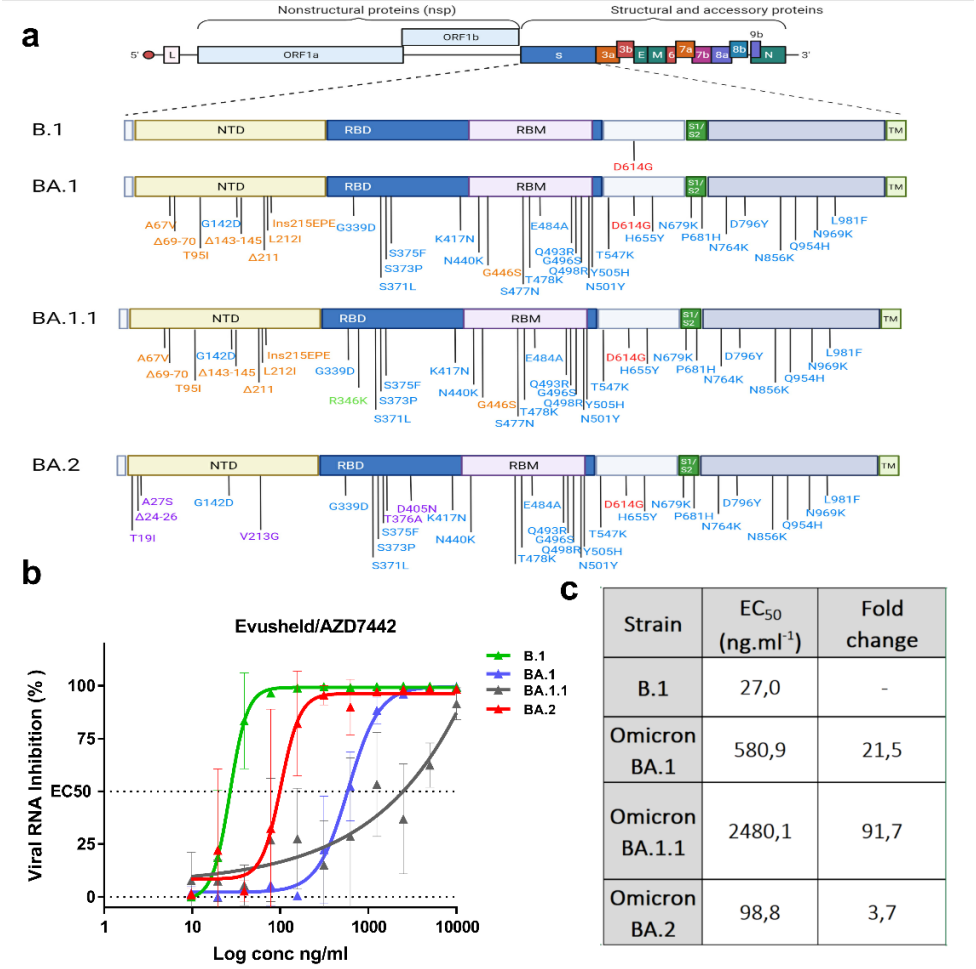

Strain	EC_{50} ($ng.ml^{-1}$)	Fold change
B.1	27,0	-
Omicron BA.1	580,9	21,5
Omicron BA.1.1	2480,1	91,7
Omicron BA.2	98,8	3,7

Figure 1: Genomic organization and in vitro evaluation of Omicron sub variant.

a) Spike substitutions in SARS-COV-2 variants Omicron BA.1, BA.1.1 and BA.2 compared to the ancestral strain B.1. Omicron BA.1, BA.2 and BA.5 sequences used for the graphical representation are the strains sequences used in this study. Red color indicates the mutation that is present in all strains. The blue color indicates the mutations, which are common to BA.1, BA.1.1 and BA.2. The blue color indicates the mutations, which are common to BA.1. BA.1.1 and BA.2.The orange color indicates the mutations that are specific to BA.1 and BA.1.1. The green color indicates the specific mutation of BA.1.1. The purple color indicated the mutations, which are specific to BA.2. b) Dose response curves reporting the susceptibility of the SARS-CoV-2 BavPat1 D614G (B.1) ancestral strain, and Omicron sub variant BA.1 BA.1.1 and BA.2 variant to Evusheld/AZD7742. c) Interpolated EC50 values (ng/mL) and fold change to B.1. Data presented are from three technical replicates in VeroE6-TMPRSS2 cells, and error bars show mean ±s.d.C) Activity of therapeutic antibodies against B.1, Omicron BA.1, BA.1.1 and BA.2 variants. Interpolated EC50 values are expressed in ng/mL. This figure was created with BioRender.com.

AZD7442 evaluation in the hamster model

We evaluated the efficacy of AZD7442 on two clinical strains, of the Omicron variant (BA.1: 2021/FR/1514 ; BA.2: 2022/FR/TCO) using the hamster model and an ancestral B.1 (G614) strain as reference. Animals received pre-exposure prophylaxis by intraperitoneal injection of 2, 4, 16 or 32 mg/kg of AZD7442. Animals were infected intranasally ($3x10^4$ $TCID_{50}$) seven days later with the BA.1 variant, the BA.2 variant or the G614 strain, and sacrificed at 3 days post-infection (dpi) (**figure 2a**).

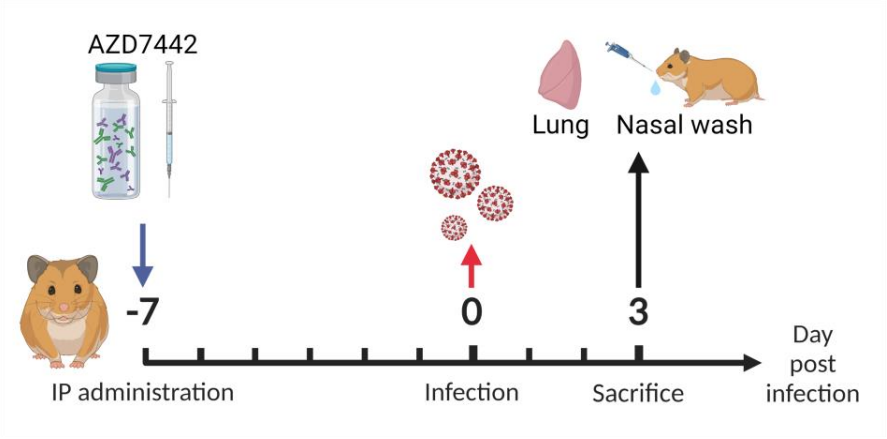

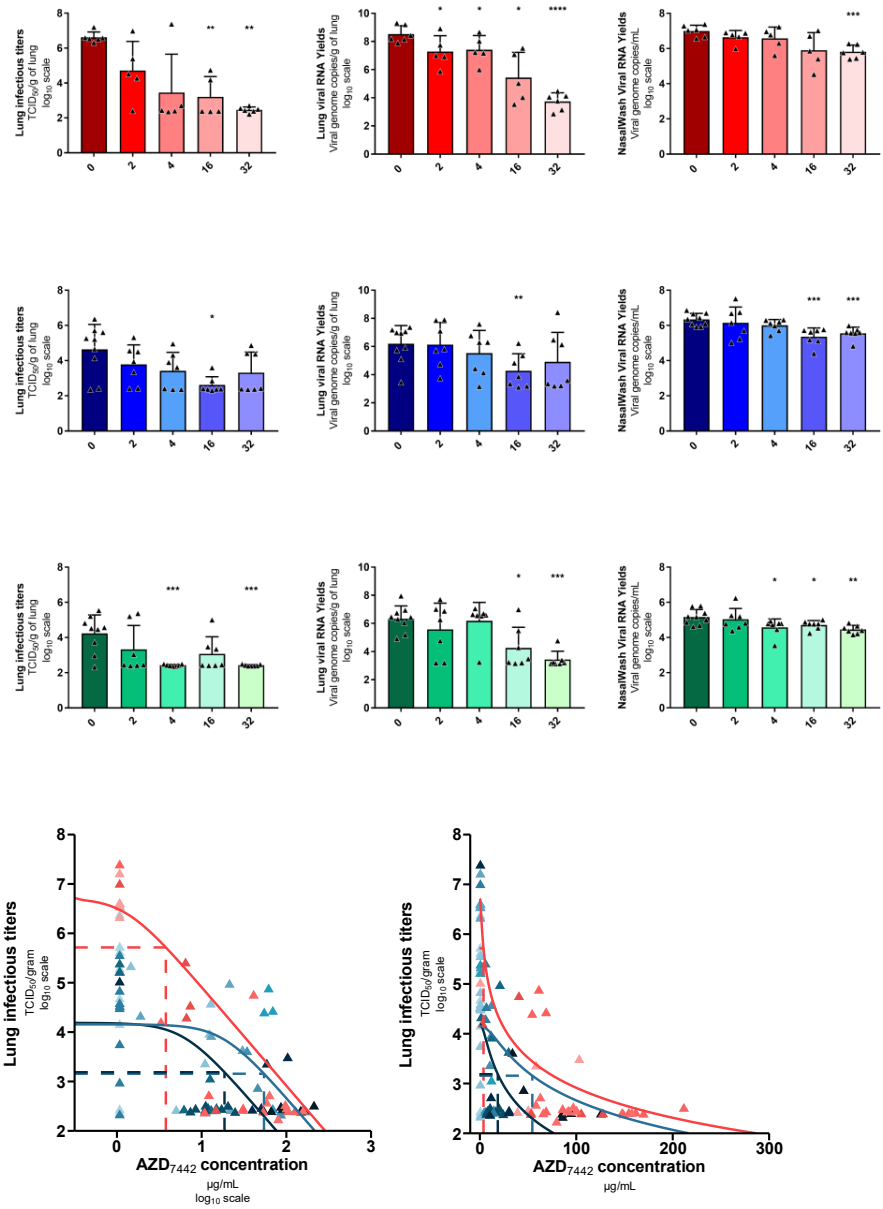

Figure 2: In vivo efficacy of pre-exposure prophylaxis of AZD7442 on G614 strain and Omicron BA.1 and BA.2 variants

(**a**) Experimental timeline (realized on biorender.com). Groups of hamsters were intraperitoneally treated with 0 (n=6 ; untreated group), 2, 4, 16 or 32 mg/kg of AZD7442 (n=5 per group for the G614 strain ; n=7 per group for the both Omicron variants). Seven days later, animals were intranasally infected with 3×10^4 $TCID_{50}$ of virus and sacrificed at 3 dpi. (**b**) Lung infectious titers measured using a $TCID_{50}$ assay. Viral RNA yields in lungs (**c**) and in nasal washes (**d**) measured using a RT-qPCR assay. (**b-d**) Data represent mean ± SD of individual data of hamsters. ****, ***, ** and * symbols indicate that the average value for the group is significantly lower than that of the untreated group with a p-value < 0.0001, ranging between 0.0001–0.001, 0.001–0.01, and 0.01–0.05, respectively. (Two-sided statistical analysis were performed using Shapiro–Wilk normality test, Student t-test, Mann–Whitney test, and Welch's test). (**e**) Dose-response curves based on lung infectious titers were established to determine 90% effective concentrations in plasmas of animals. Animals infected with the G614 strain, the BA.1 or the BA.2 Omicron variant were represented in red, blue and green respectively. Clinical follow-up of this experiment is presented in Supplemental Figure 1.

In animals infected with strain G614, administration of AZD7442 resulted in a dose-dependent decrease in infectious titers and viral RNA levels in the lungs (**figure 2b-c**). This decrease in infectious titers is significant with the dose of 16 and 32 mg/kg when compared with untreated animals (p=0.0043 and p=0.0022 respectively). For viral RNA levels, significant reduction is observed with all doses (p=0.0425 for 2 mg/kg, p=0.0468 for 4 mg/kg, p=0.0156 for 16 mg/kg and p<0.0001 for 32 mg/kg). With regard to viral load in nasal washes, a dose-dependent reduction in the amount of viral RNA is also observed but to a lesser extent than in the lungs. (**figure 2d**). It is significant with the higher dose when compared with untreated animals (p=0.0002). Regarding the impact of AZD7442 administration on the weight of the animals, we found that all doses induced a clinical attenuation of the disease at 3dpi (**supplemental figure 1**).

In animals infected with the Omicron BA.1 variant, administration of AZD7442 also induced a dose-dependent reduction in infectious titers and viral RNA levels in the lungs (**figure 2b-c**). This decrease is significant for infectious titers and viral RNA at the dose of 16 mg/kg (p=0.0115 and p=0.0088 respectively). As with strain G614, a limited dose-dependent decrease is also observed in nasal washes (**figure 2d**). It is significant with the two highest doses used when compared with untreated animals (p=0.0004 for 16 mg/kg and p=0.0006 for 32 mg/kg). As BA.1 Omicron infection has no detectable effect on the weight of the animals in our model, the impact of AZD7442 administration on the clinical course of the disease could not be assessed in this way. (**supplemental figure 1**)(27).

In animals infected with the Omicron BA.2 variant, administration of AZD7442 also induced a dose-dependent reduction in infectious titers and viral RNA levels in the lungs (**figure xxx**). This decrease is significant for infectious titers at the dose of 4 and 32 mg/kg (p=0.0008 for both) and for viral RNA at the dose of 16 and 32 mg/kg (p=0.0229 and p=0.0002 respectively). Once again, a limited dose-dependent decrease is also observed in nasal washes (**figure xxx**). It is significant with the three highest doses used when compared with untreated animals (p=0.0311 for 4 mg/kg, p=0.0263 for 16 mg/kg and p=0.0015 for 32 mg/kg). Similarly to BA.1 Omicron, the BA.2 variant infection has no detectable effect on the weight of the animals in our model, the impact of AZD7442 administration on the clinical course of the disease could not be assessed here either. (**supplemental figure 1**)

Next, the concentration of AZD7442 in plasma was measured in animals sacrificed at 3 dpi. Variable exposures were observed for identical doses, which may be related to the intraperitoneal route of administration. This variability allowed investigating the relationship between animal exposure to AZD7442 and infectious viral loads in the lungs (**figure 2e**). We conducted a nonlinear regression of infectious viral titers against plasma concentration of AZD7442. It allowed estimating 90% effective concentrations (EC_{90}) in plasma to reduce lung infectious titers with each viral strain: 3.8 µg/mL (95% confidence interval (95%CI): 0-8.8), 54.4 µg/mL (95%CI: 0-142.4) and 18.6 µg/mL (95%CI: 0-50.5) for the G614 strain, the BA.1 variant and the BA.2 variant respectively, indicating a ~18 and ~5 fold change between the ancestral and BA.1/BA.2 strain, respectively.

Discussion

Overall, our results indicate that AZD7442, when used as pre-exposure prophylaxis, has inhibitory activity *in vivo* against the Omicron BA.1 variant, although this activity is less than against a B.1 G614 virus. This is in line with previous results obtained *in vitro* (6-11) and a recent *in vivo* study in which a curative treatment with 5mg/kg of antibody cocktail, synthesized without any modification in their Fc region, efficiently inhibited the Omicron variant replication in lungs of hamsters (28). The U.S. Food Drug Administration (FDA) has published pharmacokinetic data obtained after intramuscular administration of 300mg of AZD7442 (29), the dose used successfully in the PROVENT clinical trial (NCT04625725)(30). The mean serum concentrations peak at ~30µg/mL two weeks after dosing and remain above 12 µg/mL for more than 150 days, with limited inter-individual variability (coefficient of variation was 25-39% even beyond 200 days after dosing). In our study, the plasma EC_{90} value estimated from hamsters treated preventively and infected with the G614 strain are largely below these concentrations. In contrast, the EC_{90} value estimated in hamsters infected by Omicron is close to the abovementioned exposures observed in humans after the dose of 300mg. However, the linear and dose-dependent pharmacokinetics of AZD7442 between the 300mg and 3000mg doses suggest that the 600mg dose, currently being tested in the TACKLE, ACTIV-2/3 and DisCoVeRy clinical trials (D8851C00001, NCT04723394, NCT04518410, NCT04501978 and NCT04315948), may be a recourse to compensate for the diminished efficacy of this monoclonal antibody cocktail against the Omicron variant. This increase in AZD7442 dosage has just been recommended by the U.S. FDA for pre-exposure prophylaxis of SARS-CoV-2 infection (31).

References

1. Murano K, Guo Y, Siomi H. The emergence of SARS-CoV-2 variants threatens to decrease the efficacy of neutralizing antibodies and vaccines. Biochem Soc Trans. 2021;49(6):2879-90.
2. Viana R, Moyo S, Amoako DG, Tegally H, Scheepers C, Althaus CL, et al. Rapid epidemic expansion of the SARS-CoV-2 Omicron variant in southern Africa. Nature. 2022.
3. Karim SSA, Karim QA. Omicron SARS-CoV-2 variant: a new chapter in the COVID-19 pandemic. Lancet (London, England). 2021;398(10317):2126-8.
4. Kumar S, Thambiraja TS, Karuppanan K, Subramaniam G. Omicron and Delta variant of SARS-CoV-2: A comparative computational study of spike protein. Journal of medical virology. 2022;94(4):1641-9.
5. Yamasoba D, Kimura I, Nasser H, Morioka Y, Nao N, Ito J, et al. Virological characteristics of the SARS-CoV-2 Omicron BA.2 spike. Cell. 2022;185(12):2103-15 e19.
6. Touret F, Baronti C, Bouzidi HS, de Lamballerie X. In vitro evaluation of therapeutic antibodies against a SARS-CoV-2 Omicron B.1.1.529 isolate. bioRxiv. 2022:2022.01.01.474639.
7. Aggarwal A, Stella AO, Walker G, Akerman A, Milogiannakis V, Brilot F, et al. SARS-CoV-2 Omicron: evasion of potent humoral responses and resistance to clinical immunotherapeutics relative to viral variants of concern. medRxiv. 2021:2021.12.14.21267772.
8. Planas D, Saunders N, Maes P, Guivel-Benhassine F, Planchais C, Buchrieser J, et al. Considerable escape of SARS-CoV-2 Omicron to antibody neutralization. Nature. 2021.
9. Cao Y, Wang J, Jian F, Xiao T, Song W, Yisimayi A, et al. Omicron escapes the majority of existing SARS-CoV-2 neutralizing antibodies. Nature. 2021.
10. Cameroni E, Bowen JE, Rosen LE, Saliba C, Zepeda SK, Culap K, et al. Broadly neutralizing antibodies overcome SARS-CoV-2 Omicron antigenic shift. Nature. 2021.
11. VanBlargan LA, Errico JM, Halfmann PJ, Zost SJ, Crowe JE, Jr., Purcell LA, et al. An infectious SARS-CoV-2 B.1.1.529 Omicron virus escapes neutralization by therapeutic monoclonal antibodies. Nat Med. 2022.
12. Iketani S, Liu L, Guo Y, Liu L, Chan JF, Huang Y, et al. Antibody evasion properties of SARS-CoV-2 Omicron sublineages. Nature. 2022;604(7906):553-6.
13. Zhou H, Tada T, Dcosta BM, Landau NR. Neutralization of SARS-CoV-2 Omicron BA.2 by Therapeutic Monoclonal Antibodies. bioRxiv. 2022.
14. Bruel T, Hadjadj J, Maes P, Planas D, Seve A, Staropoli I, et al. Serum neutralization of SARS-CoV-2 Omicron sublineages BA.1 and BA.2 in patients receiving monoclonal antibodies. Nat Med. 2022;28(6):1297-302.
15. Dong J, Zost SJ, Greaney AJ, Starr TN, Dingens AS, Chen EC, et al. Genetic and structural basis for recognition of SARS-CoV-2 spike protein by a two-antibody cocktail. bioRxiv. 2021:2021.01.27.428529.
16. Stuver R, Shah GL, Korde NS, Roeker LE, Mato AR, Batlevi CL, et al. Activity of AZD7442 (tixagevimab-cilgavimab) against Omicron SARS-CoV-2 in patients with hematologic malignancies. Cancer Cell. 2022;40(6):590-1.
17. Benotmane I, Velay A, Vargas GG, Olagne J, Thaunat O, Fafi-Kremer S, et al. Pre-exposure prophylaxis with 300 mg Evusheld elicits limited neutralizing activity against the Omicron variant. Kidney Int. 2022.
18. Tada T, Zhou H, Dcosta BM, Samanovic MI, Chivukula V, Herati RS, et al. Increased resistance of SARS-CoV-2 Omicron variant to neutralization by vaccine-elicited and therapeutic antibodies. EBioMedicine. 2022;78:103944.
19. Touret F, Baronti C, Bouzidi HS, de Lamballerie X. In vitro evaluation of therapeutic antibodies against a SARS-CoV-2 Omicron B.1.1.529 isolate. Sci Rep. 2022;12(1):4683.

20. Touret F, Baronti C, Goethals O, Van Loock M, de Lamballerie X, Querat G. Phylogenetically based establishment of a dengue virus panel, representing all available genotypes, as a tool in dengue drug discovery. Antiviral Res. 2019;168:109-13.
21. Touret F, Gilles M, Barral K, Nougairede A, van Helden J, Decroly E, et al. In vitro screening of a FDA approved chemical library reveals potential inhibitors of SARS-CoV-2 replication. Sci Rep. 2020;10(1):13093.
22. Delang L, Li C, Tas A, Querat G, Albulescu IC, De Burghgraeve T, et al. The viral capping enzyme nsP1: a novel target for the inhibition of chikungunya virus infection. Sci Rep. 2016;6:31819.
23. Weiss A, Touret F, Baronti C, Gilles M, Hoen B, Nougairede A, et al. Niclosamide shows strong antiviral activity in a human airway model of SARS-CoV-2 infection and a conserved potency against the Alpha (B.1.1.7), Beta (B.1.351) and Delta variant (B.1.617.2). PLoS One. 2021;16(12):e0260958.
24. Touret F, Driouich JS, Cochin M, Petit PR, Gilles M, Barthelemy K, et al. Preclinical evaluation of Imatinib does not support its use as an antiviral drug against SARS-CoV-2. Antiviral Res. 2021;193:105137.
25. Kaptein SJF, Goethals O, Kiemel D, Marchand A, Kesteleyn B, Bonfanti JF, et al. A pan-serotype dengue virus inhibitor targeting the NS3-NS4B interaction. Nature. 2021;598(7881):504-9.
26. Driouich JS, Cochin M, Lingas G, Moureau G, Touret F, Petit PR, et al. Favipiravir antiviral efficacy against SARS-CoV-2 in a hamster model. Nature communications. 2021;12(1):1735.
27. McMahan K, Giffin V, Tostanoski LH, Chung B, Siamatu M, Suthar MS, et al. Reduced Pathogenicity of the SARS-CoV-2 Omicron Variant in Hamsters. bioRxiv. 2022:2022.01.02.474743.
28. Uraki R, Kiso M, Imai M, Yamayoshi S, Ito M, Ujie M, et al. Therapeutic efficacy of antibodies and antivirals against a SARS-CoV-2 Omicron variant, PREPRINT (Version 1) available at Research Square [https://doi.org/10.21203/rs.3.rs-1240227/v1]. 2022.
29. USaFoodaandaDrugaAdministration. Fact sheet for health care providers: Emergency Use Authorization for Evusheld (tixagevimab co-packaged with cilgavimab). https://www.fda.gov/media/154701/download. Accessed February 17, 2022. 2022.
30. AstraZeneca. Evusheld long-acting antibody combination retains neutralizing activity against Omicron variant in independent FDA study. Published December 16, 2021. https://www.astrazeneca.com/. Accessed February 21, 2022. 2022.
31. USaFoodaandaDrugaAdministration. FDA authorizes revisions to Evusheld dosing . https://www.fda.gov/drugs/drug-safety-and-availability/fda-authorizes-revisions-evusheld-dosing. Accessed February 26, 2022. 2022.

Acknowledgments

We thank Pr C Drosten for providing the SARS-CoV-2 BavPat strain through EVA GLOBAL. We thank Dr Cécile Baronti (Unité des Virus Émergents) for isolation, production and characterisation of the SARS-CoV-2 Omicron BA.1, and making it available through EVA-GLOBAL.

This work was conducted in the framework of the Preclinical Study Group of the French agency for emerging infectious diseases (ANRS-MIE). It was supported by the ANRS-MIE (BIOVAR project of the EMERGEN research programme) and by the European Commission (European Virus Archive Global project (EVA GLOBAL, grant agreement No 871029) of the Horizon 2020 research and innovation programme).

Declaration of interests

The authors declare no competing interests.

Contributors

AN and XDL conceived the experiments. XDL proposed the study. JSD, LL, MC, PMSV, GM, PRP, FT and AN performed the experiments. JSD, GL, LL, MC, JG and AN analyzed the results. JSD, AN and XDL wrote the paper. All the authors reviewed and edited the paper.

Annexe 4 : Matériel supplémentaire du chapitre 5

PNAS
www.pnas.org

Supplementary Information for

Modeling SARS-CoV-2 viral kinetics and association with mortality in hospitalized patients from the French Covid cohort

Nadège Néant[1]*, Guillaume Lingas[1]*, Quentin Le Hingrat[1,2]*, Jade Ghosn[1,3], Ilka Engelmann[4], Quentin Lepiller[5], Alexandre Gaymard[6,7], Virginie Ferré[8], Cédric Hartard[9], Jean-Christophe Plantier[10], Vincent Thibault[11], Julien Marlet[12,13], Brigitte Montes[14], Kevin Bouiller[15], François-Xavier Lescure[3], Jean-François Timsit[16], Emmanuel Faure[17], Julien Poissy[18], Christian Chidiac[19], François Raffi[20,21], Antoine Kimmoun[22], Manuel Etienne[23], Jean-Christophe Richard[24], Pierre Tattevin[25], Denis Garot[26], Vincent Le Moing[27], Delphine Bachelet[28], Coralie Tardivon[28], Xavier Duval[1,29], Yazdan Yazdanpanah[1,3], France Mentré[1,28], Cédric Laouénan[1,28]*, Benoit Visseaux[1,2]*, Jérémie Guedj[1]*, for the French COVID cohort investigators and study group

*: the authors equally contributed

Corresponding author: Nadège Néant

nadege.neant@inserm.fr

This PDF file includes:

Supplementary Information Text

1) Data description

A- Viral load data

Ct results were transformed into log_{10} RNA copies/mL using the relationship assessed by Pasteur Institute for both E and RdRp genes [1].

In order to homogenize viral loads after transformations from Ct to log_{10} RNA copies/mL, gene E log_{10} viral loads were converted to IP4 log_{10} viral loads, using regression analysis coefficients determined on patients whose RT-PCR for both genes had been performed (N=72, r=0.95, $p<10^{-5}$).

Thus, the relationship between viral load transformation from E gene viral load to IP4 viral load was:

$$log_{10}\, VL_{IP4} = -2{,}26321 + 1{,}1211 \times \left(VL_{Egene}\right)$$

B- Lower respiratory tract (LRT) samples

LRT samples were available in 98 patients, and included tracheal aspirate, broncho-alveolar lavage and bronchial aspirate (see Table S1). We compared the mortality in patients for which at least one LRT was available and those for which no LRT data was available (Fig. S9). Finally we compared the viral load levels in individuals having samples at the same time (+/- 2 days). In individuals having several pairs of observations, only the first one was considered.

C- Viral load and survival

We performed a Kaplan Meier survival analysis to compare the cumulative incidence of mortality among patient with high (≥6 log_{10} copies/mL) and low viral load (<6 log_{10} copies/mL) at different time points, i.e., 3, 7 and 14 days (+/- 2 days) after symptom onset. Log rank testing was used to compare the cumulative incidence of mortality between these two groups.

2) Viral dynamic modeling

A- Mathematical models of antigen-driven immune response

We tested several models with an antigen-driven immune response, noted F. For the sake of comparison, we used models with a similar parameterization and the same number of unknown parameters. In all models we assumed that F was dimensionless and we fixed $d_f=0.4\ d^{-1}$

Model A. Target-cell limited model with an eclipse phase

$$\frac{dT}{dt} = -\beta V_i T$$

$$\frac{dI_1}{dt} = \beta V_i T - kI_1$$

$$\frac{dI_2}{dt} = kI_1 - \delta I_2$$

$$\frac{dV_i}{dt} = p\mu I_2 - cV_i$$

$$\frac{dV_{ni}}{dt} = p(1-\mu)I_2 - cV_{ni}$$

Model B: Immune effector F leads to protection of target cells

$$\frac{dT}{dt} = -\beta V_i T - \phi \frac{F}{F+\theta} T$$

$$\frac{dI_1}{dt} = \beta V_i T - kI_1$$

$$\frac{dI_2}{dt} = kI_1 - \delta I_2$$

$$\frac{dV_i}{dt} = p\mu I_2 - cV_i$$

$$\frac{dV_{ni}}{dt} = p(1-\mu)I_2 - cV_{ni}$$

$$\frac{dF}{dt} = I_2 - d_f F$$

Model C: Immune effector F blocks viral production

$$\frac{dT}{dt} = -\beta V_i T$$

$$\frac{dI_1}{dt} = \beta V_i T - kI_1$$

$$\frac{dI_2}{dt} = kI_1 - \delta I_2$$

$$\frac{dV_i}{dt} = p \times \left(1 - \phi \frac{F}{F+\theta}\right) \times \mu I_2 - cV_i$$

$$\frac{dV_{ni}}{dt} = p \times \left(1 - \phi \frac{F}{F+\theta}\right) \times (1-\mu) I_2 - cV_{ni}$$

$$\frac{dF}{dt} = I_2 - d_f F$$

Model D: Immune effector F blocks cell infection

$$\frac{dT}{dt} = -\beta \times \left(1 - \phi \frac{F}{F+\theta}\right) \times V_i T$$

$$\frac{dI_1}{dt} = \beta \times \left(1 - \phi \frac{F}{F+\theta}\right) \times V_i T - kI_1$$

$$\frac{dI_2}{dt} = kI_1 - \delta I_2$$

$$\frac{dV_i}{dt} = p\mu I_2 - cV_i$$

$$\frac{dV_{ni}}{dt} = p(1-\mu) I_2 - cV_{ni}$$

$$\frac{dF}{dt} = I_2 - d_f F$$

Model E: Immune effector F increases viral clearance

$$\frac{dT}{dt} = -\beta V_i T$$

$$\frac{dI_1}{dt} = \beta V_i T - kI_1$$

$$\frac{dI_2}{dt} = kI_1 - \delta I_2$$

$$\frac{dV_i}{dt} = p\mu I_2 - cV_i - \phi \frac{F}{F+\theta} V_i$$

$$\frac{dV_{ni}}{dt} = p(1-\mu) I_2 - cV_{ni} - \phi \frac{F}{F+\theta} V_{ni}$$

$$\frac{dF}{dt} = I_2 - d_f F$$

Model F: Immune effector F increases the elimination of infected cells

$$\frac{dT}{dt} = -\beta V_i T$$

$$\frac{dI_1}{dt} = \beta V_i T - kI_1$$

$$\frac{dI_2}{dt} = kI_1 - \delta I_2 - \phi \frac{F}{F+\theta} I_2$$

$$\frac{dV_i}{dt} = p\mu I_2 - cV_i$$

$$\frac{dV_{ni}}{dt} = p(1-\mu) I_2 - cV_{ni}$$

$$\frac{dF}{dt} = I_2 - d_f F$$

B. Alternative models for the time-dependent change in the elimination rate of infected cells

Model F provided the best fit to the data, suggesting an antigen-dependent effect in the loss rate of infected cells (Table S4).

Next, we tested different other models accounting for the changes in the loss rate of infected cells after day 12, which was the median time of antibody seroconversion. We also considered simpler models where that F and I_2 were in quasi-steady state. However none of these models improved the data fitting (SI appendix, Table S5).

Model F1. Loss rate of productive infected cells takes on a new value after 12 days post symptom onset

$$\frac{dT}{dt} = -\beta V_i T$$

$$\frac{dI_1}{dt} = \beta V_i T - kI_1$$

$$\frac{dI_2}{dt} = kI_1 - \delta I_2$$

$$\frac{dV_i}{dt} = p\mu I_2 - cV_i$$

$$\frac{dV_{ni}}{dt} = p(1-\mu)I_2 - cV_{ni}$$

$$\delta = \delta_0 + \delta_1 I_{\{time>12\}}$$

Model F2. Loss rate of productive infected cells increases continuously after 12 days post symptom onset

The model assumed a saturation after day 30 to reflect the saturation of antibody levels over time

$$\frac{dT}{dt} = -\beta V_i T$$

$$\frac{dI_1}{dt} = \beta V_i T - kI_1$$

$$\frac{dI_2}{dt} = kI_1 - \delta_\tau I_2$$

$$\frac{dV_i}{dt} = p\mu I_2 - cV_i$$

$$\frac{dV_{ni}}{dt} = p(1-\mu)I_2 - cV_{ni}$$

$$\delta_\tau = \delta_0 \, exp^{w \times min((t-12),30)} I_{\{time>12\}}$$

Model F3: F and I_2 are in quasi steady-state

We studied the case where F and I_2 are in quasi steady state ($F = a \times I_2$), assuming in addition with $\theta \gg F$, leading to a simplification of model F as follows:

$$\frac{dT}{dt} = -\beta V_i T$$

$$\frac{dI_1}{dt} = \beta V_i T - kI_1$$

$$\frac{dI_2}{dt} = kI_1 - \delta I_2 - \phi I_2^2$$

$$\frac{dV_i}{dt} = p\mu I_2 - cV_i$$

$$\frac{dV_{ni}}{dt} = p(1-\mu)I_2 - cV_{ni}$$

Fig. S1. Cumulative incidence of mortality according to the level of viral load at 3 (a), 7 (b) and 14 (c) days since symptom onset.

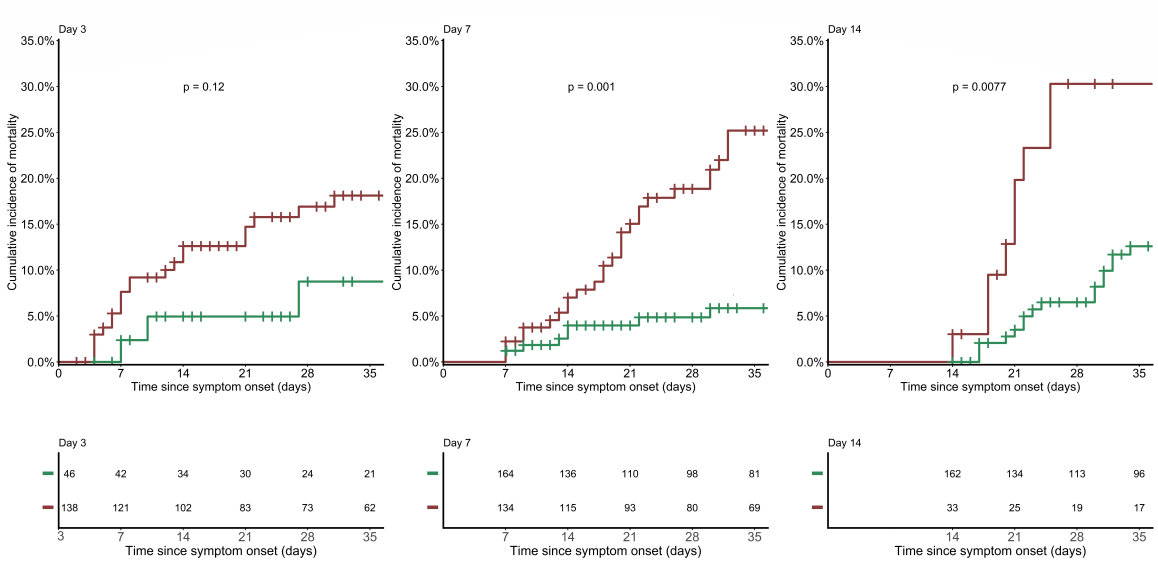

Green line are patient with viral load < 6 $\log_{10}$ copies/mL and red line are patients with viral load ≥ 6 $\log_{10}$ copies/mL at 3, 7 and 14 days post symptom onset (+/- 2 days). Below are the number of patients included in each analysis (first time point) and still available over time.

Fig. S2. The viral kinetic models tested.

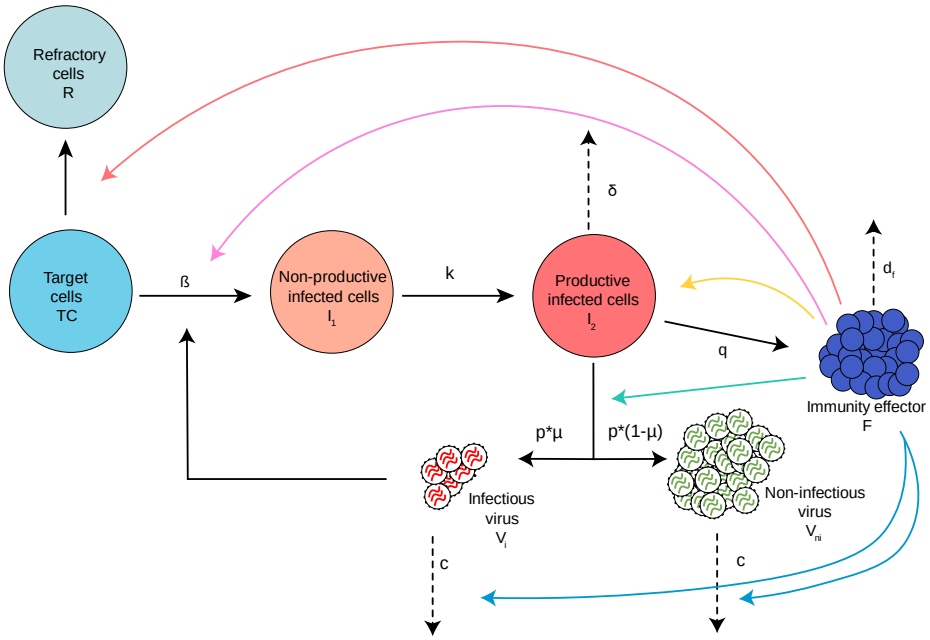

Five models incorporating immune response compartment (F) were compared with the standard model (target-cell limited model): reducing viral infectivity, leading to cells refractory to infection (red arrow), decreasing the rate of viral production (green arrow) and the infection rate (pink arrow), increasing the viral clearance (blue arrow) or the loss rate of infected cell (yellow arrow).

Fig. S3. Individual predictions of nasopharyngeal viral kinetic in the 131 patients for which 3 serial NP samples were available.

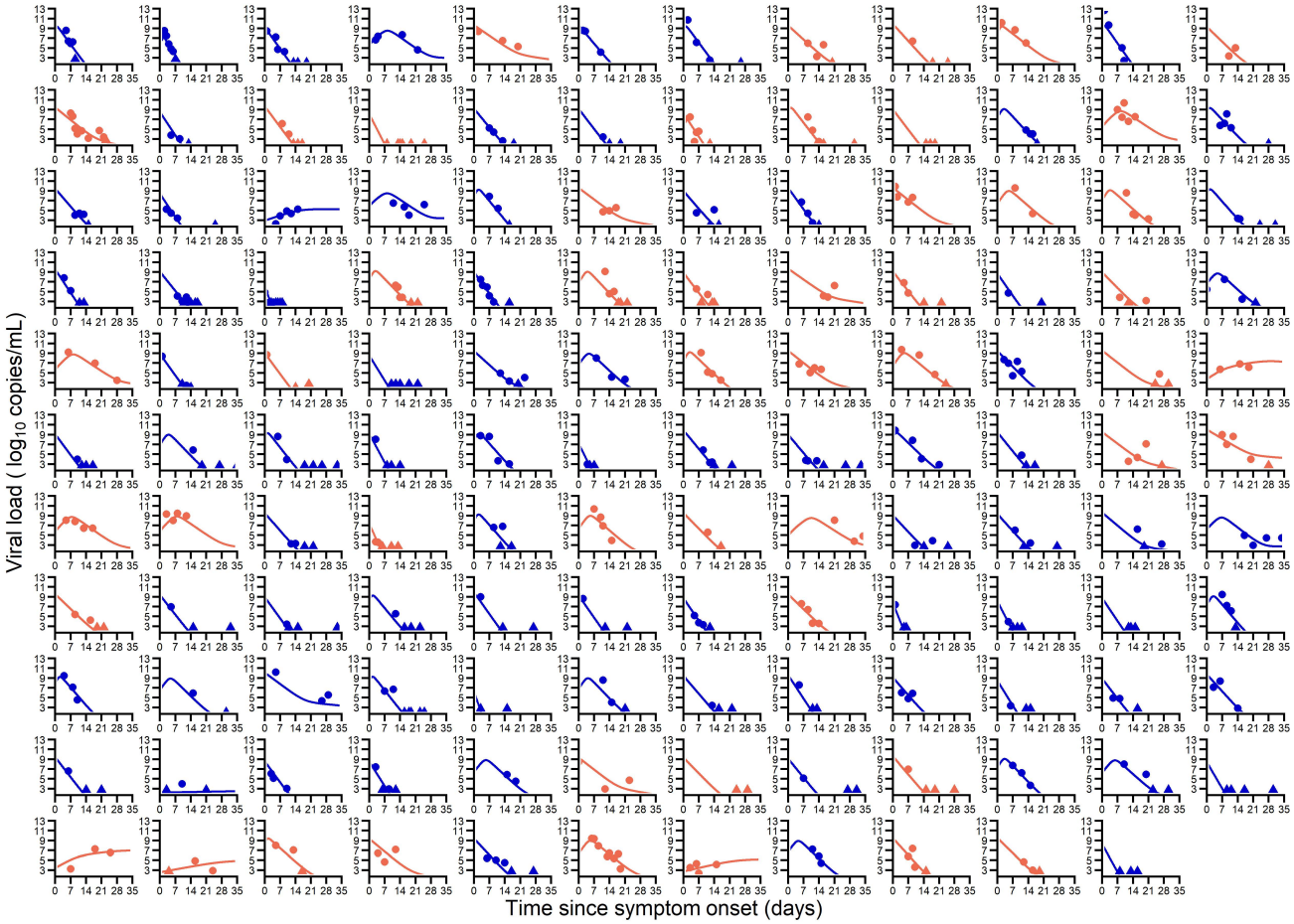

The solid line is the individual prediction of viral load and the circles are the observed data according to age (Blue: age <65 year. Orange: age ≥65). Triangles are data below the limit of detection.

Fig. S4. Visual predictive check of cytotoxic model.

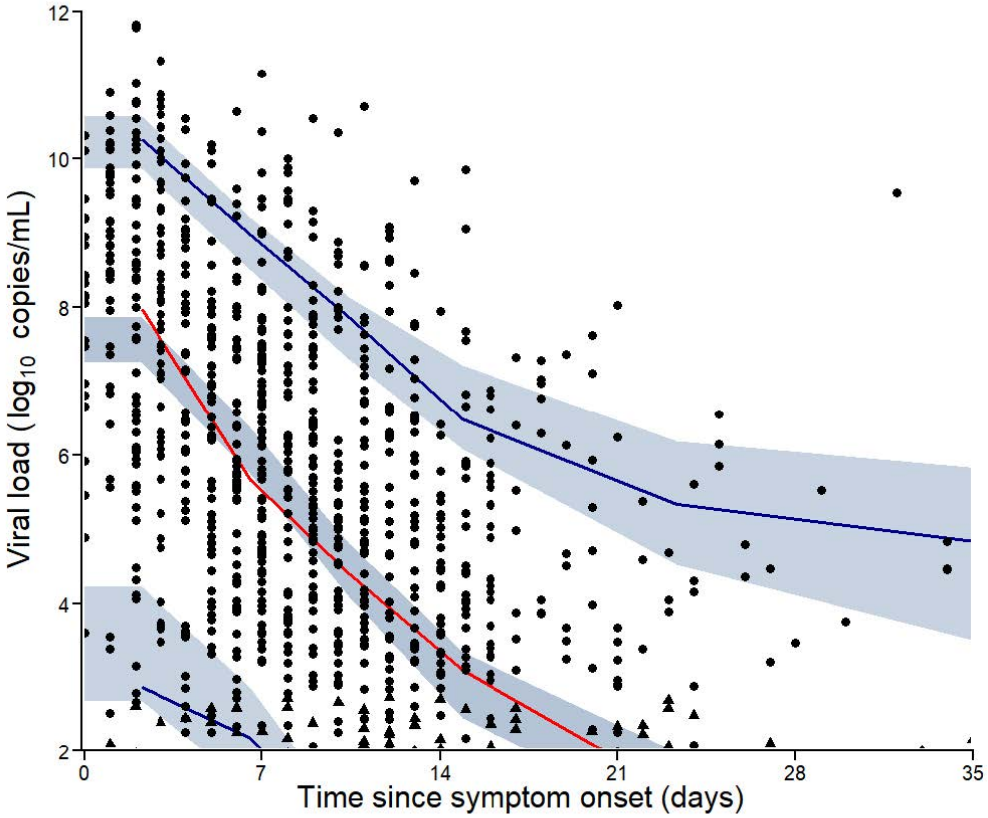

The circles represent the observed data. The triangles represent data below the limit of detection. The red line indicates the 50th percentiles of the observed data. The blue lines indicate the 5th and 95th percentiles of the observed data. The shaded areas represent 90% confidence interval (CI) of the simulated 50th, 5th and 95th percentiles.

Fig. S5. Predicted time to viral clearance according corticosteroid treatment (a) or antiviral treatment (b).

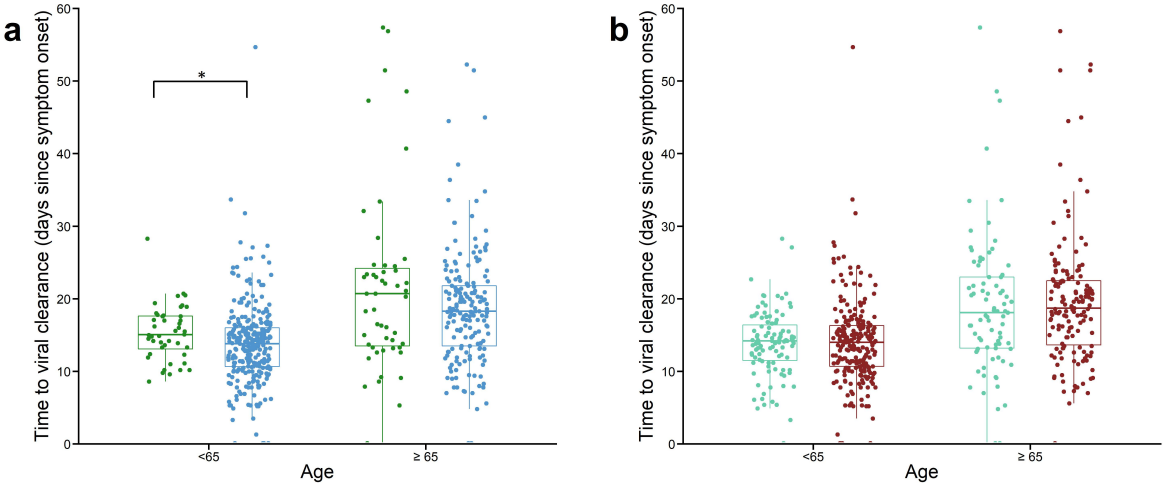

Green: patients treated by corticosteroid, blue: patients not treated by corticosteroid. * Significant difference was found between patients <65 (p=0.01). b) Light green: patients treated by antiviral, brown: patients not treated by antiviral treatment.

Fig. S6. Cumulative incidence of seroconversion IgG againstSARS-CoV-2 since symptom onset in 76 patients. (Blue: age < 65 year. Orange: age ≥ 65).

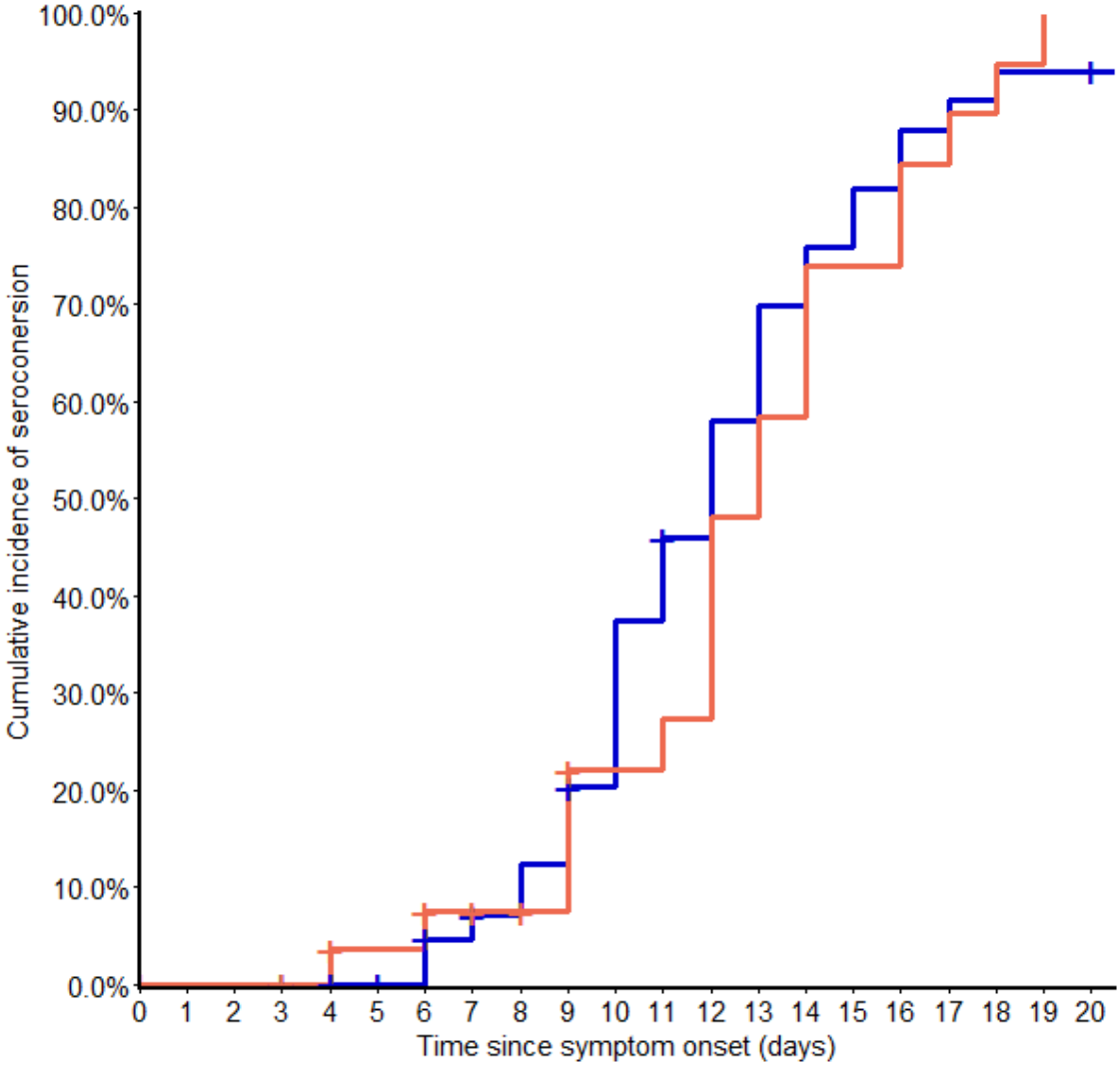

Fig. S7. Sensitivity analysis on fixed parameters.

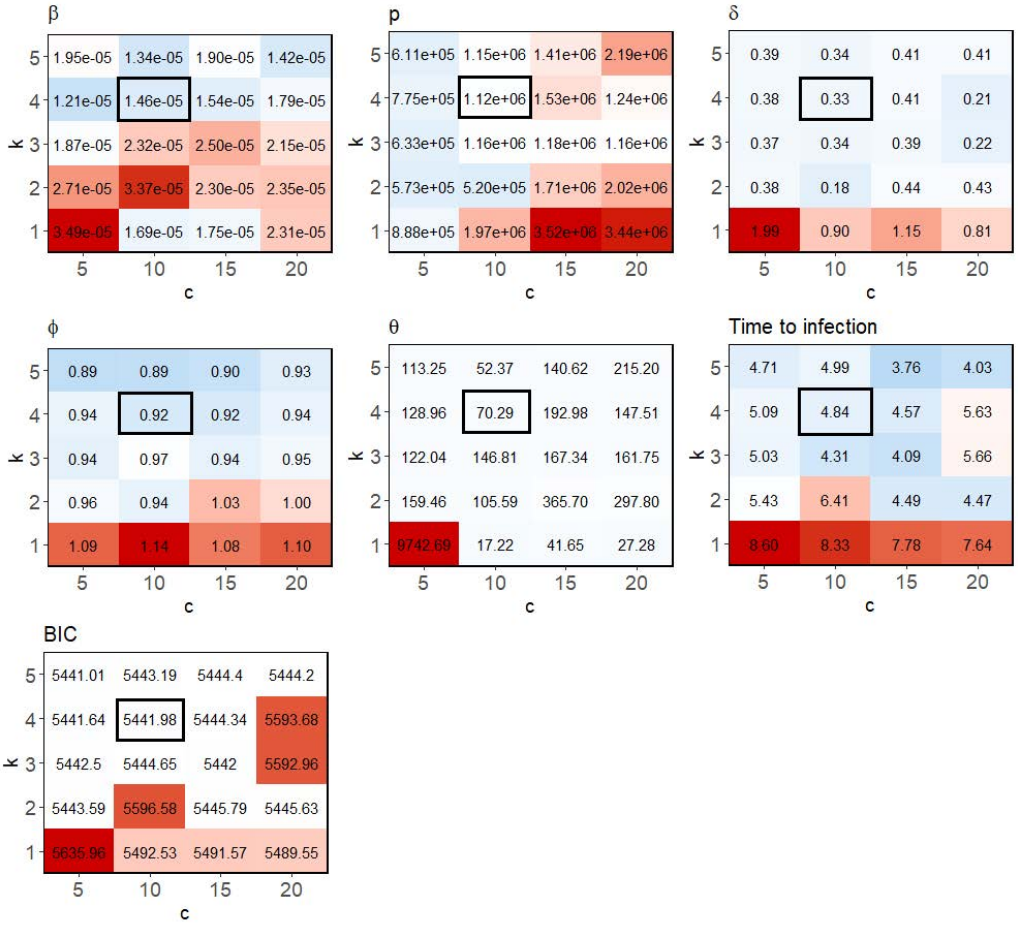

Estimation was performed with different value for each fixed parameter using the final model. BIC values and estimated population median values for $\beta, p, \delta, \phi, \theta$ and time of infection are reported. Colors indicate BIC or parameter values, with dark blue indicating lower values, white indicating median values and dark red indicating larger estimated values. The reference model is k=4 d^{-1} and c=10 d^{-1}(black border). The model fit with $T_0=1.33\times10^5$ cells.mL^{-1}, $d_f = 0.4$ d^{-1}, $\mu=0.0001$.

Fig. S8. Viral load at the time of death. Left: observed viral load at the time of death (+/- 2 days); Right: predicted viral load at the time of death using the final model

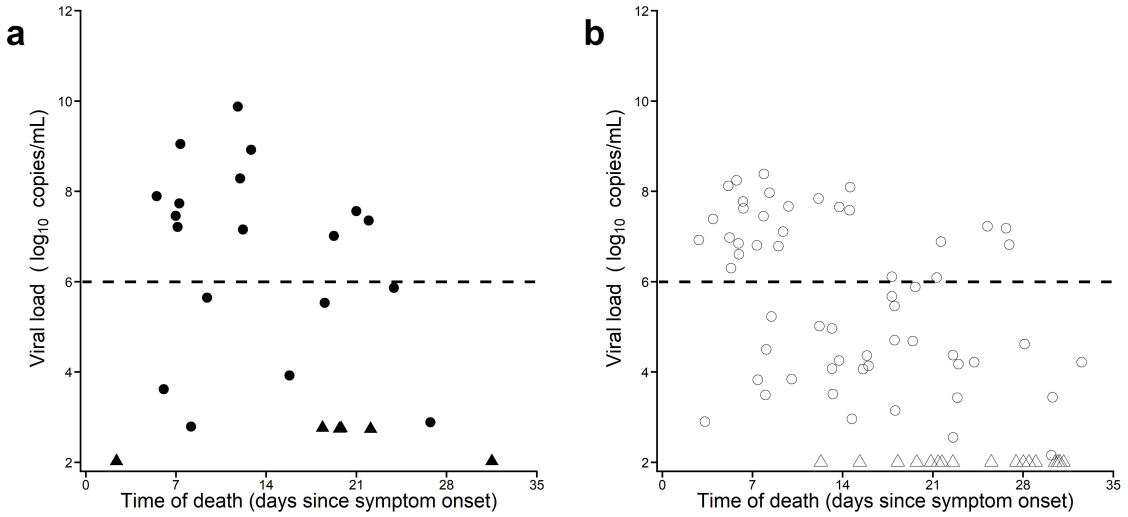

The dark circles and the black triangles represent the observed data and the data below the limit of detection, respectively. The empty circles and the empty triangles represent the viral load data predicted by the model at the time of death. Black horizontal dashed line represents threshold of positive culture.

Fig. S9. Visual predictive check of the predicted mortality.

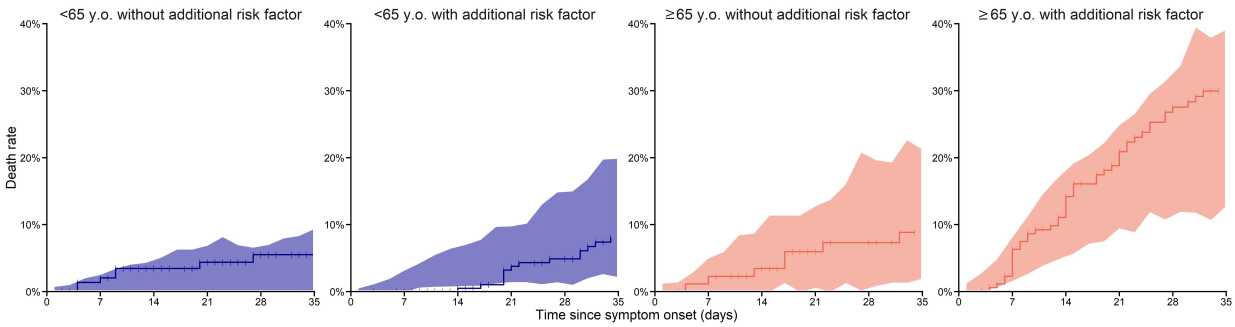

The shaded area are the 90% prediction interval using the technique proposed in Tardivon et al [2].

The solid line are the Kaplan-Meier estimates of survival in each population category.

Figure S10. a) Cumulative incidence of mortality in patients having at least one LRT sample (N=98, black) and those having no LRT samples (N=557, grey). Log-rank test (P < 0.0001) b) Correlation between NP and LRT viral load data in patients sampled on the same day (+/- 2 days).

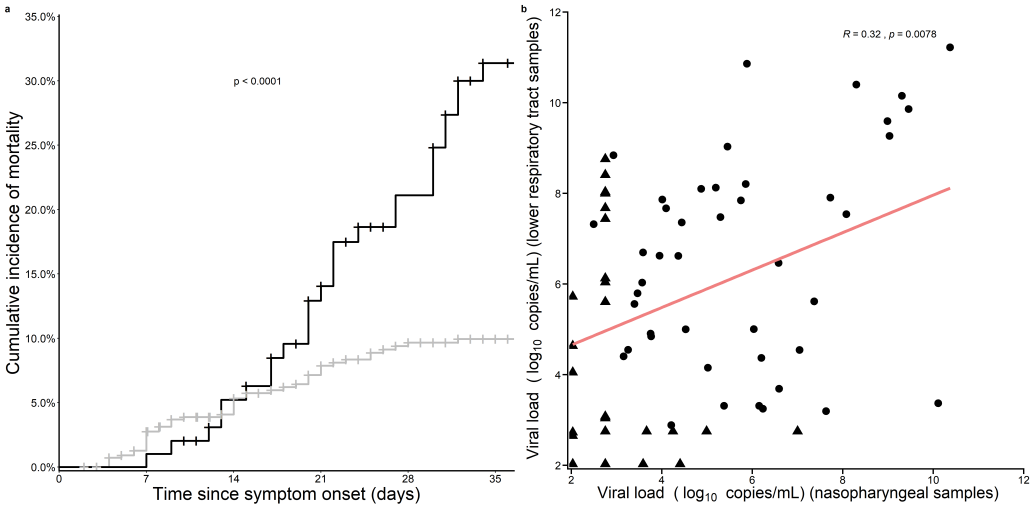

In patients having several pairs of data points, only the first one was used. Triangles are data below the limit of detection.

Table S1. Linear regression analysis on the factors associated with viral load at admission.

	Univariate analysis		Multivariate analysis	
Parameter	Coefficient	*P-value*	Coefficient	*P-value*
Time since symptom onset	-0.22	**$<10^{-5}$**	-0.21	**$<10^{-5}$**
Age ≥65	0.13	0.53		
Male gender	-0.16	0.45		
Chronic cardiac disease	0.6	**0.01**	0.62	**0.009**
Chronic pulmonary disease	0.15	0.65		

Table S2. Number of patients having nasopharyngeal (NP) samples or lower respiratory tract (LRT) samples according to the phase of the disease.

	Number of patients having NP samples			**Number of patients having LRT samples**		
Data points available in each phase	0-7 days since symptom onset N=326	7-14 days since symptom onset N=371	≥14 days since symptom onset N=222	0-7 days since symptom onset N=15	7-14 days since symptom onset N=46	≥14 days since symptom onset N=65
1	292 (89.6%)	289 (77.9%)	144 (64.9%)	13 (86.7%)	30 (65.2%)	21 (32.3%)
2	27 (8.3%)	58 (15.6%)	36 (16.2%)	1 (6.7%)	9 (19.6%)	19 (29.2%)
3	4 (1.2%)	20 (5.4%)	23 (10.4%)	1 (6.7%)	7 (15.2%)	15 (23.1%)
≥4	3 (0.9%)	4 (1.1%)	19 (8.5%)			

Table S3. Description of alternative models of immune response.

Models	Description of the model	Equation
Model A: TCL model (without immune response)	The model assumes a constant loss rate of infected cells	$\frac{dI_2}{dt} = kI_1 - \delta I_2$
Model B: F leads target cells refractory to infection	The model assumes a protection of target cells by rendering them definitely refractory to the infection	$\frac{dT}{dt} = -\beta V_i T - \phi \frac{F}{F+\theta} T$
Model C: F decreases the rate of viral production	The model assumes a decrease of non-infectious and infectious viruses' production in the same fashion	$\frac{dV_i}{dt} = p \times \left(1 - \phi \frac{F}{F+\theta}\right) \times \mu I_2 - cV_i$ $\frac{dV_{ni}}{dt} = p \times \left(1 - \phi \frac{F}{F+\theta}\right) \times (1-\mu) I_2 - cV_{ni}$
Model D: F decreases infection rate	The model assumes a protection of target cells by decreasing infection rate, decreasing the number of infected cells	$\frac{dT}{dt} = -\beta \times \left(1 - \phi \frac{F}{F+\theta}\right) \times V_i T$ $\frac{dI_1}{dt} = \beta \times \left(1 - \phi \frac{F}{F+\theta}\right) \times V_i T - kI_1$
Model E: F increases viral clearance	The model assumes two mechanisms of viral elimination	$\frac{dV_i}{dt} = p\mu I_2 - cV_i - \phi \frac{F}{F+\theta} V_i$
Model F: F increases the clearance of infected cells	The model assumes two mechanisms of cell elimination	$\frac{dI_2}{dt} = kI_1 - \delta I_2 - \phi \frac{F}{F+\theta} I_2$

Table S4. Selection procedure of longitudinal models tested.

Model	BIC	Residual error
Model A	4485.54	1.53
Model B	4504.24	1.54
Model C	4503.78	1.57
Model D	4488.10	1.54
Model E	4503.75	1.56
Model F	4487.59	1.45

The quality of model fit was evaluated by both the BIC and residual error for each of the models tested. The model providing both the lowest BIC and the lowest residual errors was retained.

Table S5. Description of alternative models of immune response that did not include an explicit antigen-dependent stimulation.

Models	Description of the model	Equation
Model F with an age-dependent immune response	The model assumes two mechanisms of cell elimination The parameter φ is age-dependent	$\frac{dI_2}{dt} = kI_1 - \delta I_2 - \phi \frac{F}{F+\theta} I_2$ $\phi = \phi_0 + \phi_1 I_{\{age>65\}}$
Model F1: TCL model with a time dependent adaptive immune response	The model assumes a constant loss rate of infected cells The parameter δ changes at time t=12 days post symptom onset to reflect antibody increase	$\frac{dI_2}{dt} = kI_1 - \delta I_2$ $\delta = \delta_0 + \delta_1 I_{\{time>12\}}$
Model F2: TCL model with a time dependent adaptive immune response	The model assumes a constant loss rate of infected cells The parameter δ increases exponentially from t=12 days post symptom onset to t=30 days to reflect the progressive increase of antibody increase	$\frac{dI_2}{dt} = kI_1 - \delta I_2$ $\delta_\tau = \delta_0 + \delta_1 \, exp^{w \times min((t-12),30)} I_{\{time>12\}}$
Model F3: Assuming that F and I_2 are in quasi steady-state at all times ($F = a \times I_2$) and that $\theta >> a \times I_2$	The model assumes two mechanisms of cell elimination, one linear and one quadratic The quadratic term φ is age-dependent	$\frac{dI_2}{dt} = kI_1 - \delta I_2 - \phi I_2^2$ $\phi = \phi_0 + \phi_1 I_{\{age>65\}}$

Table S6. Parameter estimates of alternative models of immune response.

	Model F	Model F1	Model F2	Model F3
Longitudinal model	*Fixed effect (RSE%)*			
$\boldsymbol{\beta}$ **(mL.virus^{-1}. d^{-1})**	1.46×10^{-5}(23.4)	1.17×10^{-5} (21.2)	4.85×10^{-5} (16.7)	2.2×10^{-5}(> 100)
$\boldsymbol{pT_0}$ **(virus.mL^{-1}.d^{-1})**	1.48×10^{11} (26.8)	1.77×10^{11}(34.3)	5.71×10^{10}(31)	1.50×10^{11} (33)
$\boldsymbol{\delta}$ **(d^{-1})**	0.33 (30.0)	–	–	1.04 (6.5)
$\boldsymbol{\delta_2}$ **(d^{-1})**	–	0.13 (37.7)	–	–
$\boldsymbol{\delta_{age}(< 65)}$ **(d^{-1})**	–	1.23 (5.8)	1.04 (6.3)	–
$\boldsymbol{\delta_{age}(\geq 65)}$ **(d^{-1})**	–	0.98 (22.3)	0.82 (19.9)	–
$\boldsymbol{\omega}$ **(d^{-1})**	–	–	0.005 (52.3)	–
$\boldsymbol{\phi_{age}(< 65)}$ **(d^{-1})**	0.92 (8.67)	–	–	1.14×10^{-5} (14.8)
$\boldsymbol{\phi_{age}(\geq 65)}$ **(d^{-1})**	0.65 (23.3)	–	–	1.22×10^{-5}(572)
$\boldsymbol{\theta}$ **(F.mL^{-1})**	70 (80.8)	–	–	–
$\boldsymbol{T_{inf}}$ **(d)**	4.8 (3.2)	5.8 (8.5)	6.4 (6.0)	5.15 (8.6)
Survival Model	*Hazard Ratio (RSE%)*			
Viral load (log$_{10}$ copies/mL)	1.31 (17)	1.30 (16.1)	1.29 (19.3)	1.30 (15.8)
Age ≥65	2.58 (37.9)	2.58 (42.3)	2.58 (24.4)	2.83 (23.8)
Male gender	2.55 (25.2)	2.54 (33.1)	2.51 (42.9)	2.53 (25.6)
Chronic pulmonary disease	2.31 (36.8)	2.30 (30.7)	2.78 (46.5)	2.27 (32)
BIC	5441.98	5446.20	5457.06	5472.23

β: infection rate; δ: loss rate of infected cells; ω: exponential coefficient of increase immune response; p: rate of viral production; ϕ: maximal rate of immune cell clearance; θ: F concentration giving 50% of ϕ; T_{inf}: time to infection; T_0: uninfected target cells at baseline; σ: residual variability; RSE: relative standard error; BIC: Bayesian Information Criterion

Table S7. Survival analysis (using an exponential model for the baseline hazard function).

	Univariate analysis		Multivariate analysis	
Parameter	**Hazard ratio**	***P-value***	**Hazard ratio**	***P-value***
Obesity	1.29	0.31		
Age ≥65	3.22	$<10^{-5}$	3.02	$<10^{-5}$
Male gender	2.55	$<10^{-4}$	2.63	0.0003
Chronic cardiac disease	1.12	$<10^{-5}$		
Chronic pulmonary disease	3.12	$<10^{-4}$	2.47	0.0003

Table S8. Parameter estimates in the reference survival model and in survival models assuming a hazard starting at the day of infection, day of symptom onset, 7 and 10 days of infection.

	Reference model (RSE, %): with hazard starting at day of admission)		**Model H1: with hazard starting at day of infection**		**Model H2: with hazard starting at day of symptom onset**		**Model H3: with hazard starting at day 7 of infection**		**Model H4: with hazard starting at day 10 of infection**	
Male gender	2.55 (25.2)	<0.001	2.49 (22)	<0.001	2.48 (30.2)	<0.001	2.47 (129%)	>0.05	2.47 (33.6)	0.002
Age ≥65	2.58 (37.9)	<0.001	2.88 (28.5)	<0.001	2.80 (23.4)	<0.001	2.63 (32%)	0.002	2.47 (53.1)	>0.05
Chronic pulmonary disease	2.31 (36.8)	<0.001	2.25 (32.4)	0.002	2.23 (32)	0.002	2.24 (39.3%)	0.01	2.30 (35)	0.004
Log_{10} viral load	1.30 (17)	<0.001	1.05 (61.5)	0.10	1.11 (50.3)	0.04	1.21 (77%)	>0.05	1.35 (14.6)	<0.001
-2LL	5325.26		5408.54		5387.73		5361.95		5352.26	
BIC	5441.98		5525.26		5504.45		5478.68		5468.99	

Annexe 5 : Matériel supplémentaire du chapitre 6

Supplementary data

This file includes:

Supplementary Materials and Methods

Supplementary Figures S1 to S6

Supplementary Tables S1 to S6

Materials and Methods:

Plasma drug determination

Remdesivir requires triphosphorylation by intracellular kinases to be pharmacologically active. After administration, it is metabolized into two main sub-compounds: first GS-441524, the predominant active plasma metabolite, and then GS-443902, which is the PBMC-associated pharmacologically most active metabolite. In a subset of patients from several centers, plasma samples were collected and centralized to measure remdesivir and GS-441524 at day 1 for maximal concentration (C_{max}) and at days 2, 5 and 8 after treatment initiation for trough concentrations (C_{trough}). Both remdesivir and GS-441524 were measured using Liquid Chromatography coupled with tandem Mass Spectrometry, after plasma protein's precipitation with a lower limit of quantification at 1 ng/mL.

Fig. S1. Flowchart of data selection in viral kinetic modeling

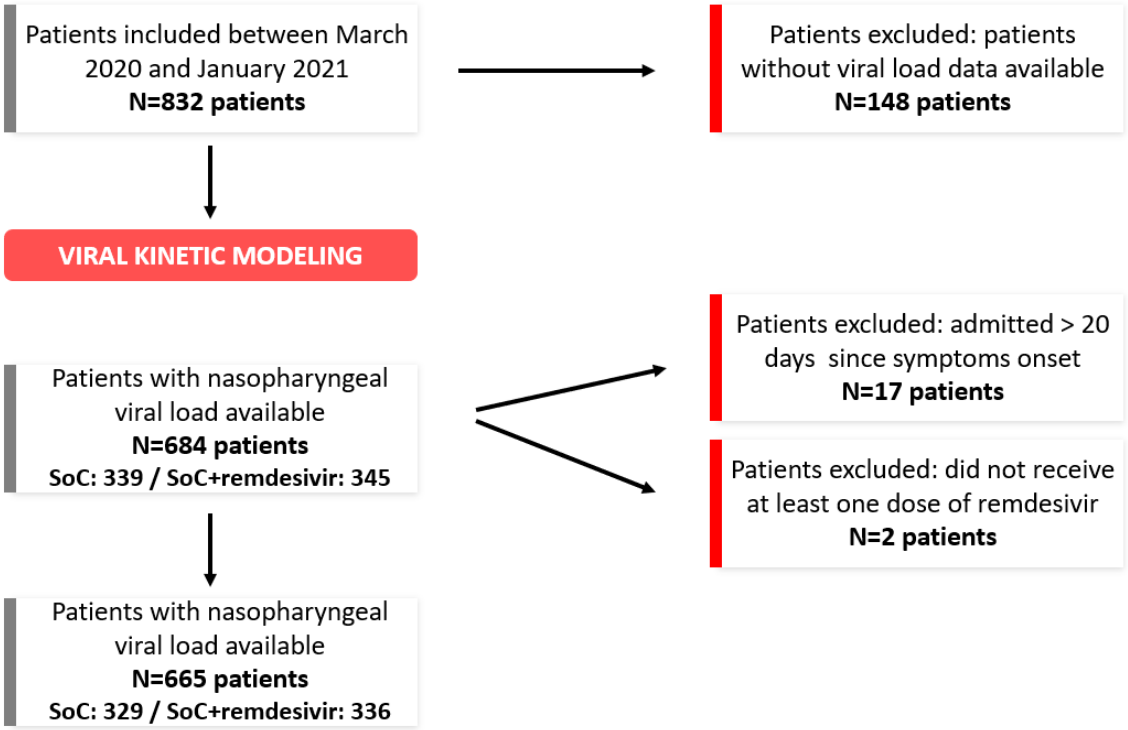

Fig. S2. Distribution of randomization times since symptom onset. Red: patients receiving remdesivir + SoC. Green: patients receiving SoC only.

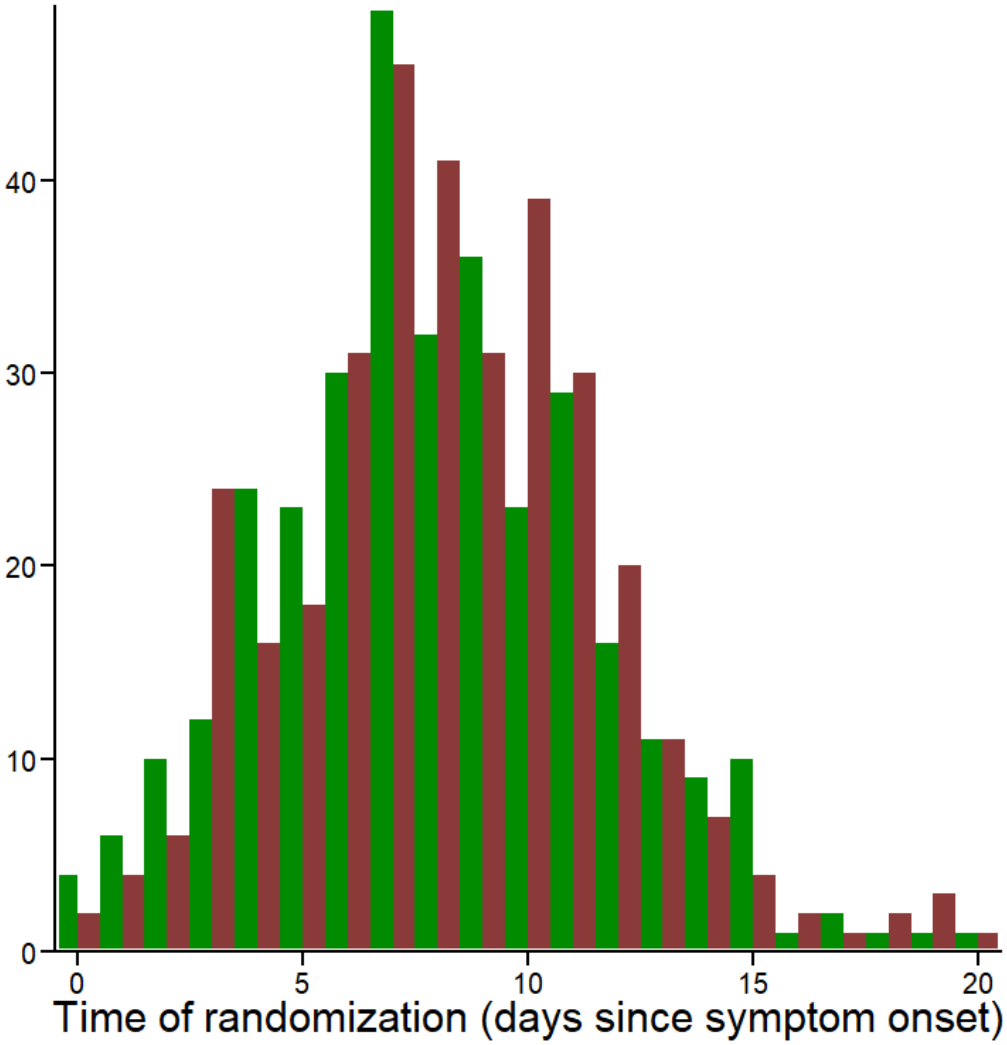

Fig. S3. Viral dynamics predicted by the model in time since randomization. Top: Median predicted nasopharyngeal viral dynamics according to the time since randomization. Bottom: Cumulative incidence of the predicted time to viral clearance. Left: Whole population. Right: Patients with viral load at baseline ≥ 3.5 $\log_{10}$ copies/10^4 cells. Red: patients receiving remdesivir + SoC. Green: patients receiving SoC only. The simulated individuals presented here are the same as in Figure 2 & 4, centered on time of randomization.

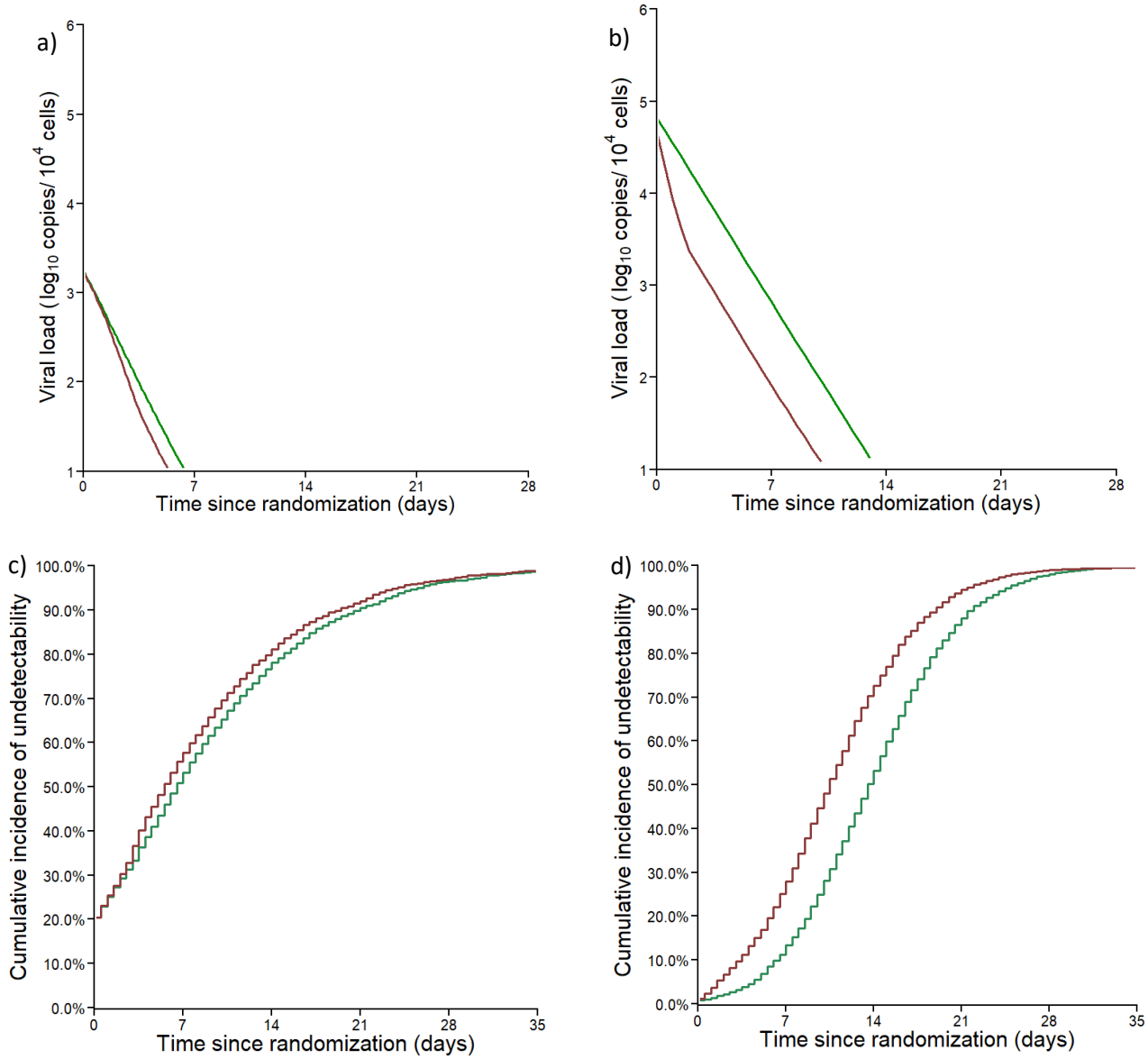

Fig. S4. Nasopharyngeal viral load data in 665 patients from DisCoVeRy trial analyzed in the present study. SARS-CoV-2 nasopharyngeal viral load according to the time since randomization in patients admitted within the first week of symptom onset (N=210, a) and after the first week of symptom onset (N=455, b). Data are presented as means (95%CI). Red: patients receiving Remdesivir + SoC. Green: patients receiving SoC only.

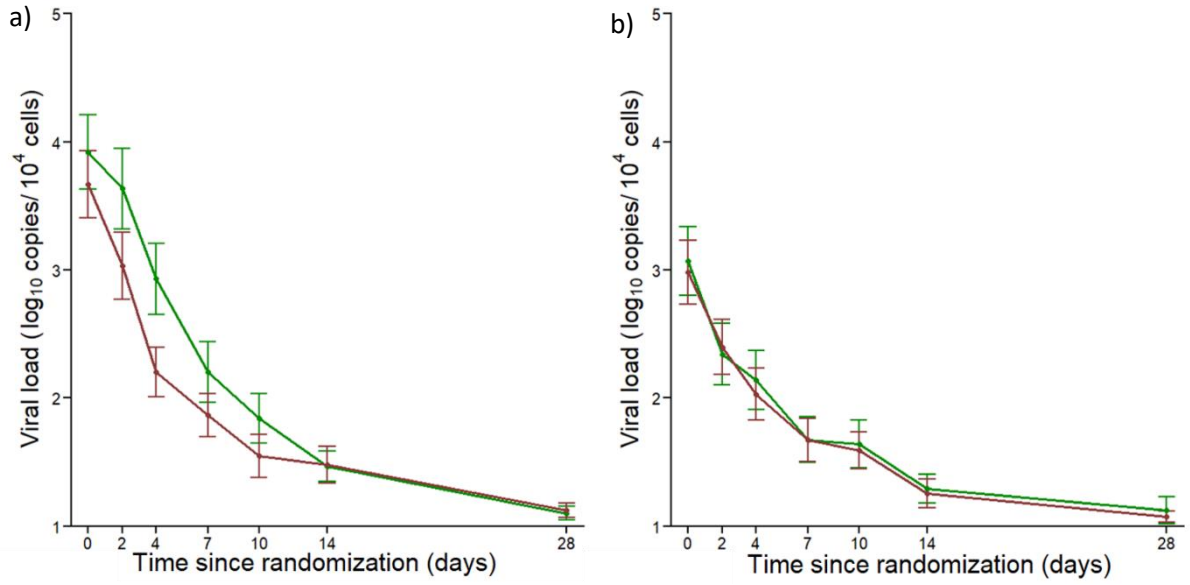

Fig. S5. AUC of viral loads for 5000 simulated patients treated 3, 5, 7 or 9 days after symptom onset, or left untreated. a) Whole population. b) Subpopulation with viral load at baseline ≥ 3.5 $\log_{10}$ copies/10^4 cells. The individual parameters are identical to the ones used in Figure 2 & 4, except for the time of treatment initiation.

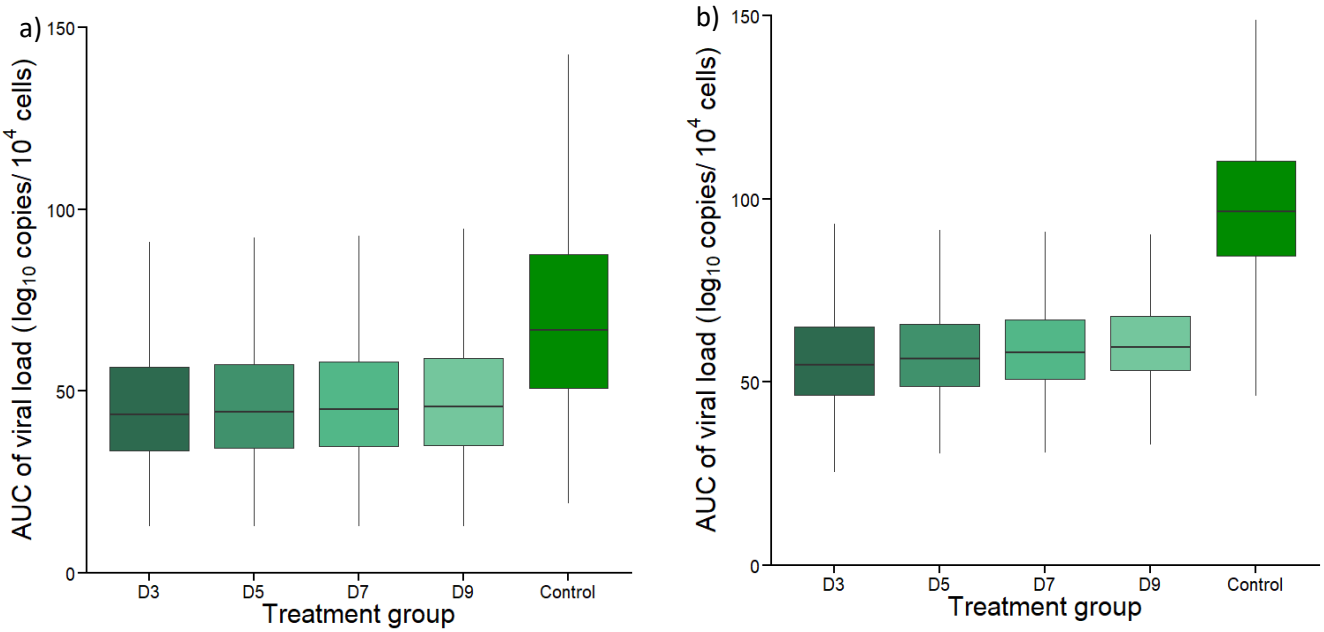

Fig. S6. Pharmacokinetic/pharmacodynamic effect. Predicted individual time to viral clearance versus C_{max} at D1 (N=17, a) and C_{trough} at D2 (N=18, b) of GS-441524 in patients with viral load at baseline > 3.5 log_{10} copies/10^4 cells

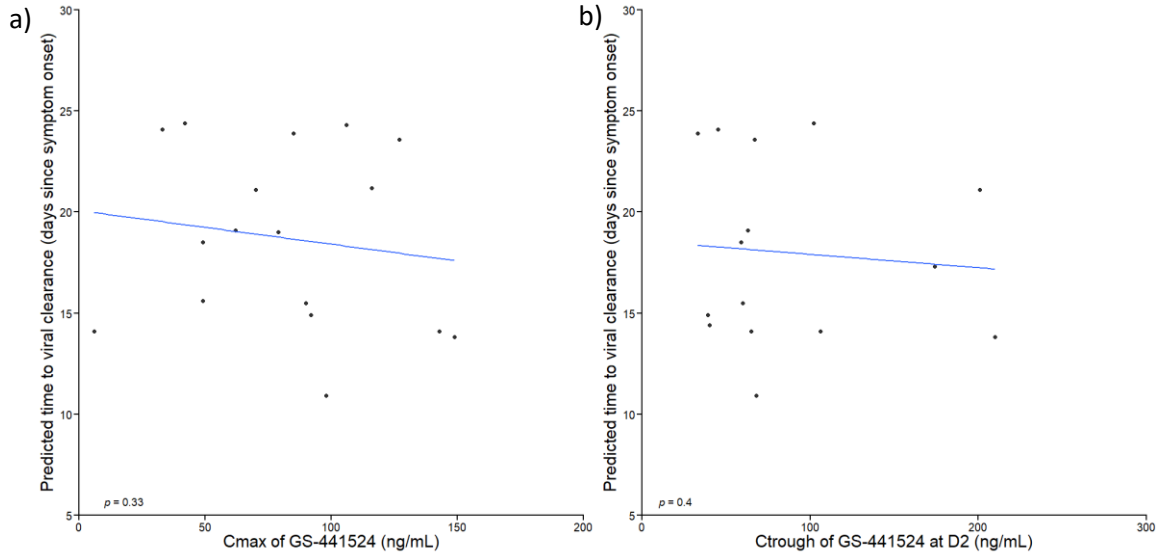

Table S1. Population parameters of models including remdesivir efficacy starting between 0 and 5 days after randomization

T_{lag}	**0**		**1**		**2**		**3**		**4**		**5**	
	Fixed effect (RSE)	Random effect SD	Fixed effect (RSE)	Random effect SD	Fixed effect (RSE)	Random effect SD	Fixed effect (RSE)	Random effect SD	Fixed effect (RSE)	Random effect SD	Fixed effect (RSE)	Random effect SD
R_0	10.2 (11.7)	0.50	10.0 (9.2)	0.50	10.6 (10)	0.50	10.7 (10.2)	0.50	11.1 (10.4)	0.50	10.8 (10.8)	0.50
$\delta_{age}(< 65)$ (d^{-1})	0.89 (4.5)		0.90 (4.2)		0.88 (4.7)		0.88 (4.5)		0.88 (4.4)		0.88 (4.4)	
$\delta_{age}(\geq 65)$ (d^{-1})	0.74 (29.2)	0.45	0.75 (32.0)	0.45	0.73 (25)	0.46	0.73 (30.1)	0.46	0.73 (31.2)	0.46	0.73 (31.0)	0.45
p (10^6 virus. $cells^{-1}.d^{-1}$)	1.30 (16.9)	0.32	1.4 (13.5)	0.31	1.20 (25.0)	0.40	1.20 (21.0)	0.40	1.20 (19.3)	0.34	1.20 (19.7)	0.35
ε (%)	**49 (27.0) p-value=0.020**	0.87	**50 (17.9) p-value=0.033**	0.81	**53 (13.3) p-value=0.0026**	0.74	**52 (16.1) p-value=0.0024**	0.74	**43 (35.2) p-value=0.19**	1.36	**37 (27.9) p-value=0.42**	0.86
σ (virus.mL^{-1})	1.14 (2.27)	–	1.14 (2.18)	–	1.14 (2.18)	–	1.14 (2.28)	–	1.14 (2.19)	–	1.14 (2.30)	–

T_{lag}: pharmacological delay between the administration and the beginning of antiviral efficacy; R_0: basic reproductive number; δ: loss rate of infected cells; p: rate of viral production; ε: remdesivir efficacy; σ: residual variability; RSE= relative standard error.

Table S2a. Population parameters of models including remdesivir efficacy starting between 0 and 5 days after randomization in patients randomized ≤7 days since symptom onset

T_{lag}	**0**		**1**		**2**		**3**		**4**		**5**	
	Fixed effect (RSE)	Random effect SD	Fixed effect (RSE)	Random effect SD	Fixed effect (RSE)	Random effect SD	Fixed effect (RSE)	Random effect SD	Fixed effect (RSE)	Random effect SD	Fixed effect (RSE)	Random effect SD
R_0	17.3 (19.1)	0.50	17.9 (20.6)	0.50	18.4 (30.9)	0.50	18.5 (39.6)	0.50	17.6 (22.3)	0.50	17.4 (20.6)	0.50
$\delta_{age}(< 65)$ (d^{-1}) $\delta_{age}(\geq 65)$ (d^{-1})	0.92 (7.5) 0.84 (91.5)	0.51	0.92 (7.5) 0.84 (91.5)	0.53	0.90 (9.4) 0.81 (89)	0.53	0.89 (11.4) 0.80 (90)	0.53	0.91 (7.9) 0.82 (89.2)	0.51	0.93 (7.4) 0.85 (90.5)	0.51
p (10^6 virus. $cells^{-1}.d^{-1}$)	2.36 (25.5)	0.24	2.43 (30.5)	0.25	2.36 (20.9)	0.25	2.16 (26.8)	0.29	2.18 (33.8)	0.24	2.48 (31.5)	0.20
ε (%)	**12 (80.5) p-value=0.13**	1.48	**6 (97) p-value=0.16**	1.21	**43 (31.3) p-value=0.058**	1.21	**0.36 (49.7) p-value=0.045**	1.70	**18 (57.8) p-value=0.53**	1.30	**14 (51.8) p-value=0.51**	1.08
σ (virus.mL^{-1})	1.11 (3.4)	–	1.11 (3.4)	–	1.11 (3.4)	–	1.11 (3.2)	–	1.11 (3.5)	–	1.11 (3.4)	–

T_{lag}: pharmacological delay between the administration and the beginning of antiviral efficacy; R_0: basic reproductive number; δ: loss rate of infected cells; p: rate of viral production; ε: remdesivir efficacy; σ: residual variability; RSE= relative standard error.

Table S2b. Parameters distribution using model averaging (Median, 95% CI) in patients randomized ≤7 days since symptom onset

	Parameter estimates	
Parameter	**Fixed effects (Median. 95% CI)**	**Random effect SD (Median. 95% CI)**
$\mathbf{R_0}$	18.09 (6.29-30.26)	0.5
$\mathbf{\delta_{age}(< 65)\ (d^{-1})}$ $\mathbf{\delta_{age}(\geq 65)\ (d^{-1})}$	0.90 (0.72-1.07) 0.82 (0.66-0.98)	0.52 (0.44-0.60)
p (10^6 virus.cell^{-1}.d^{-1})	2.20 (1.10-3.40)	1.43 (0.24-3.07)
ε (%)	30 (0*-68)	0.55 (0*-1.85)

R_0: basic reproductive number; δ: loss rate of infected cells; p: rate of viral production; ε: remdesivir efficacy ; *values <0 were set to 0

Table S3a. Population parameters of models including remdesivir efficacy starting between 0 and 5 days after randomization, in patients randomized >7 days since symptom onset

T_{lag}	**0**		**1**		**2**		**3**		**4**		**5**	
	Fixed effect (RSE)	Random effect SD	Fixed effect (RSE)	Random effect SD	Fixed effect (RSE)	Random effect SD	Fixed effect (RSE)	Random effect SD	Fixed effect (RSE)	Random effect SD	Fixed effect (RSE)	Random effect SD
R_0	6.74 (18.3)	0.50	6.76 (14.7)	0.50	6.92 (9.8)	0.50	6.98 (9.8)	0.50	7.77 (9.51)	0.50	7.50 (9.34)	0.50
$\delta_{age}(< 65)$ (d^{-1}) **$\delta_{age}(\geq 65)$ (d^{-1})**	0.94 (5.6) 0.77 (84.5)	0.35	0.94 (5.5) 0.77 (25.8)	0.35	0.94 (5.3) 0.77 (25.4)	0.34	0.94 (5.2) 0.76 (24.9)	0.34	0.92 (4.9) 0.75 (25.4)	0.36	0.93 (5.0) 0.76 (24.5)	0.35
p (10^5 virus. $cells^{-1}$. d^{-1})	6.66 (84.5)	0.63	7.50 (60)	0.60	6.80 (30.1)	0.62	7.00 (31.3)	0.60	8.70 (20.8)	0.48	8.82 (25.1)	0.47
ε (%)	**46 (59.6) p-value=0.9**	0.85	**52 (27.9) p-value=0.9**	0.73	**49 (20.7) p-value=0.9**	0.63	**51 (20) p-value=0.7**	0.61	**41 (47.1) p-value=0.8**	0.88	**41 (24.5) p-value=0.7**	0.61
σ ($virus.mL^{-1}$)	1.14 (2.8)	–	1.14 (2.8)	–	1.14 (2.8)	–	1.14 (2.8)	–	1.14 (2.8)	–	1.14 (2.8)	–

T_{lag}: pharmacological delay between the administration and the beginning of antiviral efficacy; R_0: basic reproductive number; δ: loss rate of infected cells; p: rate of viral production; ε: remdesivir efficacy; σ: residual variability; RSE= relative standard error.

Table S3b. Parameters distribution using model averaging (Median, 95% CI) in patients randomized >7 days since symptom onset

	Parameter estimates	
Parameter	**Fixed effects (Median. 95% CI)**	**Random effect SD (Median. 95% CI)**
$\mathbf{R_0}$	6.91 (4.97-8.65)	0.5
$\mathbf{\delta_{age}(< 65)\ (d^{-1})}$ $\mathbf{\delta_{age}(\geq 65)\ (d^{-1})}$	0.94 (0.84-1.04) 0.77 (0.68-0.87)	0.34 (0.28-0.41)
p (10^5 virus.cell^{-1}.d^{-1})	7.1 (0*-15)	0.61 (0.03-1.19)
ε (%)	50 (16-82)	0.69 (0.05-1.41)

R_0: basic reproductive number; δ: loss rate of infected cells; p: rate of viral production; ε: remdesivir efficacy; *values <0 were set to 0

Table S4a. Parameters distribution using model averaging (Median, 95% CI) in patients with viral load at admission ≥3.5 log_{10} copies/10^4 cells

	Parameter estimates	
Parameter	**Fixed effects (Median. 95% CI)**	**Random effect SD (Median. 95% CI)**
R_0	8.68 (6.59-10.75)	0.5
$\delta_{age}(< 65)$ (d^{-1}) **$\delta_{age}(\geq 65)$ (d^{-1})**	0.70 (0.63-0.77) 0.65 (0.55-0.75)	0.21 (0.15-0.27)
p (10^6 virus.$cell^{-1}$.d^{-1})	3.51 (2.80-4.20)	0.11 (0.02-0.21)
ε (%)	80 (64-96)	2.17 (0.67-3.73)

R_0: basic reproductive number; δ: loss rate of infected cells; p: rate of viral production; ε: remdesivir efficacy

Table S4b. Population parameters of models including remdesivir efficacy starting between 0 and 5 days after randomization in patients with viral load at admission ≥3.5 log_{10} copies/10^4 cells

T_{lag}	**0**		**1**		**2**		**3**		**4**		**5**	
	Fixed effect (RSE)	Random effect SD	Fixed effect (RSE)	Random effect SD	Fixed effect (RSE)	Random effect SD	Fixed effect (RSE)	Random effect SD	Fixed effect (RSE)	Random effect SD	Fixed effect (RSE)	Random effect SD
R_0	8.66 (11.6)	0.50	8.68 (13)	0.50	9.63 (12.8)	0.50	9.94 (11.5)	0.50	9.46 (11.7)	0.50	9.51 (11.6)	0.50
$\delta_{age}(<65)$ (d^{-1}) **$\delta_{age}(\geq 65)$ (d^{-1})**	0.70 (5.2) 0.65 (63.6)	0.21	0.70 (5.3) 0.65 (60.5)	0.21	0.71 (6.6) 0.65 (54.3)	0.22	0.71 (5.0) 0.65 (55)	0.23	0.74 (5.0) 0.67 (58.6)	0.23	0.74 (5.36) 0.68 (61.9)	0.23
p (10^6 virus. $cells^{-1}.d^{-1}$)	3.56 (7.7)	0.11	3.49 (12.1)	0.12	3.36 (20.6)	0.13	3.50 (8.9)	0.10	3.72 (10)	0.08	3.53 (8.5)	0.09
ε (%)	**80 (10.4) p-value<10^{-5}**	2.16	**82 (9.8) p-value<10^{-5}**	2.22	**50 (62.1) p-value<10^{-4}**	3.33	**55 (43) p-value=10^{-4}**	3.09	**18 (78) p-value=0.59**	2.47	**10 (128) p-value=0.81**	2.64
σ (virus.mL^{-1})	1.09 (3.3)	–	1.08 (3.4)	–	1.10 (3.4)	–	1.10 (3.3)	–	1.12 (3.3)	–	1.12 (3.3)	–

T_{lag}: pharmacological delay between the administration and the beginning of antiviral efficacy; R_0: basic reproductive number; δ: loss rate of infected cells; p: rate of viral production; ε: remdesivir efficacy; σ: residual variability; RSE= relative standard error.

Table S5a. Parameters distribution using model averaging (Median, 95% CI) in patients with viral load at admission < 3.5 log_{10} copies/10^4 cells

	Parameter estimates	
Parameter	**Fixed effects (Median. 95% CI)**	**Random effect SD (Median. 95% CI)**
R_0	55.48 (11.31-110.70)	0.5
$\delta_{age}(< 65)$ (d^{-1}) **$\delta_{age}(\geq 65)$ (d^{-1})**	0.49 (0.40-0.58) 0.48 (0.33-0.64)	0.47 (0.38-0.55)
p (10^4 virus.cell^{-1}.d^{-1})	1.26 (0.025-2.61)	0.56 (0*-1.37)
ε (%)	64 (0*-1)	2.35 (0*-7.47)

R_0: basic reproductive number; δ: loss rate of infected cells; p: rate of viral production; ε: remdesivir efficacy; *values <0 were set to 0

Table S5b. Population parameters of models including remdesivir efficacy starting between 0 and 5 days after randomization, in patients with viral load at admission < 3.5 log_{10} copies/10^4 cells

T_{lag}	**0**		**1**		**2**		**3**		**4**		**5**	
	Fixed effect (RSE)	Random effect SD	Fixed effect (RSE)	Random effect SD	Fixed effect (RSE)	Random effect SD	Fixed effect (RSE)	Random effect SD	Fixed effect (RSE)	Random effect SD	Fixed effect (RSE)	Random effect SD
R_0	55.3 (40.1)	0.50	60.7 (60.1)	0.50	51.2 (43.1)	0.50	65.6 (92.1)	0.50	48.7 (36.9)	0.50	64.2 (35.3)	0.50
$\delta_{age}(< 65)$ (d^{-1}) **$\delta_{age}(\geq 65)$ (d^{-1})**	0.53 (8.40) 0.52 (640)	0.43	0.52 (9.6) 0.51 (672)	0.43	0.51 (8.73) 0.50 (823)	0.44	0.49 (9.36) 0.48 (851)	0.45	0.49 (7.98) 0.48 (318)	0.46	0.48 (7.36) 0.47 (772)	0.46
p (10^4 virus. $cells^{-1}.d^{-1}$)	1.93 (40.0)	0.58	2.1 (45.4)	0.74	1.53 (43.4)	0.79	1.48 (49.5)	0.57	1.17 (42.5)	0.44	1.34 (58.5)	0.44
ε (%)	**10 (77.8) p-value=1**	0.60	**11 (67.4) p-value=1**	0.34	**30 (74.8) p-value=0.25**	0.60	**49 (88.2) p-value=0.08**	1.09	**67 (31.7) p-value=0.013**	3.92	**62 (61.4) p-value=0.014**	6.22
σ (virus.mL^{-1})	0.97 (3.6)	–	0.97 (3.6)	–	0.97 (3.6)	–	0.97 (3.6)	–	0.97 (3.6)	–	0.97 (3.6)	–

T_{lag}: pharmacological delay between the administration and the beginning of antiviral efficacy; R_0: basic reproductive number; δ: loss rate of infected cells; p: rate of viral production; ε: remdesivir efficacy; σ: residual variability; RSE= relative standard error.

Table S6. Characteristics of the population with in lower respiratory tract samples

Characteristics	Patients with LRT samples (N=120)
Male gender*	88 (72.7%)
Age*	67.5 (59-73)
Age <65	46 (38.3%)
Age ≥65	74 (61.7%)
Admitted in Intensive Care Units	105 (87.5%)

Modélisation de la dynamique virale du SARS-CoV-2 : Implication pour l'évaluation thérapeutique

Au cours des deux dernières décennies, la modélisation a largement contribué à élucider les déterminants de l'interaction hôte/pathogène des infections virales, à identifier les populations les plus vulnérables et à optimiser les stratégies de traitement. Lors d'une pandémie, l'identification rapide des paramètres clés de la dynamique virale peut fournir des éléments de compréhension de l'histoire naturelle de la maladie, et répondre à des questions essentielles telles que la pertinence de certaines stratégies de traitement. Dans le contexte du SARS-CoV-2, le remdesivir, un médicament antiviral, a montré des résultats contradictoires entre les études concernant l'efficacité clinique chez les patients hospitalisés. Les objectifs de cette thèse étaient de décrire la dynamique virale chez les patients hospitalisés avec le SARS-CoV-2 depuis l'infection jusqu'à la clairance virale, d'explorer le lien entre la dynamique virale et la mortalité et d'évaluer l'effet antiviral du remdesivir chez les patients hospitalisés. Nous avons d'abord utilisé les données des écouvillons nasopharyngés des premiers patients hospitalisés au début de la pandémie, inclus dans la cohorte multicentrique French-Covid (N=655), puis les données de l'essai européen DisCoVeRy (N=665). Nous avons utilisé une approche de modélisation conjointe non-linéaire pour identifier la dynamique virale comme un prédicteur indépendant de la progression de la maladie. Dans un second temps, nous avons estimé une faible réduction de la production virale induite par le remdesivir, et que cette réduction était plus importante chez les patients ayant une charge virale élevée à l'admission. Ces travaux montrent que les molécules antivirales, à condition d'être suffisamment efficaces, ont leur place dans l'arsenal thérapeutique des patients hospitalisés.
Mots-clés : *SARS-CoV-2 ; Charge virale ; Modélisation non-linéaire à effets mixtes ; Modélisation conjointe ; Remdesivir ; Antiviraux*

Modeling SARS-CoV-2 viral dynamics : implication for therapeutic evaluation

In the last two decades, modelling has largely contributed to unravel the determinants of host/pathogen interaction of viral infections, identify the most vulnerable populations and optimize treatment strategies. During a pandemic, rapidly identifying the key parameters of viral evolution can provide elements for understanding the natural history of the disease, and answer critical questions such as the pertinence of certain treatment strategies. In the context of SARS-CoV-2, remdesivir, an antiviral drug, showed some contradictory results across studies regarding clinical efficacy in hospitalized patients. The objectives of this thesis was to describe the viral dynamics in patients hospitalized with SARS-CoV-2 from infection until viral clearance, explore the link between viral dynamics and mortality and evaluate the antiviral effect of remdesivir in hospitalized patients. We first used data of nasopharyngeal swabs from the first hospitalized patients at the beginning of the pandemic, included in the multicentric French Covid Cohort (N=655) and data from the European DisCoVeRy trial (N=665). We used a non-linear joint modelling approach to identify viral dynamics as an independent predictor of disease progression. In a second time, we estimated a weak remdesivir-induced reduction of viral production, and that this reduction was higher in patients with a high viral load at admission. This work show that antiviral molecules, provided that they are sufficiently effective, do have a place in the therapeutic arsenal for hospitalized patients.
Keywords : *SARS-CoV-2 ; Viral load ; Non-linear mixed effects modelling ; Joint modelling ; Remdesivir ; Antivirals*